



**UNIVERSITYTRANSPORTATIONCENTER**  
FOR UNDERGROUND TRANSPORTATION INFRASTRUCTURE

**EXPERIMENTAL INVESTIGATION OF ROCKBURST PHENOMENON  
IN TUNNELS USING A TRUE-TRIAxIAL APPARATUS**

**FINAL PROJECT REPORT**

by

Doandy Yonathan Wibisono  
Omid Moradian  
Marte Gutierrez

University Transportation Center for  
Underground Transportation Infrastructure  
(UTC-UTI)  
Colorado School of Mines

**Sponsorship**

US Department of Transportation  
Contract/Grant No. 69A355174711

October 31, 2024



**COLORADOSCHOOLOFMINES**  
EARTH ■ ENERGY ■ ENVIRONMENT

**Disclaimer**

The contents of this report reflect the views of the authors, who are responsible for the facts and the accuracy of the information presented herein. This document is disseminated in the interest of information exchange. The report is funded, partially or entirely, by grants from U.S. Department of Transportation's University Transportation Centers Program. However, the U.S. Government assumes no liability for the contents or use thereof.

1. Report No. 15		2. Government Accession No.		3. Recipient's Catalog No.	
4. Title and Subtitle Experimental Investigation of Rockburst Phenomenon in Tunnels Using a True-triaxial Apparatus				5. Report Date October 2024	
				6. Performing Organization Code	
7. Author(s) Doandy Wibisono (orcid.org/0000-0003-2346-2171) Omid Moradian Marte Gutierrez (Orcid.org/0000-0001-5070-8726)				8. Performing Organization Report No. UTC-UTI Report 015	
9. Performing Organization Name and Address University Transportation Center for Underground Transportation Infrastructure (UTC-UTI) Tier 1 University Transportation Center Colorado School of Mines Coolbaugh 308, 1012 14th St., Golden, CO 80401				10. Work Unit No. (TRAIS)	
				11. Contract or Grant No. 69A355174711	
12. Sponsoring Agency Name and Address United States of America Department of Transportation Research and Innovative Technology Administration				13. Type of Report and Period Covered	
				14. Sponsoring Agency Code	
15. Supplementary Notes Report also available at: <a href="https://zenodo.org/communities/utc-uti">https://zenodo.org/communities/utc-uti</a>					
16. Abstract Brittle instabilities during tunnel excavation can cause severe consequences, including spalling, rock bursts, and even tunnel collapse. These detached rock fragments compromise tunnel stability and pose significant safety risks to personnel and equipment, often halting operations. Although in-situ studies and lab tests over past decades have advanced understanding of brittle failure, the mechanisms behind the progression and extent of damage remain insufficiently understood, limiting effective prediction and prevention strategies. This project aims to enhance the understanding of brittle instabilities in tunnels through laboratory experiments. The study involves (1) developing an analog brittle rock model, (2) conducting tunnel model tests using a true-triaxial loading cell, a miniature tunnel boring machine (TBM), and acoustic emission (AE) monitoring, and (3) proposing improved analytical and predictive methods for brittle failure. The analog rock was designed to replicate brittle sedimentary rock behavior while maintaining low uniaxial compressive strength (UCS). This allowed for larger specimen sizes and compatibility with low-capacity loading equipment, making it easier to observe progressive tunnel failure. Using the true-triaxial setup and mock TBM enabled realistic simulations of tunneling, capturing the effects of stress unloading and face support. Detailed post-mortem analysis revealed damage mechanisms such as surficial spalling and V-shaped notches caused by progressive shear fracturing, reflecting a brittle-to-ductile transition. AE sensors monitored microcracking in real-time, identifying early indicators of brittle failure. The study also introduced triaxial extension (TE) tests to improve predictions of spalling under more representative stress conditions compared to traditional triaxial compression (TC) tests. TE tests better captured damage characteristics such as entry angles and fracture depth. In tunnel models, steeply angled thin spalling suggested shear-driven fractures rather than purely extensional ones, with fracture surfaces likely forming from shear-induced dilation and friction mobilization. A novel aspect of the research is the use of quadratic Bézier curves to track fracturing progression based on damage and breakout width. This method offers a more accurate depiction of tunnel damage under anisotropic stress than traditional models relying solely on friction angle and logarithmic spirals. In summary, this project advances the understanding of brittle failure in tunnel excavation. The experimental methods and models developed provide practical tools for mitigating spalling and rockburst risks, contributing to safer and more reliable designs in brittle rock environments.					
17. Key Words: Tunneling, slope stability, landslide, deterministic, probabilistic, factor of safety				18. Distribution Statement No restrictions.	
19. Security Classification (of this report) Unclassified		20. Security Classification (of this page) Unclassified		21. No of Pages 93	
				22. Price NA	

## ABSTRACT

Brittle instabilities in tunnel excavation have led to severe consequences such as spalling, violent rock ejection or rock burst, and tunnel collapse. Detached rocks from the tunnel boundary not only compromise the structural integrity of tunnels but also pose significant safety risks to personnel and construction equipment, disrupting the operations. Over the past decades, in-situ studies and laboratory tests have contributed to understanding the brittle failure mechanisms. However, the factors contributing to the progression and extent of brittle failure damage remain not fully understood, limiting the predictive and preventive capabilities.

This dissertation aims to improve the understanding of tunnel brittle instabilities through laboratory experiments. The research focused on (1) developing an analog brittle rock model, (2) performing a series of tunnel model tests using a true-triaxial cell, a mock miniature tunnel boring machine (TBM), and acoustic emission (AE) monitoring, and (3) proposing more robust analytical methods and predictive models for brittle failures.

The analog rock was designed to mimic the brittle behavior of sedimentary rock while maintaining a low uniaxial compressive strength (UCS). This combination of weak and brittle response was vital, as it allowed for using a lower-capacity true-triaxial loading apparatus and enabled large specimens, making it accessible to observe and document the progressive failure inside the excavated tunnel. The true-triaxial setup and mock miniature TBM allowed for realistic tunneling simulations, capturing unloading stress paths and face support behavior. Damage progression observation and post-mortem investigation provide detailed identification of damage mechanisms around the tunnel boundary, such as surficial spalling and damage zone development, as a V-shaped notch formed from progressive shear fracturing and resembled brittle-to-ductile transition. Real-time data on microcracking progression was captured using acoustic emission (AE) sensors during the loading stage, revealing potential precursors on brittle failure onset.

Additionally, triaxial extension (TE) tests were introduced to improve the accuracy of spalling predictions. These tests provided a more representative biaxial stress state and unloading conditions in spalling that proved more robust than conventional triaxial compression (TC) tests, providing factors such as the entry angles and damage depth. In this study, the thin spalling with a steep angle measured from the minor principal stress direction in the tunnel model provided evidence of shear-driven fractures rather than extensional fractures. While steep angles may resemble extensional fractures, appearing perpendicular to minor principal stress, this likely results from shear-induced dilation along the fracture surface, triggering the mobilization of friction angle.



Another novel contribution of this work is the development of quadratic Bézier curves in capturing the successive progression of fracturing based on damage factors and breakout width. This method offers a more robust representation of tunnel damage under anisotropic stress conditions and improves the theoretical logarithmic spiral plastic slip lines that rely solely on friction angle. In conclusion, this research improves the understanding of brittle failure mechanisms in tunneling, contributing to safer and more reliable tunnel designs in brittle rock environments. The developed experimental methods and predictive models offer valuable tools for mitigating the risks of spalling and rockburst during underground excavations.

## TABLE OF CONTENTS

ABSTRACT .....	iii
LIST OF FIGURES .....	ix
LIST OF TABLES.....	xviii
ACKNOWLEDGMENTS .....	xix
DEDICATION .....	xxi
CHAPTER 1 INTRODUCTION, LITERATURE REVIEW, MOTIVATION, AND RESEARCH OBJECTIVES .	1
1.1 Literature Review.....	3
1.1.1 Methodologies to Study Brittle Failure at Tunnel Excavation .....	3
1.1.2 Laboratory-Scale Experimental Models Simulating Brittle Failure in Tunneling.....	9
1.2 Motivation.....	11
1.3 Research Objectives.....	12
1.4 Research Tasks.....	12
1.4.1 Tasks Related to “Objective 1” .....	13
1.4.2 Tasks Related to “Objective 2” .....	13
1.4.3 Tasks Related to “Objective 3” .....	13
1.4.4 Tasks Related to “Objective 4” .....	13
1.5 Organization of Dissertation .....	13
CHAPTER 2 DEVELOPMENT OF A VERY WEAK ANALOGUE SEDIMENTARY ROCK FOR EXPERIMENTAL STUDY TO MODEL BRITTLE INSTABILITY IN TUNNELING.....	15
2.1 Abstract.....	15
2.2 Introduction.....	15
2.3 Experimental Framework.....	19
2.3.1 Selection of Analogue Rock Mixing Method and Constituent.....	20
2.3.2 Material Preparation .....	21
2.3.3 Description of Testing Setup and Acceptance Criteria.....	23
2.4 Material development .....	25
2.4.1 Use of Uniformly Graded Fine Aggregate .....	25
2.4.2 Low Cement Content.....	25
2.4.3 Thermal Exposure.....	26
2.4.4 Curing and Testing Time .....	26
2.4.5 Air-Entraining Admixture Usage .....	26

2.4.6	Saturation and Freezing Before Thermal Exposure.....	27
2.5	Results and Discussions .....	27
2.5.1	Effect of Cement Content Variation .....	28
2.5.2	Effect of Thermal Exposure .....	29
2.5.3	Effect of Air-Entraining Admixture (AEA) .....	29
2.5.4	Effect of Saturation and Freezing Exposure.....	29
2.5.5	Peak Dilation Angle and Elastic Modulus.....	36
2.5.6	Brittleness Assessment .....	38
2.5.7	Micropores Idealization and Cracking Mechanisms .....	41
2.5.8	Comparison of Analogue Material Properties with Natural Sedimentary Rock.....	43
2.6	Conclusions.....	45
CHAPTER 3 EXPERIMENTAL INVESTIGATION OF TUNNEL DAMAGE AND SPALLING IN BRITTLE		
	ROCK USING A TRUE-TRIAXIAL CELL.....	47
3.1	Abstract.....	47
3.2	Introduction.....	47
3.3	Experimental Framework.....	51
3.3.1	Sample Preparation and Characterization.....	51
3.3.2	True-Triaxial Cell and Miniature TBM Setup.....	53
3.4	Experimental Procedure.....	56
3.4.1	Preliminary Works.....	56
3.4.2	Tunnel Excavation using a Miniature TBM .....	57
3.4.3	Stage-Wise Loading .....	58
3.4.4	Post-Experimental Investigation.....	59
3.5	Results and Discussion .....	59
3.5.1	Synthetic Sandstone Properties.....	59
3.5.2	TBM Performance During Excavation.....	65
3.5.3	Induced Damage and Spalling.....	66
3.6	Conclusions.....	73
CHAPTER 4 INVESTIGATION OF TUNNEL SPALLING USING A LARGE-SCALE TUNNEL MODEL AND		
	TRIAXIAL EXTENSION EXPERIMENTS.....	74
4.1	Abstract.....	74
4.2	Introduction.....	75
4.3	Experimental Setup.....	77

4.3.1	Tunnel Model Test Apparatus and Procedures.....	77
4.3.2	Analog Brittle Rock.....	79
4.3.3	Tunnel Model Test Results.....	80
4.4	New Experimental Procedure to Determine Tunnel Spalling Potential.....	83
4.4.1	Three-Dimensional State-of-Stress at Tunnel Wall.....	83
4.4.2	Triaxial Compression and Triaxial Extension States-of-Stress .....	84
4.4.3	Comparisons of Results of TC and TE Element Tests .....	86
4.4.4	Spalling Strength Predictions .....	90
4.4.5	Depth of Spalling Predictions.....	92
4.4.6	Spalling Geometry Predictions .....	94
4.5	Implication to Tunnel Spalling Predictions .....	100
4.6	Summary and Conclusions.....	101
4.7	Supporting Information.....	102
CHAPTER 5 ROCKBURST ANALYSIS IN TUNNEL UNDER ANISOTROPIC LOADING BASED ON LARGE-SCALE TUNNEL MODEL EXPERIMENT AND TRIAXIAL EXTENSION TEST.....		
5.1	Abstract.....	103
5.2	Introduction.....	104
5.3	Experimental Frameworks .....	109
5.3.1	Material Characterization, Tunnel Model Experiment, and Loading Path.....	109
5.3.2	Laboratory Tests for Prediction Points of Spalling Initiation.....	113
5.4	Results.....	116
5.4.1	Excavation Process, Tunnel Geometry, Loading Path, and Acoustic Emission Counts .....	116
5.4.2	V-Notch Spalling Generation throughout Time during Loading, Final Deducted Damage Zones .....	118
5.4.3	Analog Rock Failure Envelopes .....	121
5.4.4	Spalling Initiation Prediction.....	124
5.5	Brittle Failure Geometry.....	125
5.5.1	Depth of Failure <b><i>D<sub>f</sub></i></b> .....	127
5.5.2	Analytical Plastic Slip Line Prediction using Progressive Bézier Curving .....	130
5.6	Conclusions.....	134
5.7	Supporting Information.....	135
CHAPTER 6 SUMMARY AND CONCLUSIONS .....		
6.1.	Summary of Work Done.....	136

6.2.	Major Conclusions .....	137
6.3.	Recommendations for Future Work.....	138
REFERENCES		139
APPENDIX A IDENTIFYING ACOUSTIC EMISSION PRECURSORS FOR ROCK SPALLING ONSET USING TUNNEL MODEL IN A TRUE-TRIAXIAL APPARATUS.....		157
A.1	Abstract .....	157
A.2	Introduction.....	157
A.3	Methodology .....	159
A.4	Results.....	165
A.5	Discussions .....	179
A.6	Conclusions.....	181

## LIST OF FIGURES

Figure 1.1	Brittle failure challenges were encountered at (a) the long-distance water transfer TBM excavation (Kawata et al., 2014) and (b) the Ohio River Tunnel Project in Louisville, KY (des Rivières and Goodman, 2023). Both brittle failures encountered at the tunnel wall caused nuisances to the project and demanded additional efforts to ensure the safety of the personnel.....	2
Figure 1.2	(a) S-shaped failure criterion for brittle rock masses divided into low and high confinement behavioral regions with illustrations of different failure modes (after Castro et al. 2012 and Kaiser 2019); (b) Empirical depth of failure chart in terms of radius of failure in circular opening (after Kaiser 2016). The case studies are taken from Martin et al. (1997) and Diederichs et al. (2009). The damage limit shown in the red line is added according to Perras and Diederichs (2016) and is the anticipated mean depths of failure in brittle failing rock $dfm/RT$ .....	7
Figure 1.3	Schematic illustration for transversal and longitudinal cross sections of the different zones of induced damage around the tunnel constructed with TBM under isotropic loading (modified after Read 2004 and Perras and Diederichs 2016).....	8
Figure 1.4	Failed sample documentation for true-triaxial test with prefabricated hole simulating circular tunnel under three-dimensional high stress conditions; (a) $290 \times 290 \times 290$ mm <sup>3</sup> rock-like mortar sample (Cheon et al. 2011) and (b) $100 \times 100 \times 100$ mm <sup>3</sup> red sandstone sample Gong et al. (2018). ....	10
Figure 2.1	S-shaped or tri-linear failure criterion for brittle rock masses divided into low and high confinement behavioral regions with illustrations of different failure modes (after Castro et al. 2012 and Kaiser 2019). Three envelopes are used to generate this criterion, which are damage threshold/crack initiation (CI), spalling limit ( $\sigma_1/\sigma_3 \approx 10$ to 20), and long-term strength of lab samples/crack damage (CD). ....	17
Figure 2.2	Preparation of cylindrical specimen for laboratory characterization. (a) Pre-mixing of Type I/II Portland cement and F-75 Ottawa sand; (b) Adding water and mixing process in a stand mixer; (c) Tamping and rough surfacing for each layer to ensure the thorough compaction and dense analogue sedimentary rock; (d) Cylindrical specimens in the mold before placement in desiccator chamber. ....	22
Figure 2.3	Displays of three engineering treatments incorporated in the development of the analogue sedimentary rock within trial-and-error framework. Note that the arrangement is following a chronological way to get the final design (mix B) as follows: (a) incorporation of air-entraining admixture while mixing, (b) cylindrical specimens undergo freezing treatment inside a chest freezer with a cooling range of up to -25 °C, and (c) cylindrical specimens undergo thermal exposure, monitored with a digital thermometer for the chamber temperature. ....	25
Figure 2.4	Development process summary with engineering treatment applied and stress-strain curves record as follows: (a) cement content variation, (b) thermal exposure, and (c) air entraining admixture (AEA) usage. Note that for (b) and (c), two different curing times (12 and 28 days) and test times (rest and immediate) were tested. ....	28
Figure 2.5	Freezing temperature and thermal exposure treatments diagram for (a) mix A that underwent only saturation and thermal exposure and (b) mix B that underwent saturation,	

	freezing temperature, and thermal exposure. Sample surface temperature is continually monitored using a FLIR One Pro LT thermal camera.....	30
Figure 2.6	Thin section images and pore size distribution from (a) mix O, (b) mix A, and (c) mix B, each sampled from a $5 \times 9$ mm area.....	31
Figure 2.7	The specimens of both mixes A and B after UCT: (a) UCT and (b) UCT-AE-Ext. mix B specimens exhibited failure characterized by more sub-vertical fractures, parallel to major principal stress extensional fractures, in contrast to the failure pattern observed in mix A. ...	33
Figure 2.8	Mohr circles at failure for unconfined and triaxial compression tests with the best fitting for Mohr-Coulomb and Hoek-Brown failure envelopes for a) mix O—preliminary design, b) mix A—only saturation and thermal exposure, and c) mix B—with additional freezing exposure. ....	34
Figure 2.9	Full stress-strain (upper) and volumetric strain curves (lower) associated with both unconfined and triaxial compression tests for a) mix A—only saturation and thermal exposure, and b) mix B—with additional frost exposure.....	35
Figure 2.10	Configuration for additional data sets from UCT: (a) using circumferential extensometer to measure diametrical deformation (UCT Ext), and (b) integrating an acoustic emission (AE) sensor alongside the extensometer (UCT-AE-Ext). Notably, the AE sensor is not directly associated with diametrical deformation readings. Instead, its inclusion in the figure is intended to illustrate the potential confinement effects, considering the very weak UCS of the specimen. ....	36
Figure 2.11	Calculated properties with the normalized confining pressure to the <i>UCS</i> for mixes O, A, and B; (a) peak dilation angle and (b) elastic modulus <i>E</i> <sub>50</sub> . The first values for each mix were obtained from the UCT under assumed confinement. These assumptions stem from the setup configuration, which includes the circumferential extensometer and the placement of acoustic emission (AE) transducer (refer to Figure 2.10).....	37
Figure 2.12	Evaluations of the brittleness of the analogue material based on the UCT stress-strain curves analogue using (a) burst energy coefficient <i>R</i> and (b) brittleness index modified <i>BIM</i> . ....	40
Figure 2.13	Visual representation of perceived alterations in the microstructure of air voids/entrained micropores across different mixtures, as affected by the different engineering treatments used to prepare the analogue material. Three selected mixes are presented as mixes O, A, and B that were discussed in Section 2.4. These figures serve solely as an illustrative tool for idea comprehension and are generated with assumed and obtained parameters such as micropore sizes, spacings between micropores, and porosity. ....	42
Figure 2.14	Population of growing cracks under triaxial stress condition adopting two-dimensional wing crack model (after Ashby and Sammis, 1990). ....	43
Figure 2.15	Comparative plot depicting the properties of very weak analogue sedimentary rocks developed in this study, alongside data collected from previous studies on natural rock and rock-like materials: (a) Poisson’s ratio (Gercek, 2007), (b) density (Johnson and Olhoeft, 1989; Lama and Vutukuri, 1978), (c) modulus ratio, and (d) strength ratio (Tatone et al. 2023). ....	44
Figure 3.1	Schematic illustration for transversal and longitudinal cross sections of the different zones of induced damage around the tunnel constructed with TBM under hydrostatic loading (modified after Read (2004) and Perras and Diederichs (2016)).....	48

Figure 3.2	Preparation of a cubical specimen for true-triaxial testing. (a) Mold and pre mixing of cement and F-75 Ottawa sand until visually homogeneous solid mix is prepared; (b) freshly mixed synthetic sandstone with consistent homogeneity after adding water and thorough mixing process; (c) tamping rod is adjusted according to the suitable size for different sample geometry; and (d) moisture control and monitor for the specimen inside the mold. ....	53
Figure 3.3	Conceptual illustrations of: (a) concrete backing and cell body; (b) top view of the true-triaxial apparatus configuration without the steel top lid; (c) isometric view of the specimen showing AE sensor placement and tunnel position; and (d) the miniature TBM mounted on the true-triaxial cell. The actual experimental setup is shown in (e). ....	55
Figure 3.4	(a) Positioning the sample into the true-triaxial cell; (b) top view of the sample in the true-triaxial cell before mounting the top steel lid. Annotated for the grouted sides (passive faces) and steel plate jacks (active faces), also the outlet for the hydraulic and AE lines; (c) installing the top steel lid; (d) miniature TBM setup mounted on the true-triaxial cell. ....	57
Figure 3.5	Applied hydrostatic stresses step graph throughout the loading stages. The Roman numerals represent the corresponding loading stage at each hydrostatic condition ( $p_0/\sigma_c$ ). ..	58
Figure 3.6	(a) Axial stress-strain plot representing the majority of the Unconfined Compression Tests, with an error bar (vertical-dotted) to account for variability due to the number of results; (b) axial stress-strain plot representing SCLUC test for one of rockburst criteria evaluations. The red dotted line shows the extrapolation of the unloading curve; and (c) Mohr's circles for unconfined compression and triaxial tests with the best fitting for Mohr-Coulomb and Hoek-Brown failure envelopes. ....	61
Figure 3.7	Photographs of the test samples after loading showing axial dominant and shear failure where the tests were performed at 28 days curing time of the synthetic sandstone. (a) Unconfined compression tests (UCT) and (b) SCLUC tests. ....	62
Figure 3.8	Calculation of synthetic sandstone bursting criteria using stress-strain curve analysis methods: (a) brittleness index modified <b>BIM</b> , (b) burst energy coefficient <b>R</b> , and (c) strain energy storage index <b>F</b> . ....	63
Figure 3.9	Monitoring record of miniature TBM parameters during the excavation stage; (a) face pressure/thrust; and (b) advance rate. ....	65
Figure 3.10	(a) Endoscopic camera to record the spalling behavior inside the tunnel opening using a manual scaling system; (b) images from a perpendicular view of the tunnel axis; and (c) closer tunnel axis view of the final spalling outcomes on the tunnel profile inside the tunnel portal. ....	66
Figure 3.11	Slabbed rock tunnel specimen half axial cross-sections at approximately 50 mm advance length from the tunnel portal. HA denoting Half-Axial, whereas the following codes include the slab number in respect to distance from portal and spot of shots (upper, medium, and lower). Different types and colors of demarcating lines indicate different zones of induced damage around the tunnel boundary. ....	67
Figure 3.12	Slabbed rock tunnel specimen half axial cross-sections at approximately 100 mm advance length from the tunnel portal. HA denoting Half-Axial, whereas the following codes include the slab number in respect to distance from portal and spot of shots (upper, medium, lower, and invert). ....	68



Figure 3.13 Slabbed rock tunnel specimen longitudinal cross-section. LU and LL denoting the longitudinal upper and longitudinal lower, respectively, whereas the following number is the shots numbering.....	69
Figure 3.14 Digitized tracing results in tunnel deformation from longitudinal cut. (a) scatter plot with point picking from tunnel invert and crown. (b) Tunnel deformation and spalling failure along the longitudinal profile of the loaded tunnel with 5x exaggeration for the deformed ground. Note that the initial excavation with miniature TBM resulted in an irregular tunnel shape.....	72
Figure 4.1 Brittle failure challenge in the TBM-excavated tunnel project, showing spalling with low-entry failure angles oriented sub-parallel to the tunnel boundary during excavation (after Kawata et al. 2014).....	75
Figure 4.2 Laboratory-scale tunnel model experiment designed to study tunnels in brittle rock; (a) actual setup at Colorado School of Mines featuring a mounted miniature TBM on top of a true-triaxial cell, (b) conceptual drawings of the excavation unit, (c) digital borehole caliper used to measure initial tunnel diameter, and (d) conceptual drawings of the incremental loading unit.....	78
Figure 4.3 a) Initial tunnel profile after excavation with miniature TBM, (b) final tunnel profile after the loading stage VII, and (c) Effective far-field stress $po'$ applied during the loading stage to the specimen in miniature TBM and true-triaxial cell experimental schematics. Yellow dashed lines in (b) highlight the final spalling failure. In (c), the visible spalling failure was first observed during the transition from loading stage IV to stage V at $po' = 3.2$ MPa, indicated with a red cross mark. (For interpretation of the references to color in this figure legend, the reader is referred to the Web version of this article.) .....	80
Figure 4.4 (a) Longitudinal section of the recovered specimen with cured epoxy resin (red color), (b) half-axial section located 100 mm from the tunnel portal. Epoxy resin was injected into the opening after the final loading stage to preserve final deformation. Annotations show the infiltrated resin (plastic radius $RP$ or $EDZ$ ) and the thickness of spalled rock observed in the section. (c) and (d) provide a closer view of the tunnel damage observed in (b). (For interpretation of the references to color in this figure legend, the reader is referred to the Web version of this article.).....	82
Figure 4.5 Visualizations of the stress state at the tunnel boundary: (a) two-dimensional cross-sectional view showing tangential and radial stress distribution and (b) three-dimensional view illustrating tangential, radial, and longitudinal stress distribution throughout the tunnel length.....	83
Figure 4.6 Initial and final configurations of the laboratory cylindrical tests (element tests) for (a) the TC test, (b) the TE test performed in this study, and (c) the illustration of the stress paths in these tests and post-mortem investigation to obtain failure plane angle $\alpha_{exp}$ and fracture depth $D_{frac}$ . The required stress to induce failure is adopted as $\sigma_{\theta f}$ and will be referred to for each test as $\sigma_f - test$ .....	85
Figure 4.7 Derived failure envelopes from the best-fit hyperbolic curves, generated using data from: (a) BST and TC tests (TC-fitting) and (b) BST and TE tests (TE-fitting). (c) provides the mobilized friction angle $\phi t(m)$ resulting from varying normal stress further from the tunnel, which estimated using Kirsch's elastic solution. ....	88

Figure 4.8	Failed specimens from (a) TC at 0 MPa confinement showing sub-parallel failure planes and (b) TC at 1.5 MPa confinement showing a distinct shear plane. Black dashed lines indicate an approximated fracture plane in the specimens. ....	89
Figure 4.9	Failed specimens from TE tests indicating distinct fracture planes. The failure angle $\alpha_{exp}$ measurements are highlighted by dashed black lines, while dashed red arrows represent the distance between the fracture plane and the unloaded side $D_{frac}$ : (a) complete axial unloading to 0 MPa, (b) partial axial unloading to 0.1 MPa, and (c) partial axial unloading to 0.4 MPa. ....	90
Figure 4.10	Comparison of experimental data and fitted points from cylindrical element tests (TC, TE, BST), along with tangential stress $\sigma_\theta$ values from the tunnel model experiment at the visible spalling initiation and the final loading stage. ....	91
Figure 4.11	Applied stress conditions on the $300 \times 300 \times 300$ mm <sup>3</sup> specimen with a 51 mm circular opening and acoustic emission (AE) monitoring counts during the loading stage. The plot shows the isotropic effective far-field stresses ( $p_o$ , $\sigma_v$ , $\sigma_H$ , $\sigma_h$ ), AE counts, and the cumulative AE counts from six channels. Using a two-dimensional elastic solution, UCT and TE prediction (blue cross marks) are close to loading stage I and II, respectively. ....	92
Figure 4.12	Depth of spalling $D_f$ comparison from the laboratory-scale model with the predicted spalling depth from the TE test $D_f - TE$ and empirical spalling depth correlations (after Martin et al. 1999 and Diederichs 2010). The y-axis shows the absolute spalling depth with $RT=25.52$ mm. In the original equation, the UCS $\sigma_c$ is used in the x-axis, while in this study, it is represented with the element failure strength $\sigma_f$ . ....	94
Figure 4.13	(a) Illustration of theoretical plastic slip lines (after Heuer and Hendron 1971) and developed equiangular log-spiral slip lines around the tunnel boundary with (a) $\phi t - UCT = 44.8^\circ$ from TC-fitting and (b) $\phi t - UET = 54.5^\circ$ from TE-fitting. ....	96
Figure 4.14	Equiangular log-spiral slip lines prediction (black dashed lines) with $\phi t - UCT = 44.8^\circ$ and $\phi t - UET = 54.5^\circ$ , overlaid on half-axial tunnel model cross-sections (after Wibisono et al. 2024). The distances from the portal to the section (tunnel advance) are (a) 50 mm and (b) 100 mm. The white and green dashed lines indicate the spalled region and plastic radius $R_p$ in the original half-axial section. Axes units are in mm. (For interpretation of the references to color in this figure legend, the reader is referred to the Web version of this article.) ....	97
Figure 4.15	Equiangular log-spiral slip lines prediction (yellow dashed lines) with $\alpha_{exp} - UCT = 13^\circ$ and $\alpha_{exp} - UET = 5^\circ$ , overlaid on half-axial tunnel model cross-sections (after Wibisono et al. 2024). The distances from the portal to the section (tunnel advance) are as follows: (a) 50 mm and (b) 100 mm. The white dashed lines indicate the spalled region in the original half-axial section. Axes units are in mm. (For interpretation of the references to color in this figure legend, the reader is referred to the Web version of this article.) ....	99
Figure 5.1	Rock mechanics testing methodology for modeling stress states adjacent to the underground excavation. $\sigma_1$ , $\sigma_2$ , and $\sigma_3$ represent the major, intermediate, and minor principal stresses applied to the specimen, respectively. In tunnel model experiments, applied far-field stresses are denoted by $\sigma_v$ , $\sigma_H$ , and $\sigma_h$ . ....	105
Figure 5.2	Tunnel model experimental schematics: (a) Photo and details of the excavation unit arrangement (after Arora et al. 2021); (b) Loading unit arrangement, including details of the AE transducer locations and applied loading illustration on the cubical specimen (Wibisono et al., 2023a). ....	109

Figure 5.3	Tunnel model experiment with true-triaxial cell and miniature-TBM: (a) two excavation heads for pilot and main tunnel excavation, (b) specimen, loading unit, and AE transducers assembly, (c) tunnel profile measurement using digital borehole caliper, and (d) loading path plan. Of note, the least far-field stress $\sigma_h$ is applied parallel to the tunnel axis. ....	112
Figure 5.4	Simulation of stress states at the tunnel boundary during excavation-induced unloading using cylindrical laboratory tests: (a) two-dimensional consideration using UCT and (b) three-dimensional consideration using triaxial extension (TE) test. ....	115
Figure 5.5	Applied stress conditions on the $300 \times 300 \times 300 \text{ mm}^3$ specimen with a 51 mm circular opening and acoustic emission (AE) monitoring counts during the loading stage. The plot shows the effective far-field stresses ( $\sigma_v$ , $\sigma_H$ , $\sigma_h$ ) and the cumulative AE counts from all channels, with the red cross marking the point of visible spalling initiation. The loading stages are marked with Roman numerals, as shown in the plot. (For interpretation of the references to color in this figure legend, the reader is referred to the Web version of this article.).....	117
Figure 5.6	(a) Progression of spalling failure throughout the loading stage with increasing anisotropy $k = \sigma_v/\sigma_H$ , (b) final failure of the tunnel before cleanup, (c) final failure of the tunnel after cleanup, and (d) specimen recovery process showing the complete failure of the cubical specimen. ....	119
Figure 5.7	Cross-section cuts from recovered specimen with roman numeral markings, with four macro-photographed denoted with A, B, C, and D. Red color indicates the solidified resin that was injected into the failed tunnel profile before unloading. ....	120
Figure 5.8	Failed tunnel specimen from cross-section cuts digitization: (a) isometric view, (b) portal view, and (c) top view. Yellow cross marks represent the digitization of actual fracture locations from the images in Figure 5.7. The light red surface represents the interpolated spline between these points to illustrate the final tunnel profile. The brown surface is digitized from the recovered failed specimen. In (b) and (c), the white highlights indicate the initial main tunnel profile, with the actual recovered specimen shown adjacent to the digitized representation. ....	121
Figure 5.9	Failed specimens from (a) TC and (b) TE tests showing fracture planes. (c) illustrates the measurement of fracture depth $D_{frac}$ in TE tests and the failure plane angle $\alpha_{exp}$ measurements from both tests. ....	123
Figure 5.10	Failure envelopes from the best-fit curve based on data from the following: (a) BST and TC tests (TC-fitting) and (b) BST and TE tests (TE-fitting). ....	124
Figure 5.11	(a) Failure envelope in $\sigma_1 - \sigma_3$ plane, illustrating potential failure modes and fracturing from cylindrical tests across the brittle-to-ductile transition as confinement increases, and (b) the corresponding changes for the fracturing angles, with the entry angle $\alpha_n$ and exit angle $\omega_n$ , as the damage progresses radially outward from the tunnel wall under increasing confinement.....	126
Figure 5.12	(a) Illustration of observed spalling progression in the model tunnel cross-section with hypothesized stress-strain curves of the tunnel wall extending into the rock mass, (b) stress-strain curves, and (c) volumetric strain curves of mix B from both UCT and TC tests. Annotations (1), (2), and (3) in the stress-strain plots indicate increasing ductility with radial distance from the tunnel wall represented as $> x/RT$ . ....	127

Figure 5.13 (a) Depth of spalling measurement $Df$ from digitized cross-section Section I-V and (b) comparison of the measured spalling depth $Df$ with the predicted spalling depth $Df - BT D$ and empirical damage predictions (after Martin et al. 1999). Measured data points from each section were slightly offset to prevent overlap, as they share the same x-values corresponding to the final loading stage.....	129
Figure 5.14 (a) Plastic slip line delineation using the Bézier curve method with three control points and (b) progressive Bézier approach considering mobilized fracturing angles to fit the failed tunnel profile. ....	131
Figure 5.15 Bézier slip line modeling of the final failure profiles from (a) Section-II, (b) Section-III, (c) Section-IV, and (d) Section-V. The darker to brighter gradient dashed lines represent the progression of the fracturing angles following the brittle-to-ductile transition. The bottom left and right legends show the parameters used to fit the actual failure profiles (breakout width $\beta$ , damage factor $\zeta$ , and notch tip counter-clockwise rotation) at the left and right springline, respectively. (For interpretation of the references to color in this figure legend, the reader is referred to the Web version of this article). ....	133
Figure 5.15 Continued. ....	134
Figure A.1 Experimental setup: (a) loading schematics illustration, (b) loading path, (c) actual test assembly with opened steel top lid, showing specimen placement, loading schematics, hydraulic lines, and AE routing.....	159
Figure A.2 Temporal deconstruction methods examples for AE analysis during the loading stage: (a) time intervals using discrete 100-second windows, (b) time intervals with smooth overlapping windows ( $\pm 25\%$ ), and (c) moving number of hits, using windows with 1,000 hits and 25% steps. ....	162
Figure A.3 Progression of spalling failure documentation throughout the loading stage from the portal. Time is shown in minutes and seconds (mm:ss) and has been synchronized with the AE data. ....	166
Figure A.4 Applied stress conditions on the $300 \times 300 \times 300$ mm <sup>3</sup> specimen with a 51 mm circular opening, along with acoustic emission (AE) monitoring data during (a) the first 12 minutes and (b) the 3-6 minute interval of the loading stage. The plot displays the effective far-field stresses ( $\sigma_v$ , $\sigma_H$ , $\sigma_h$ ), AE counts, and the cumulative AE counts from all channels. Additionally, the red cross mark highlights the point of visible spalling onset. ....	167
Figure A.5 Average frequency and peak amplitude clustering during loading stage with time remark on visible spalling initiation (4:35). The clustering limit for each category is based on a previous study of AE characterization on an identical mix design (Gautam and Gutierrez, 2024).....	168
Figure A.6 AF-RA plot over 10 minutes of loading stage with time remark on visible spalling initiation (4:35).....	169
Figure A.7 Average frequency and peak amplitude clustering during loading stage with time remark on visible spalling initiation (4:35). The clustering limit for each category is based on a previous study of AE characterization on an identical mix design (Gautam and Gutierrez, 2024).....	170

Figure A.8	Diverging bar charts showing the temporal evolution of tensile-shear percentage based on the selected $AF - RA$ reference line with 0.2 second time sampling. Two approaches were used, which are (a) direct and (b) moving average.....	171
Figure A.9	(a) FMD plot from time interval 270s-280s with $b$ -value calculation with goodness-of-fit (GFT) tests method and (b) GFT plot for determining AE magnitude of completeness $M_c$ (blue vertical dashed lines). $N$ denoted the number of hits considered in each $b$ -value estimation. ....	172
Figure A.10	Statistical relationship between AE amplitude and frequency during loading stage: (a) the cumulative amplitude distribution and (b) the amplitude distribution. ....	173
Figure A.11	$b$ -values assessments using multiple approaches focusing on minutes 3-6, highlighting the onset of visible spalling. Plots (a), (b), (d), and (f) show the MAXC method for 10-second smooth interval, 20-second discrete interval, 20-second smooth interval, and 1500 hits moving window, respectively. Plots (c), (e), and (g) illustrate the GFT method for a 20-second discrete interval, 20-second smooth interval, and 1500 hits moving window, respectively. The trends indicate varying precursor visibility through $b$ -value fluctuations concerning spalling onset. ....	174
Figure A.12	$b$ -values assessments using multiple approaches focusing on minutes 3-6, highlighting the onset of visible spalling. Plots (a), (b), (d), and (f) show the MAXC method for 10-second smooth interval, 20-second discrete interval, 20-second smooth interval, and 1500 hits moving window, respectively. Plots (c), (e), and (g) illustrate the GFT method for a 20-second discrete interval, 20-second smooth interval, and 1500 hits moving window, respectively. The trends indicate varying precursor visibility through $b$ -value fluctuations concerning spalling onset. ....	176
Figure A.13	$b$ -values assessment closer to the time of visible spalling onset (4:35—275 seconds) using 1500 hits moving window and MAXC. Displayed plots are from CH 6 with an observation period of 240 to 300 seconds. ....	177
Figure A.14	$b$ -values assessment closer to the time of visible spalling onset (4:35—275 seconds) using 1500 hits moving window and MAXC. Displayed plots are from CH 6 with an observation period of 240 to 300 seconds. ....	178
Figure B.1	Permission from publisher to include portions of published ARMA conference papers in Santa Fe, New Mexico 2022 and Atlanta, Georgia 2023. ....	<b>Error! Bookmark not defined.</b>
Figure B.2	Permissions from co-authors to include portions of a published ARMA conference papers in Atlanta, Georgia 2023. ....	<b>Error! Bookmark not defined.</b>
Figure B.2	Continued. ....	<b>Error! Bookmark not defined.</b>
Figure B.3	Permission to use the contents of Wibisono et al. (2024) whose contents have been reproduced in this dissertation with permission from Elsevier. ....	<b>Error! Bookmark not defined.</b>
Figure B.4	Permissions from co-author to include portions of a journal paper, published ARMA conference paper in Santa Fe, New Mexico 2022, and published EUROCK 2023 paper in Helsinki, Finland, 2023. ....	<b>Error! Bookmark not defined.</b>
Figure B.5	Permission for Figures 1.1a and 4.1 from the Japanese Society for Rock Mechanics (JSRM). Pictures taken from Kawata et al. (2014) ....	<b>Error! Bookmark not defined.</b>

Figure B.6	Permission for Figures 1.1b. Picture taken from des Rivières and Goodman, (2023). ....	<b>Error! Bookmark not defined.</b>
Figure B.7	License for Figures 1.2a and 2.1. ....	<b>Error! Bookmark not defined.</b>
Figure B.8	License for Figure 1.2b. ....	<b>Error! Bookmark not defined.</b>
Figure B.9	License for Figures 1.3 and 3.1. ....	<b>Error! Bookmark not defined.</b>
Figure B.10	License for Figure 1.4a.....	<b>Error! Bookmark not defined.</b>
Figure B.11	License for Figure 1.4b .....	<b>Error! Bookmark not defined.</b>
Figure B.12	License for Figure 2.15 .....	<b>Error! Bookmark not defined.</b>

## LIST OF TABLES

Table 1.1	Brittle failure hazard classification chart examples. These charts are developed on certain brittle failure cases (spalling/rockbursting). The charts visualize the indices used for classification, with the following marks: N for none, L for low, M for moderate, H for high, and VH for very high. The last chart has sub-classes for the hazards: moderate-low (M-L), moderate-medium (M-M), and moderate-high (M H).....	5
Table 2.1	Summary of mix design and proportions (by weight) for the analogue sedimentary rock. ....	23
Table 2.2	Summary of mix design (engineering treatments, cement content, water to cement ratio) and laboratory test results (material physical and mechanical properties) for mixes O, A, and B. ....	32
Table 2.3	Brittleness assessment with rock bursting criteria used for the analogue sedimentary rock mixes O, A, and B. ....	41
Table 3.1	Summary of mix design and proportions for synthetic sandstone mix. ....	52
Table 3.2	Summary of the synthetic sandstone test results (physical properties, UCT, Brazilian, SCLUC, and triaxial).....	60
Table 3.3	Summary of current synthetic sandstone mix characterization to the rock bursting criteria used in this study. ....	64
Table 4.1	Summary of analog sandstone mechanical properties from previous laboratory characterization. The mix design is denoted with Mix O.....	80
Table 4.2	Summary of the initial tunnel model boundary condition and experiment results, including tangential stress $\sigma_\theta$ , final spalling depth $Df$ , and depth of plastic radius $Rp$ or excavation damage zone $EDZ$ based on resin infiltration.. ....	81
Table 4.3	Summary of TE and TC test results, including minor confining pressure at failure $\sigma_3$ , differential stress $\sigma_1 - \sigma_3$ , measured failure plane angle $\alpha_{exp}$ , and depth of fracture $D_{frac}$ . The last two parameters were measured from the failed cylindrical specimens (see Figures 4.6 and 4.7). ....	87
Table 5.1	Laboratory studies of spalling around circular openings with true-triaxial cells under anisotropic loading. The presentation order in the table is organized by the experiment type and chronological order. ....	106
Table 5.2	Summary of mechanical properties of analog sedimentary rock mix and Mohr-Coulomb fitting parameters based on previous laboratory characterization results. The mix design, called Mix B, exhibits improved brittle response with reduced UCS (Wibisono, 2024). ....	110
Table 5.3	Summary of TE and TC test results, including minor confining pressure at failure $\sigma_3$ , differential stress $\sigma_1 - \sigma_3$ , measured failure plane angle $\alpha_{exp}$ , and depth of fracture $D_{frac}$ . The last two parameters were measured from the failed cylindrical specimens (see Figures 5.6 and 5.7). ....	122

## ACKNOWLEDGMENTS

First and foremost, praise goes to the One to whom I owe it all—thank God, my savior Jesus Christ. Thank You for your goodness, loving care with your sovereignty and wisdom, and for walking beside me throughout this journey. I am truly nothing without You.

I would like to thank my advisor and mentor, Professor Marte Gutierrez, for his kind guidance and patience, which have helped me strive in the experimental mechanics of tunneling. The topic of brittle failure is challenging and caused me significant struggles, but I am grateful to have learned this subject with his support and inspiration. In addition to the technical aspects, I gained precious insights into professionalism and a strong work ethic from him. Professor Gutierrez's dedication and work ethic have impacted me, embodying what I learned as the "samurai way of teaching." His influence has instilled in me the spirit to be independent and precise in my work.

This study is financially supported by the University Transportation Center for Underground Transportation Infrastructure (UTC-UTI) at the Colorado School of Mines, Golden, Colorado, under Grant No. 69A3551747118 from the US Department of Transportation (DOT). The opinions expressed in this dissertation are solely those of the author and do not reflect the views of the DOT. I am grateful to the rest of my dissertation committee, Dr. Sebnem Duzgun, Dr. Shiling Pei, and Dr. Wendy Zhou, for all their time and valuable insights throughout this journey since the qualifying exam. I want to thank my professors/faculty members and staff at Mines who were not a part of my dissertation committee but contributed to my education. Special thanks go to Lori Tunstall, Ahmadreza Hedayat, Gabriel Walton, Alexandra Wayllace, Roel Snieder, Hugh Miller, Mike Mooney, Junko Marr, Jamal Rostami, Bruce Yoshioka, Jennifer Briggs, Ryan Lambert, Kimberly Brock, Megan Abbey, Sarah Gould, and Christine Monroe for their insightful support throughout my academic journey.

To my predecessors and post-doctorate fellows, some of whom I have worked with, namely, Simon Prassetyo, Ketan Arora, Xiongyu Hu, Pradeep Gautam, Dipaloke Majumder, Gauen Alexander, Omid Moradian, Jesse Hampton, and Luke Frash, thank you for all remote or direct technical support and fruitful conversations we shared. Next, to the members of Professor Gutierrez's research group, past and present—*"the last samurai"*—Bibek Karki, Linqi Liu, Wonhi Lee, Abhishek Shetty, Steve Benfield, Simon Faundez, Mair Beesley, John Dosch, Gustavo Miguel, thank you for your friendship and for walking this stage of life with me. A big shoutout to BE126 office mates Joey Verkler, Gav Houston, Aubrie Caldwell, Awais Butt, Robin Cheng, Alexa Garin, Rakshith Shetty, Sana Zafar, and Yunsik Jung for helping me balance the rigors of my Ph.D. journey with plenty of fun distractions.

My gratitude extends to the ARMA Colorado School of Mines student chapter board members for the opportunity to serve, particularly my Rock Blasters teammates, Akash Chaurasia and Isabella West,



for our success as runner-up in the ISRM Congress's Rock Bowl Austria. I would also like to thank the Indonesian Student Association (Permias) Golden for the camaraderie and shared moments of joy that made life in Golden feel warm, cheerful, and welcoming, particularly Farid Rahman, Rilga Syafidra, Gama Firdaus, Hafidha Aristien, Abraham Purba, Shaskia Putri, Sandra Labobar, Damanhuri Nasution, Ryan Pratama, Henri Setiaji, Hanaga Simabrata, Fitra Isa, Bias Adibrata, Dzulfaqar Ariq, Aditya Juganda, Ahmad Jeli, Jayanti Tangdiombo, Dwi Siregar, Wiwin Febrianto, Celestlin Hutagalung, Fitrah Pratama, Luthfi Saifudin, Akbar Laksana, Ekky Harun, Erika, Aldifa Afimanya, Viska Putri, Kofa Dewanda, Hayati Agustini, Irfan Putra, Wendy Airlangga, Dessy Sapardina, Aldis Ramadhan, Enos Napitupulu, Yudha Jatmiko, Yonas Dwiananta, Mirza Pratama, Cahyo Angkoso, Tressna Gandapradana, Rizky Al Fadhli, Ida Bagus Bram, Apim Atmaja, Bryan Prasetyo, and the rest of the group.

I sincerely thank my mentors and colleagues at PT Anggun Permai Tekindo (Aptekindo) in Indonesia. I am incredibly thankful to Pak Mohamad Sadikin, Bu Eryani, Pak Eddy Juliansyah, Okky Chandra Perdana, and Cyrillus Arthur Saputra for their unwavering support and guidance. I also gratefully acknowledge partial financial support from Aptekindo. To my colleagues and friends at Mines or around the world who are always up for life and technical discussions, Derrick Chambers, Rick Wenzel, Mark Neuroth, David Joseph Hutaaruk, Terry Thompson, Joe and Debbie Burke, Doug and Katie Neely, Pema Lama, Alvin Bayudanto, Fauzan Yudho Pratomo, Bernando Sihaloho, Alfonso Tampubolon, Johannes Riter, David Sihotang, Krisna Darmawan, Susanto Prakoso, Adriel Aritonang, Louisa Panggabean, Dineta Oki, Indra Gandawijaya, Max Nababan, Herani Kurnia, Nirmana Fiqra Qaidahiyani, Kevin Manullang, Bung Eduard Pupella, Andri Suprayitno, Apresio Kefin, Gita Andhika, Muthia Amanda, Joel Napitupulu, Marthen Lalang, Pradipto, Efraim Mangiwa, Sandy Herho, Agung Hariyadi, Sam Lolon, Michael Hutahaeon, Rahmadi Aryo, Lintang Andika 'Diko', Aditya Rachmanto, Bung Zethi, Yudhi Wicaksana, and Aditya 'Papol' Nugraha<sup>†</sup>. Your belief in me has been a driving force, encouraging me to keep pushing forward and to continue learning. I am blessed with meaningful experiences and the opportunity to work alongside you on this journey.

Finally, I would like to thank my wife, Kenny Meylitta Nauli, for her endless love and support, without which this dissertation would not have been possible. I also want to take a moment to send my love to my twelve-month-old (and counting) baby girl, Kana Donda Geraldine. Hi Kana, you have been a true blessing and the source of countless joyful moments these past few months. I will always love you!

This dissertation is dedicated to my family.

First, to my wife, Kenny Meylitta Naully,  
who has been an endless source of support, sacrificial love, and friendship.

Second, to my little one, Kana Donda Geraldine, who arrived here during my PhD journey.

You have made this whole experience worthwhile.

May you always know how dearly loved you are.

To my brothers and sisters, Andre, Hendrick, and Christy, for being an inspiration and for your prayers.

Finally, to my parents (Ricardo Mangunsong<sup>†</sup> and Sri Hedy Yati), whose many years of sacrifice, love, encouragement, and support have been invaluable.

*Yet in all these things  
we are more than conquerors  
through Him who loved us.  
(Rome 8:37)*

*For Yours is the kingdom,  
and the power  
and the glory forever.  
Amen.*

## CHAPTER 1 INTRODUCTION, LITERATURE REVIEW, MOTIVATION, AND RESEARCH OBJECTIVES

The brittle, violent failure of rock poses a significant threat to subsurface engineering endeavors, such as deep tunneling projects. As infrastructure development projects expand into mountainous regions, transportation and hydroelectric tunnels are being excavated to unprecedented depths (Zhu et al., 2019). For example, the Olmos Trans-Andean Tunnel in Peru encountered overburdens of up to 1930 meters, the Gotthard Base Tunnel in Switzerland was constructed with an overburden of up to 2300 meters, and the tunnels of Jinping II in China reached a maximum overburden of 2525 meters (Eberhardt et al., 2016). In such substantial depths with brittle rock formations, potential damage can manifest in various forms, including spalling, rockbursting, and developing of excavation damage zones. Consequently, civil tunnel engineers are becoming more cognizant of the challenges associated with construction of deep-level tunnels, particularly those excavated by tunnel boring machines (TBM) (Rojat et al., 2009).

A recently published report discusses that compressive failure modes and degradation of tunnel wall integrity occurred during a TBM-excavated tunnel, although not necessarily at great depths or in hard rock. In the case of the Ohio River Tunnel Project in Kentucky, United States, the brittle failure phenomena have been reported to delay the final lining installation progress (Figure 1.1a). The 6.1 meters diameter TBM-driven tunnel encountered tunnel was excavated through sedimentary rock at a depth of approximately 60.9 meters below ground elevation (des Rivières and Goodman, 2023). The high horizontal stresses induced by the glacial event in the region are likely responsible for the overstress condition at the tunnel boundary, evident from the significant failure observed in the crown and invert areas. Another example is the Pahang-Selangor Raw Water Transfer Tunnel Project in Malaysia, where the depth of overburden reached only 1246 meters (Figure 1.1b). Despite the relatively shallower depth, brittle failure during TBM excavation caused significant nuisance throughout the project (Kawata et al., 2014).

When considering rock mass instability in underground excavations from an engineering perspective, it can be broadly classified into two categories: 1) structurally controlled or gravity-driven fallout, and 2) strength-controlled or stress-driven rock mass yield (Diederichs, 2003). Typically, the former is more prevalent in low-stress environments, while the latter is more common in high-stress environments. Prediction of potential damage and failure in high-stress environment, massive, and brittle rock formations, therefore, remains a critical challenge in rock mechanics. When underground excavations are undertaken, the stresses surrounding the tunnel boundaries are inevitably perturbed, leading to induced damage to the rock mass. The extent of this damage is mainly influenced by the in-situ stress levels and rock mass properties.

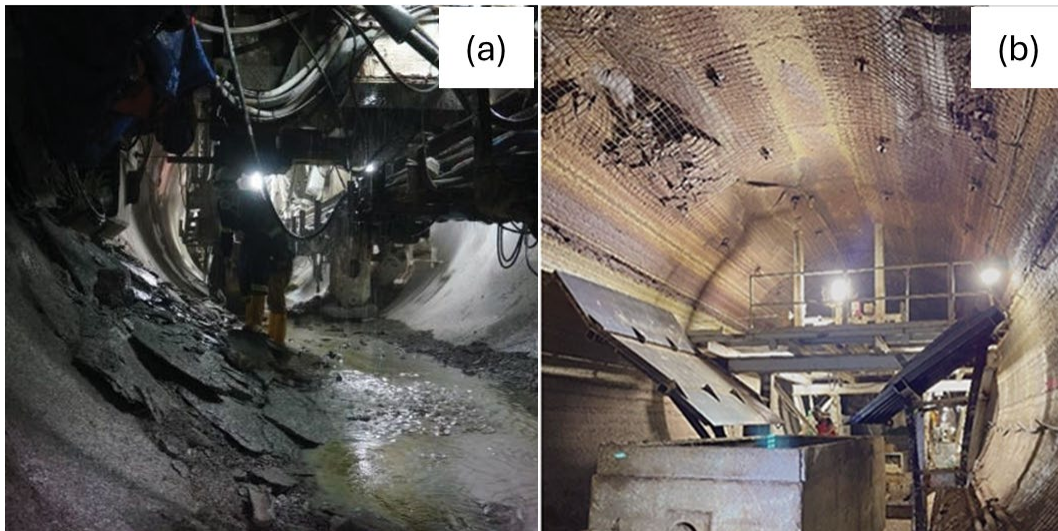


Figure 1.1 Brittle failure challenges were encountered at (a) the long-distance water transfer TBM excavation (Kawata et al., 2014) and (b) the Ohio River Tunnel Project in Louisville, KY (des Rivières and Goodman, 2023). Both brittle failures encountered at the tunnel wall caused nuisances to the project and demanded additional efforts to ensure the safety of the personnel.

Unlike ductile rocks with more contractive response and gradual deformation to failure, brittle rocks exhibit distinct behavior under stress. Brittle fracture, as defined by Brady and Brown (2007), is defined as a rapid loss of strength without significant or long-term plastic deformation. Brittle fractures demonstrate a well-defined peak shear strength, indicating their ability to withstand a certain extent of stress. Beyond this peak shear strength, though, there is a pronounced reduction in strength, known as strain softening to residual shear strength (Nygård et al., 2006). This reduction in strength is accompanied by increased fracturing and damage within the rock mass, which has profound implications for tunnel excavation projects.

The occurrence of strain softening in brittle rocks can result in rapid and catastrophic failure of tunnel walls, particularly during certain stages of the excavation phase when the rock mass is exposed without ground support. The tunnel boundary would be exposed to the initiation, propagation, and coalescence of fractures at a perturbed rock mass that can compromise the stability and structural integrity of the tunnel. Nevertheless, the fractures in the rock mass can develop without interacting with each other, but eventually, they merge, causing a rapid decrease in rock strength (Perras and Diederichs, 2016). In stiff materials under high stress, a brittle failure process can lead to rockburst, a violent form of brittle failure. The process of brittle failure, whether violent or not, can lead to spalling failure. Hence, it is crucial to have thorough comprehension over the characteristics and behavior of brittle rocks to ensure successful planning, execution, and upkeep of tunneling excavations.

To overcome the challenges associated with tunneling through brittle rock formations, it is crucial to develop mitigating techniques for assessing potential damage and failure. When analyzing the potential damage, it is worth distinguishing between the source mechanism and the mechanism of damage. This differentiation helps us to understand the cause-and-effect relationship between these two elements. Understanding the distinction leads to providing accurate and efficient strategies to address the unique properties of brittle rocks and take preventive measures or make necessary modifications to mitigate the potential damage from the subsequent mechanism. This approach enables the planning, execution, and maintenance of safe tunneling projects with confidence.

## **1.1 Literature Review**

To investigate the issue of brittle failure in tunnel excavations, numerous methodologies have been proposed. These approaches typically rely on field observations, laboratory experiments, and numerical and physical simulations of tunnels to understand their inherent brittle failure. This section provides an overview of these methodologies, as well as the laboratory physical models that have been developed to analyze tunnel excavation under brittle ground conditions.

### **1.1.1 Methodologies to Study Brittle Failure at Tunnel Excavation**

The understanding of brittle failure, in rock engineering, relies on the development of two classical theories. These theories approach brittle failure from different perspectives that contribute to each other, one through empirical observations and the other through physical model developments (Kaiser and Kim, 2015). The first approach involves defining a specific failure criterion based on an empirical approach that is consistent with the observed failure conditions. The second approach establishes a physical model of the brittle failure process that can be theoretically demonstrated.

Particular to the underground excavation projects, the encountered properties of rock and the stresses can vary significantly and are considerably site-specific. This variability makes it difficult to rely solely on analytical approaches to predict the behavior of the rock mass accurately, unlike other engineering domains where materials and conditions can be more precisely controlled and predicted (Hajiabdolmajid and Kaiser, 2003). In this study, there are three enlisted empirical approaches that were developed for guidelines in terms of brittle failure susceptibility, hazard, and damage prediction in underground excavations: (1) hazard classification based on certain factor indices, (2) brittle failure proneness assessment, and (3) potential damage analysis.

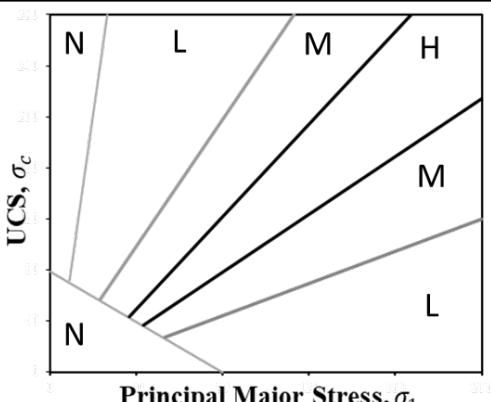
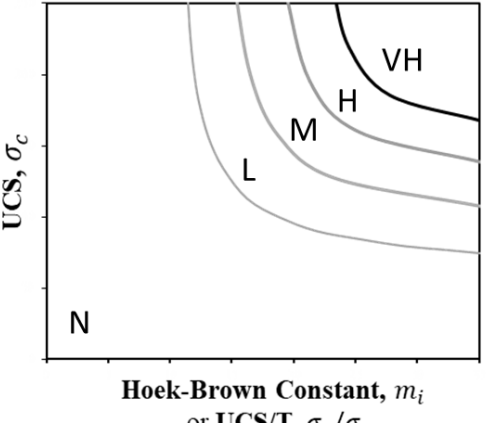
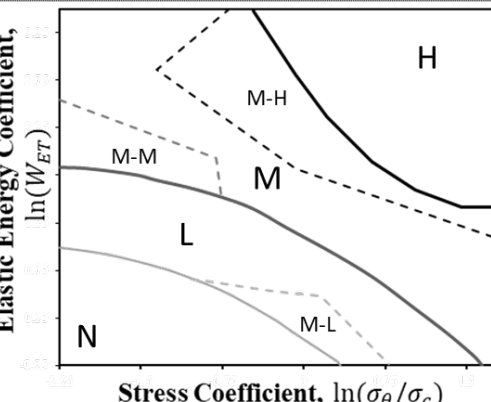
The first type of listed approach is the empirical chart related to brittle failure hazard classification (Barton et al., 1974; Diederichs et al., 2009; Farhadian, 2021; Palmström, 1995; Russenes, 1974). These are remarkable efforts to articulate the brittle failure potential in form of spalling or rockburst to the underground excavation based on certain factor indices from the rock mass (e.g. uniaxial

compressive strength  $\sigma_c$ , principal major stress  $\sigma_1$ , Hoek-Brown constant  $m_i$ ). The development of this hazard classification continues to grow with updated brittle failure cases, including the multi-dimensional prediction of the hazard potential with inclusion of additional rock mass indices (Farhadian, 2021). However, general usage of these empirical charts appears to be limited for the preliminary assessment of brittle failure potential and needs to include more factors into consideration. Table 1.1 summarizes some examples of the developed empirical charts along with the indices used.

The second listed empirical approach is often associated with brittleness assessment. Some methods to assess this brittle failure proneness are including but not limited to rock mass strength parameters calculation (e.g. strength brittleness index  $B_1$ ) and unconfined compression test (UCT) stress-strain curve analysis (brittleness index modified  $BIM$ , strain energy storage index  $W_{ET}$ , and burst energy coefficient  $R$ ). Gong et al. (2020) reported 20 criteria that were developed to estimate the brittle failure potential solely from the cylindrical core specimens. The stress-strain curve can provide insights on how the intact rock behaves under loading and unloading, which translated to the rock mass response due to the tunneling excavations. This empirical approach should be used in caveat with broader consideration on other parameters such as the in-situ stress condition, excavation shapes, and both geological and man-made structures at the vicinity of the underground excavation.

The potential damage analysis, as the third empirical approach, elaborates the following aspects: (1) failure modes, (2) rock mass properties, (3) encountered stress, and (4) assessment of the depth of failure/yield. Kaiser (2019) integrated the term in-situ "stress level index" SLI to the rock mass quality RMQ to characterize different modes of rock mass failure including brittle failure. The stress level index is the ratio between the maximum tangential stress at the tunnel boundary  $\sigma_{\theta max}$  to the unconfined compressive strength of the rock  $\sigma_c$ . This inclusion allows a broader view on assessing the brittle failure modes that are predominantly a function between stress-level and rock mass properties.

Table 1.1 Brittle failure hazard classification chart examples. These charts are developed on certain brittle failure cases (spalling/rockbursting). The charts visualize the indices used for classification, with the following marks: N for none, L for low, M for moderate, H for high, and VH for very high. The last chart has sub-classes for the hazards: moderate-low (M-L), moderate-medium (M-M), and moderate-high (M-H).

Empirical Charts	References	Remarks
 <p>UCS, <math>\sigma_c</math></p> <p>Principal Major Stress, <math>\sigma_1</math></p>	<p>(Barton et al 1974; Russenes 1974; Palmström 1995)</p>	<ul style="list-style-type: none"> <li>- Some of the early works used the point load strength index that further correlated to the UCS.</li> <li>- Summarized into graphical chart by Zhou et al. (2016).</li> </ul>
 <p>UCS, <math>\sigma_c</math></p> <p>Hoek-Brown Constant, <math>m_i</math> or <math>UCS/T, \sigma_c/\sigma_t</math></p>	<p>(Diederichs et al 2009)</p>	<ul style="list-style-type: none"> <li>- Higher value in y-axis resembles the energy potential level, while higher value in x-axis reflects the spalling potential.</li> <li>- Weaker rocks can undergo spalling without strain bursting, often linked to low potential energy.</li> </ul>
 <p>Elastic Energy Coefficient, <math>\ln(W_{ET})</math></p> <p>Stress Coefficient, <math>\ln(\sigma_\theta/\sigma_c)</math></p>	<p>(Farhadian 2021)</p>	<ul style="list-style-type: none"> <li>- Elastic energy coefficient, also known as strain energy storage index <math>W_{ET}</math> (Kidybiński, 1981)</li> <li>- Analyzed from the stress-strain curves of unconfined compression test (UCT) with unloading.</li> <li>- This chart is developed by integrating 20 case studies with different type of rocks.</li> </ul>

One thing that is notable with this potential damage analysis empirical approach is that the observed feature that brittle failure mode may vary with the effect of confinement. Tensile stresses induced during anisotropic loading of heterogeneous rock, as explained by Diederichs (2007a), resulted in Griffith type extension fracturing with a depressed failure envelope in the low confinement zone, where fracture propagation causing spalling is not suppressed by the available confining pressure. The resulting failure envelope for a rock mass in the minor-major principal stress domain is then an s-shaped or the trilinear shape curve, which can be divided into two behavioral zones; (1) spalling dominated stress fracturing at low confinement and (2) shear rupture dominated behavior at high confinement. Figure 1.2a presents the S-shaped failure criterion for brittle rock masses with stress space zoning in underground rock engineering and failure mode highlights.

Furthermore, the function is also compliant with the depth of failure  $d_f$  assessment that is developed based on observed case histories on spalling (Figure 1.2b). The depth of failure  $d_f$  is the point at which a rock mass fails and unravels if it is not supported, or the maximum depth of notch formation by spalling recorded in a tunnel domain (Hoek and Martin, 2014). The initial trends of the normalized depth of failure to the tunnel radius  $d_f/R_T$  based on the stress level index SLI is defined by:

$$\frac{d_f}{R_T} = 1.25 SLI - 0.51 \quad (1.1)$$

This linear fitting was first adopted, until Perras and Diederichs (2016) observed the non-linear correlation at higher SLI and included the term excavation damage zones based on the calibrated numerical modeling. Kaiser (2019) added that the previously defined depth of failure  $d_f$  should be annotated as 'extreme' depth of failure  $d_f^e$  and added the range for the mean depth of failure  $d_f^m$  to cover the highly damage zone from the numerical model. Therefore, Eq. (1.1) expands into semi-empirical relations to anticipate extreme and mean depths of failure in brittle failing rocks:

$$\frac{d_f^e}{R_T} = 1.25 SLI - 0.51 \pm 0.1, \text{ for } SLI \leq 1 \quad (1.2)$$

$$\frac{d_f^e}{R_T} = 0.75 SLI - 0.51 \pm 0.1, \text{ for } 1 < SLI \leq 1.5 \quad (1.3)$$

$$d_f^m \approx \frac{d_f^e}{3.5 \text{ to } 4.5} \quad (1.4)$$



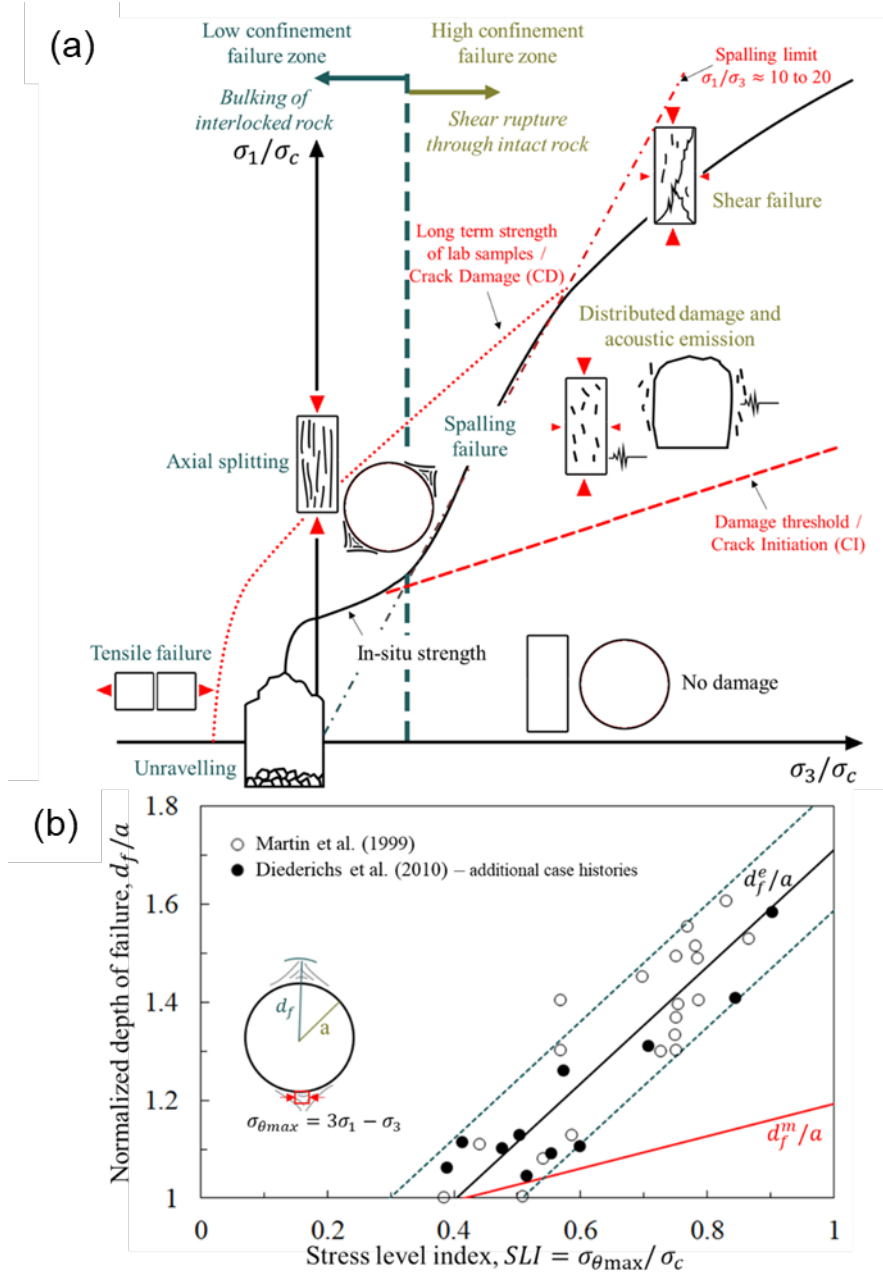


Figure 1.2 (a) S-shaped failure criterion for brittle rock masses divided into low and high confinement behavioral regions with illustrations of different failure modes (after Castro et al. 2012 and Kaiser 2019); (b) Empirical depth of failure chart in terms of radius of failure in circular opening (after Kaiser 2016). The case studies are taken from Martin et al. (1997) and Diederichs et al. (2009). The damage limit shown in the red line is added according to Perras and Diederichs (2016) and is the anticipated mean depths of failure in brittle failing rock  $d_f^m/R_T$ .

In addition to the damage analysis, there are terminologies used for the excavation damage zones, which are primarily employed in an underground radioactive waste disposal to improve the understanding of how damage is induced and how permeability is changed around an excavation (Tsang et al. 2005; Siren 2015). Figure 1.3 depicts the schematic diagrams for the different zones of induced damage around a circular excavation in brittle rock (modified after Read 2004 and Perras and Diederichs 2016).

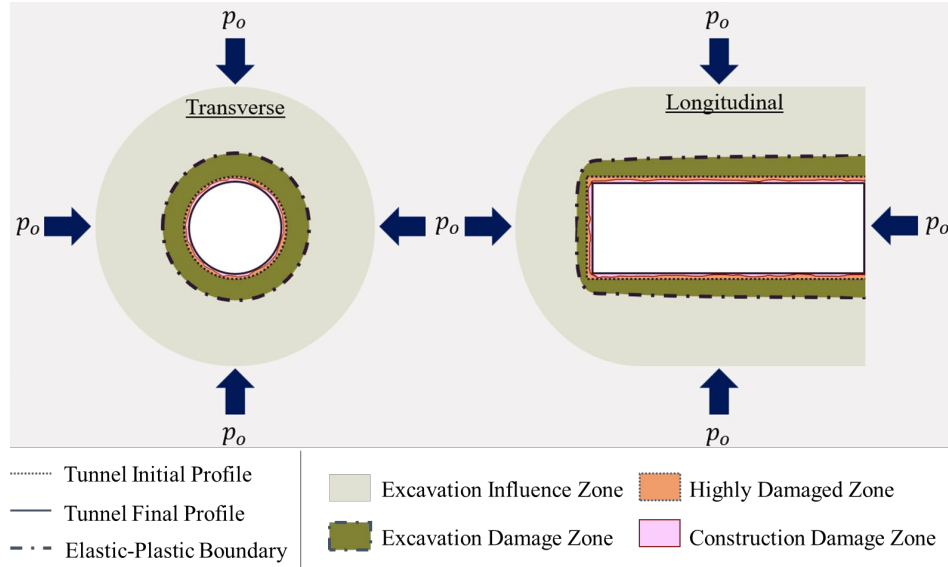


Figure 1.3 Schematic illustration for transversal and longitudinal cross sections of the different zones of induced damage around the tunnel constructed with TBM under isotropic loading (modified after Read 2004 and Perras and Diederichs 2016).

The different zones of induced damage in the tunnel wall are classified as follows:

- i. Construction Damage Zone  $CDZ$ , also termed as construction-induced excavation damage zone  $EDZ_{CI}$ , is observed as irreversible damage and highly depends on the construction method.
- ii. Highly Damaged Zone  $HDZ$ , typically characterized by fracturing close to the tunnel boundary due to crack propagation within localized zones and may promote spalling, slabbing and/or dog-eared. This fracturing occurs after the shear strength of the rock has been reached and the rock is in the strain softening regime where pronounced damage from fracturing occurs.
- iii. Excavation Damage Zone  $EDZ$  is associated with irreversible and significant rock damage due to plastic deformation. The stresses reach the peak shear strength of the rock but may not have reached strain softening.
- iv. Excavation Influenced Zone  $EIZ$ , which was previously called the excavation disturbed zone and renamed to minimize confusion. In this zone, the rock is anticipated to experience elastic deformation, demonstrating reversible damage.

Other than the  $CDZ$ , it is expected that different zones from the tunnel boundary towards the rock mass will be in the pre-peak, peak, and post-peak regimes of the stress-strain behavior in the  $EIZ$ ,  $EDZ$ ,

and *HDZ*, respectively. Although distinguishing the boundary between the rest of the zones can be difficult, it is crucial to consider induced damage delineation to ensure a safe and durable tunnel excavation design.

Regarding the physical model development, some researchers use large-scale in-situ tests, while others scaled it down to the laboratory-scale. These tests aim to capture the underlying mechanisms that lead to brittle failure in a more theoretical and fundamental manner. Over the past decades, several in-situ studies have contributed to understanding the brittle failure mechanism. These field studies include wellbore breakout observations through borehole televiewer reflectivity in granitic rock in South Carolina (Zoback et al., 1985), Mine-By-Experiment (MBE) in Canada's Underground Research Laboratory (URL) (Read and Martin, 1991), brittle failure experiment at Äspö Hard Rock Laboratory in Sweden (Andersson et al., 2004), Posiva's Olkiluoto Spalling Experiment (POSE) in Finland (T. Siren et al., 2015a), and rock spalling investigation in China's Jinping Underground Laboratory Phase II (CJPL-II) (Feng et al., 2018). Some of the in-situ experiments contributed to the following: (1) the development of empirical criteria as previously discussed, (2) failure mode validation such structurally controlled brittle failure due to anisotropy, and (3) numerical model of brittle failures using continuum or discontinuum approaches (Barton and Shen, 2017; Hajiabdolmajid, 2017; Martin et al., 1997). Conducting in-situ tests on large-scale geotechnical structures are time-consuming and expensive; however, carefully designed physical model tests are an effective alternative to investigate the stability and failure of geotechnical structures (Lin et al., 2015). The following section will elaborate more on the laboratory-scale physical modelling for brittle failure investigation.

### **1.1.2 Laboratory-Scale Experimental Models Simulating Brittle Failure in Tunneling**

Laboratory-tested results have been critical in understanding brittle failure phenomena (Ulusay, 2015). Researchers have performed various laboratory tests to investigate spalling and brittle failure mechanisms, e.g. uniaxial, biaxial, triaxial, and true-triaxial tests on rock specimens. In the context of the uniaxial compression test, Carter (1992) studied fractures on the tunnel boundary using a block of rock with a central circular opening. Jacobsson et al. (2015) recently performed uniaxial compression of a large hard rock specimen with a distinct shape (curved handle dumbbell) to recognize the critical area for spalling along the tunnel boundary. The uniaxial tests contributed to the scale effects consideration, but not able to simulate realistic in-situ condition.

Moreover, Labuz et al. (1996) developed a biaxial testing apparatus to investigate the splitting-to-shear failure mechanism that allows the failure plane to propagate unrestrictedly. Cho et al. (2010) built a bending test configuration to simulate the maximum tangential stress distribution on the circular excavation through axially compressed beams. Kusui et al. (2016) proposed a uniaxial compressive strength to the induced stress ratio to estimate the spalling at tunnel boundaries based on biaxial loading to

the specimen. The biaxial test has significantly contributed to the comprehension of spalling and brittle failure by simulating plane strain conditions to observe the brittle behavior (Qaidahiyani and Widodo, 2016).

With a series of triaxial tests of cylindrical specimens, Martin and Chandler (1994) investigated the progressive fracture in a granite material, focusing on cohesive and frictional strength. Pinto and Fonseca (2013) performed a triaxial test with eccentric axial loading on a granite block. In the opening sidewalls of the specimen, spalling with the propagation of cracks was reported in their work. Meanwhile, developing a true-triaxial cell for brittle failure investigation is thought to yield more accurate results than conventional triaxial testing due to independent manipulation of the three principal stresses (Kwaśniewski 2012).

Since the early 1990s, true-triaxial cells have been used for studying brittle failure under varying configurations. Some notable developments include Lee and Haimson (1993). They investigated the borehole breakout phenomenon in a granite specimen resulting in a "dog ear" shape due to a sequential spalling failure. Years later, Cheon et al. (2011) studied an opening in mortar rock-like brittle specimens under true-triaxial stress. The opening size was 60 mm in diameter in a cubic specimen of  $290 \times 290 \times 290 \text{ mm}^3$ , where one of the failed specimen documentations is shown in Figure 1.4a. The investigation focused on the damage depth and characterized the failure type through multiple loading configurations. Nonetheless, the characterization of the brittle rock-like specimen was not discussed in detail, particularly in terms of its brittleness properties.

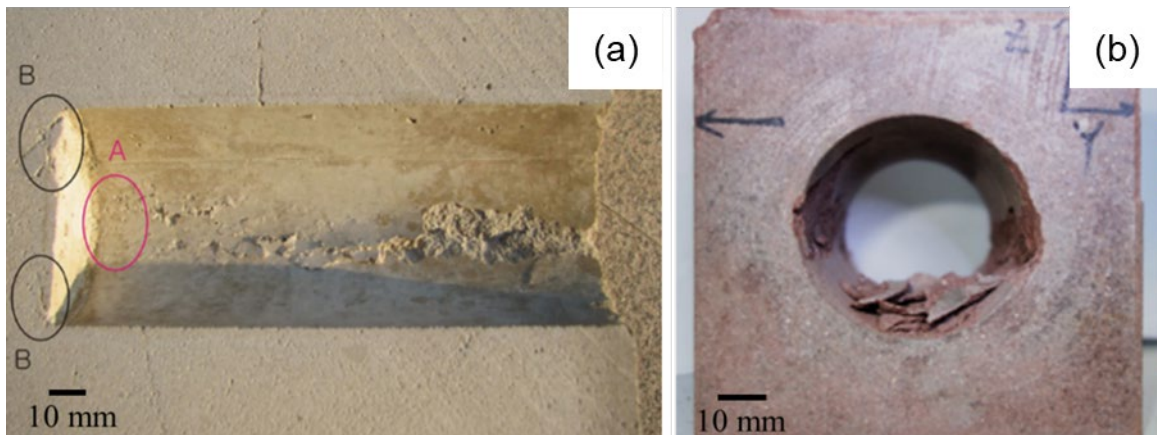


Figure 1.4 Failed sample documentation for true-triaxial test with prefabricated hole simulating circular tunnel under three-dimensional high stress conditions; (a)  $290 \times 290 \times 290 \text{ mm}^3$  rock-like mortar sample (Cheon et al. 2011) and (b)  $100 \times 100 \times 100 \text{ mm}^3$  red sandstone sample Gong et al. (2018).

Beginning in 2007, the term true-triaxial has also been expanded with one-side unloading to simulate the condition of the tunnel wall when exposed immediately after excavation. He et al. (2010) developed a strain burst testing machine, modifying true-triaxial apparatus to allow sudden unloading as

the main unit of the testing machine to capture violent, brittle failure phenomena. There were numerous tests followed since then, with further investigation on the loading path used, number of rapid unloading sides, and inclusion of impact-induced rockburst through the superposition of static and dynamic loads (Du et al., 2016; Hu et al., 2021; Su et al., 2017; Sun et al., 2016; Zhao et al., 2014). These tests were categorized as direct experimental methods that can reproduce rockburst failure with three main components (He et al., 2023), which are: (1) the high-stress state, (2) sufficient elastic strain energy accumulation, and (3) free face from unloading. Arguments were raised that when the stress is not very high, the sudden unloading process can be ignored, until the experiment trend returns to include the initial free face concept.

With similar apparatus, Gong et al. (2018) continued and adopted cube samples with a prefabricated circular hole to simulate the tunnel induced failure under true-triaxial stress condition. They studied the effect of spalling failures that induce rockburst events on the laboratory scale to perform deep tunnel simulation. Their experiment was observed through a 50 mm diameter prefabricated opening in a red sandstone cubical specimen  $100 \times 100 \times 100 \text{ mm}^3$  in size. In their study, the failure was characterized by the rock ejection as the concentrated tangential stress exceeded the uniaxial compressive strength (UCS) of the rock around the tunnel boundary (Figure 1.4b). This ratio between the concentrated maximum tangential stress and the UCS when failure ( $\sigma_{\theta_{max}}/\sigma_c$ ) is evaluated as the critical failure strength, like the so-called stress level index SLI introduced earlier. However, the prefabricated opening without loading does not represent real tunnelling conditions where the tunnel is excavated under load.

## 1.2 Motivation

The following question persists as the motivation of this research: *How can we improve the understanding and prediction of tunneling-induced brittle failure?* To ensure the successful execution of tunneling projects, it is crucial to comprehensively understand the behavior of brittle rock mass and its damage potential damage and failure. While numerous studies have focused on brittle rock characterization and in-situ testing (e.g. Andersson et al. 2004; Martino and Chandler 2004; Martin and Christiansson 2009; Klammer et al. 2017; Gottsbacher et al. 2020), there remains a critical need for in-depth investigation through laboratory experimental studies. The experimental laboratory-scale model allows us to replicate the complex and dynamic conditions encountered during tunnel excavation, providing valuable insights into the mechanisms and factors contributing to brittle failure.

As previously discussed in Section 1.1.2, the documented laboratory-scale investigations on brittle failure are limited. Some of the models were unable to replicate tunnel advance, some were not created for field stress levels, and others were only applicable to certain geomaterials. Also, to the extent of current knowledge, there is a lack of investigations focusing on the simultaneous development of reproducible, brittle-analogous synthetic material and a controlled experimental model to simulate brittle

failure characteristics. A combination of material and physical testing variability can contribute experimentally to verified insights in developing analytical and numerical models. These models will benefit tunneling projects in deep and challenging ground conditions. This research would enable development of a deeper understanding of the fundamental principles governing brittle failure, paving the way for the design and implementation of effective risk management strategies.

### **1.3 Research Objectives**

The general objective of this research effort is to develop an improved understanding of tunneling-induced brittle failure by performing laboratory-scale investigation schemes. The schemes include simultaneous development of reproducible, brittle-analog sediment rock and methodology for a laboratory-scale experimental model to simulate brittle failure phenomena at the tunnel boundary under varying loading configuration.

To meet this purpose, four research objectives will be pursued:

1. Develop and characterize an analog sediment rock material for laboratory experimental study with weak and brittle characteristics.
2. Perform a series of laboratory-scale experiments of brittle failure at a freshly excavated model tunnel wall under realistic in-situ condition using a true-triaxial and miniature TBM setup to capture spalling and damage zones around the excavation.
3. Develop new reliable procedures to predict tunnel spalling based on specimen-scale and laboratory-scale experiments investigation results.
4. Develop new reliable procedures to predict tunnel rockburst based on specimen-scale and laboratory-scale experiments investigation results.

By fulfilling the above objectives, the simultaneous development of analog rock and investigation of a laboratory-scale model tunnel can help in distinguishing source mechanism and mechanism of damage of tunneling-induced brittle failure. With the identification of these aspects, experimentally validated procedures can be developed to effectively mitigate tunnel instabilities. The research output and knowledge gained will benefit the infrastructure tunneling operation and other deep underground excavations such as mining operations, wellbore oil production, geothermal extraction, and hydrofracturing projects that can reach greater depths with a higher stress state.

### **1.4 Research Tasks**

The objectives of this dissertation, which were discussed in Section 1.3, were pursued through an experimental testing program and an extensive analysis of the experimental data. The tasks that were performed to achieve the research objectives are described in the following sub-sections.

#### **1.4.1 Tasks Related to “Objective 1”**

- Identify the constituents for fabricating an analog rock that exhibits brittle response while low in uniaxial compressive strength (UCS).
- Perform multiple trial mixes to determine the final mix composition and engineering treatments for the analog brittle rock. The evaluation criteria are bursting tendency and stress-strain behavior in the unconfined compression test (UCT) and triaxial compression test.
- Characterize the analog brittle rock to report its physical and mechanical properties and compare it with the naturally occurring sedimentary rock for assessment.

#### **1.4.2 Tasks Related to “Objective 2”**

- Conduct experiments to characterize damage and spalling at the tunnel wall at incremental isotropic and anisotropic stress levels.
- Record the excavated tunnel model from the portal during loading to capture the damage progression.
- Identify damage zones in the recovered specimen from the tunnel model experiment through post-mortem investigation using macrophotography.

#### **1.4.3 Tasks Related to “Objective 3”**

- Explore additional contributing factors to the extent of spalling and damage development based on tunnel model testing results.
- Develop testing schematics to validate the effects of intermediate confinement on the predictions of spalling strength and geometry.
- Evaluate the depth of failures in the tunnel model experiment with empirical and analytical models.

#### **1.4.4 Tasks Related to “Objective 4”**

- Explore additional contributing factors to the extent of brittle failure and rockburst progression based on tunnel model testing results.
- Evaluate the depth of failures in the tunnel model experiment with empirical and analytical models.
- Improve the theoretical predictions of plastic slip lines to capture the successive fracturing progression into the tunnel wall.

### **1.5 Organization of Dissertation**

The dissertation consists of four individual papers that have been published or are undergoing revisions for publication in peer-reviewed international journals. The main chapters of this dissertation are presented in the form in which they were originally published or submitted as individual manuscripts. Therefore, each chapter has its abstract, introduction, main body, results, discussions, conclusions, and

acknowledgements. Minor formatting variations, however, were made to maintain the consistency and the flow of the dissertation. All the references in the development of the dissertation are presented collectively at the end of the dissertation.

The chapters in the dissertation were organized in the order of the dissertation objectives as described above, with six chapters in total, as follows.

Chapter 2 presents the development and characterization of an analog sediment rock material for laboratory experimental studies.

Chapter 3 presents the physical model setup designed to study circular tunnels under isotropic loading conditions.

Chapter 4 focuses on the analysis in spalling failure characterization from a circular tunnel under isotropic loading conditions that include new reliable spalling prediction using triaxial extension tests.

Chapter 5 addresses the analysis of episodic brittle failure and rockburst progression from a circular tunnel under anisotropic loading conditions with an improved plastic slip lines prediction methodology and brittle-to-ductile transition consideration.

Chapter 6 presents the major conclusions and suggestions for future research.

In addition to the development of tunnel brittle failure experiment and the improvement of spalling strength, geometry analysis, and consideration of brittle-to-ductile transition, the dissertation proposed one additional methodology relating to acoustic emission (AE). Appendix A provides the AE analysis work based on anisotropic loading experiment with enhanced temporal deconstruction and frequency domain analysis to explore precursors of damage and visible spalling onset.



## CHAPTER 2 DEVELOPMENT OF A VERY WEAK ANALOGUE SEDIMENTARY ROCK FOR EXPERIMENTAL STUDY TO MODEL BRITTLE INSTABILITY IN TUNNELING<sup>1</sup>

### 2.1 Abstract

This paper presents the development process of fabricating an analogue sedimentary rock in the laboratory. This analogue material is characterized by a notably low uniaxial compressive strength, yet it exhibits brittle behavior. The main objective of this paper is to develop with a mix of constituents, sample preparation procedures, and engineering treatment within a trial-and-error framework to achieve a material with desired behavior. The developed analogue sedimentary rock is primarily aimed to support the study of brittle failure instabilities encountered during tunnel excavation. Laboratory tests such as unconfined compression, Brazilian splitting, and triaxial compression tests were conducted to characterize the behavior of the analogue material. These targeted rock mechanical characteristics of the analogue materials encompass four key aspects: (1) showing a very weak uniaxial compressive strength of approximately 1.5 MPa, coupled with a post-peak strain softening behavior; (2) exhibiting an uniaxial compressive to indirect tensile strength ratio within the range of 8–10; (3) enhancing Hoek-Brown constant  $m_i$ ; and (4) achieving selected brittleness indices such as strength brittleness index, brittleness index modified, and burst energy coefficient that are associated with bursting tendency. Several engineering treatments were methodically explored, including uniformly graded fine aggregate usage, lower cement content, curing time reduction, air-entraining admixture usage, saturation and freeze temperature exposure, and thermal exposure. The result is a uniform and isotropic analogue rock that can be replicated, similar to mortar mixing. The mixture includes fine-grained F-75 Ottawa sand, type I/II Portland cement, and distilled water, with a low cement content of 4% and a water-to-cement ratio of 1.2. This analogue rock provides a controlled, replicable framework for investigating brittle failure instabilities such as spalling and dog-earing in a laboratory-scale tunnel excavation model.

### 2.2 Introduction

Brittle instability poses a significant threat to tunneling in rocks with high in-situ stress conditions. As infrastructure development projects expand into mountainous regions or deeper underground, transportation and hydroelectric tunnels are being excavated to unprecedented loads. For

---

<sup>1</sup> This chapter will be submitted as a full journal paper for publication in the ASTM Geotechnical Testing Journal. Partial contents of this chapter have also been submitted and presented at the 56th US Rock Mechanics/Geomechanics Symposium, Santa Fe, New Mexico, USA, June 2022 (Wibisono et al., 2022) and 57th US Rock Mechanics/Geomechanics Symposium, Atlanta, Georgia, USA, June 2023 (Wibisono et al., 2023a)

example, the Olmos Trans-Andean Tunnel in Peru encountered overburdens of up to 1930 m, the Gotthard Base Tunnel in Switzerland was constructed with an overburden of up to 2300 m, and the tunnels of Jinping II in China reached a maximum overburden of 2525 m (Eberhardt et al. 2016). In such great depths with brittle rock formations, potential damage can manifest in various forms due to the stress condition, including spalling, rockbursting, and development of excavation damage zones. Consequently, tunnel engineers are becoming more cognizant of the challenges associated with the construction of tunnels at high in-situ stress conditions, particularly those excavated by tunnel boring machines (TBMs).

Figure 2.1 illustrates the different types of failure in tunnel excavation depending on the level of effective confinement of Castro et al. (2012). Tensile stresses induced during anisotropic loading of tunnel wall, as explained by Diederichs (2007), resulted in Griffith type extension fracturing with a depressed failure envelope in the low confinement zone, where fracture propagation causing spalling is suppressed towards the emergence of confining pressure. The failure envelope for a rock mass in the minor-major principal stress domain forms an s-shaped or trilinear shape curve, which can be divided into two zones: (1) spalling-dominated stress fracturing at low confinement and (2) shear rupture-dominated behavior at high confinement. This criterion is generated using three envelopes: the damage threshold/crack initiation (CI), spalling limit ( $\sigma_1/\sigma_3 \approx 10$  to 20), and long-term strength of lab samples/crack damage (CD). These envelopes depend on rock properties, further motivating this study, particularly regarding rock microstructure.

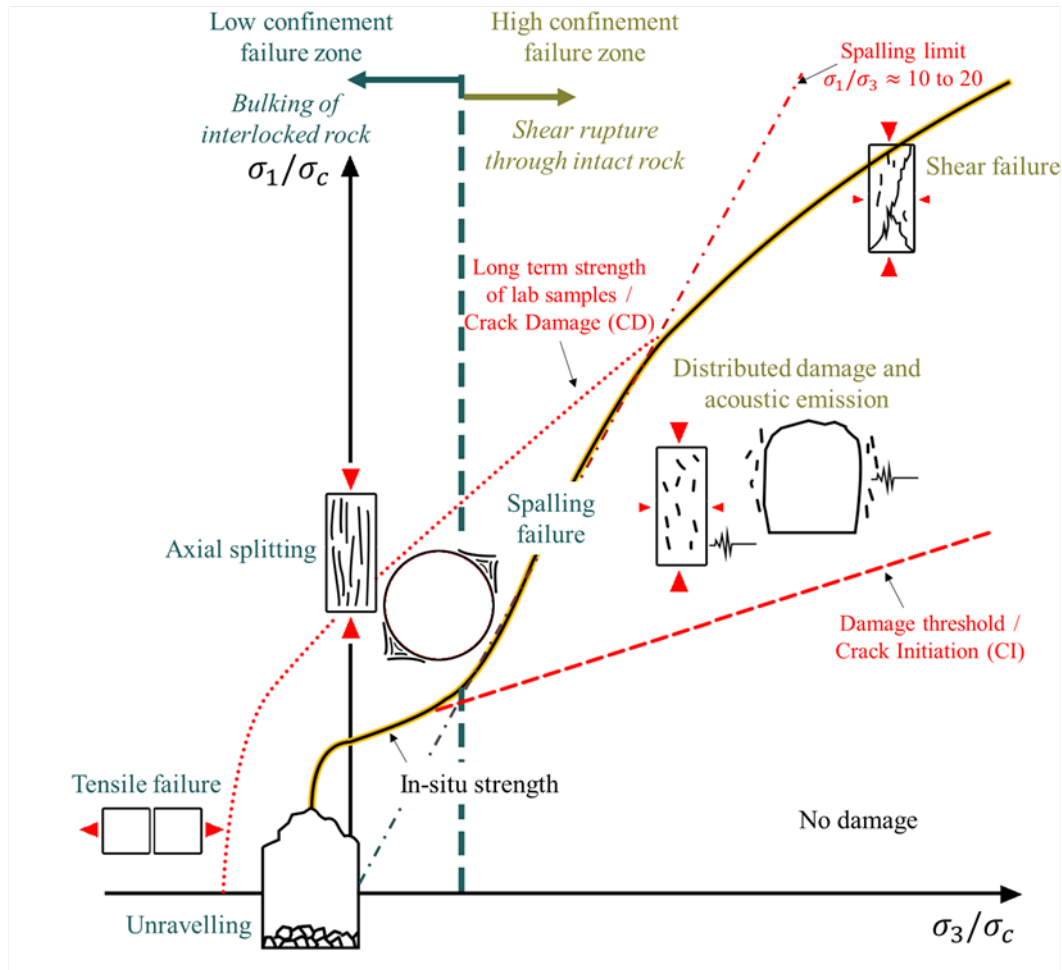


Figure 2.1 S-shaped or tri-linear failure criterion for brittle rock masses divided into low and high confinement behavioral regions with illustrations of different failure modes (after Castro et al. 2012 and Kaiser 2019). Three envelopes are used to generate this criterion, which are damage threshold/crack initiation (CI), spalling limit ( $\sigma_1/\sigma_3 \approx 10$  to  $20$ ), and long-term strength of lab samples/crack damage (CD).

In contrast to ductile rocks, which display a more contractive response and large deformations leading to plastic failure, brittle rocks demonstrate uncontrollable behavior when subjected to stress. According to Brady and Brown (2007), brittle behavior is characterized by a sudden decrease in strength without substantial plastic deformation. Brittle rocks exhibit a distinct peak shear strength followed by a sudden and well-defined strain softening response. Notably, once the peak shear strength is surpassed, there is a significant decrease in strength with increasing strain leading to the residual shear (Nygård et al. 2006). For very brittle rocks, the residual shear stress can drop to zero. The decrease in mechanical strength is accompanied by an escalation in fracturing and disintegration of the rock formation, which are very difficult to control during tunnel excavation. Rock failure is often very violent with large energy release posing hazards to construction personnel and equipment.

The phenomenon of strain softening in brittle rocks can lead to a rapid and catastrophic failure of tunnel walls, especially during specific phases of excavation when the rock mass is exposed without any form of ground support. The stability and structural integrity of the tunnel may be compromised by the initiation, propagation, and coalescence of fractures within a disturbed rock mass, which can affect the tunnel wall. The fractures within the rock mass have the potential to develop independently of one another at an early stage. However, over time, these fractures may propagate and coalesce, resulting in a significant reduction in the overall strength of the rock (Perras and Diederichs 2016). In the context of materials under high stress, the occurrence of a brittle failure process can result in a phenomenon known as rockburst, which is an intense manifestation of brittle failure. The phenomenon of brittle failure, depending on its intensity, has the potential to result in spalling or dogearing failure characterized by violent detachment of pieces of rock from the tunnel wall.

Laboratory testing is a viable method for improving understanding of the behavior and failure mechanisms exhibited by rocks. The analogue rock developed in this study will be subsequently employed in the scale-model testing of tunneling using a true-triaxial and a miniature TBM (Frash et al., 2014; Arora et al., 2019). The setup requires large cubic-shaped rock specimens, with each side measuring 300 mm in length. Acquiring large rock specimens that are both representative and unaltered is inherently difficult if not impossible. Additionally, the use of natural specimens has the potential to introduce unknown variables to the experiment, thereby affecting the reproducibility of the investigation (Johnston and Choi, 1986). Therefore, the development of an analogue material is essential to ensure experimental consistency.

The prepared analogue rock material is designed to be weak yet brittle. Low shear strength is desired to reduce the requirement for a large capacity loading apparatus, while accommodating a large-sized specimen. A larger specimen size facilitates visual observation of the tunnel model. Brittleness is required to study tunnels in brittle rock (Wibisono et al., 2022). Despite being categorized as medium-strength rocks, brittle failure has been documented to happen in sedimentary rocks lithology (Gong et al., 2012a; Naji et al., 2019; des Rivières and Goodman, 2023; Sun et al., 2016). In recent years, researchers have tried to create analogue rock that resembles natural sandstone with isotropic and homogeneous characteristics. The preparation methods include using chemical reactions, artificial cement, 3D printing, natural sand grain sintering with artificial beads, and other techniques (David et al., 1998; Huang and Airey, 1998; Rice-Birchall et al., 2021; Wu et al., 2020). Particular to the study of brittle failure phenomena, Klammer et al. (2023) developed rock-like specimens conforming to ultra-high-performance concrete (UHPC) to investigate rockburst phenomena. The specimens displayed brittle properties, which were observed during compression tests. The uniaxial compressive strength  $UCS$  are in the range of 62 to 192 MPa, with variations observed based on the specific type of aggregate employed. Nevertheless, such

a high level of *UCS* would inevitably require the implementation of a high-capacity loading system, even when conducting a tunnel model experimental investigation.

Several studies have provided justification for employing low-strength materials as a viable repeatable substitute for rocks. In addition to low shear strengths, these materials can yield comparable ratios of uniaxial compressive to the indirect tensile strength (*UCS/UTS*) and Young's modulus to the uniaxial compressive strength (*E/UCS*) (Barton, 1970; Indraratna, 1990; Stimpson, 1970) that correspond to brittle materials. These studies suggested a procedure for analogue rock fabrication with designated properties. Following the justification based on comparable modulus ratio or the strength ratio to the rock, this research endeavors to create a brittle but a weak analogue material that can be consistently replicated in laboratory settings with varying geometries. The material is aimed to serve as a model material to the advancement of our understanding of brittle rock instability. The ease in fabricating the test material in this study stems from the wide availability of its constituents and the standardized procedures for their mixing.

The term “very weak” is adopted following the International Society of Rock Mechanics (1978) rock strength classification. The assessment of rock strength classifies weak rocks as extremely weak (R0 with *UCS* of 0.25 to 1 MPa), very weak (R1 with *UCS* of 1 to 5 MPa), and weak (R2 with *UCS* of 5 to 25 MPa). The shear strength of the material developed in study is designed to be very weak to avoid requiring a large load capacity apparatus. To achieve a 4-10 ratio of applied stress to strength, the *UCS* of the analogue rock should be in the range of 1.3-3 MPa to meet the 13 MPa capacity of the applied stress from the true-triaxial setup (Wibisono et al., 2023b).

This study presents experimental results that are based on a synthesis between material conceptualization, preparation and engineering treatment within a trial-and-error framework. Some major takeaways and limitations will also be outlined that could be useful for future research. The following section provides a more detailed explanation of the experimental framework that covers the selection of an analogue mixing method and constituents, sample preparation procedure, and a description of testing setup. Section 2.4 covers the material development in stage. Next, Section 2.5 of the paper provides a comprehensive rock mechanical characterization of the produced analogue rock. Finally, Section 2.6 will provide a summary of the conclusions derived from the study.

### **2.3 Experimental Framework**

The objective of obtaining a very weak analogue rock can be achieved by mimicking sandstone as one of the most prevalent types of sedimentary rocks. Sandstone is a type of siliciclastic sedimentary rock that originates from the processes of transportation, deposition, compaction, and cementation of sand grains with varying mineral compositions (Haldar and Tišljär, 2014). The primary constituents of sand grains are predominantly composed of quartz sand. The grains are also occasionally accompanied by

substantial quantities of feldspar, silt, and clay. Sandstone is a prevalent type of sedimentary rock, constituting between 20 to 25 percent of the Earth's crust (Boggs, 2006). It ranks as one of the most abundant sedimentary rocks, second only to shale. Although sedimentary rock is commonly associated with stratified layers, it is important to note that the present experiment focuses solely on examining a sandstone like rock that is isotropic (uniform in all directions), homogeneous (uniform in composition), and densely compacted. In geological scenarios, this type of sample can be comparable with thick sandstone bed—typically considered when it reaches a thickness of at least 1.5 meters (Chipping, 1972).

The experimental framework consists of three stages that lead to the attainment of final results; (1) mixing, (2) treatment and (3) characterization stages. A trial-and-error is followed to achieve the desired material qualities. The mixing stage includes a selection of an analogue mixing method and constituent, general sample preparation. Engineering treatments are employed to introduce defects in the form of microcracks to weaken and embrittle the material (Wibisono et al., 2023a). The characterization stage covers the laboratory tests and acceptance to the designated criteria. The details of each stage will be discussed in the following subsections.

### **2.3.1 Selection of Analogue Rock Mixing Method and Constituent**

Existing mortar mixing procedures that have been standardized and followed in the construction industry are employed. On the laboratory scale, the mortar mixing process is also routinely performed as typical quality assurance and quality control (QA/QC) to achieve a specified target and designated purpose. In a general sense, mortar is produced by mixing binding material and fine aggregate with water (Arizzi and Cultrone, 2021). Immediately after mixing, the mixture is still workable and can be molded to a certain geometry. Conforming to the mold shape, the water will continue to hydrate the cementing agent, and the hydrated cementing agent will bond the fine aggregates together over time. This is known as the curing time. When the mixture solidifies as cured mortar, it exhibits similarities to sedimentary rock. The analogue sedimentary rock is therefore intended to demonstrate reproducibility, flexibility in terms of shape, and convenience of sample preparation using the mortar mixing methods.

The developed analogue sedimentary rock consists of F-75 Ottawa sand (Dakoulas and Sun, 1992), Type I/II Portland cement (ASTM, 2021a), and distilled water. Serving as the hydration agent, distilled water was selected to reduce the effects of the contained minerals, which may affect the cement hydration process in the synthetic sandstone. In other words, the selection process ensures the consistency on investigated variables in the developed mix. The water addition to the mix is controlled by the ratio of water to a cementitious mixture  $w/cm$ .

Type I/II Portland cement is the commercially available cementitious constituent with adhesive and cohesive properties that is capable of binding together mineral fragments within a matrix. To enhance its capabilities as the binding agent, the presence of water is indispensable. The Type I/II Portland cement

is primarily composed of calcite minerals, along with alkaline substances and trace amounts of various other elements that chemically react with water. This selected type of cement produced by Quikrete satisfies the ASTM-C150 requirements and possesses a specific gravity of 3.15, denoted as cement  $G_{cm}$ .

As fine aggregates, the F-75 Ottawa sand is characterized by a substantial amount of silicate mineral (98%  $\text{SiO}_2$ ) that mainly constitutes the analogue sedimentary rock. F-75 Ottawa sand has a specific gravity  $G_s$  of 2.65, and grain median diameter  $D_{50}$  of 0.182 mm (Mirshekari et al., 2018). The silicate mineral inherently has more tendency to brittleness when compared to the calcite mineral. This characteristic has been investigated in relation to the brittle-ductile transition throughout confining pressure, with experimental observations supporting this correlation (Mogi, 1966). It is anticipated that materials with a higher calcite content will exhibit increased ductility when compared to materials with similar  $UCS$ . Consequently, the selection of the analogue constituents incorporates a composition featuring a higher proportion of silicate, constituting a minimum of 84% of the mix's matrix by mass. The determination of the quantity of cement to be incorporated into the mixture is established by the cement content parameter, denoted as  $C$ , and defined as the ratio of cement mass to total solids mass, which includes both cement and fine aggregates. The formation of cement hydration products is influenced by various factors, including but not limited to the water-to-cement ratio  $w/cm$  and the duration of the curing process.

### 2.3.2 Material Preparation

The material constituents can be mixed using table-mounted industrial mixers or by using hand grout mixers (i.e., an electric drill with a mixer attachment). The selection between the two methods depends on the volume of the mixture, with the latter being more suitable for larger specimens that are beyond current investigation. The procedure for analogue sedimentary rock preparation is as follows:

The procedure for synthetic sandstone preparation is as follows:

- i. First, the F-75 Ottawa sand and type I/II Portland cement are pre-mixed in a dry container according to the cement content  $C$  until mixed thoroughly.  $C$  is defined as a percentage of the cement mass to the total solid mass (cement and sand). With a relatively low cement content of 4-8%, visual observation during the pre-mixing is necessary to ensure perfect mix homogeneity (see Figure 2.2a). As both solids have distinct colors, a homogeneous mix is judged by the absence of distinct regions with a dominant color, resulting in an overall compound appearance of gray. The solid compound is then poured into the mixer.
- ii. Distilled water is then added at a specified ratio, which is determined based on the water-to-cement ratio  $w/cm$ . The mixer can be operated now to thoroughly mix the dry constituents and the water. It is recommended that the mixing process maintains a minimum speed of 40 revolutions per minute (RPM). As the moisture from the water covers the pre-mixed material, the

- mixture should have consistent homogeneity after up to ten minutes of thorough mixing (see Figure 2.2b).
- iii. The process of casting and tamping of the specimen involved layering, ideally with a minimum of three layers to achieve the desired specimen size (e.g., for 100 mm height, then each layer needs to be at least 33 mm). Before placing the subsequent layer, the surface is roughened/keyed to a depth of 5-10% layer thickness (see Figure 2.2c). This procedure establishes interconnections between the layers, prevents flat shear planes, and ensures the specimen remains isotropic.
  - iv. The specimen is cured for specified days, with the curing treatment according to the American Society for Testing and Materials (ASTM) Standards C192 and C511 (ASTM, 2021b, 2021c). Further adjustment to the curing duration will be elaborated on in Section 2.4.4.
  - v. The procedure can be modified for additional treatments, if needed, such as the addition of air-entraining admixture, thermal treatment, saturation treatment, and freezing treatment.

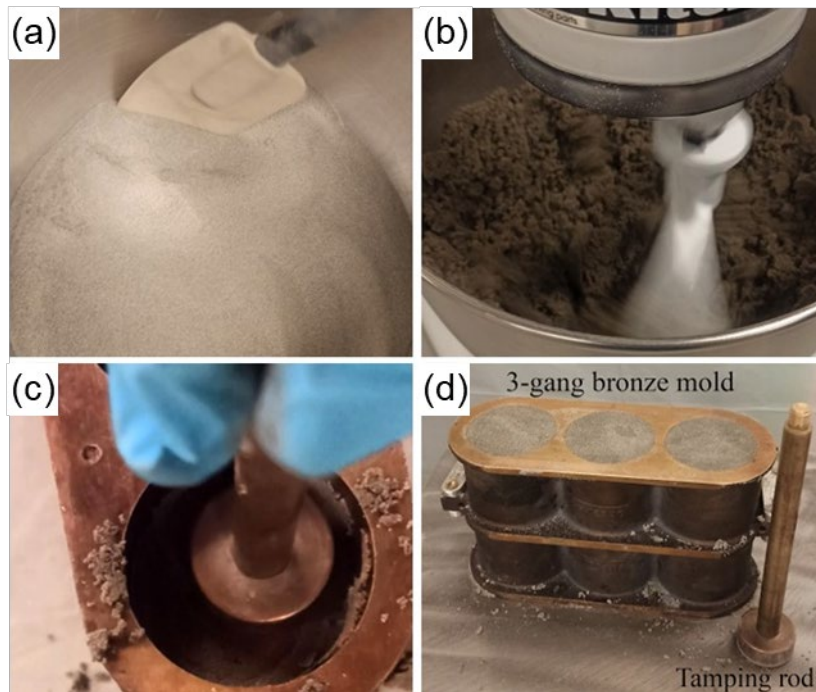


Figure 2.2 Preparation of cylindrical specimen for laboratory characterization. (a) Pre-mixing of Type I/II Portland cement and F-75 Ottawa sand; (b) Adding water and mixing process in a stand mixer; (c) Tamping and rough surfacing for each layer to ensure the thorough compaction and dense analogue sedimentary rock; (d) Cylindrical specimens in the mold before placement in desiccator chamber.

All the specimens used in this investigation were built with a three-gang cast bronze cylinder mold manufactured by Humboldt (see Figure. 2.2d). This mold allows the casting of cylindrical specimens with a diameter of 51 mm and a height of 102 mm, meeting the dimensional specifications outlined in the ASTM standards for unconfined and triaxial compression tests (ASTM, 2017). The



Brazilian tension test involved cutting the cylinder to a disk length equal to the radius of the cylinder, in accordance with the ISRM standard (ISRM, 1978).

Table 2.1 provides the details of three different mix designs and proportions, denoted as mixes O, A, and B, used for creating 1 m<sup>3</sup> of the analogue material. Each mixture represents a significant point in the development of very weak but brittle analogue sedimentary rock through various engineering treatments. Detailed engineering treatments for each mix will be discussed further in Section 2.4.

Table 2.1 Summary of mix design and proportions (by weight) for the analogue sedimentary rock.

Properties	Mix O	Mixes A and B
Cement Content, $C$	8%	4%
Water to cement, $w/cm$	1.2	1.2
Mass of F-75 Ottawa sand* (kg)	1963.4 (83.94%)	2269.6 (91.6%)
Mass of cement* (kg)	170.7 (7.30%)	94.5 (3.82%)
Volume of water* (l)	204.9 (8.76%)	107.9 (4.35%)
Volume of AEA* (l)	N/A	5.6 (0.22%)

\*For 1 m<sup>3</sup> of the specimen

### 2.3.3 Description of Testing Setup and Acceptance Criteria

The predominant approach used in laboratory testing for the purpose of material characterization primarily involves the use of cylindrical specimens. In the characterization process, a series of physical property tests, including unconfined compression tests (UCT), Brazilian tension tests, and triaxial compression tests are performed. The physical characterization of the specimen includes the determination of density and porosity for each variant of the specimen. Thin section image analysis for select specimens is also performed with the ImageJ tools (Schneider et al., 2012) to evaluate the effect of specimen treatment on its microstructure. The process was conducted iteratively, with steps taken and feedback incorporated throughout the development process to assess and document the material modifications as function of the interventions implemented.

The complete stress-strain curves generated from the UCT were used to determine the peak shear strengths and subsequent post-peak behavior of every mix design that was tested. The compression test used a displacement-controlled scheme, wherein the testing setup exhibited significantly greater stiffness compared to the analogue rock being studied. This characteristic enabled controlled failure during the test, thereby facilitating the acquisition of a complete stress-strain curve (Hudson et al., 1972).

It is well-known that rock brittleness and ductility are not necessarily intrinsic properties but can be dependent on the level of stress confinement (Nygård et al. 2006). Rocks tend to become more ductile with increasing confining stress. The decreased brittleness may be accompanied by the development of compaction bands (Wong and Baud, 2012). In addition to acquiring the Hoek-Brown and Mohr-Coulomb failure envelope, the complete stress-strain curves were used to ascertain the resulting brittle-to-ductile transition of the analogue material. These characterization results are examined further in terms of meeting acceptance criteria to the final design of the very weak but brittle analogue sedimentary rock.

The triaxial compression tests (with  $\sigma_1 > \sigma_2 = \sigma_3$ ) are carried out on the cylindrical rock specimen also according to the ISRM suggested method to determine the shear behavior of the rock under different confining pressures (Ulusay and Hudson, 2007). The triaxial compression test system consists of a Hoek cell positioned in the stiff loading frame of an ELE International ACCU-TEK 250 Range Digital Series compression tester. This setup is also used for UCT and has an axial loading capacity of 1,112 kN. A dual Teledyne ISCO 65DM syringe pump system, programmed with Disco software (Frash 2016), is connected to the Hoek cell to apply the confining pressure to the tested specimen. The software records the hydraulic fluid volume that is introduced into or expelled from the Hoek cell. The volumetric strain can be calculated as follows (Arzúa and Alejano, 2013):

$$\varepsilon_v = \frac{\Delta V}{V} (\%) = \frac{100}{V} \left[ fV_0 - \Delta h \left( \pi r^2 - \frac{F}{E} \right) \right] \quad (2.1)$$

where  $V_0$  is the volume of fluid displaced,  $V$  is the original sample volume,  $f$  is the compressibility factor for the hydraulic fluid,  $r$  is the radius of the Hoek cell,  $F$  is the axial force acting on the ram,  $E$  is the elasticity modulus of the ram's steel, and  $\Delta h$  is the measured axial displacement.

The target properties for the analogue material encompass four key aspects: (1) very weak *UCS* of 1.5 MPa or less, coupled with post-peak strain softening behavior; (2) indirect tensile strength exhibiting an uniaxial compressive to indirect tensile strength (*UCS/UTS*) ratio within the range of 8–10; (3) enhanced Hoek-Brown constant  $m_i$ ; and (4) selected brittleness indices. Regarding the brittleness indices, there are two brittleness assessment methods selected, which are based on strength parameters and the shape of the UCT stress-strain curves. The strength-based method is represented by the brittleness index  $B_1$  (Hucka and Das, 1974), while the methods based on UCT stress-strain curves include the Brittleness Index Modified *BIM* (Aubertin et al., 1994) and burst energy coefficient  $R$  (Cai 2016a). These selected methods are discussed below and are based on their established reputation for evaluating rock bursting susceptibility (Meng et al., 2021). In addition, testing results obtained in this study will also be evaluated using the adopted framework from Tatone et al. (2023) that compares the analogue material to natural sedimentary rock based on modulus ratio, strength ratio, Poisson's ratio  $\nu$ , and density  $\rho$ .

## 2.4 Material development

The development process involved six mixing treatments within a trial-and-error framework. Figure 2.3 shows the tested engineering treatments in chronological order, which include air-entraining admixture, saturation and freeze exposure, and thermal exposure. Additional treatments involved using uniformly graded fine aggregate, low cement content, and variations in curing and testing times. These treatments will also be further detailed in the following subsections.

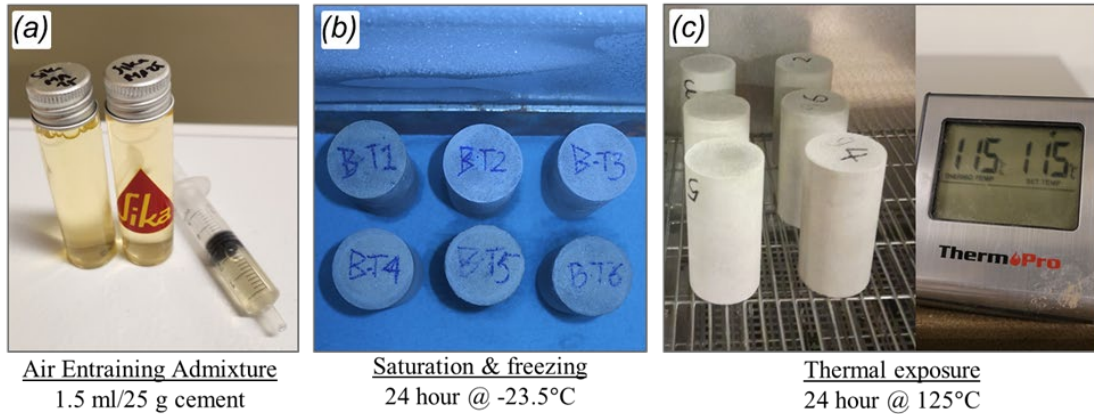


Figure 2.3 Displays of three engineering treatments incorporated in the development of the analogue sedimentary rock within trial-and-error framework. Note that the arrangement is following a chronological way to get the final design (mix B) as follows: (a) incorporation of air-entraining admixture while mixing, (b) cylindrical specimens undergo freezing treatment inside a chest freezer with a cooling range of up to -25 °C, and (c) cylindrical specimens undergo thermal exposure, monitored with a digital thermometer for the chamber temperature.

### 2.4.1 Use of Uniformly Graded Fine Aggregate

The aggregate distribution in mortars is of great importance in achieving a cohesive mix and a strong bond within the matrix. Cementitious mixtures with well-graded aggregates show higher *UCS* due to better void filling for geometric interlocking (Mehta and Monteiro, 2014). In contrast, usage of uniformly graded aggregates with small size variation appears to leave larger voids. Mortars with coarse sand exhibit greater deformability and ductility, with a smoother post-peak branch in the stress-strain curve compared to those with fine sands (Haach et al., 2011). Therefore, using uniformly graded fine aggregate is expected to induce brittle behavior, likely due to the fragmented void structure within the matrix.

### 2.4.2 Low Cement Content

The analogue sedimentary rock is developed with low cement content. The rock matrix is primarily bound by hydrated cement, but the strength is lower due to the reduced cement proportion relative to the total solids. Lower cement content requires higher water content to maintain mortar

workability, especially when using fine sand with a greater specific surface area (Westerholm et al., 2008). Initial tests were conducted to determine an appropriate mix design. To obtain representative stress-strain curves from UCT, three distinct cement content mixes of 8%, 6% and 5% were examined, with all other variables held constant.

#### **2.4.3 Thermal Exposure**

Both aggregate and hydrated cement in the cementitious mixtures exhibit thermal expansion when subjected to temperatures from 0 to 100 °C. In the range of 100-150 °C, the aggregates expand, concurrent with the evaporation of unbound water in the cement paste, causing the paste to shrink. This shrinkage, combined with aggregate expansion can initiate microcracks within the matrix (Kassir et al., 1996). The objective behind subjecting the analogue sedimentary rock to thermal exposure was to intentionally induce a state of 'semi-controlled' microcracking, resulting from the expansion of the material (Cruz and Gillen, 1980). This occurrence of microcracking was expected to contribute to the brittle tendency exhibited by the analogue rock specimens. In the present investigation, all specimens subjected to thermal exposure treatment were placed within an oven set at a temperature of 125°C for a duration of 24 hours prior to undergoing testing (Figure 2.3c).

#### **2.4.4 Curing and Testing Time**

In cementitious mixtures, the mechanical strength typically follows an upward asymptotic trend as curing progresses, reaching approximately 99% of *UCS* after 28 days (Neville and Brooks, 2010). Reducing curing time decreases *UCS* due to less cement hydration. Aside curing time, this study tested specimens both immediately and after a resting period to highlight the effect of cooling. Abramowicz and Kowalski (2005) reported that the cooling duration post-thermal exposure affects mechanical behavior. While microcracks remain small during heating, they expand during cooling (Kassir et al., 1996). This expansion is expected to promote brittle behavior due to accelerated crack propagation.

#### **2.4.5 Air-Entraining Admixture Usage**

Air-entraining admixtures (AEA) in cementitious mixtures contain surfactants to stabilize air voids, protecting against frost damage (Tunstall et al., 2021). However, in the developed analogue sedimentary rock, the AEA serves a different purpose. It is intended to promote accelerated crack propagation in the event of a sudden brittle failure in the specimen. This additional treatment involves incorporating the AEA in liquid form during mixing using a volumetric plastic syringe (Figure 2.3a).

The specimen was prepared by compaction with tamping rod, incorporating a high dosage of AEA, using low cement content, and uniformly graded fine aggregate, followed by exposure to thermal conditions before testing. Rath et al. (2017) observed that increasing the AEA dosage decreased the volume of coarse air bubbles while increasing fine air bubbles. This presence of distributed fine air

bubbles, represented into distributed micropores seems reasonable in facilitating accelerated crack propagation. The testing procedures from Section 2.4.3 were replicated with consistent AEA dosage. The experiment involved two curing periods and testing durations of 12 and 28 days, allowing for immediate testing or rest period before testing. Sika® Multi-Air 25, an AEA meeting ASTM C-260 standard (ASTM, 2010), was used at a consistent dosage of approximately 1.5 ml per 25 g of cement. The AEA was mixed with water before combining with other constituents, with water quantity adjusted to maintain the prescribed water-to-cement ratio  $w/cm$ .

#### **2.4.6 Saturation and Freezing Before Thermal Exposure**

The process of saturation and freezing before thermal exposure was intended to enlarge the micropores in the specimens, as water expands during freezing (Powell-Palm et al., 2020). The method of cold-water saturation (Safiuddin and Hearn, 2005) appears suitable for short curing periods and high porosity (25-30%) cementitious mixture. Upon saturation, the micropores become filled with water, which crystallizes and grows when exposed to freezing at -25 °C (Tunstall, 2016). Thawing of the ice in the specimen during subsequent thermal exposure is assumed to result in larger micropores.

Limited pore closure or crack closing under confinement can lead to earlier ductile transition (Wong and Baud, 2012). However, with deliberately regulated and closely spaced enlarged micropores, the analogue rock is hypothesized to show an extended brittle behavior. This assumption is based on the concept that larger micropores, when closed under confinement, form larger microcracks, facilitating easier crack propagation throughout the specimens. This method was evaluated based on the criteria for a higher Hoek-Brown constant  $m_i$ , which is reported to be associated with the brittle-ductile transition (Rahjoo, 2019). Figure 2.3b shows the specimens in a freezing chamber (chest freezer) with a cooling range of up to -25 °C.

### **2.5 Results and Discussions**

Throughout the development of very weak analogue sedimentary rock, there are three characterized rock-like designs (Mixes O, A, and B) that become milestones of the process of getting more brittle characteristics for the tunnel model specimen experimental study. These mixes proportions are mentioned earlier in Table 2.1. Mix B is the final design, exhibiting the most brittle characteristics observed. Numerous laboratory investigations and trial-and-error approaches were used to get from mix O to mix B, including mechanical and physical properties tests of the respective mix. The following subsections will present laboratory test results, where the discussions in subsections 2.5.1-2.5.3 are summarized in Figure 2.4.

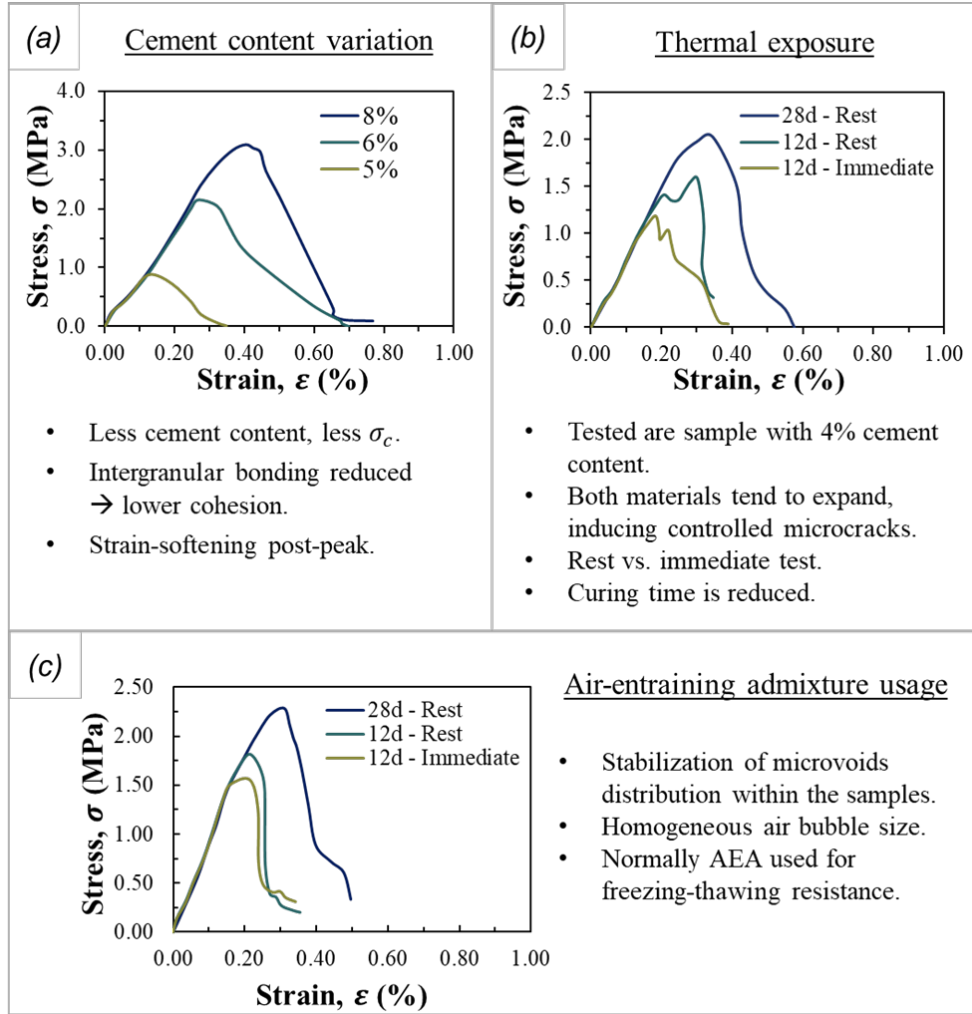


Figure 2.4 Development process summary with engineering treatment applied and stress-strain curves record as follows: (a) cement content variation, (b) thermal exposure, and (c) air entraining admixture (AEA) usage. Note that for (b) and (c), two different curing times (12 and 28 days) and test times (rest and immediate) were tested.

### 2.5.1 Effect of Cement Content Variation

From the UCT, mix O was observed to have  $UCS=3.07$  MPa, with 8% cement content design in the mixture. Figure 2.4a presents the UCT stress-strain curves for varying cement content (from 5%-8%), as the preliminary effort in improving the brittleness yet reducing the  $UCS$  from mix O design. From Figure 2.4a, the  $UCS$  values were decreasing following the decrease of cement content  $C$ . The post-peak stress-strain behavior notes that with less cement content, the analogue rock tends to be less brittle, shown from the strain-softening behavior that become less steep. Presumably, less cement content leads to less bonding into the rock-like matrix, affecting both the  $UCS$  and brittleness. With this finding, a further process was implemented and observed; as mentioned in Section 2.4.3, the additional treatment applied to increase the brittleness included the introduction of a thermal exposure to the sample.

### 2.5.2 Effect of Thermal Exposure

In this study, all specimens subjected to thermal exposure treatment were placed in an oven at one day prior to the completion of designated curing period. The UCT result indicates that the thermal exposure has a positive effect on the *UCS* after 28 days of curing. Two alternatives were implemented, namely the reduction of curing time and the decrease in cement content. Figure 2.4b shows the stress-strain relationship after thermal exposure with cement content limited to 4%, and two of the three specimens subjected only 12 days of curing. The minimum cement content ensures adequate binding of fine aggregates.

Post-peak behavior observations revealed that specimens with a rest period (cooling) before testing demonstrated greater *UCS* compared to those tested immediately. However, strain softening was more pronounced in cooled specimens, indicating a more brittle response (Figures 2.4b and 2.4c). The microcracks formed during heating are due to the expansion of both cement hydration product and fine aggregates (Cruz and Gillen, 1980). During cooling, bond restoration within the interfacial zone seems reasonable to increase *UCS*. Nevertheless, cooling also induces microcrack expansion (Kassir et al. 1996), which seems reasonable to align with the observed brittle behavior.

### 2.5.3 Effect of Air-Entraining Admixture (AEA)

Similar testing procedures are employed when administering a consistent dosage of air-entraining admixture (AEA). Following from previous findings with thermal exposure, the investigation documents two different curing durations, namely 12 and 28 days, as well as two testing times, specifically immediate testing and testing after thermal exposure. Figure 2.4c presents the stress-strain curves from the UCT after introduction of AEA. The inclusion of AEA in the sample demonstrates potential in brittleness enhancement, as the behavior observed after reaching the peak shear strength displayed a notable drop in strength following a limited post-yield strain. The homogeneous distribution of entrained air voids (micropores), as outlined in Section 2.4.5, seems reasonable for facilitating an accelerated propagation of cracks.

### 2.5.4 Effect of Saturation and Freezing Exposure

The treatment of saturation and freezing exposure was incorporated and tested using thin section analysis and triaxial tests. Two highlighted specimen designs, which are introduced earlier as mixes A and B, were compared with the same mix proportion (water-to-cement ratio  $w/cm$ , cement content  $C$ , AEA dosage), curing time, and test time. Both mixes were contrasted as follows:

- Mix A: underwent only saturation and thermal exposure (Figure 2.5a)
- Mix B: underwent saturation, freezing and thermal exposure (Figure 2.5b)

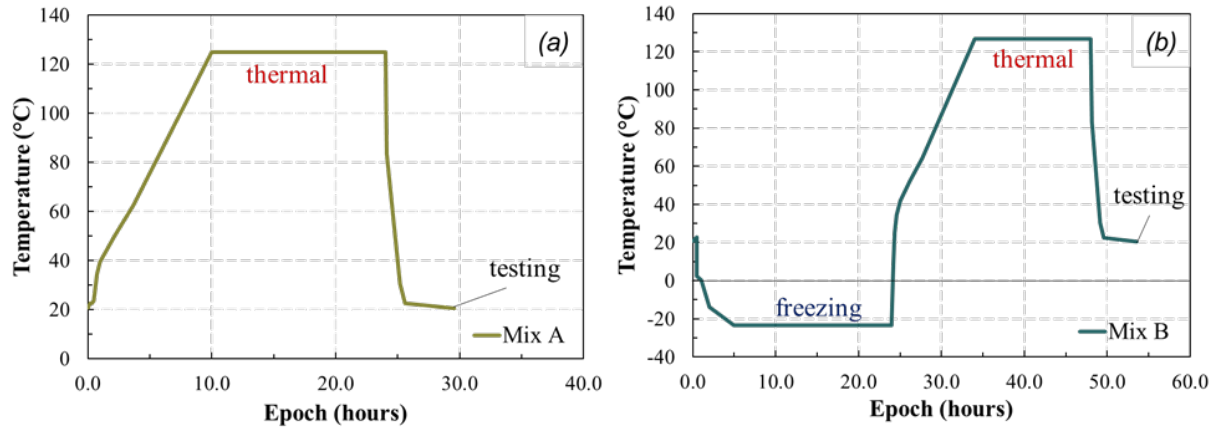


Figure 2.5 Freezing temperature and thermal exposure treatments diagram for (a) mix A that underwent only saturation and thermal exposure and (b) mix B that underwent saturation, freezing temperature, and thermal exposure. Sample surface temperature is continually monitored using a FLIR One Pro LT thermal camera.

The measurement reported in Figure 2.5 was based on sample surface temperature, measured continually using FLIR One Pro LT thermal camera. Both freezing and thermal exposures are extended for several hours to ensure that the designated temperatures of  $-23.5^{\circ}\text{C}$  for freezing and  $125^{\circ}\text{C}$  for thermal treatments was reached completely within the specimen. Approximate freezing and thermal rates were calculated at  $-5^{\circ}\text{C}/\text{minute}$  and  $0.16^{\circ}\text{C}/\text{minute}$ , respectively. After taking out the specimen from the oven, the cooling rate down to room temperature was approximately  $-0.96^{\circ}\text{C}/\text{minute}$ . All specimens were tested at room temperature. The thermal exposure condition applies to the findings summarized in Figures 4b and 4c.

#### *Thin-section image analysis*

Thin sections from mixes O, A, and B were analyzed to verify the effects of the treatments on inducing larger micropores and better pore distribution within the specimens. The thin-section billet size was  $25\text{ mm} \times 40\text{ mm} \times 10\text{ mm}$  for all specimens and was impregnated with epoxy resin containing a blue dye injected into the pore system. Since mixes A and B had a 24-hour gap in treatments at the end of curing stage (Figure 2.5), the timing for epoxy resin injection and thin-section imaging was carefully synchronized for both. This timing consistency ensures that the effect of different treatments can be compared accurately.

Figure 2.6 presents sampled thin section images ( $5 \times 9\text{ mm}$ ) and corresponding pore size histograms for all mixes. In the upper images, the blue coloration represents the impregnated resin dye, which surrounds the grains and cement bonds to highlight pore areas. The lower images show the processed thin sections using ImageJ software with binary and watershed processing. The histograms were generated from these processed images using particle analysis to illustrate the distribution of pore sizes.



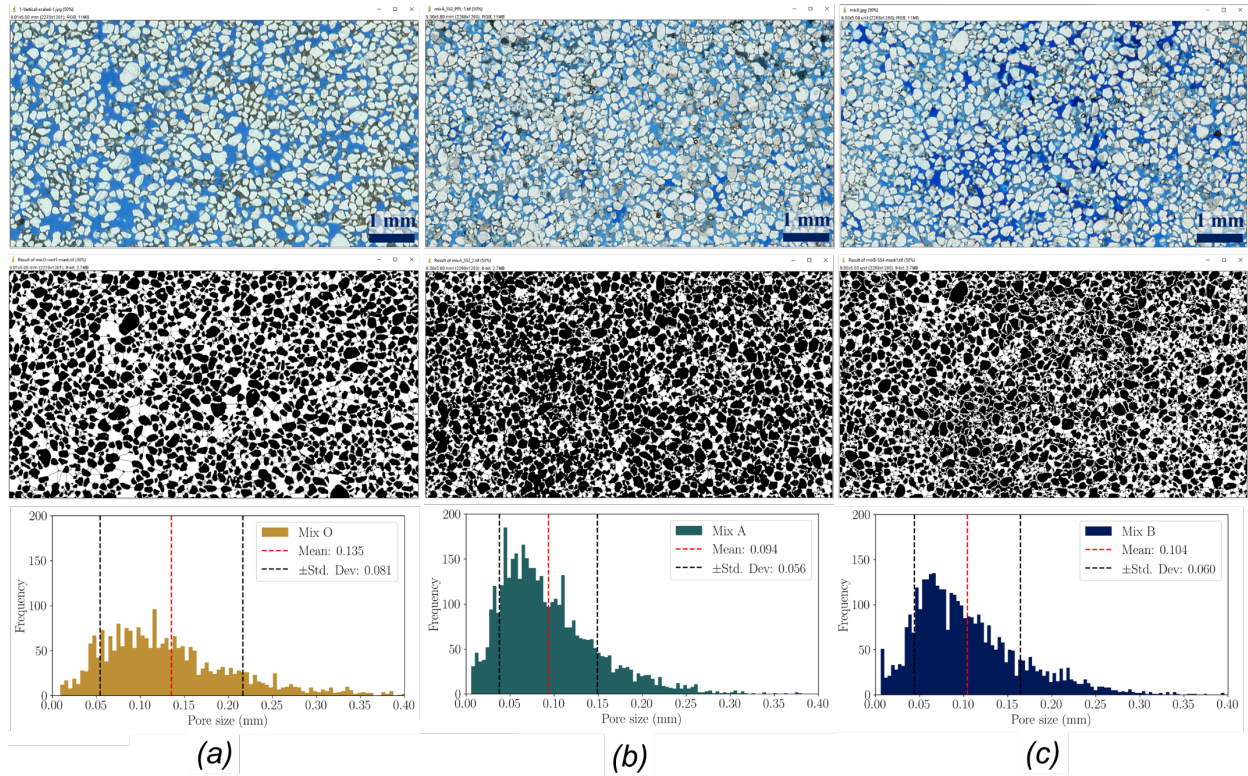


Figure 2.6 Thin section images and pore size distribution from (a) mix O, (b) mix A, and (c) mix B, each sampled from a  $5 \times 9$  mm area.

The thin section images display a relatively dense matrix with fine aggregate particles, consistent with the mix constituents. The pores in Figure 2.6a appear visually scattered and larger than those observed in the other mixes. The well-distributed aggregate particles in mixes A and B indicate enhanced compaction and isotropy. In mix A (Figure 2.6b), the micropores are smaller compared to those in mix B, where they appear slightly larger and more irregular in shape (Figure 2.6c). The histograms show mean pore Feret diameter measurements of  $0.135 \pm 0.081$ ,  $0.094 \pm 0.056$  and  $0.104 \pm 0.060$  mm for mixes O, A and B, respectively. These measurements support the trend of increasing micropore size from mix A to B, as described in Section 2.4.6. Additionally, about 20% reduction in standard deviation suggests that the use of AEA is effective in controlling pore size distribution.

#### *Unconfined and triaxial compression test*

The results of unconfined and triaxial compression tests conducted on both mix A and B, including mix O are presented herein. Table 2.2 summarizes the engineering treatments, mix design, average porosity, *UCS*, *UTS*, and Mohr-Coulomb and Hoek-Brown failure envelope fit values observed in this study among mixes O, A, and B.

Table 2.2 Summary of mix design (engineering treatments, cement content, water to cement ratio) and laboratory test results (material physical and mechanical properties) for mixes O, A, and B.

Properties	Mix O	Mix A	Mix B
<i>Treatment remarks</i>	<i>28 days curing</i>	<i>12 days curing, AEA, thermal</i>	<i>12 days curing, AEA, saturation-freezing, thermal</i>
Cement Content, $C$	8%	4%	4%
Water to cement, $w/cm$	1.2	1.2	1.2
Saturated unit weight, $\gamma_{sat}$ (kN/m <sup>3</sup> )	17.8	18.4	18.5
Dry unit weight, $\gamma_{dry}$ (kN/m <sup>3</sup> )	16.7	16.9	16.8
Average porosity, $n$	11.51%	29.71%	30.59%
Average uniaxial compressive strength, $UCS$ (MPa)	3.07	1.82	1.68
Average tangent Young's modulus at 50% peak shear strength, $E_{50}$ (GPa)	0.94	0.81	0.76
Average indirect tensile strength, $UTS$ (MPa)	0.45	0.22	0.19
Cohesion, $c$ (MPa)	1.06	0.35	0.28
Friction angle, $\phi$ (°)	21.4	43.18	43.24
Poisson's ratio, $\nu$	0.21	0.22	0.22
Hoek-Brown constant, $m_i$	4.89	19.93	20.58

According to the data presented in Table 2.2, it can be observed that the porosity increased significantly from mix O to mix B. When subjected to engineering treatment, both the  $UCS$  and  $UTS$  exhibit a decrease. The reduction in  $UTS$  indicates the improvement on the brittleness, that will be assessed further through strength parameter brittleness criteria. In addition of brittleness improvement, Figure 2.7 presents the failed specimen for both mixes A and B. The failure specimen for mix B predominantly exhibited more significant axial splitting with brittle faulting (sub-vertical fractures) compared to mix A with splitting with shear faulting.

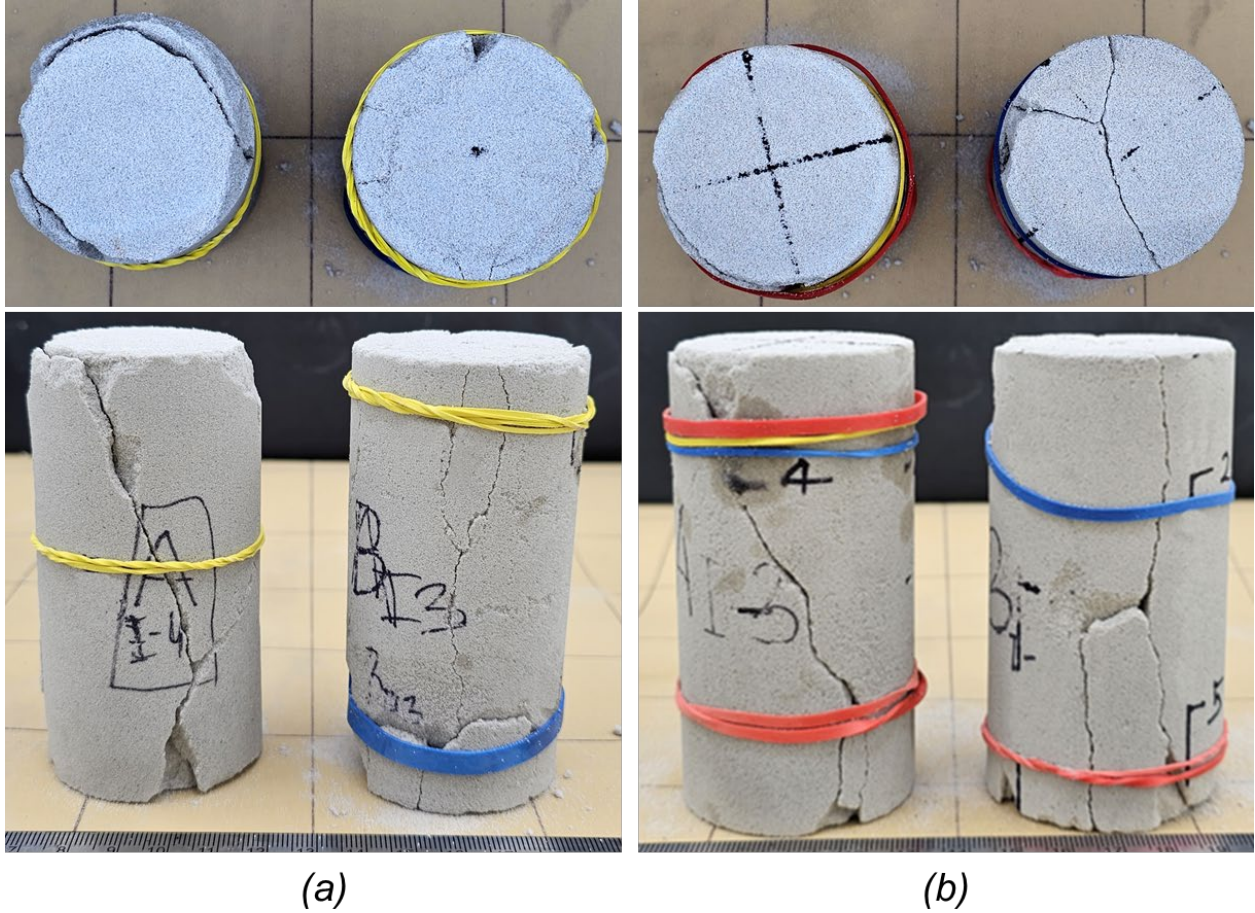


Figure 2.7 The specimens of both mixes A and B after UCT: (a) UCT and (b) UCT-AE-Ext. mix B specimens exhibited failure characterized by more sub-vertical fractures, parallel to major principal stress extensional fractures, in contrast to the failure pattern observed in mix A.

For the UCT results, mix B has the lowest  $UCS$  among select mixes of 1.68 MPa. Particularly compared with mix A, the inclusion of freezing treatment caused an approximate 7.7% reduction of  $UCS$ . This reduction of strength could be attributed to the porosity and average Feret diameter measurements discussed in the previous Section. Zhu et al. (2010) provided an equation to estimate the peak shear strength ( $UCS$  in unconfined compression) based on the stress intensity factor, inverse square root of pore radius, and porosity following power law. The equation that valid for porosity less than 40% is as follows:

$$\sigma_c = \frac{1.325}{n^{0.414}} \times \frac{K_{IC}}{\sqrt{\pi r}} \quad (2.2)$$

where  $n$  is porosity,  $K_{IC}$  is the stress intensity factor, and  $r$  is the pore radius. Plugging in the porosity and pore radius values for mix A and mix B, the calculated reduction of  $UCS$  from mix A to mix B is predicted to be 9.2%, that is relatively close to current observation. It is assumed that the stress intensity factor  $K_{IC}$  for both mixes are the same due to same mix design to build the specimen.

Triaxial tests were performed at three different confining pressures for each mix; mix O with higher UCS (3.07 MPa) is tested with 1.5, 3, and 4.5 MPa, whereas mix A and B with smaller UCS (1.82 and 1.68 MPa, respectively) are tested with 0.6, 0.8, and 1 MPa. Reported unconfined compressive strength and triaxial data are processed using RSData (Rocscience Inc., 2022) to generate Mohr-Coulomb and Hoek-Brown failure envelopes for each mix. Figure 2.8 presents the plots of the obtained failure envelopes along with Mohr intrinsic circles from the test.

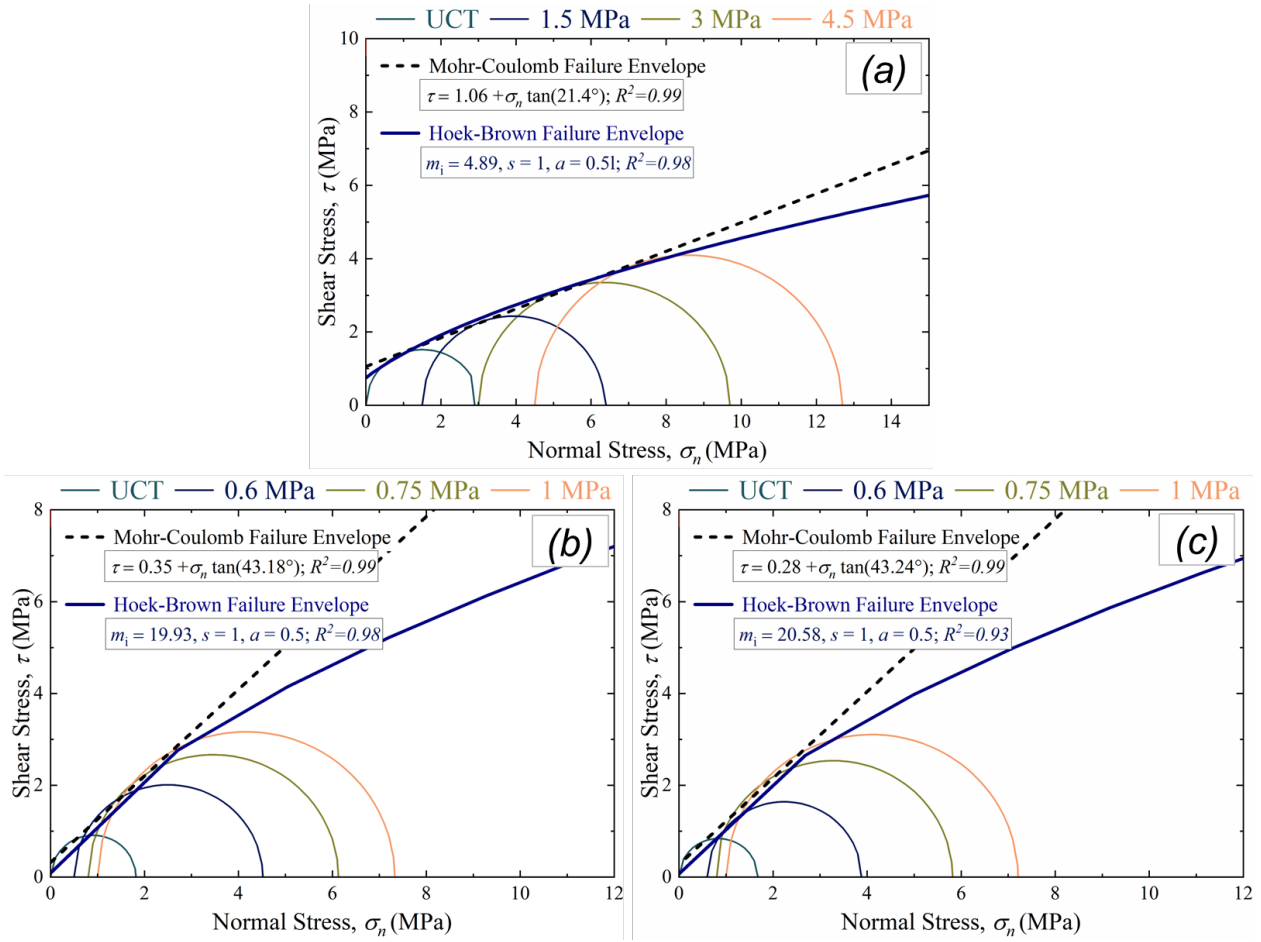


Figure 2.8 Mohr circles at failure for unconfined and triaxial compression tests with the best fitting for Mohr-Coulomb and Hoek-Brown failure envelopes for a) mix O—preliminary design, b) mix A—only saturation and thermal exposure, and c) mix B—with additional freezing exposure.

The effect of freezing treatment in mix B (Figure 2.8c) demonstrates a reduction in cohesion but a slight increase in the internal friction angle  $\phi$ . The effect can also be indicated from the increase of the Hoek-Brown constant  $m_i$ , that can lead to higher brittle-ductile transition. The brittle-ductile transition is reported to have a correlation to the Hoek-Brown constant as following:



$$\frac{\sigma_3^*}{\sigma_c} = \left( \frac{m_i + \sqrt{m_i^2 + 4d^2}}{2d^2} \right) \quad (2.3)$$

where  $\sigma_3^*$  is expected confinement at the brittle-ductile transition and  $d$  is ductility number. Aside from the failure envelopes, the stress-strain curves and volumetric strains measurement are plotted to support the findings. Figure 2.9 presents the summarized results that include unconfined and triaxial compression test.

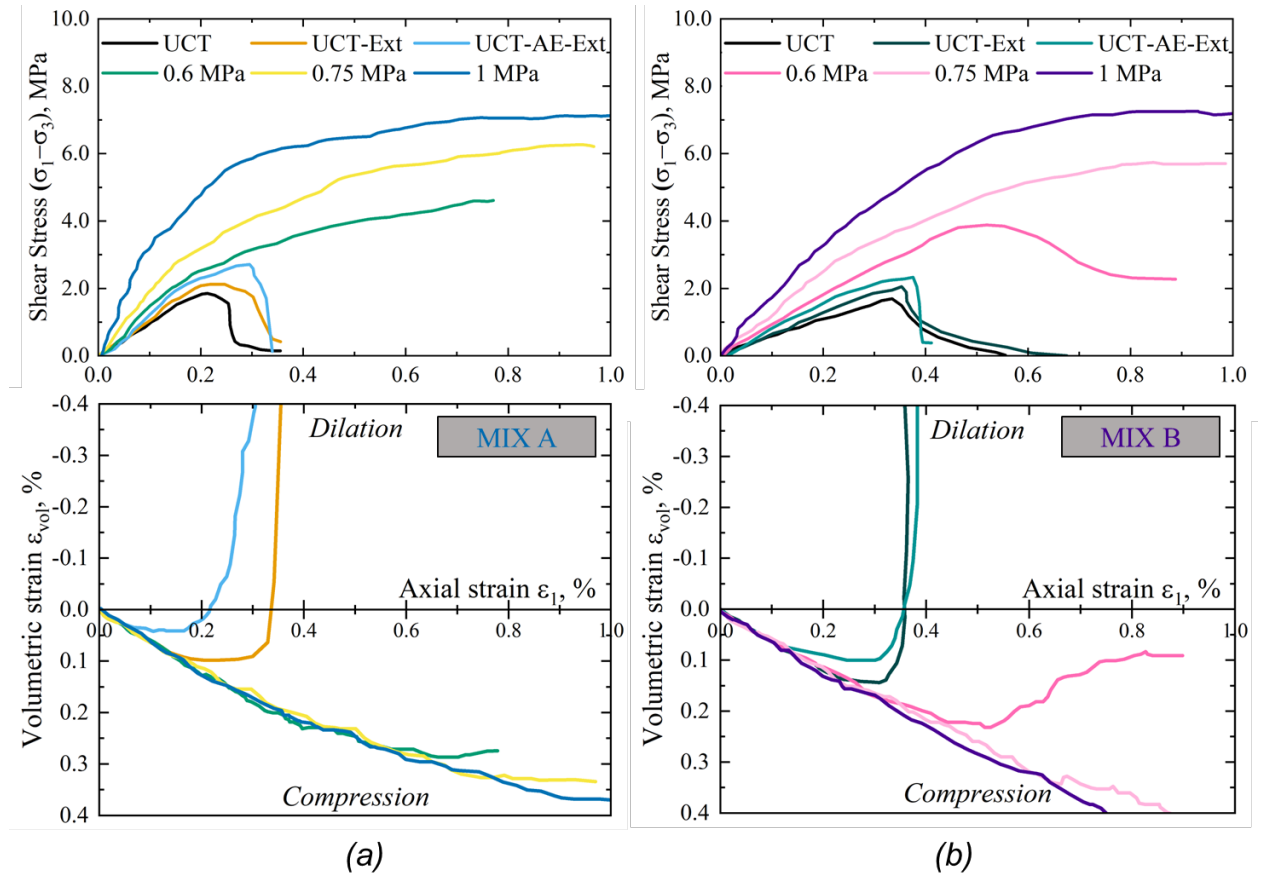


Figure 2.9 Full stress-strain (upper) and volumetric strain curves (lower) associated with both unconfined and triaxial compression tests for a) mix A—only saturation and thermal exposure, and b) mix B—with additional frost exposure.

The stress-strain responses of both mixes are shown in terms of the shear stress ( $\sigma_1 - \sigma_3$ ) vs. axial strain  $\epsilon_1$  curves in Figure 2.9. One can note that both mixes A and B display strain-softening response under the UCT. However, the strain-softening response is still observed for Mix B (Figure 2.9b) at 0.6 MPa applied confinement. This observation is perceived to indicate higher brittle-ductile transition in mix B compared to mix A. In the volumetric strain plots, the volumetric responses of both mixes are shown in

terms of volumetric strain  $\varepsilon_{vol}$  vs. axial strain  $\varepsilon_1$  curves with different level of applied confinement. Under higher confinement (more than 0.6 MPa), both mixes A and B exhibit a purely contractive reaction, which is represented by a positive trend indicating inward volumetric movement of the specimen.

Two additional data sets were included for calculating the peak dilation angle (Figures 2.9a and 2.9b) based on the test with chain extensometer only (UCT-Ext) and chain extensometer with acoustic emission (AE) sensor configuration (UCT-AE-Ext). Figure 2.10 presents the setup of the UCT-Ext and UCT-AE-Ext. The configuration on the acoustic emission sensor placement may slightly add confinement due to usage of electrical tape around the specimen. Additionally, the chain extensometer itself appeared to increase shear strength, likely due to its added confinement effect. Discussions on AE results of mixes A and B can be found in Gautam and Gutierrez (2024). Based on the developed Mohr-Coulomb failure envelopes (Figure 2.8), the estimated confinements for mixes A and B are 0.1 MPa with the UCT-Ext configuration and 0.2 MPa with the UCT-AE-Ext configuration.

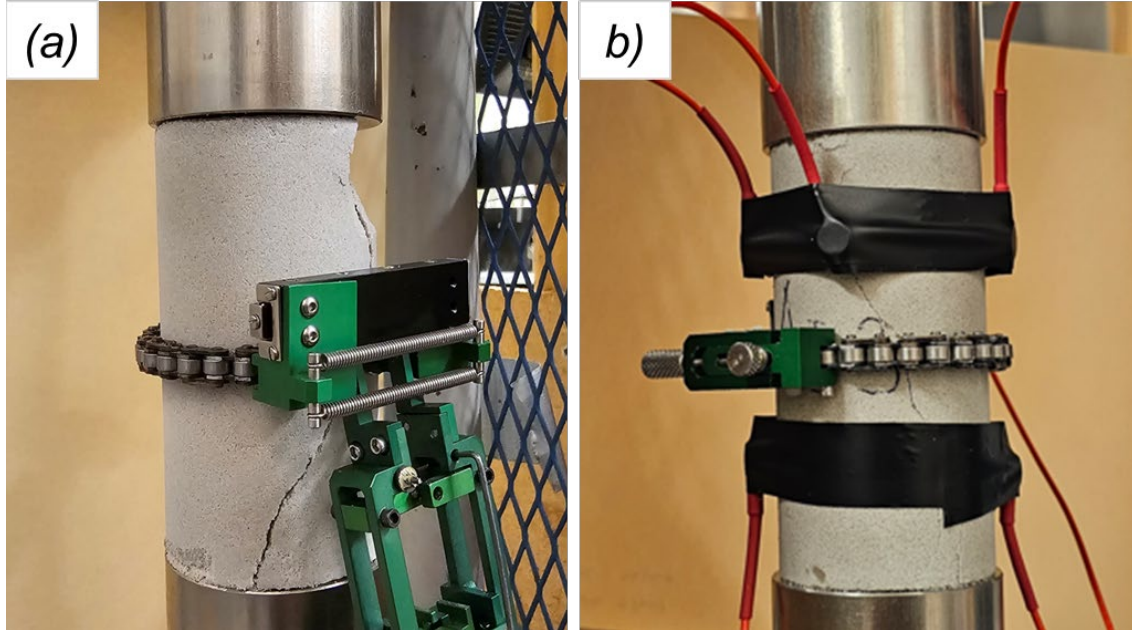


Figure 2.10 Configuration for additional data sets from UCT: (a) using circumferential extensometer to measure diametrical deformation (UCT Ext), and (b) integrating an acoustic emission (AE) sensor alongside the extensometer (UCT-AE-Ext). Notably, the AE sensor is not directly associated with diametrical deformation readings. Instead, its inclusion in the figure is intended to illustrate the potential confinement effects, considering the very weak UCS of the specimen.

### 2.5.5 Peak Dilation Angle and Elastic Modulus

In this study, the peak dilation angle  $\psi$  based on the volumetric strain measurement is also reported for all mixes O, A, and B. The dilatancy is understood to be typically associated with brittle

deformation mechanisms—crack formation and opening (Kim et al., 2021). To calculate the peak dilation angle  $\psi$ , the following formula was used:

$$\psi = \arcsin \frac{1 + \left| \frac{d\varepsilon_{vol}}{d\varepsilon_1} \right|_{max}}{3 - \left| \frac{d\varepsilon_{vol}}{d\varepsilon_1} \right|_{max}} \quad (2.4)$$

where  $\varepsilon_{vol}$  is the volumetric strain and  $\varepsilon_1$  is the axial strain that is presented in Figure 2.9. Other than the dilation angle, elastic modulus variation is also presented to give insight on the confinement dependency of this very weak analogue sedimentary rock. Figure 2.11 presents the dilation angle and elastic modulus variation between mixes O, A and B.

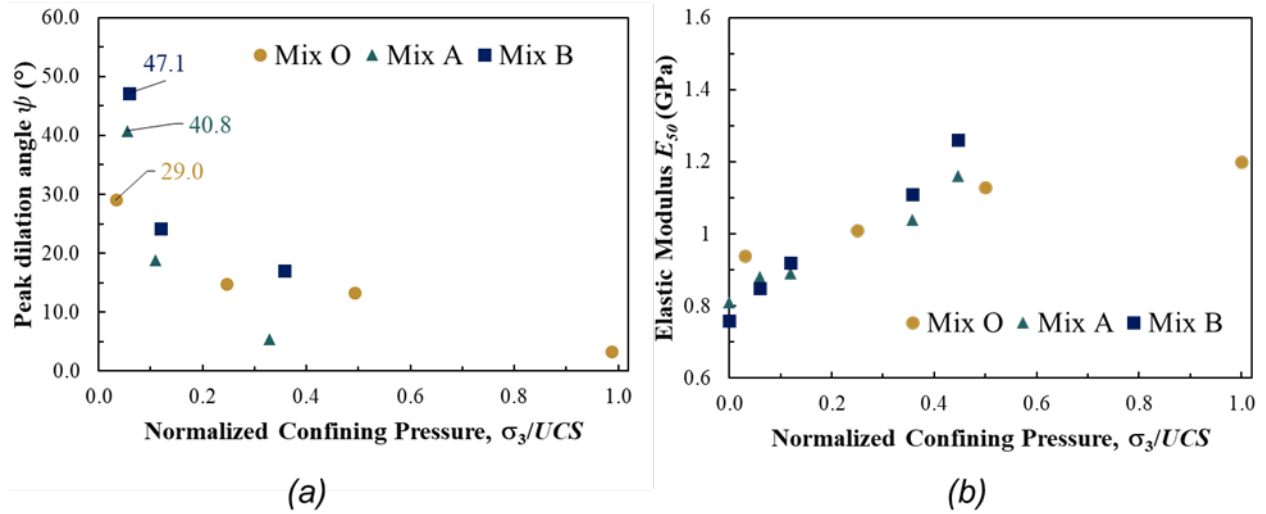


Figure 2.11 Calculated properties with the normalized confining pressure to the  $UCS$  for mixes O, A, and B; (a) peak dilation angle and (b) elastic modulus  $E_{50}$ . The first values for each mix were obtained from the UCT under assumed confinement. These assumptions stem from the setup configuration, which includes the circumferential extensometer and the placement of acoustic emission (AE) transducer (refer to Figure 2.10).

From Figure 2.11a, one can notice that the peak dilation angles were only reported for the unconfined compression and low confinement triaxial tests. For mix O, the UCT data was only from the UCT-Ext configuration, with 0.08 MPa confining pressure approximated from corresponding Mohr-Coulomb failure envelope (Figure 2.8). The y-axes of confining pressure are normalized to provide better comparison among the mixes. The highest peak dilation angle for each mix was observed from the UCT-Ext with 29.0° for mix O, 40.8° for mix A, and 47.1° for mix B (Figure 2.11a). Generally, the peak dilation angle tends to be close to zero with increasing confinement. This indicates a diffused deformation as the ductile shear response becomes the dominant deformation mechanism (Nygård et al. 2006). The absence of phase transformation—the transition from contractive to dilative response—can also be observed in Figure 2.9 when examining the volumetric strain under increased confinement.

Figure 2.11b, on the other hand, presents the increase in elastic modulus along with the applied confining pressure. This finding aligns with the observation made by Addis et al. (1990), which noted a confinement dependency on the elastic modulus of the weak analogue material. The elastic modulus demonstrates an almost twofold increase when subjected to the highest level of confinement, compared to the lowest level of confinement for mixes A and B. In addition, a high porosity level for both mix A and mix B would affect this elastic modulus dependency. The effect is less pronounced for mix O, potentially due to lower porosity of the mix. Although focusing only on UCT, Palchik (1999) reported that high porosity has an effect of rock stiffness. The densification and increased grain-to-grain contact resulting from the pore closure under confinement pressure contribute to the stiffness enhancement of the specimen.

### 2.5.6 Brittleness Assessment

For assessing the brittleness based on the strength parameter, the calculation involves the ratio between *UCS* and *UTS* of the rock that define the strength brittleness index  $B_1$ . The ratios pertaining to mixes O, A, and B are approximately 8, with specific values of 7.36, 8.27, and 8.84, correspondingly. Moreover, the acquired values exhibit a greater alignment with Griffith's crack theorem when considering specimens that possess microcracks. The calculated values of brittleness assessment for all mixes are summarized in Table 2.3.

For two other assessments of the brittleness index modified *BIM* and burst energy coefficient *R*, the UCT stress-strain curve analysis for brittleness assessment is summarized in Figure 2.12. The rock bursting tendency can be preliminarily assessed using the brittleness index modified *BIM*, which is based on a comprehensive analysis of over 300 uniaxial compression test results conducted on more than 50 distinct rock types of various origins (Aubertin et al., 1994; Gong et al., 2020). *BIM* can be described as the quantification of the entire input energy density during the pre-peak phase, relative to the elastic strain energy density at the peak. The criterion is represented by the equation  $BIM = A_2/A_1$ , where  $A_1$  is the peak elastic strain energy density that is achieved by considering the deformation modulus at 50% of the peak strength and  $A_2$  is defined as the cumulative integral of the stress-strain curve up to the point of maximum compressive strength. The components of  $A_2$  and  $A_1$  can be calculated from following equations as also illustrated in Figure 2.12a:

$$\varepsilon_c = OC + CB = \varepsilon_p + \varepsilon_e \quad (2.5a)$$

$$A_2 = \Delta OAB = \int_0^{\varepsilon_c} f_c(\varepsilon) d\varepsilon \quad (2.5b)$$

$$A_1 = \Delta ABC = \int_{\varepsilon_p}^{\varepsilon_c} f_2(\varepsilon) d\varepsilon \quad (2.5c)$$



This  $A_1$  value is assumed to correspond to the unloading curve, which is represented as a parallel line to the stress-strain curve starting from the point of peak strength. The region bounded by the linear unloading curve represents the maximum elastic strain energy density. For mix B with  $BIM$  of 1.11, the  $A_1$  and  $A_2$  are  $2.8 \times 10^{-3}$  and  $3.1 \times 10^{-3}$ , respectively. This  $BIM$  reflects the higher tendency for bursting rock, compared to mix O and A.

Figure 2.12b illustrates the procedure for calculating the burst energy coefficient  $R$  on mix O, mix A, and mix B UCT stress-strain curves. The ratio between accumulated strain energy before peak  $W_E$  to dissipated strain energy after peak  $W_P$  is defined as the burst energy coefficient  $R$  (Cai 2016). This full stress-strain curve is typically obtained from a stiff UCT system as the system responds to gradual deterioration in load-carrying capacity through automatic reduction in the applied load (Goodman, 1989). The accumulated and dissipated strain energy are reflected in the left portion and right portion of the full stress-strain curve, respectively. Both accumulated and dissipated strain energy ( $W_E$  and  $W_P$ ) components can be calculated from following equations:

$$\varepsilon_{total} = OC + OB = \varepsilon_c + \varepsilon_{ss} \quad (2.6a)$$

$$W_E = \Delta OAC = \int_0^{\varepsilon_c} f_c(\varepsilon) d\varepsilon \quad (2.6b)$$

$$W_P = \Delta ABC = \int_{\varepsilon_c}^{\varepsilon_{total}} f_{ss}(\varepsilon) d\varepsilon \quad (2.6c)$$

As an empirical criterion, the ratio larger than one shows a tendency for the rock to burst or fail in a brittle, violent manner. From Table 2.3, mix B shows the highest burst energy coefficient  $R$ . This finding demonstrates that the listed engineering treatments are significant in producing more brittle material while keeping the  $UCS$  low.

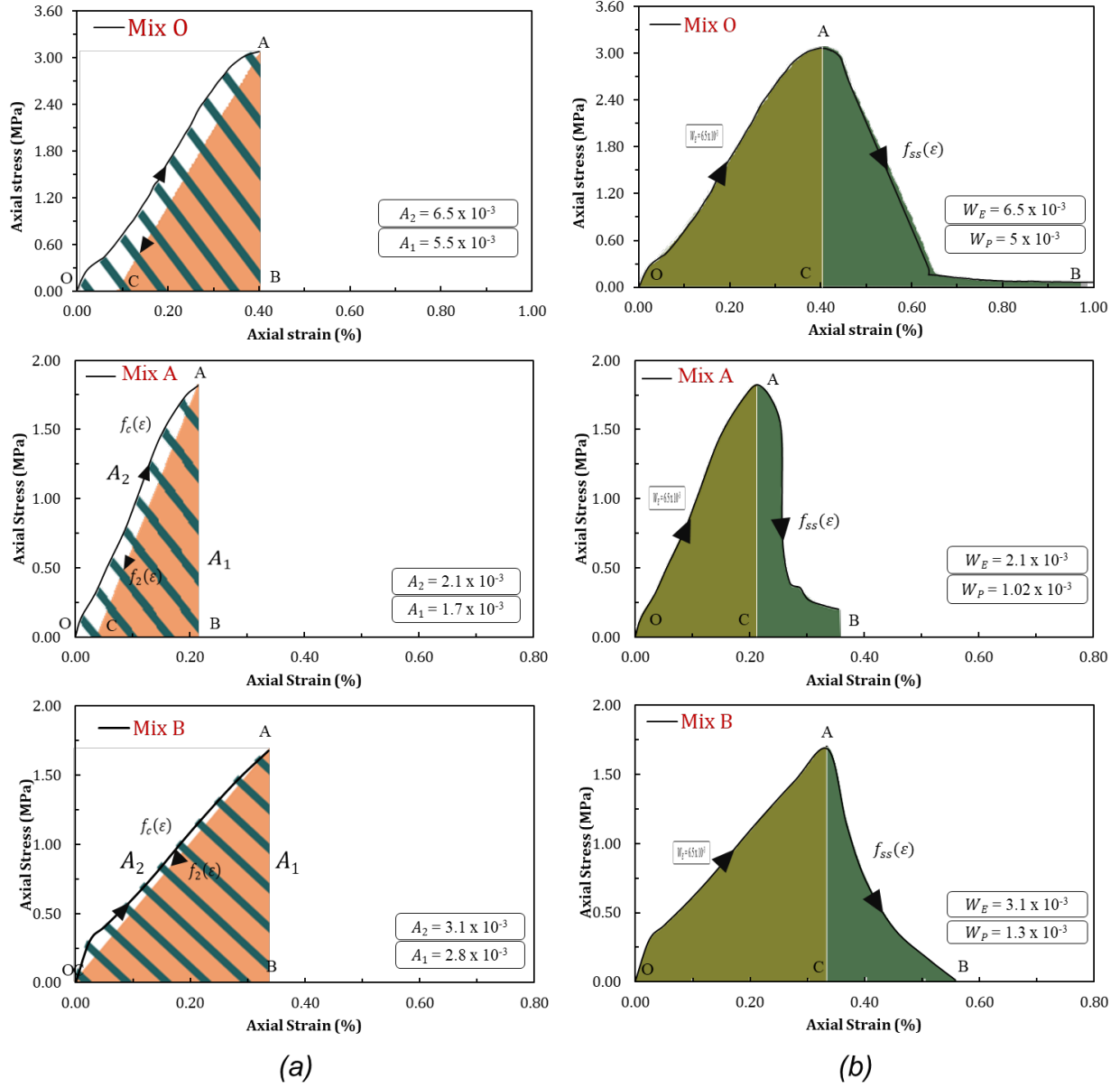


Figure 2.12 Evaluations of the brittleness of the analogue material based on the UCT stress-strain curves analogue using (a) burst energy coefficient  $R$  and (b) brittleness index modified  $BIM$ .

Table 2.3 Brittleness assessment with rock bursting criteria used for the analogue sedimentary rock mixes O, A, and B.

Bursting Criteria	Source	Mix O	Mix A	Mix B	Typical Ranges for Bursting
Strength brittleness index, $B_1 = \sigma_c / \sigma_t$	Hucka and Das (1974)	7.36	8.27	8.84	< 14.5 (High)
Brittleness index modified, $BIM = A_2 / A_1$	Goodman (1989)	1.18	1.38	1.11	1.0 - 1.2 (High), 1.2-1.5 (Moderate)
Burst energy coefficient, $R = W_E / W_P$	Aubertin et al. (1994)	1.3	1.56	2.50	> 1.0 (Moderate-High)

### 2.5.7 Micropores Idealization and Cracking Mechanisms

Figure 2.13 depicts the illustration of apparent air voids microstructure changes in each mixture with the various treatments applied. The illustrations are based on Python code written using Matplotlib library. The code enables simulation of two-dimensional porosity to some extent in the specimen. The micropores are assumed in circular geometry that is randomly distributed for visualization purposes. Furthermore, one can specify the distribution type for micropores generation (in this case using normal distribution—maximum, mean, standard deviation) and minimum distance between each pore to avoid micropores coalescences for more relevant pore area calculation. The generation of the micropores will be completed when the sum of pore area meets the predetermined porosity percentage, which represents the ratio between the area occupied by micropores and the overall specimen area.

The micropore input size for mixes A and B is taken from the Feret diameter distribution obtained through thin section imaging (Figure 2.6). Mixes A and B contrast to mix O due to the air-entraining admixture that perceived to stabilize the air voids inside the specimen, which gives small variance of the micropore size (Tunstall, 2016). Notably, air voids are unavoidable in the hydrated cement paste, with various types of voids, amounts, and significance (Mehta and Monteiro, 2014). In the absence of an air-entraining admixture, the air voids in the hydrated cement paste are mostly formed by entrapped air with the largest size among the types of the air voids. Also, the entrapped air is associated with relatively irregular size.

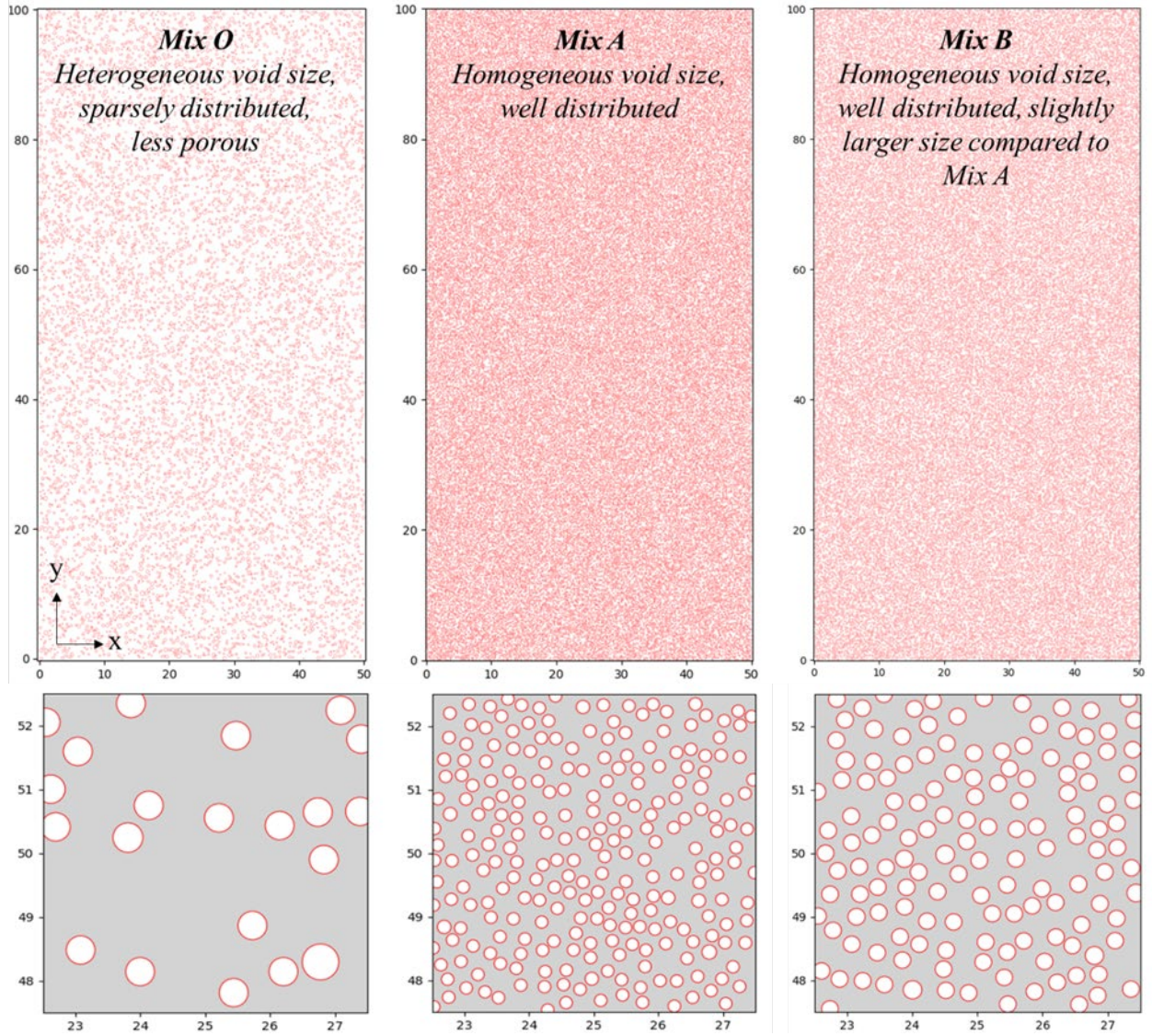


Figure 2.13 Visual representation of perceived alterations in the microstructure of air voids/entrained micropores across different mixtures, as affected by the different engineering treatments used to prepare the analogue material. Three selected mixes are presented as mixes O, A, and B that were discussed in Section 2.4. These figures serve solely as an illustrative tool for idea comprehension and are generated with assumed and obtained parameters such as micropore sizes, spacings between micropores, and porosity.

As the confining pressure increases in triaxial testing, crack-like micropores undergo a gradual closure process, often starting with those possessing the smallest aspect ratio (Detournay and Cheng, 1993). Figure 2.14. illustrates an array of through-cracks, growing in a two-dimensional linear-elastic medium under a triaxial stress field  $\sigma_1$  and  $\sigma_3$ . The triaxial stress field  $\sigma_1$  and  $\sigma_3$  causes a shear stress  $\tau$  and a normal stress  $\sigma$  across faces of the initial cracks, forming crack slides that open the mouth of each wing crack. Ashby and Sammis (1990) summarized the following equations for determining the sliding force at the initial crack  $F_3$ :

$$\tau = \frac{\sigma_3 - \sigma_1}{2} \sin 2\beta \quad (2.7a)$$

$$\sigma = \frac{\sigma_3 + \sigma_1}{2} + \frac{\sigma_3 - \sigma_1}{2} \cos 2\beta \quad (2.7b)$$

$$F_3 = (\tau + \mu\sigma)2a \sin \beta \quad (2.7c)$$

where  $\mu$  is the coefficient of friction acting across the crack faces and  $\beta$  is the angle between the crack sliding surface and the wing crack plane (Figure 2.14). The Eq. (2.7c) demonstrates the linearity between sliding force  $F_3$  and initial crack size  $a$ , indicating that additional sliding force can be expected from mix A to mix B.

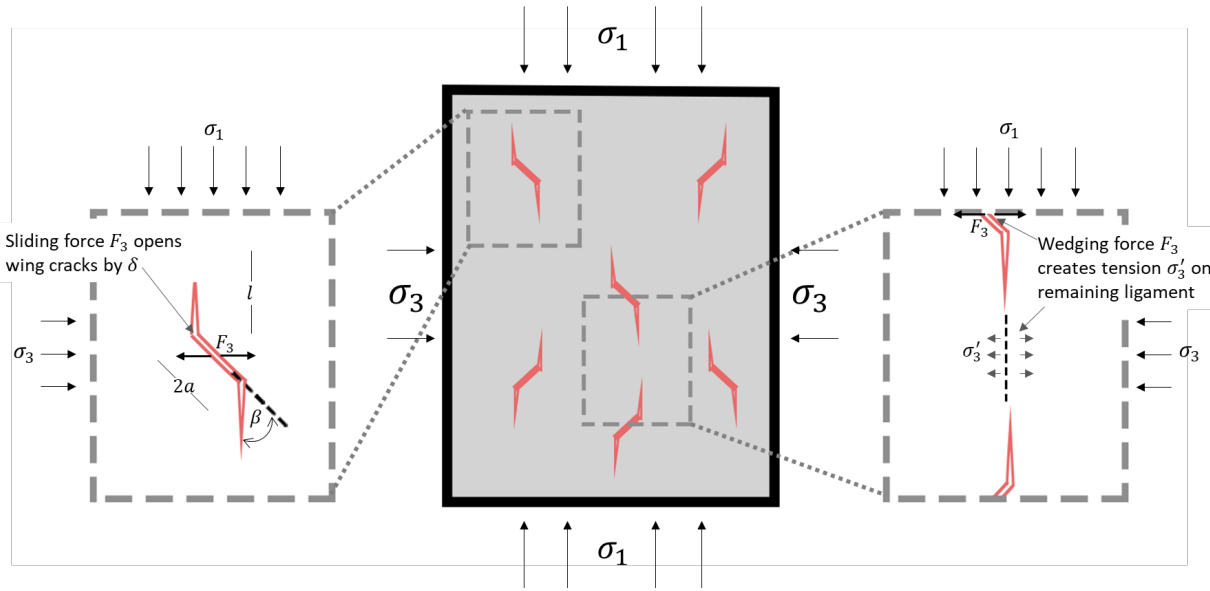


Figure 2.14 Population of growing cracks under triaxial stress condition adopting two-dimensional wing crack model (after Ashby and Sammis, 1990).

The concentration from the pore surface leads to the initiation of fractures that propagate parallel to the direction of maximum compression. As the cracks propagate, they begin to interact, and if their mean spacing is sufficiently small, crack propagation becomes unstable (Wong and Baud, 2012), possibly leading to crack coalescence in a scenario analogous to microstructural observations reviewed above. The implementation of saturation and freezing at enlarging pore size and ensuring a well-distributed structure within mix B is thought to support crack propagation and coalescence upon reaching the peak shear strength. This, in turn, leads to a more brittle response in the analogue material.

### 2.5.8 Comparison of Analogue Material Properties with Natural Sedimentary Rock

This section compares the properties of the developed analogue rock with natural sedimentary rocks using the framework from Tatone et al. (2023). Key properties such as Poisson's ratio, density,

elastic modulus ratio, and strength ratio (Table 2.2) were assessed. Figure 2.15 shows the plots of the materials developed in this study in conjunction with previously collected data on natural rock and developed rock-like materials (Addis et al., 1990; Cheon et al., 2011; David et al., 1998; Klammer et al., 2023; Tatone et al., 2023; Wu et al., 2020).

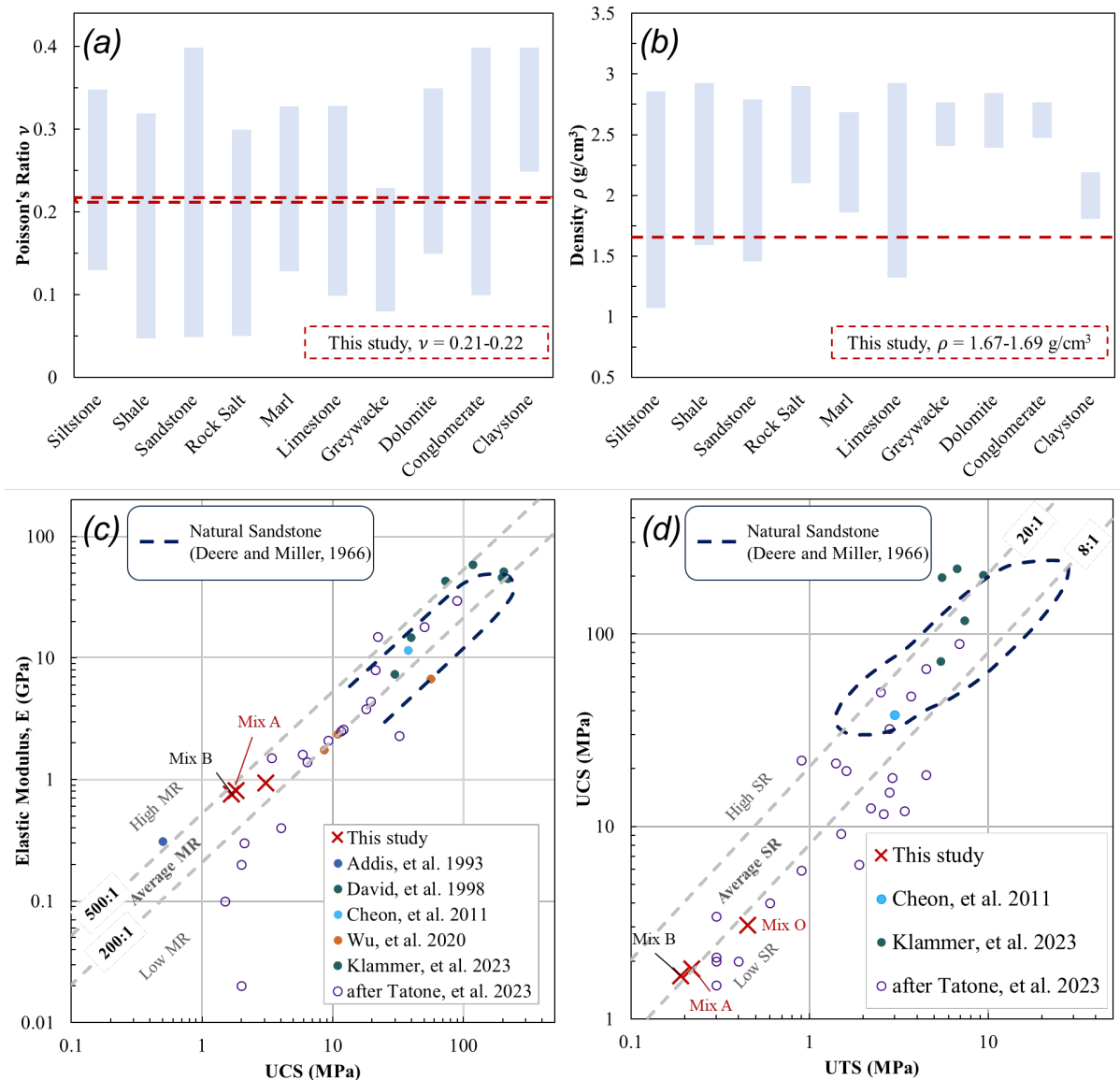


Figure 2.15 Comparative plot depicting the properties of very weak analogue sedimentary rocks developed in this study, alongside data collected from previous studies on natural rock and rock-like materials: (a) Poisson's ratio (Gercek, 2007), (b) density (Johnson and Olhoeft, 1989; Lama and Vutukuri, 1978), (c) modulus ratio, and (d) strength ratio (Tatone et al. 2023).

Figures 2.15a and 2.15b present the comparison of the Poisson's ratio and density of very weak analogue to natural sedimentary rocks. The Poisson's ratio value is fit to the sedimentary rocks range, while the density value falls within the lower bound of certain sedimentary rock types, such as siltstone, sandstone, shale, and limestone. This low density would be attributed to the porosity values of the

developed mixes. Therefore, the material developed in this study is found to exhibit characteristics that made it analogous to sedimentary rocks.

Figures 2.15c and 2.15d show that the elastic modulus and strength ratios for mixes O, A, and B predominantly fall within the lower left corner of the plots. This indicates the predesignated very weak *UCS* and, consequently, the low elastic modulus *E* to the developed analogue sedimentary rock. The classification boundary for sandstone, according to Deere and Miller (1966), remains open at their lower end due to numerous test results showing low *UCS* and *E* values. These low values are attributed to the cemented, porous texture, and the anisotropy from bedding in the tested sandstone. Nevertheless, the general range of sandstone covers the developed analogue rock in this study. The plotted values, particularly mix B, align within the range of average modulus typical of most natural sedimentary rocks. Mix B is then well-suited for further laboratory experiments requiring weak but brittle characteristics.

## 2.6 Conclusions

This study presented the development process and findings of a very weak analogue sedimentary rock while enhancing its brittleness for further study in underground brittle failure phenomena. The development stage consisted of mixing and characterization stages within the experimental trial-and-error framework. The experimental results can be summarized as follows:

- (1) An analogue sedimentary rock exhibiting brittle characteristics was developed using readily available mortar mix constituents, ensuring reproducibility and consistency in results.
- (2) The analogue material was easily prepared and molded into various sizes and geometries due to the simple material preparation and the availability of commercially sourced constituents.
- (3) Several conceptual frameworks were validated through controlled laboratory testing, including the use of uniformly graded fine aggregate, low-cement content, thermal exposure, curing-testing time, and saturation-freezing treatments prior to thermal exposure.
- (4) During the development process, an improvement in the post-peak behavior of strain-softening was observed. The observed enhancement suggested a more brittle response with the engineering treatments from mix O to mix B.
- (5) The strain-softening response for mix B at 0.6 MPa applied confining pressure, compared to mix A, demonstrated an extension of brittle-ductile transition due to the engineering treatments. The triaxial test results from mix O to mix B revealed higher values of the Hoek-Brown constant  $m_i$  for the final mix B.
- (6) Assessments of brittleness measures such as strength brittleness, brittleness index modified, and burst energy coefficient also supported the findings, classifying the very weak analogue sedimentary rock as brittle.

- (7) The developed material was classified as sedimentary rock-like based on its Poisson's ratio, density, elastic modulus ratio, and strength ratio. Specifically, for mix B, both the elastic modulus and strength ratios fell within the average range typical with natural sedimentary rocks. This suggested that mix B closely mimicked the behavior of natural sedimentary rocks, making it well-suited for experiments requiring weak yet brittle characteristics.



## CHAPTER 3 EXPERIMENTAL INVESTIGATION OF TUNNEL DAMAGE AND SPALLING IN BRITTLE ROCK USING A TRUE-TRIAxIAL CELL<sup>1</sup>

### 3.1 Abstract

Deep underground excavations in brittle rocks are subject to several ground stability hazards such as spalling and rockburst. These hazards are typically associated with brittle failure mechanisms for hard and massive rock mass. In this study, an experimental investigation has been carried out to evaluate the mechanisms underlying these induced hazards in deep underground excavations. The main objective of this study is to investigate the behavior of a freshly excavated circular unsupported tunnel in a brittle synthetic rock with a focus on induced damage and spalling response. The experiment used a miniature tunnel boring machine (TBM) to excavate a tunnel in a cubical specimen placed in a true-triaxial cell. The material selected for this experiment was a reproducible synthetic rock analogous to sandstone with brittle characteristics. In the experiment, the specimen was loaded with increasing confining stress under incremental isotropic conditions in the true-triaxial cell until the tunnel failed. Macro-photography was utilized to verify the excavation damage zones and failure mechanisms around the tunnel boundary. The main observed failure mechanism of the model tunnel was spalling, which occurred due to brittle failure and a sudden stress release at the tunnel excavation boundary. In addition to spalling, three zones of damage were identified by macro-photography in the tunnel due to damage from construction, fracturing, and plastic rock deformation. The outcomes point to a unique and in-depth comprehension of how damage and spalling failure during underground excavation develop and its impact on tunnel stability.

### 3.2 Introduction

Forecasting and mitigating damage and failure in tunnels and caverns excavated through massive and brittle rocks remain critical challenges in rock mechanics. Underground excavations perturb the stresses around the tunnel boundary, contributing to induced damage dependent on the in-situ stress and rock mass properties. Brittle rocks exhibit well-defined peak shear strength followed by pronounced strain softening and pronounced damage from fracturing. Brittle rock characteristics have profound implications in tunneling. In underground excavations, brittle failure of rocks is often violent and uncontrolled, which is difficult to control and requires special provisions to achieve stable construction and ensure the safety of workers.

---

<sup>1</sup> This chapter is based on a paper published in *International Journal of Rock Mechanics and Mining Sciences* (Wibisono et al., 2024). Partial contents of this chapter have also been presented at the EUROCK 2024, Helsinki, Finland, November 2022 (Wibisono et al., 2023b).

Figure 3.1 depicts the schematic diagrams for the different zones of induced damage around a circular excavation in brittle rock (modified after Read (2004) and Perras and Diederichs (2016)). The different zones of induced damage in the tunnel wall are classified as follows:

- i) Construction Damage Zone  $CDZ$ , also termed as construction-induced excavation damage zone  $EDZ_{CI}$ , is observed as irreversible damage and highly depends on the construction method.
- ii) Highly Damaged Zone  $HDZ$ , typically characterized by fracturing close to the tunnel boundary due to crack propagation within localized zones and may promote spalling, slabbing and/or dog-earing. This fracturing occurs after the shear strength of the rock has been reached and the rock is in the strain softening regime where pronounced damage from fracturing occurs.
- iii) Excavation Damage Zone  $EDZ$  is associated with irreversible and significant rock damage due to plastic deformation. The stresses reach the peak shear strength of the rock but may not have reached strain softening.
- iv) Excavation Influence Zone  $EIZ$ , which was previously also called the excavation disturbed zone and renamed to minimize confusion. In this zone, the rock is anticipated to experience elastic deformation, demonstrating reversible damage.

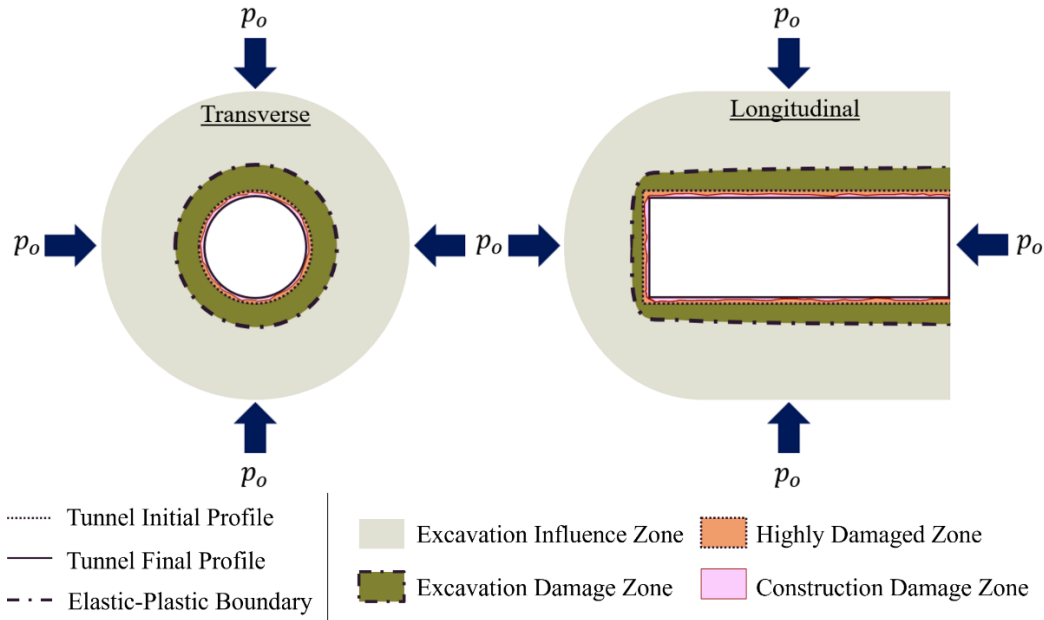


Figure 3.1 Schematic illustration for transversal and longitudinal cross sections of the different zones of induced damage around the tunnel constructed with TBM under hydrostatic loading (modified after Read (2004) and Perras and Diederichs (2016)).

Other than the  $CDZ$ , it is expected that different zones from the tunnel boundary towards the rock mass will be in the corresponding pre-peak, peak, and post-peak regimes of the stress-strain behavior in the  $EIZ$ ,  $EDZ$ , and  $HDZ$ , respectively (Vazaios et al., 2019). Although distinguishing the boundary

between the rest of the zones can be difficult, it is crucial to consider induced damage delineation to ensure a safe and durable tunnel excavation design. Further discussion on this induced damage will be presented in Section 3.3, along with the observed damage and spalling response in the experiment carried out in this study. The terminologies used for the excavation damage zones are primarily employed in underground radioactive waste disposal to improve the understanding of how damage is induced and how permeability is changed around an excavation (Siren, 2015; Tsang et al., 2005). The terminologies are also adopted in this paper.

Spalling observed in the *HDZ* is a particularly undesirable brittle rock mass failure along the tunnel boundary, frequently occurring in large underground excavations under high in-situ stress conditions (Cai and Kaiser, 2014). Spalling can be violent or nonviolent depending on progressive damage stages and is also adversely associated with rock-bursting susceptibility (Diederichs et al., 2009; Hoek and Kaiser, 1995). Spalling is a type of brittle rock failure characterized by the progressive release of strain energy in hard and massive rock from the initiation and propagation of extensional (Diederichs et al., 2004; Ortlepp and Stacey, 1994). Spalling under strong compressive loading is characterized by the production of apparent crack extension and dilation along the excavation boundary. In addition, spalling can also produce a V-shaped notch on the tunnel surface with slabs that vary in thickness and originate in the highest tangential stress regime at the tunnel boundary (Martin and Christiansson, 2009). Spalling takes place commonly in excavations through hard rock at great depth. However, spalling has also been reported in excavations through soft rock at comparatively shallow depths (Read, 2004; Yu et al., 2015). Induced damage and spalling can compromise tunnel stability and pose major safety threats, financial loss, and technical difficulties. Therefore, an in-depth understanding of the key contributing factors to brittle failure can greatly improve tunnel design. For instance, a detailed investigation of the induced damage under various in-situ stress conditions is a fundamental aspect of developing effective mitigation techniques.

Laboratory-tested results have been crucial in understanding damage and spalling phenomena (Ulusay, 2015). Since in-situ tests on large-scale geotechnical structures are time-consuming and expensive, researchers have performed various laboratory tests to investigate spalling and brittle failure mechanisms. These include: (i) uniaxial compression using a block of rock with a central circular opening (Carter, 1992) and large hard rock specimen with a distinct shape (curved handle dumbbell) to recognize the critical area for spalling along the tunnel boundary (Jacobsson et al., 2015); (ii) biaxial testing to investigate splitting-to-shear failure mechanism that allows the failure plane to propagate unrestrictedly (Labuz et al., 1996), to simulate the maximum tangential stress distribution on the circular excavation through axially compressed beams (Cho et al., 2010), and to estimate spalling and failure onset in plane strain conditions (Kusui et al., 2016); (iii) triaxial testing to focus on cohesive and frictional strength and to observe the cracks propagation with eccentric axial loading on a granite block (Martin and Chandler,

1994); and (iv) true-triaxial testing for brittle failure investigation that is thought to yield more accurate results due to independent manipulation of the principal stresses that reflect better to actual conditions (Pinto and Fonseca, 2013).

Since the early 1990s, true-triaxial cells have been used for studying induced damage and spalling. Some notable developments include Lee and Haimson (1993). They investigated the borehole breakout phenomenon in a granite specimen resulting in a "dog ear" shape due to a sequential spalling failure. Years later, Cheon et al. (2011) studied an opening in mortar rock-like brittle specimens under true-triaxial stress. The opening size was 60 mm in diameter in a cubic specimen of  $290 \times 290 \times 290 \text{ mm}^3$ . The investigation focused on the damage depth and characterized the failure type through multiple loading configurations. Nonetheless, the characterization of the brittle rock-like specimen was not discussed in detail, particularly in terms of its brittleness properties.

Recently, Gong et al. (2018) studied the effect of spalling failures that induce rockburst events on the laboratory scale. The experiment was observed through a 50 mm diameter prefabricated opening in a red sandstone cubical specimen  $100 \times 100 \times 100 \text{ mm}^3$  in size. In this study, the early stage of sidewall failure was characterized by the ejection of a few tiny particles as the concentrated tangential stress exceeded the unconfined compressive strength of the rock around the tunnel boundary. However, the prefabricated opening does not represent real tunneling conditions because the tunnel was not excavated under load.

To the extent of current knowledge, there is a lack of investigations focusing on the simultaneous development of reproducible-analogous synthetic material and a controlled tunnel model to simulate brittle failure characteristics. In this context, the prime focus of the present study is to analyze the mechanical response of an excavated circular unsupported tunnel in a brittle synthetic rock specimen with due consideration to induced damage and spalling occurrences. The experimental configuration allows the tunnel to be excavated under conditions that correspond to realistic in-situ stresses. A combination of material and physical testing variability can contribute to developing analytical and numerical models that will benefit tunneling design.

This study presents experimental results of induced damage and spalling in a freshly excavated, unsupported tunnel through brittle-synthetic rock. A miniature TBM was designed to excavate the tunnel through a cubic rock specimen under controlled in-situ stresses in a true-triaxial cell. The selected material to be investigated is a reproducible brittle rock specimen developed as an analog synthetic sandstone. The investigation seeks to capture tunnel damage and spalling failure at the post-mechanical excavation stage, aiming to create safer and more efficient tunneling practices in the future.

### **3.3 Experimental Framework**

In geotechnical engineering, physical models serve two purposes: (i) qualitative assessment by achieving geometry similarity and (ii) quantitative analysis to develop a model that meets the conditions of "similitude" (Stimpson, 1970). The test specimens must have the characteristics of the investigated phenomenon. In this investigation, the test specimens were prepared to exhibit brittle response at the tunnel boundary. Developing a repeatable analog rock mix was vital, as collecting natural, homogeneous, and undisturbed specimens of large sizes from the field were difficult. Natural specimens often introduce heterogeneities, and the statistical probability of obtaining consistent ones decreases as sample size increases. This variability could compromise the investigation plan. Hence, the material selection, the mix proportion, and the mixing method play a significant role in developing the appropriate mix for specimen preparation. Along with the controlled tunnel model, the experimental framework scheme in this paper would capture a comprehensive view of the induced damage and spalling in tunneling.

#### **3.3.1 Sample Preparation and Characterization**

A synthetic sandstone was developed for testing in the true-triaxial testing cell as a specimen. The synthetic rock is expected to exhibit isotropic-homogeneous behavior, repeatability, and ease of preparation, particularly for large-scale tests. The proposed synthetic sandstone consists of F-75 Ottawa sand (Dakoulas and Sun, 1992), commercially available Type I/II Portland cement (ASTM, 2021a), and water. These molded specimens are designed to exhibit a brittle response and relatively low porosity, imitating the characteristics of weak sandstone (Wibisono et al., 2022). Additionally, weak synthetic rock reduces the need for a large capacity loading configuration and allows for specimens that comply with size effects. The mix design and proportions for 1 m<sup>3</sup> of the synthetic specimen, developed after several trials, are presented in Table 3.1.

Table 3.1 Summary of mix design and proportions for synthetic sandstone mix.

Components	Values
Cement content, $C$ (%)	8.0
Water to cement ratio by weight, $w/cm$	1.2
F-75 Ottawa Sand* (kg)	1963.4
Cement* (kg)	170.7
Water* (l)	204.9

\* for 1 m<sup>3</sup> of specimen.

The procedure for synthetic sandstone preparation is as follows:

- i. First, the F-75 Ottawa sand and cement are pre-mixed in a dry container according to the cement content percentage  $C$  (see Table 3.1) until mixed thoroughly.  $C$  is defined as a percentage of the cement mass to the total solid mass (cement and sand). With a relatively low cement content of 8%, a homogeneous mix is ensured through visual observation during the pre-mixing.
- ii. Water is added at a designated ratio (see Table 3.1) and mixed using a hand grout mixer (i.e., electric drill with mixer attachment) with a minimum of 40 revolutions per minute (RPM). As the moisture from the water covers the pre-mixed material, the mix should have consistent homogeneity after up to ten minutes of thorough mixing.
- iii. The casting of the sample is performed in layers (preferably at least three layers to reach the designated specimen size), with light tamping of 10-20 mm thick layers. This procedure creates an interconnection between the layers. Figure 3.2 shows photographs of the 300 mm cubical testing specimen preparation process.
- iv. Finally, the specimen is cured for 28 days, according to the American Society for Testing and Materials (ASTM) Standards C192 and C511 (ASTM, 2021b, 2021c).

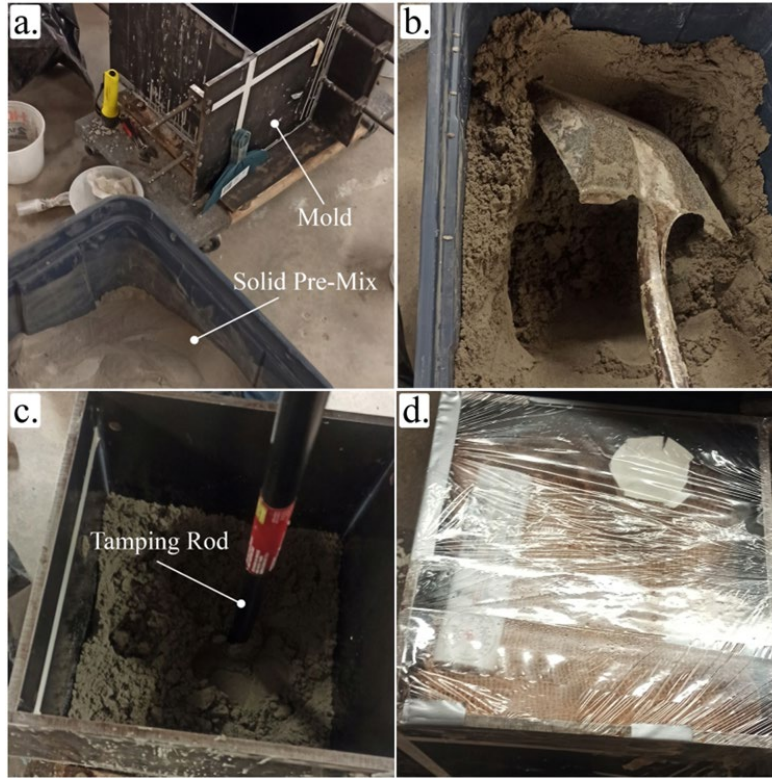


Figure 3.2 Preparation of a cubical specimen for true-triaxial testing. (a) Mold and pre mixing of cement and F-75 Ottawa sand until visually homogeneous solid mix is prepared; (b) freshly mixed synthetic sandstone with consistent homogeneity after adding water and thorough mixing process; (c) tamping rod is adjusted according to the suitable size for different sample geometry; and (d) moisture control and monitor for the specimen inside the mold.

In addition to the  $300 \times 300 \times 300 \text{ mm}^3$  cubical specimen constructed for the main test in the true-triaxial setup, additional cylindrical samples are prepared for material characterization. In the characterization process, a series of physical property tests, including Unconfined Compression Tests (UCT), Brazilian tension tests, Single-Cyclic Loading-Unloading Uniaxial Compression (SCLUC) tests, and triaxial tests are performed. These characterization results are examined further in terms of brittleness and burst-prone behavior through several rock-bursting criteria, such as the strength brittleness index  $B_1$  (Hucka and Das, 1974; Wang and Park, 2001), burst energy coefficient  $R$  (Goodman, 1989), brittleness index modified  $BIM$  (Aubertin et al., 1994), and strain energy storage index  $F$  (Kwaśniewski et al., 1994).

### 3.3.2 True-Triaxial Cell and Miniature TBM Setup

The present experimental investigation used a true-triaxial cell and a miniature soft-ground open-face TBM developed at the Colorado School of Mines (CSM). The true-triaxial cell (Frash et al., 2014a) is combined with a miniature TBM to develop a tunnel model test to investigate instabilities in excavation (Arora et al., 2022). The subsequent sections provide explanations for each component.

### 3.3.2.1 True-triaxial cell

The true-triaxial cell is designed to test cubical rock specimens up to  $300 \times 300 \times 300 \text{ mm}^3$  in size. Figure 3.3a presents the isometric view of the true-triaxial cell configuration without the steel top lid. The main cell body is constructed of structural steel with a yield strength of 250 MPa, while the steel top lids have a yield strength of 700 MPa. Figure 3.3b presents the top view of the true-triaxial cell configuration before mounting the steel top lid. With the top lid removed, the cell is accessible, allowing the placement of the cubical rock specimen, acoustic emission (AE) monitoring, and loading configuration.

The load is applied to three active faces through Freysinnet flexible flat jacks behind stiff metal platens. This loading configuration can apply normal stresses of up to 13 MPa on each side. The opposing passive sides are composed of cast-in-place high-strength cement grout to ensure uniform contact between the specimen and the cell body. The flat jacks are manually pumped with Enerpac hand jacks to apply each principal stress to the specimen faces. Pressure gauges are equipped to monitor the applied load to each flat jack.

As shown in Figure 3.3c, the specimen in this study was subjected to an isotropic confining stress field (i.e.,  $\sigma_1 = \sigma_2 = \sigma_3 = p_o$ ). When the steel top lid is placed on the true-triaxial cell, hydraulic and sensor lines can go through the 63 mm circular opening on top. The steel top lid contains another 75 mm circular opening at the center, furnished for the excavation access. More details about this true-triaxial setup can be found in Frash et al. (2014a).



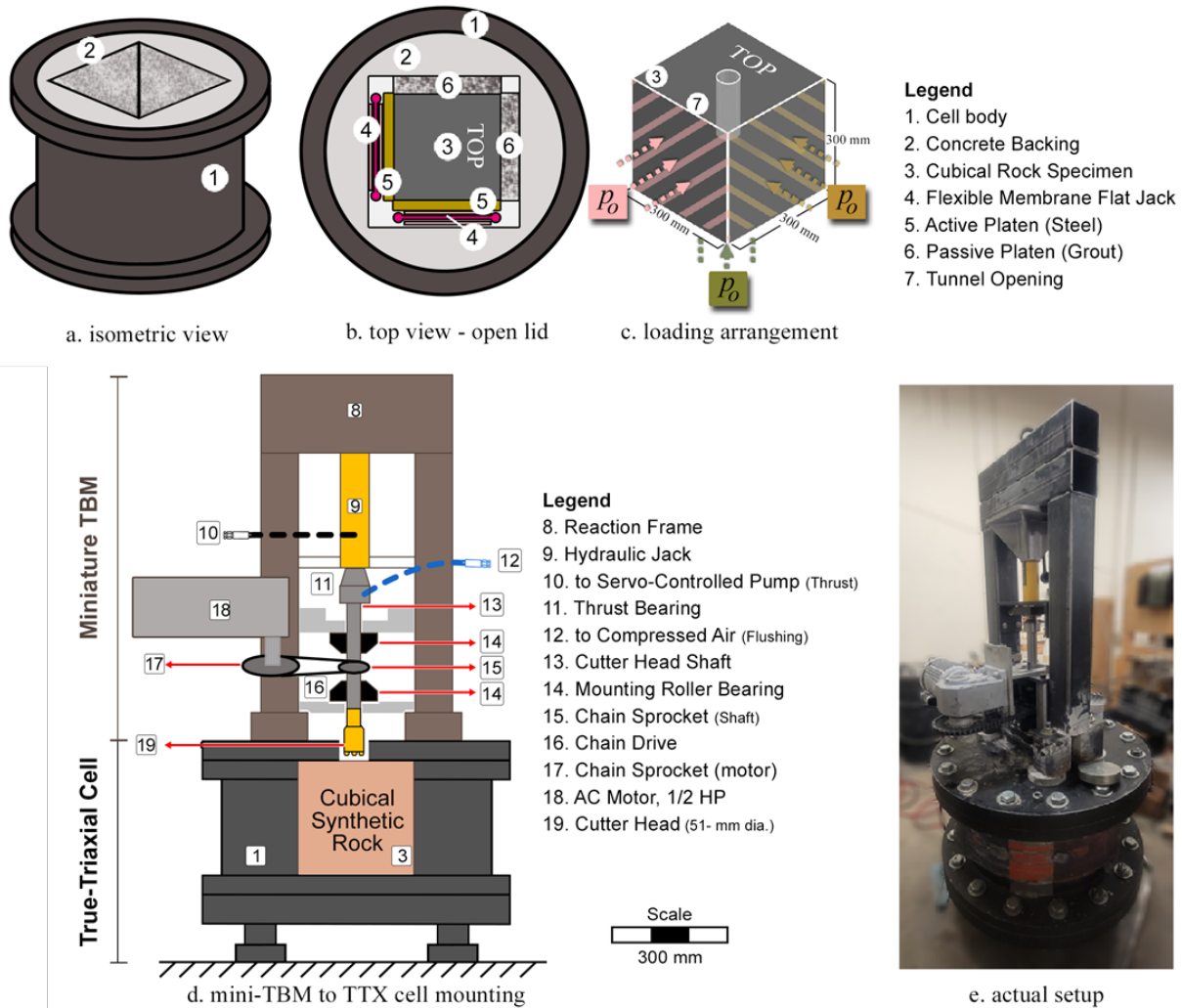


Figure 3.3 Conceptual illustrations of: (a) concrete backing and cell body; (b) top view of the true-triaxial apparatus configuration without the steel top lid; (c) isometric view of the specimen showing AE sensor placement and tunnel position; and (d) the miniature TBM mounted on the true-triaxial cell. The actual experimental setup is shown in (e).

### 3.3.2.2 Miniature TBM setup

A miniature TBM setup simulates a mechanical excavation in a cubical rock specimen subjected to field/in situ stress levels under a true-triaxial condition (Figure 3.3d). The adopted mechanical excavation system incorporates a vertically-mounted rotary and down-the-hole drill with a compressed air flushing system. The miniature TBM also consists of a reaction frame that holds the entire system of thrust, torque, cutting, and supporting units. The thrust unit includes a hydraulic jack, a pair of servo-controlled pumps, and a thrust bearing, while the torque unit consists of a constant-speed AC motor, two chain sprocket gears, and a chain. In addition, the cutting unit has a 51 mm diameter tungsten-carbide-button-bit attached to the hollow drilling rod. The reaction frame as the supporting unit is fabricated from

ASTM A500 structural steel and consists of two square columns, one rectangular beam, and four welded rectangular bracings. More details about this miniature TBM setup can be found in Arora et al. (2021).

The location of the tunnel excavation opening is along the center line of the specimen, drilled top to bottom through diameter opening at the steel top lid of the true-triaxial cell. The excavation leaves a clearance gap of approximately 124 mm (around five times of tunnel radius) between the tunnel excavation face and the specimen boundary. The magnitude of clearance is obtained by several trials such that the effects of confinement boundary are negligible on the tunnel excavation face. In the present investigation, the excavated length of the tunnel is 146 mm, which covers almost half of the specimen's length. A DiSCO (Dynamic Teledyne Isco D-series Syringe Pump Control) control program developed using LabVIEW monitors the TBM parameters, including cutter head thrust or face pressure, total tunnel progress, and tunnel advance rate (Frash, 2016). The tunnel face pressure determined from the hydraulic jack pressure provides input command to the program with a continuous constant pressure (CCP) mode. The control program also computes and logs the miniature TBM's advance rate and total advance by measuring the amount and flow rate of hydraulic fluid flowing into the hydraulic jack from the pump

### **3.4 Experimental Procedure**

This section describes the different stages of the experimental procedure performed in the present study. The four major stages of this procedure are as follows: (i) preliminary works, (ii) tunnel excavation using a miniature TBM, (iii) stage-wise loading using the true-triaxial cell, and (iv) post-experimental investigation.

#### **3.4.1 Preliminary Works**

At first, the true-triaxial cell was prepared for the tunnel model experiment. This step includes removing the steel top lid and cleaning debris from the previous testing. The loading system consisting of hydraulic cylindrical expansive jacks and square steel plates were installed as the active sides on three cubical specimen sidewalls—bottom, front, and side (Figures 3.3b and 3.4b). Supporting frame, hydraulic lines arrangement, and steel footing were also prepared beforehand to hold the loading system and the rock specimen. The rock specimen was extracted from the casting mold and transferred to the true-triaxial cell using a hydraulic crane setup (Figure 3.4a). A spirit level was used to ensure the specimen was placed horizontally correctly. The steel top lid of the true-triaxial cell was then tightened, and the three hydraulic lines were connected with the corresponding jacks (i.e.,  $\sigma_1$ ,  $\sigma_2$ ,  $\sigma_3$ ), as shown in Figures 3.4b and 3.4c.

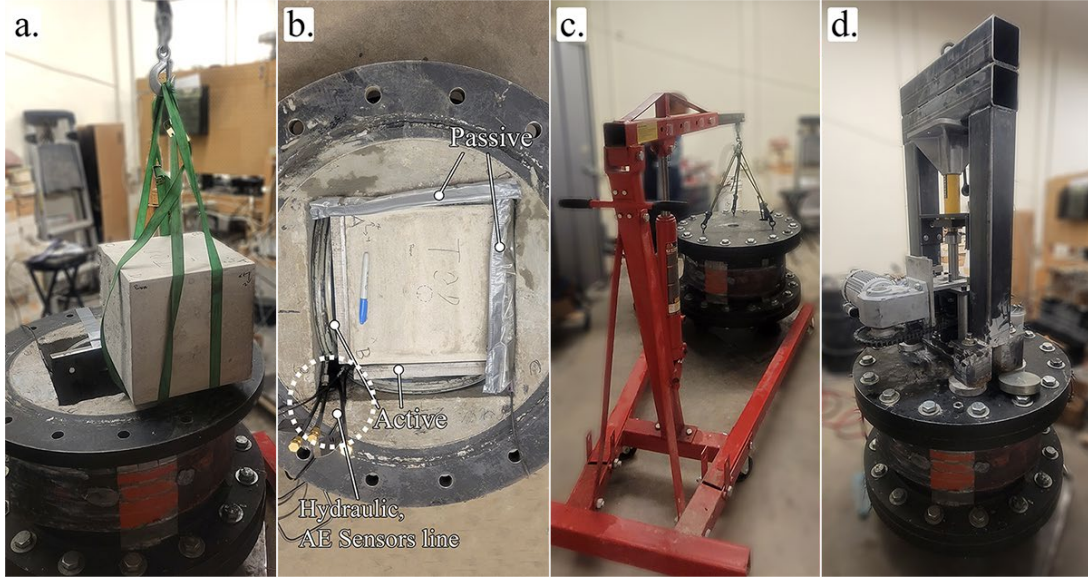


Figure 3.4 (a) Positioning the sample into the true-triaxial cell; (b) top view of the sample in the true-triaxial cell before mounting the top steel lid. Annotated for the grouted sides (passive faces) and steel plate jacks (active faces), also the outlet for the hydraulic and AE lines; (c) installing the top steel lid; (d) miniature TBM setup mounted on the true-triaxial cell

### 3.4.2 Tunnel Excavation using a Miniature TBM

In this stage, the miniature TBM reaction frame was mounted on the steel top lid of the true-triaxial cell (Figure 3.4d). The position of the vertical reaction frame was fixed through the arrangement of the bolts to ensure its stability and verticality during tunnel excavation. After mounting the reaction frame, the respective power source and hydraulic line attachment enabled the torque and thrust unit to operate. In addition, a flushing system was enabled through a connection to the compressed air line. Before the cutter head touches the specimen, however, multiple tests were conducted to ensure that the miniature TBM system operate properly.

Once the miniature TBM is ready to excavate the tunnel, the rock specimen was pre-loaded under isotropic confining stress  $p_0$  of  $0.5 \cdot \sigma_c$  ( $\sigma_c$  = UCS of the intact rock) to steadily hold the specimen while the excavation was taking place. To maintain the thrust, the miniature TBM excavates the tunnel face under continuous constant pressure (CCP) mode. Air flushing was continuously performed at 20-second intervals to primarily transport broken material outside the tunnel and minimize debris accumulation at the tunnel face. The flushing duration varies as needed and was determined by observing the debris blown out from the tunnel. When no more material is blown out, the flushing was paused. The single-phase constant speed alternating current (AC) motor controls shaft rotational speed at 14 revolutions per minute (RPM). The excavation was terminated once the tunnel advance reached the specified depth of approximately 150 mm. This process was conveyed through simple ruler measurement of hydraulic piston extension since the TBM cutter head began drilling.

### 3.4.3 Stage-Wise Loading

The isotropic loading on the rock specimen was gradually increased in stages, with the AE monitoring system continually recording the tunnel response. The initial load increment in each stage was set at  $p_0/\sigma_c = 0.5$ . Loading was increased to the next higher level once the observed AE activity (hits and events) in a respective loading stage became negligible, i.e., each loading stage lasted approximately 120 hours to promote a steady state on the tunnel boundary. The loading rate was maintained at approximately 0.45 MPa/min in all directions. This selected rate and holding duration were intended to minimize the loading rate effect that could otherwise cause apparent increase in strength. Stress relaxation was observed throughout the epochs, necessitating re-adjustment to designated isotropic loading state every 24 hours. When the specimen was expected to fail, the magnitude of the applied load increment was reduced to  $p_0/\sigma_c = 0.25$  (e.g., from  $p_0/\sigma_c = 2.75$  to  $p_0/\sigma_c = 3.0$ ).

Figure 3.5 represents the stage-wise loading in the experiment. The load increment process was completed when a sudden massive event was recorded in the AE monitoring system, along with an observable phenomenon, such as sounds and spalling in the rock mass surrounding the tunnel. Loading was also stopped when the current true-triaxial setup reached its maximum loading capacity. AE data analysis during the true-triaxial loading stage could not be performed due to data saturation. However, AE data from the excavation phase with miniature TBM has been analyzed and is available in previous studies (Gautam et al., 2023; Moradian et al., 2024).

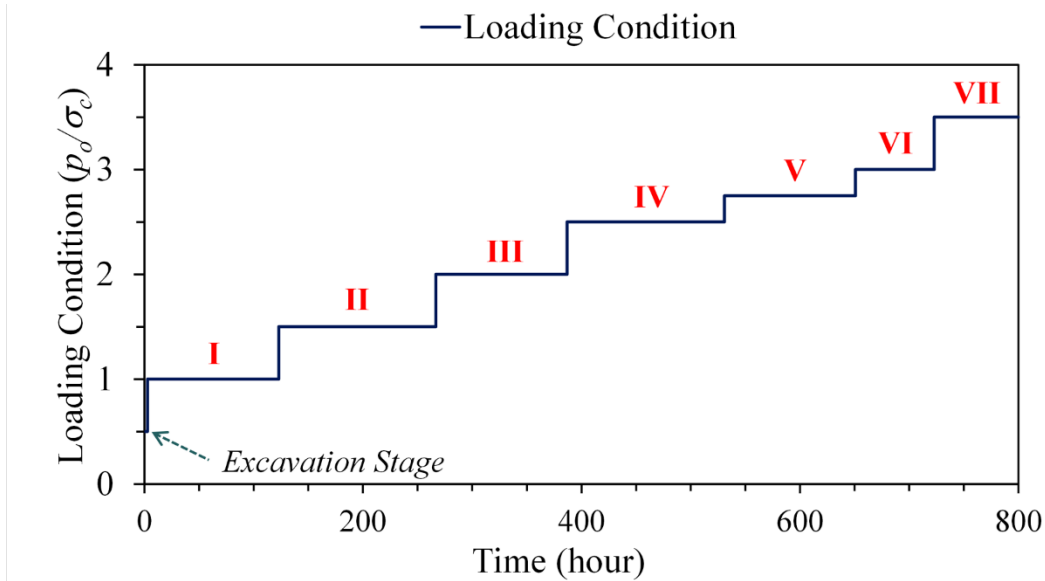


Figure 3.5 Applied hydrostatic stresses step graph throughout the loading stages. The Roman numerals represent the corresponding loading stage at each hydrostatic condition ( $p_o/\sigma_c$ )

### 3.4.4 Post-Experimental Investigation

Once the loading phase was completed, the mini-TBM was withdrawn from the tunnel opening. The tunnel wall and face were investigated for damage digitally using a 2-Megapixel borehole endoscopic camera inserted into the hole (Figure 3.10). After imaging inside the tunnel is completed, the tunnel is filled with an epoxy resin mix (West System 105 Epoxy Resin Part 1 and 207 Special Clear Epoxy Hardener) to preserve the final convergence and structure of the tunnel wall even after unloading. With a flowing viscosity suitable for permeation, the resin was poured using gravity from a constant height of 150 mm to the tunnel portal. The cubical specimen was unloaded from the true-triaxial cell after the resin fully hardened (approximately 48 hours). The specimen was then sliced and slabbed into one longitudinal section and six approximately 50-mm thick half-axial cross-sections for further examination through macro-photography. The following was the setup for the post-test macro-photography of the slabbed specimen: (a) body: Canon EOS M6 Mark II, (b) macro lens: Canon MP-E 65 mm f/2.8 1-5x, (c) adapter: EF-EOS M lens adapter, (d) flash: Yongnuo macro ring flash. The configuration gives a resolution of 32.5 megapixels, ensuring high-quality visualization of the damage zones and spalling features. The longitudinal section of the tunnel is digitized with point picking to develop final deformed tunnel profile. The characterization of the tunneling-induced damage in the rock is discussed further in Section 3.3.

## 3.5 Results and Discussion

This section discusses the experimental results recorded according to the processes prescribed in Sections 3.3 and 3.4. The experimental results include the rock specimen properties, TBM performance during excavation, spalling observation, and tunnel deformation data.

### 3.5.1 Synthetic Sandstone Properties

A series of property tests are carried out in this study to obtain the physical properties of the developed synthetic sandstone. The tests include six UCT, four Brazilian tests, three SCLUC tests, and six triaxial tests at different confining stresses. The displacement-controlled UCT and triaxial tests utilized a constant axial strain rate of  $10^{-5} \text{ s}^{-1}$  with test times typically between 8-12 minutes (ASTM, 2017). The SCLUC tests use a load-controlled setup at an 80 N/s loading rate. In addition, physical property tests also determined the dry unit weight, saturated unit weight, and porosity of the synthetic sandstone. The mean values of the unconfined compressive strength  $\sigma_c$ , tensile strength  $\sigma_t$ , and tangential elastic modulus at 50% of peak stress  $E_{50}$  are summarized in Table 3.2, together with the saturated unit weight  $\gamma_{sat}$ , dry unit weight  $\gamma_{dry}$ , and porosity  $n$ . Additionally, the axial and lateral strain measurements yielded a Poisson's ratio  $\nu$  to be 0.21.

Table 3.2 Summary of the synthetic sandstone test results (physical properties, UCT, Brazilian, SCLUC, and triaxial)

Property	Value
Saturated unit weight, $\gamma_{sat}$ (kN/m <sup>3</sup> )	17.8
Dry unit weight, $\gamma_{dry}$ (kN/m <sup>3</sup> )	16.7
Porosity, $n$ (%)	11.5
UCS, $\sigma_c^*$ (MPa)	$3.07 \pm 0.19$
UTS, $\sigma_t^*$ (MPa)	$0.45 \pm 0.11$
Elastic modulus, $E_{50}^*$ (GPa)	$0.94 \pm 0.07$
Poisson's ratio, $\nu^*$	0.21
Retained axial strain in SCLUC (%)	$0.18 \pm 0.01$
Cohesion, $c^*$ (MPa)	1.06
Internal friction angle, $\phi^*$ (°)	21.4

\* for the strain-controlled testing, the strain rate is  $10^{-5} \text{ s}^{-1}$ .

For the SCLUC test, three samples are unloaded when the first loading reaches 2.1 MPa (at 70% of peak compressive strength), and the retained axial strain is determined to be  $0.18 \pm 0.01\%$ . The axial stress-strain curves obtained from the UCT and SCLUC tests are shown in Figures 3.6a and 3.6b, respectively. As can be seen, the stress-strain curves clearly show brittle behavior with distinct peak shear strength followed by pronounced strain-softening to distinct but very low residual shear strength.

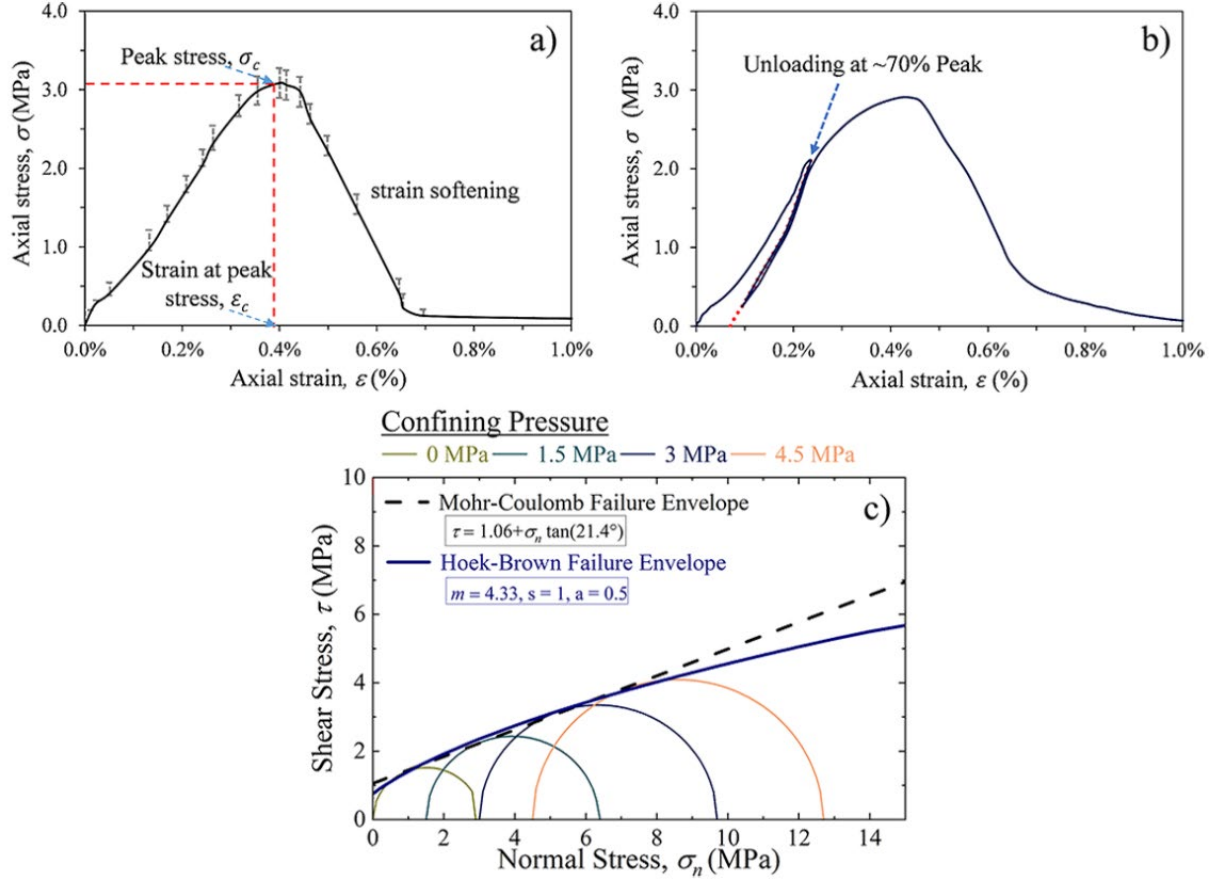


Figure 3.6 (a) Axial stress-strain plot representing the majority of the Unconfined Compression Tests, with an error bar (vertical-dotted) to account for variability due to the number of results; (b) axial stress-strain plot representing SCLUC test for one of rockburst criteria evaluations. The red dotted line shows the extrapolation of the unloading curve; and (c) Mohr's circles for unconfined compression and triaxial tests with the best fitting for Mohr-Coulomb and Hoek-Brown failure envelopes.

Six triaxial tests were performed at three different confining pressures of 1.5, 3, and 4.5 MPa, which represent  $p_o/\sigma_c = 0.5$ ,  $p_o/\sigma_c = 1.0$ , and  $p_o/\sigma_c = 1.5$ , respectively. Triaxial and unconfined compression test results were processed using RSData (Rocscience Inc., 2022) to generate Mohr-Coulomb and Hoek-Brown failure envelopes for the synthetic sandstone. Figure 3.6c shows the obtained failure envelopes and the Mohr's circles for four confining pressures, including the unconfined compression test. For the Mohr-Coulomb (MC) failure envelope, the best linear fit gives undrained cohesion  $c$  and internal friction angle  $\phi$  equal to 1.06 MPa and  $21.4^\circ$ , respectively. On the other hand, the non-linear Hoek-Brown (HB) failure envelope is obtained with the parameters  $m=4.33$ ,  $s=1$ , and  $a=0.5$ . As can be seen, there is very little difference between the MC and HB criteria. Table 3.2 summarizes all the laboratory test results of the synthetic sandstone.

Figure 3.7 shows back-to-back photographs of two samples, one for UCT and another for the SCLUC test, after the loading. Both samples clearly developed vertical/sub-vertical fractures, which



appear extensional given the dilation of the fractures. The fractures (crack damage) were observed at about 0.25% of axial strain and were fully developed after the peak shear strength has been reached. The development of extensional fractures parallel/sub-parallel to the major principal stress  $\sigma_1$  is a clear indication of the brittle characteristics of the synthetic (Nygård et al., 2006).

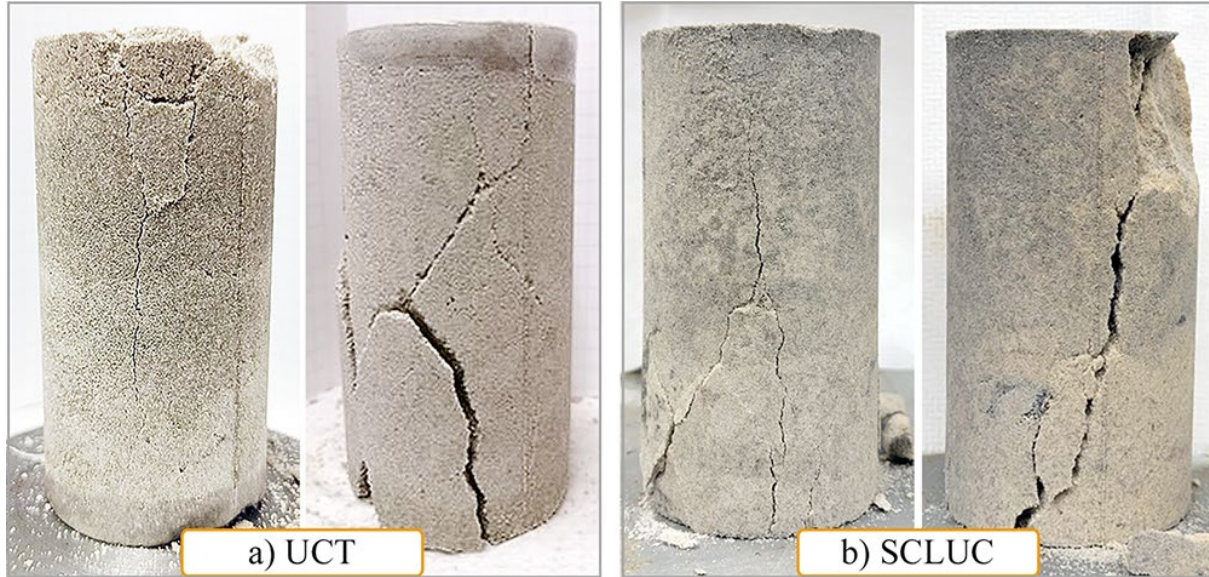


Figure 3.7 Photographs of the test samples after loading showing axial dominant and shear failure where the tests were performed at 28 days curing time of the synthetic sandstone. (a) Unconfined compression tests (UCT) and (b) SCLUC tests.

The synthetic sandstone properties contributed to determining the experimental stage-wise loading. For instance, the staged-loading confining pressure is normalized with the Unconfined Compression Strength, UCS or  $\sigma_c$ . The element test results on the cylindrical specimens, particularly the mode of failure, also serve as input for further analytical study and interpretation. The physical properties are analyzed to investigate experimental results with analytical and empirical solutions of the model tunnel test.

As mentioned, developing a synthetic sandstone that behaves as a weak, homogeneous, brittle material for investigating spalling and rockburst is vital. This study evaluated synthetic sandstone based on four empirical criteria to determine its brittleness and bursting properties. These criteria were assessed using three analysis methods: strength parameters (strength brittleness index  $B_1$ ), UCT stress-strain curve analysis (brittleness index modified  $BIM$  and burst energy coefficient  $R$ ), and SCLUC stress-strain curve analysis (strain energy storage index  $F$ ).

The strength brittleness index  $B_1$  defined as the ratio between the unconfined compressive strength of the rock to its tensile strength ( $\sigma_c/\sigma_t$ ). In the case of the synthetic sandstone mix, the strength



parameters presented in Table 3.2 were used to calculate  $B_1$  values ranging from 5.1 to 9.6. These ranges of strength brittleness index  $B_1$  suggests a strong potential for rockburst, as they are less than 14.5.

Figure 3.8 illustrates the brittleness calculations using the UCT and SCLUC test stress-strain curves. The brittleness index modified  $BIM$  is defined as the ratio of the total input energy density of the pre-peak  $A_2$  to the peak elastic strain energy density  $A_1$  based on the UCT stress-strain curve (Figure 3.8a). Based on the stress-strain curve analysis, the value of  $A_1$  and  $A_2$  are  $5.5 \times 10^{-3}$  and  $6.5 \times 10^{-3}$ , respectively, resulting in a calculated  $BIM$  of 1.18 ( $A_2/A_1$ ). According to the criterion, values ranging from 1 to 1.5 indicate a strong to moderate potential for bursting.

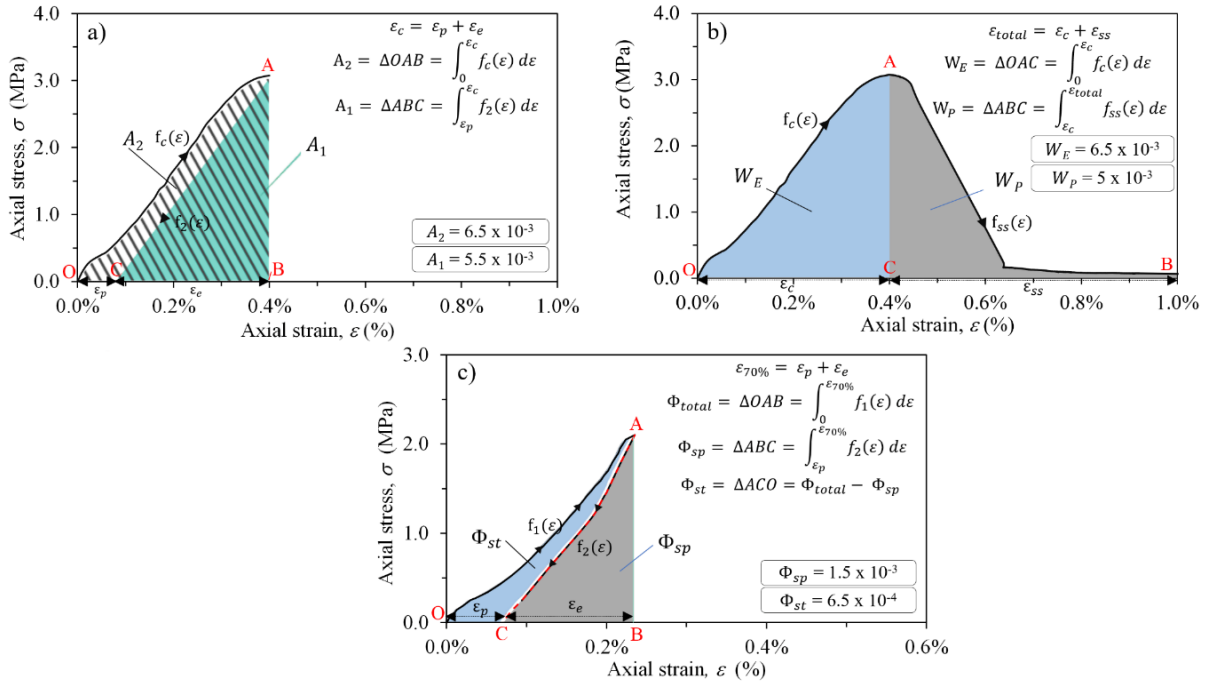


Figure 3.8 Calculation of synthetic sandstone bursting criteria using stress-strain curve analysis methods: (a) brittleness index modified  $BIM$ , (b) burst energy coefficient  $R$ , and (c) strain energy storage index  $F$ .

The burst energy coefficient  $R$  uses the complete stress-strain curve from UCT and calculates the total area under the curve before peak  $W_E$  divided by the total area under the curve after peak of the shear strength  $W_P$  (Figure 3.8b). After calculating the areas,  $W_E$  and  $W_P$  are found to be  $6.5 \times 10^{-3}$  and  $5 \times 10^{-3}$ , respectively. The burst energy coefficient  $R$  ( $W_E/W_P$ ) is then determined to be 1.3. This ratio satisfies the criterion for moderate bursting potential, as the burst energy coefficient requires a ratio greater than 1.

The strain energy storage index  $F$  is calculated by dividing the retained elastic energy  $\phi_{sp}$  by the dissipated energy  $\phi_{st}$ , as delineated from the SCLUC stress-strain curve (Figure 3.8c). The SCLUC stress-strain curve, which relies on 70% of the peak unconfined compressive strength, reveals that the retained elastic energy  $\phi_{sp}$  is  $1.5 \times 10^{-3}$ , while the dissipated energy  $\phi_{st}$  is  $6.5 \times 10^{-4}$ . The strain energy storage index criterion suggests that the an  $F$  value between 2.0 and 5.0 indicates moderate burst potential. The division of these values ( $\phi_{sp}/\phi_{st}$ ) yields a value of 2.32, which falls within the moderate burst range.

Table 3.3 provides a summary of the evaluation of the developed synthetic sandstone based on the four criteria that primarily support its brittle and bursting characteristics. The synthetic sandstone exhibits a moderate to strong bursting potential from the strength brittleness index, brittleness index modified, burst energy coefficient, and strain energy storage index criteria.

Table 3.3 Summary of current synthetic sandstone mix characterization to the rock bursting criteria used in this study.

Bursting Criteria	Measurement method	Source	Synthetic Sandstone Values	Typical Ranges for Moderate Bursting
Strength brittleness index, $B_1 = \sigma_c/\sigma_t$	Strength parameters	Hucka and Das (1974); Wang and Park (2001)	5.1 - 9.6	< 14.5
Brittleness index modified, $BIM = A_2/A_1$	UCT stress-strain curve	Goodman (1989)	1.18	1.0 - 1.5
Burst energy coefficient, $R = W_E/W_P$	UCT stress-strain curve	Aubertin et al. (1994)	1.3	> 1
Strain energy storage index, $F = \phi_{sp}/\phi_{st}$	SCLUC stress-strain curve	Kwasniewski et al. (1994)	2.32	2.0 – 5.0

### 3.5.2 TBM Performance During Excavation

TBM parameters such as face pressure and advance rate throughout the excavation stage were continuously monitored. Figure 3.9a depicts the TBM face pressure  $p_f$  while Figure 3.9b depicts the miniature TBM's measured advance rate during the excavation phase. The cumulative tunnel advance plot is superimposed on each figure. Although the TBM face pressure is maintained at around 1.69 MPa by a pair of servo-controlled pumps, Figure 3.9a shows quite a few drops in the load. These monitored drops are perceived because of a sudden loss of contact between the TBM cutter head and the advancing tunnel face (Wibisono et al., 2023b). The TBM overall advance is gradual and without impediment. However, the maximum tunnel advance is limited to 150 mm (50% of the specimen's length) to minimize the boundary effects of the cubical specimen sides over the tunnel behavior. The excavated tunnel profile is measured to be 51 mm, which is equal to the TBM cutter head diameter, resulting in 25.5 mm of tunnel radius  $R_T$ . It is worth noting that the "as-built" tunnel wall profile is not a perfectly smooth circular profile but has an undulating one.

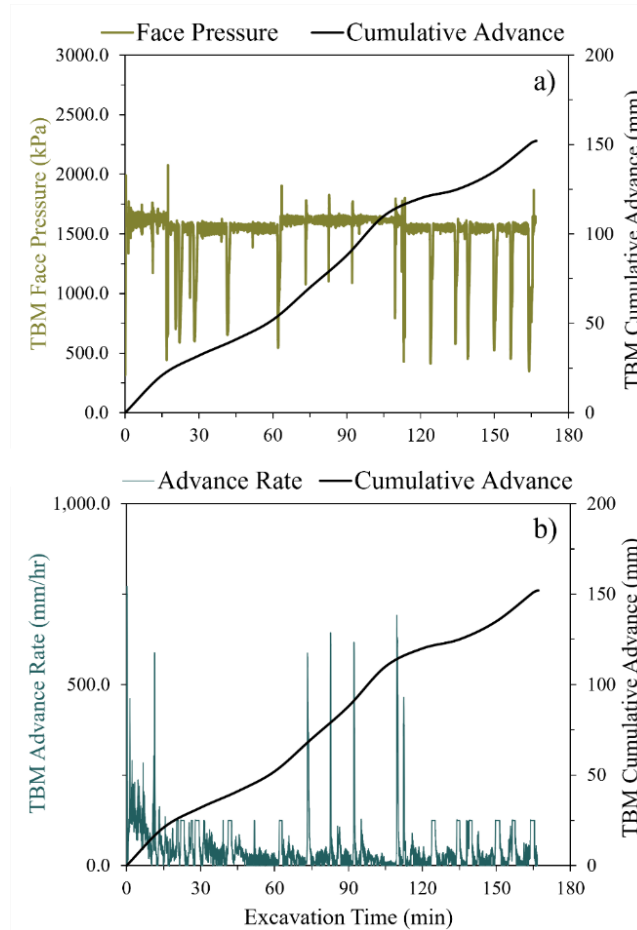


Figure 3.9 Monitoring record of miniature TBM parameters during the excavation stage; (a) face pressure/thrust; and (b) advance rate.

The advance rate in this experiment (Figure 3.9b) is calculated from the oil flow rate monitored from the control program. The average advance rate was 49.98 mm/hour, resulting in a total excavation time of approximately 2.80 hours for 146 mm of advance. In Figure 3.9b, some fluctuations are accompanied due to the abrupt loss of contact between the cutter head and the rock specimen during excavation. As part of the mechanical excavation process, it is a common practice that TBM excavation be carried out as quasi-static loading. In the present experiment, the operations of the miniature TBM follow the same procedure, influenced by the rock mass properties, to determine rock excavability, defined as the rate of excavation expressed in cutting performance in advance length per time (Bieniawski and Grandori, 2007). As mentioned, the rock mass properties, such as brittleness response, were vital in evaluating the cutter head performance in regard to the advance rate. The synthetic sandstone in this experiment was found to be brittle as discussed above. The cutter head achieved a relatively higher TBM advance rate compared to the previous experiments with the same configuration that used synthetic mudstone (Arora et al., 2022). The rocks with lower brittleness is known to absorb extra energy at the fracture tip to fulfill fracturing criteria, resulting in the TBM advance rate decrease (Gong and Zhao, 2007).

### 3.5.3 Induced Damage and Spalling

Figure 3.10 shows the imaging carried out by an endoscopic camera from inside the tunnel. As mentioned, the sample was still under load at this time. Figure 3.10b shows multiple cracks on the tunnel wall that are sub-parallel to the longitudinal tunnel axis and partial detachment of thin rock fragments along the tunnel wall, indicating spalling failure around the tunnel boundary. Figure 3.10c shows similar images of spalling looking towards the tunnel face. Note that the tunnel surface finish is not smooth but undulating. The structure of the surface influenced the damage at the tunnel, as will be discussed below.

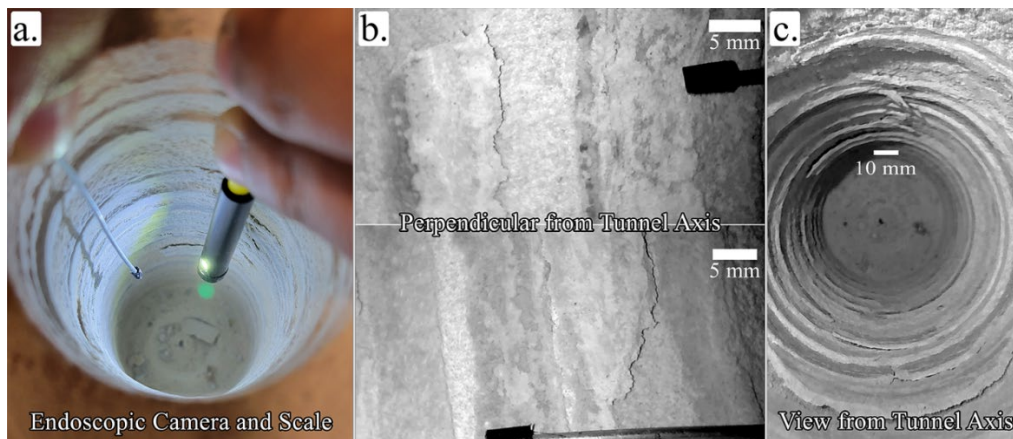


Figure 3.10 (a) Endoscopic camera to record the spalling behavior inside the tunnel opening using a manual scaling system; (b) images from a perpendicular view of the tunnel axis; and (c) closer tunnel axis view of the final spalling outcomes on the tunnel profile inside the tunnel portal.



Half axial cross and full longitudinal sections from the specimen were investigated using macro-photography after the epoxy resin was introduced into the tunnel while it was under load. The hardened epoxy resin effectively preserved the rock microstructure created by the tunneling. Figures 3.11 and 3.12 show photographs of the tunnel half cross-sections at 50 mm and 100 mm tunnel advance, respectively. Figure 3.13 shows photographs from a full longitudinal section of the tunnel.

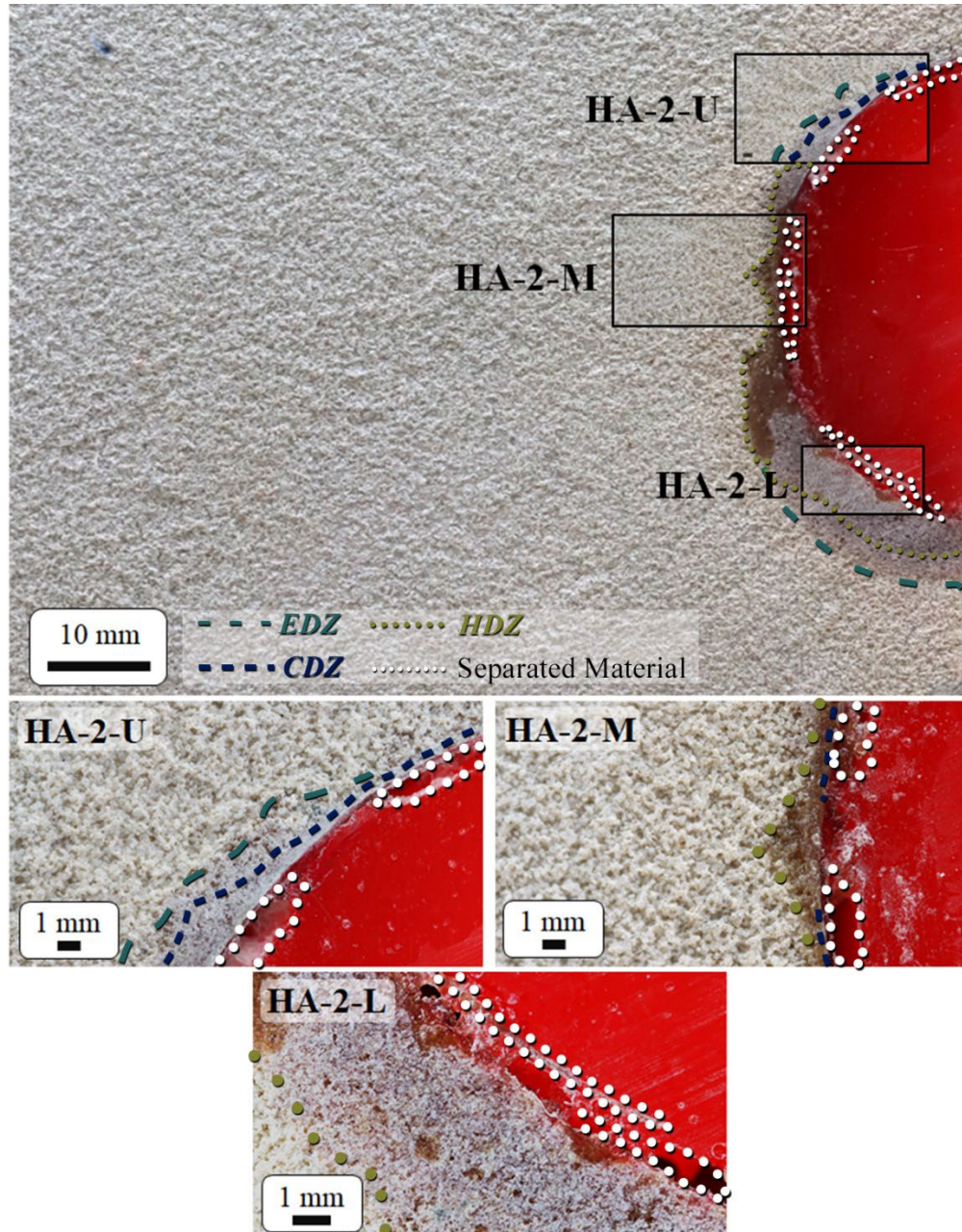


Figure 3.11 Slabbed rock tunnel specimen half axial cross-sections at approximately 50 mm advance length from the tunnel portal. HA denoting Half-Axial, whereas the following codes include the slab number in respect to distance from portal and spot of shots (upper, medium, and lower). Different types and colors of demarcating lines indicate different zones of induced damage around the tunnel boundary.



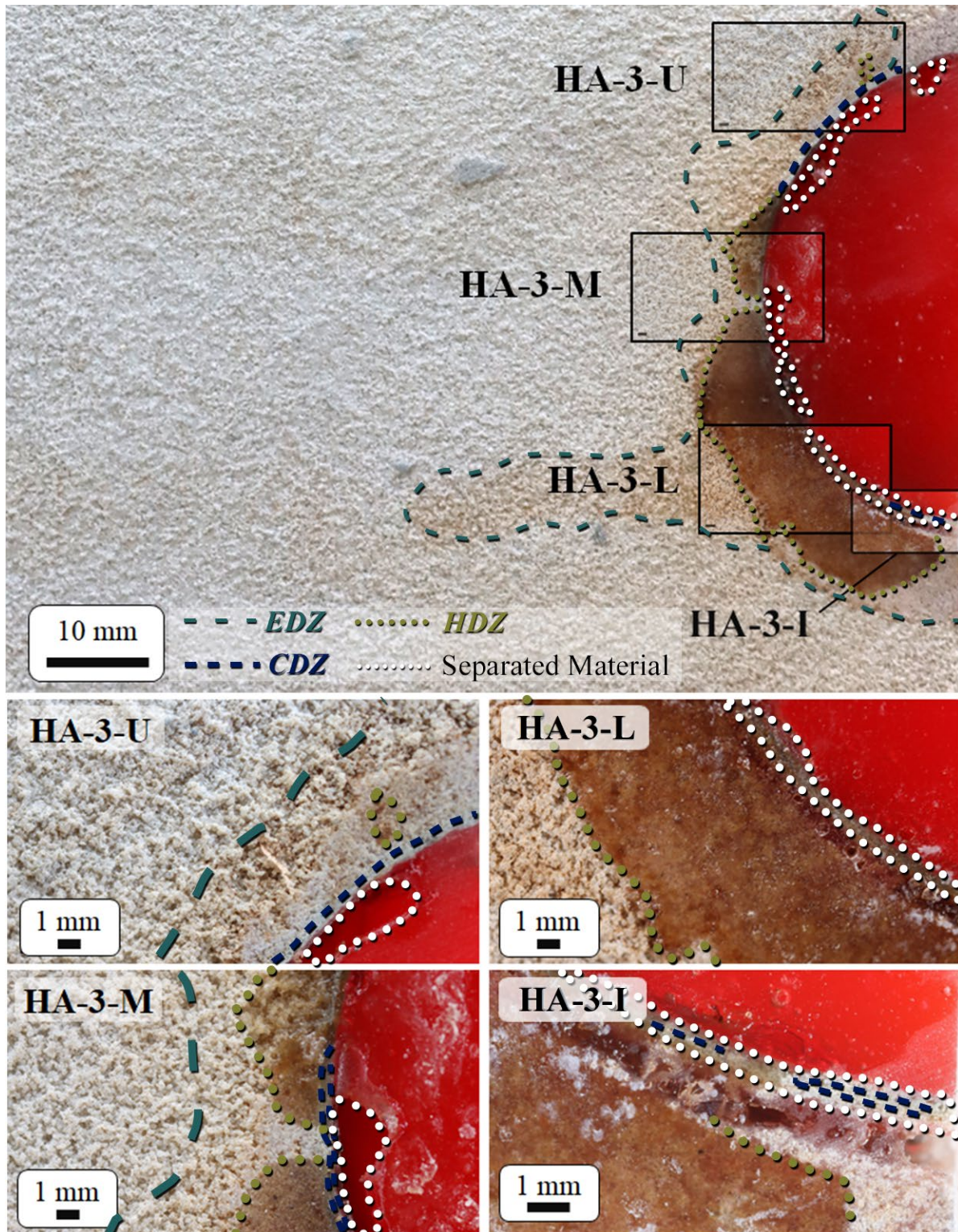


Figure 3.12 Slabbed rock tunnel specimen half axial cross-sections at approximately 100 mm advance length from the tunnel portal. HA denoting Half-Axial, whereas the following codes include the slab number in respect to distance from portal and spot of shots (upper, medium, lower, and invert).



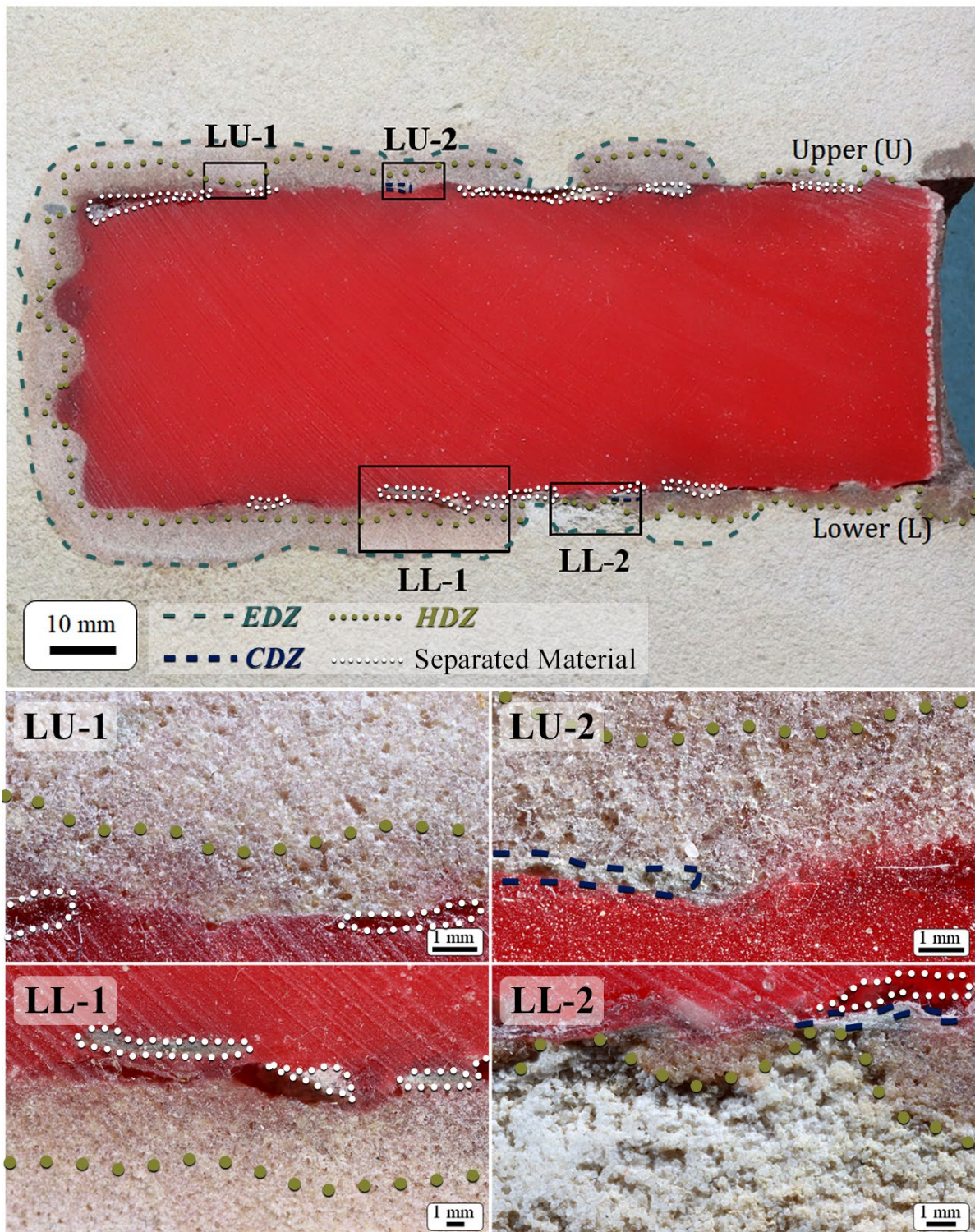


Figure 3.13 Slabbed rock tunnel specimen longitudinal cross-section. LU and LL denoting the longitudinal upper and longitudinal lower, respectively, whereas the following number is the shots numbering.

In characterizing the induced damage zones, interpreting the Excavation Influence Zone *EIZ* was difficult since the elastic deformation cannot be noticed from the macro-photograph. The outer boundary of the *EIZ* is often insignificant in an excavation with relatively minimal changes in rock mass properties.<sup>2</sup> The epoxy used to preserve the microstructure of the failed tunnel wall did not penetrate the *EIZ*. Furthermore, by removing the sample from the true-triaxial cell, the sample is unloaded and is no longer under applied load. At this time, all elastic deformation should have been released and no longer visible in the sample.

In addition to the *EIZ*, the damage induced by tunneling on the tunnel wall is further delineated into four different more visible zones. Details of the different damage zones from the experiment are discussed below. Using macro-photography, it is found that the microstructure of the tunnel wall after drilling can be characterized according to the following four damaged zones:

The Highly Damaged Zone *HDZ* is observed from the major discoloration to brown color of the resin-dominated area, indicating high macro-fracture intensity and connectivity. The resin glued the loose sand grains and broken cementitious bonds from the highly damaged intact rock. This phenomenon is similar to the in-situ condition discussed in Li (2017) about fracture intensity in an observatory borehole in an underground excavation.

The Excavation Damage Zone *EDZ* is indicated by slight discoloration due to the resin from the original synthetic sandstone color. The *EDZ* is caused by the plastic deformation and some distributed damage in the rock mass (Perras and Diederichs, 2016). Less interconnected damage presumably allows smaller penetration of resin compared to the *HDZ*.

The Construction Damage Zone *CDZ* shows porosity that looks smaller compared to other zones indicating compaction due to TBM excavation. Light greyish color also indicated predominantly hydrated cement and bonded crushed sand, disallowing penetration of the resin further.

Spalling emerges from the separation of thin materials at the tunnel wall. The notable features near the tunnel boundaries are the micro-fractures sub-parallel to the wall indicating extensional failure leading to spalling. The spalling is evidenced by material separation from the tunnel boundary. The sub-parallel feature is similar to the samples from the UCT with sub-vertical extensional fractures parallel to  $\sigma_1$  after failure (Figure 3.7). This fracturing is expected because the stress condition at the tunnel wall is similar to the UCT, where the radial stress  $\sigma_r$  is zero, corresponding to zero confinement in the UCT, and the tangential stress  $\sigma_\theta$  is the major principal stress. From the slabbed sections, the depth of spalling was measured at 2 mm, approximately 8% of the tunnel radius. To put this in perspective, a tunnel with a diameter of 10 m would have a measured spalling depth of up to 0.4 m.

Figure 3.11 shows a half cross-section at a tunnel advance of 50 mm with close-up macro-photographs taken from three locations. The top figure shows four distinct rock fragments that have



spalled at the tunnel wall. Note that the separated materials are clearly due to spalling as they are long, very thin, and detached parallel to the tunnel wall. The drilling did not create these detached materials, which would have produced irregularly-shaped drill bit cuttings. The repeated air flushing during the tunneling would have removed these cuttings. HA-2-U, HA-2-M, and HA-2-L highlight the different close-up response of the tunnel wall after excavation. Photo H-2-U shows two separate segments of the tunnel wall due to spalling. The greyish area demarcated by the dashed line indicates a *CDZ* with a relatively tighter structure compared to the rest of the rock that the resin could not penetrate. A slight *EDZ* area is observed surrounding the *CDZ*. Photo HA-2-M shows major resin penetration that strongly discolored the damaged zone to brown. Intense penetration indicates high micro-fracture intensity and connectivity and is characterized as *HDZ*. The observed depth of *HDZ* in this location ranges between 1-2 mm. The thin lines demarcating the *CDZ* are indicated since light greyish materials appear by the chipped cavities (spalled surface) marked by the dotted lines. Photo HA-2-L also shows clear indications of spalling. The separated material is approximately 0.3 mm thick and is prominently separated at up to 1.2 mm from the rest of the tunnel wall. The *HDZ* and *EDZ* are shown away from the wall with major discoloration due to resin penetration.

Figure 3.12 shows a half cross-section at a tunnel advance of 100 mm with close-up macro-photographs taken from three locations. The top figure shows four distinct thin materials that have spalled from the tunnel wall. There is a thin but clear *CDZ* at the tunnel boundary with a thickness of approximately 0.2 mm. Major discoloration up to 5 mm can be observed to indicate the *HDZ* that the *EDZ* surrounds. Photo HA-3-U shows a *CDZ* adjacent to the tunnel boundary with 0.3 mm thickness. The solid line demarcates the *EDZ*, characterized by a relatively loose structure and slight discoloration. One chipped opening can be observed that is potentially created by a spalled surface from the tunnel boundary. In photo HA-3-L, a spalling of 0.4 mm thin separated material is visible. The separation ranges from 0.8 to 1 mm. The resin penetrates up to 11.5 mm from the tunnel boundary. Photo HA-3-L shows a thin compacted layer indicative of a *CDZ* with a thickness of 0.8-1 mm. The resin penetrates further into the rock until up to 11.5 mm from the tunnel boundary. Higher magnification in Photo HA-3-I distinctively shows the major discoloration to indicate *EDZ*. A thin *CDZ* is distinct at the tunnel boundary with a thickness of approximately 0.2 mm (photo HA-3-M). Major discoloration up to 5 mm can be observed to indicate the *HDZ* that the *EDZ* surrounds. One chipped opening can be observed that is potentially left by a spalled surface from the tunnel boundary.

Figure 3.13 shows photographs along the longitudinal section of the tunnel. The top figure shows clear spalling of thin rock segments and the nearly continuous presence of a *CDZ* surrounded by *EDZ*. The boundaries of both zones appear to follow the undulations of the irregularly excavated tunnel wall. A small amount of separated material is observed in photograph LU-1 at the tunnel boundary close to the edges of the capture. However, the material is chipped and separated from the rest of the rock mass. The

dashed line demarcated the *HDZ* with reddish discoloration of the intact rock, while the rest is considered *EDZ*. In photo LU-2, the dash-dotted line follows the final tunnel boundary, which could indicate micro fracturing due to the undulating "as-built" tunnel profile before loading. Some *CDZ* is visible on the left-hand side from the tightness of the structure and light color. In LL-1, three separated materials are observed from the tunnel boundary demarcated by the dotted lines. The range of separation is from 0.5 to 2 mm. The dash-dotted line indicates the *HDZ*, whereas the rest of the rock is considered *EDZ*. Shown in photograph LL-2 is major discoloration in the *HDZ*, localized close to the tunnel boundary, which supports the probable shear localization due to the undulating "as-built" tunnel profile before loading. The rest of the colored rock portions away from the is considered as an *EDZ*.

The average resin infiltration around the tunnel wall—demarcated as *EDZ* is 11.15 mm (i.e., 43.73% of tunnel radius  $R_T$ ), giving the experimental plastic radius  $R_p = 37$  mm. The maximum radial displacement  $u_{R_{max}}$  was measured to be 2.57 mm. Figure 3.14 presents the tracing results and visualization of the radial displacement of the tunnel from point picking. Of note, the tunnel demonstrated plastic deformation on top of the detached wall that manifested as spalling. The localized strain softening due to initial tunnel irregularity after the excavation would affect the ups and downs of the deformation along the longitudinal section.

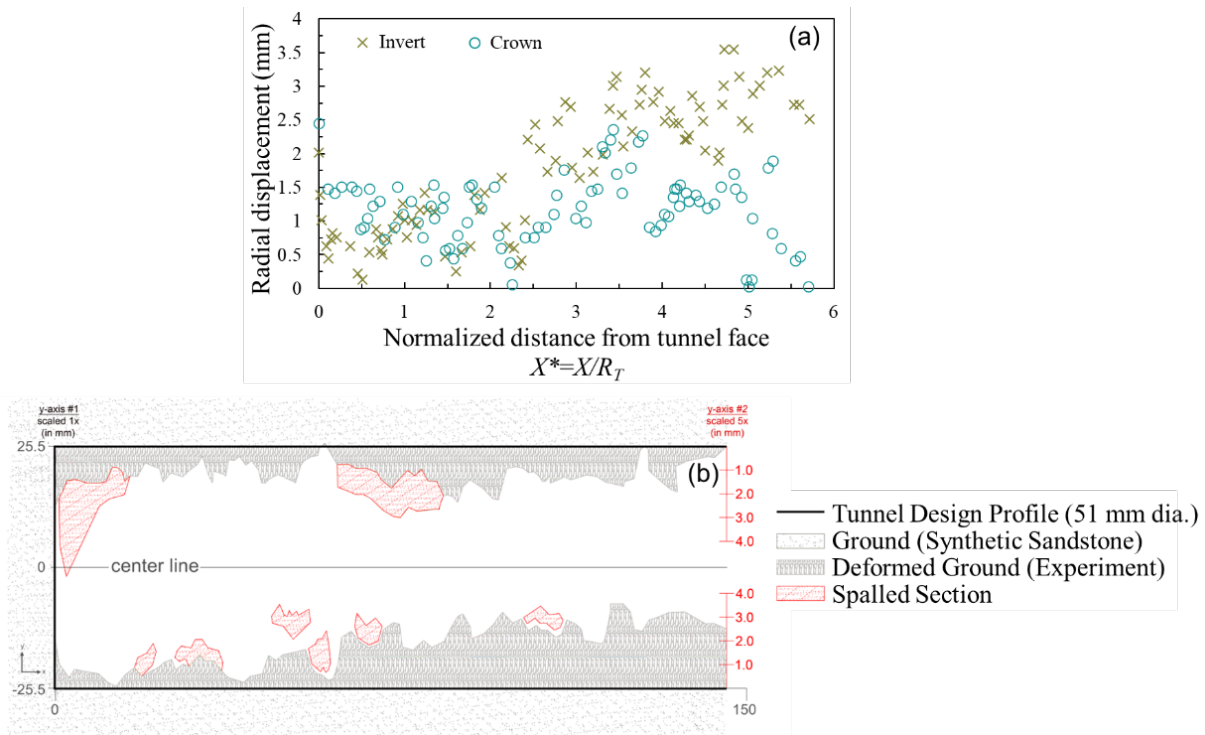


Figure 3.14 Digitized tracing results in tunnel deformation from longitudinal cut. (a) scatter plot with point picking from tunnel invert and crown. (b) Tunnel deformation and spalling failure along the longitudinal profile of the loaded tunnel with 5x exaggeration for the deformed ground. Note that the initial excavation with miniature TBM resulted in an irregular tunnel shape.

### 3.6 Conclusions

The present study investigated induced damage in a freshly excavated tunnel model in brittle-synthetic rock using the true-triaxial cell. Miniature TBM was used to excavate the scale model tunnel under conditions corresponding to realistic in-situ stresses. Laboratory element tests were performed to understand further the rock mechanical behavior, particularly the brittle response and fracturing of the synthetic rock specimen used. Post-experimental investigation using macro-photographs of the failed tunnel boundary verified the tunnel damage and failure mechanism. Spalling was one of the prevalent failure mechanisms, which developed because of increased stress intensity and concentrated tangential stresses around the tunnel boundary during stage-wise loading. The experimental results lead to the following conclusions:

- 1) The demarcated damage zones from the experiment include the Construction Damage Zone *CDZ*, Highly Damage Zone *HDZ*, and Excavation Damage Zone *EDZ*, and separated materials due to the spalling. These zones strongly corresponded to different failure mechanisms from the tunnel boundary towards the rock mass that resembles the stress-strain curve's pre-peak, peak, and post-peak regimes.
- 2) The tunnel model exhibited spalling failure at the tunnel wall with a 2 mm thickness or about 8% of the tunnel radius. This finding is critical in understanding potential hazards to tunnel construction when extrapolating to actual, in-situ conditions.
- 3) Prominent extensional failures adjacent to the tunnel boundary indicated by the failure pattern were characterized by macro-photography. The behavior of the tunnel wall and UCT test sample were in agreement, with both showing fracturing sub-parallel to the major principal stress ( $\sigma_1$  in the UCT and  $\sigma_\theta$  in the model tunnel true-triaxial test).
- 4) Post-experimental investigation in the longitudinal cross-section also provided an evidence of potential shear localization and micro-fracturing caused by the undulating "as-built" tunnel profile before loading. The Highly Damage Zone *HDZ* is closely localized and followed the final tunnel boundary.

Further research is necessary investigate different stress configurations and mitigation measure such as ground support implementation. The AE data monitoring need to be fixed to avoid saturation during the loading stage so it allows precursors detection in brittle failure scenarios. Albeit with limitations, this research showcased the experimental scheme that adequately simulated brittle tunnel. The stress-dependent brittle behavior of rock around a tunnel boundary was observed after the incremental isotropic loading stages.

## CHAPTER 4 INVESTIGATION OF TUNNEL SPALLING USING A LARGE-SCALE TUNNEL MODEL AND TRIAXIAL EXTENSION EXPERIMENTS<sup>1</sup>

### 4.1 Abstract

Brittle instabilities in tunnel excavation have led to spalling, violent rock ejection, and tunnel collapse. Previous research has primarily investigated brittle failure using two-dimensional approaches, which oversimplify in-situ stress state. Additionally, the mechanism behind the low entry angle of fracturing observed in spalling during tunnel projects is not fully understood when using standard uniaxial compression tests (UCT). This study aims to showcase these limitations using a large-scale tunnel model and triaxial extension (TE) tests. A mock miniature tunnel boring machine (TBM) excavated through an analog specimen loaded in a true-triaxial cell. Following excavation, the specimen was loaded in stages under incrementally increasing isotropic conditions, which induced failure in the tunnel. Excavated 51 mm diameter tunnel within  $300 \times 300 \times 300 \text{ mm}^3$  facilitated direct observation of spalling progression throughout the loading stage. Six wideband acoustic emission (AE) sensors were utilized to monitor microcracking intensities associated with changes in boundary stress conditions during the loading stages. At the end of the final loading stage, an epoxy resin was injected into the failed tunnel to identify the damage zone. The TE tests were introduced as a new experimental methodology to improve spalling prediction. Using conventional Hoek Cells, the TE test setup effectively represents three-dimensional in-situ stress states and yields steep angles failure plane measured from minor principal stress. This study improves our understanding of brittle failure mechanisms based on experimental evidence by comparing TE and triaxial compression (TC) results with the tunnel model spalling. The evaluations indicated that predictions using TE parameters were more accurate than those using TC parameters regarding spalling strength (element strength test), entry angle, and depth of damage. The failure envelopes for both TE and TC tests were assessed, but neither could predict a steep failure plane angle at zero confinement. However, direct entry angle measurements from the element test and theoretical log-spiral slip lines offered the most accurate fit with tunnel model spalling. Thin shear slabs with steep failure planes provided conclusive experimental evidence, confirming that classical shear failure primarily governs spalling. Ultimately, this study adds new insights for safer and more reliable tunnel designs in brittle rocks.

---

<sup>1</sup> This chapter will be submitted as a full journal paper for publication in an international peer-reviewed rock mechanics journal.

## 4.2 Introduction

Various instability mechanisms can occur when the in-situ stress magnitudes surpass the rock mass strength. One type of instability in tunnel excavation is brittle fracture, signified by rapid reduction of the general load-bearing capacity of the rock mass. The fracturing propagates sub-parallel to the maximum principal stress, typically known as extensional fractures, shear failures along pre-existing discontinuities, or combinations of both (Hoek and Marinos, 2009; Martin et al., 1999). These fractures can lead to the detachment of rock surfaces in the form of spalling or rock bursts (Gong et al., 2012b; Mazaira and Konicek, 2015; Ortlepp and Stacey, 1994; Primadiansyah, 2024). Such instabilities have significant consequences, including safety hazards, delays, and increased costs, particularly in deep tunnels under high-stress conditions (Moss and Kaiser, 2022; Naji et al., 2019; Zhu et al., 2019). Recent reports highlight brittle failure in tunnels excavated under moderate in-situ stress conditions. For example, brittle failure delayed the final lining installation in the sedimentary rock of the Ohio River Tunnel Project (des Rivières and Goodman, 2023). Spalling also impacted the progress of the TBM excavation of the Pahang-Selangor Raw Water Transfer Tunnel Project in Malaysia (Kawata et al., 2014). These cases emphasize the need for a deeper understanding of brittle failure mechanisms under complex stress conditions. As shown in Figure 4.1, spalling exhibited a low-entry angle failure mechanism near the tunnel wall, which motivates this study.



Figure 4.1 Brittle failure challenge in the TBM-excavated tunnel project, showing spalling with low-entry failure angles oriented sub-parallel to the tunnel boundary during excavation (Kawata et al. 2014).

Over the past decades, several in-situ studies have contributed to understanding the brittle failure mechanisms. These field studies include wellbore breakout observations (Zoback et al., 1985), Mine-By-Experiment (Read and Martin, 1991), the Äspö Hard Rock Laboratory (Andersson et al., 2004), Posiva's Olkiluoto Spalling Experiment (T. Siren et al., 2015b), and the Jinping Underground Laboratory Phase II (Feng et al., 2018). These investigations contributed to the following: (1) the development of empirical criteria based on the maximum tangential stress  $\sigma_\theta$  to the uniaxial compressive strength  $\sigma_c$ , (2) failure mode validation, such as structurally controlled brittle failure due to anisotropy, and (3) numerical model of brittle failure enhancement using continuum or discontinuum approaches (Hajiabdolmajid and Kaiser, 2003; Martin et al., 1997; Shen and Barton, 2018). However, in-situ tests are expensive and complex (Lin et al., 2015).

As a result, researchers have developed laboratory-scale experimental models to classify the brittle failure mechanisms in rock (Paterson and Wong, 2005). These models are essential for verifying simulation models of specific mechanisms, which can be used to explore a broader range of parameters (Einstein, 2024). Some developed models related to borehole breakout or tunneling allow simultaneous excavation under loading conditions, while others employ specimens with prefabricated openings. Experimental models that include excavation allow a closer representation of actual field conditions than prefabricated openings (Herrick and Haimson, 1994). Redistribution of stress around the tunnel boundary during the excavation follows the unloading mechanism, degrading brittle rock (Gong et al., 2023a). Borehole breakout refers to elongated sections in a vertical wellbore caused by rock failure under stress (Haimson, 2007). In tunneling, spalling failures are typically attributed to extensional fracturing in a subparallel direction to the major principal stress, resulting in stress-induced damage around the opening (Haimson and Herrick, 1989; Lee and Haimson, 1993). The damage extent depends on factors like opening orientation towards far-field stress, stress anisotropy, and rock properties (Rawlings et al., 1993). While practical, these models predominantly use anisotropic loading and infinite openings under plane stress or plane strain conditions.

Many studies demonstrate that stresses perpendicular to the tunnel axis are responsible for brittle fracturing (Cheon et al., 2011). However, confinement stresses parallel to the tunnel axis (intermediate confinement) have been found to influence brittle behavior and affect the angle of brittle faulting (Cai, 2008; Diederichs et al., 2004; Haimson and Rudnicki, 2010; Su et al., 2023). This confinement effect is linked to the role of the intermediate principal stress  $\sigma_2$ , which has been shown in general to strengthen the rock based on its magnitude (Al-Ajmi and Zimmerman, 2005; Garg et al., 2021; Su et al., 2023; Trzeciak and Sone, 2024; Yun et al., 2010). A critical knowledge gap still exists in understanding the influence extent of these intermediate confinement stresses in tunneling scenarios, particularly in spalling initiation predictions.

This study provides a comprehensive analysis of brittle failure mechanisms based on a combination of experimental methodologies. The laboratory-scale tunnel model involves a cubical analog brittle specimen with an excavated tunnel, while rock characterization and failure envelope determination are based on elemental testing of cylindrical specimens. A new methodology using triaxial extension (TE) tests is introduced, offering improved insights into tunnel spalling mechanism. TE tests yield peak failure stress  $\sigma_f$  as a spalling strength and a refined failure envelope, considering the three-dimensional stress states and unloading conditions. These results and two-dimensional analyses from triaxial compression (TC) are compared against data from the tunnel model experiment. The comparison focuses on three key aspects: spalling strength  $\sigma_f$ , depth of spalling  $D_f$ , and spalling entry angle  $\alpha$ . This study highlights enhanced experimental methods, leading to a deeper understanding of brittle failure mechanisms and more robust spalling predictions, particularly in the context of three-dimensional state-of-stress and unloading effects.

### **4.3 Experimental Setup**

#### **4.3.1 Tunnel Model Test Apparatus and Procedures**

A mock miniature TBM (Arora et al., 2021) and a true-triaxial apparatus (Frash et al., 2014b) enabled controlled excavation and simultaneous loading to a cubical analog brittle specimen. First, the  $300 \times 300 \times 300 \text{ mm}^3$  cubical specimen was placed inside the true-triaxial cell. An initial loading condition was applied to the specimen (1.0-1.5 MPa) to ensure it remained in position. Then, the miniature TBM, consisting of a 51 mm diameter tungsten-carbide-button-bit excavation head, thrust unit, and torque unit, was mounted on top of the true-triaxial cell (Figure 4.2a). The hollow drilling rod connected to a compressed air line (Figure 4.2b) allowed air flushing to remove cuttings from the tunnel face. Once half the length of the cubical specimen was excavated by the miniature TBM, the TBM was removed from the specimen. A digital borehole caliper measured the initial tunnel dimension (Figure 4.2c).



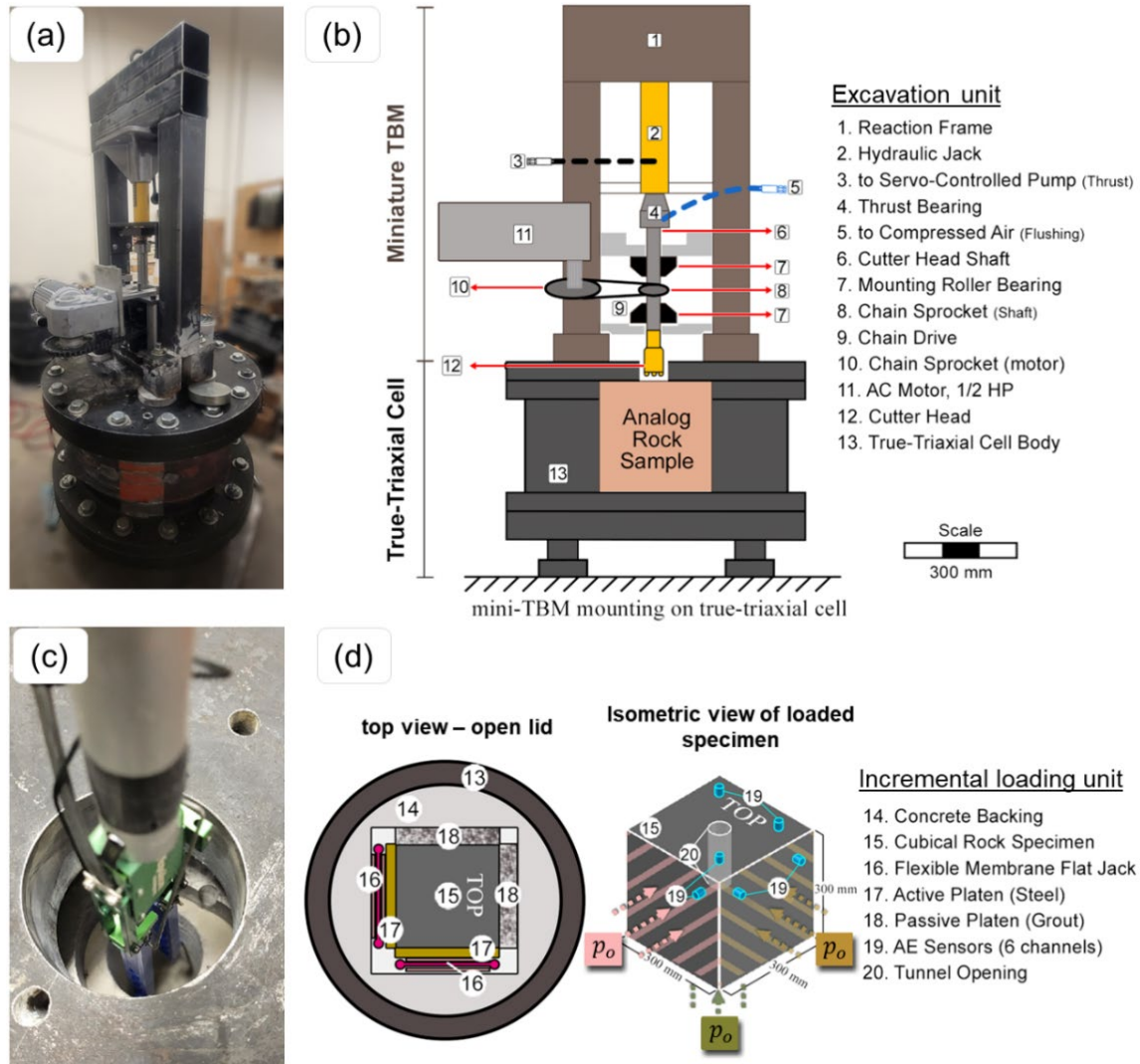


Figure 4.2 Laboratory-scale tunnel model experiment designed to study tunnels in brittle rock; (a) actual setup at Colorado School of Mines featuring a mounted miniature TBM on top of a true-triaxial cell, (b) conceptual drawings of the excavation unit, (c) digital borehole caliper used to measure initial tunnel diameter, and (d) conceptual drawings of the incremental loading unit.

Next, isotropic loads were applied gradually to the specimen. The loading was applied through three active faces with Freysinnet flexible membrane flat jacks placed behind stiff metal plates (Figure 4.2d). The opposing passive sides consisted of rigid high-strength cement grout to ensure uniform contact with the cell body. Based on the reported stress distribution near the center of the specimen (Frash et al., 2014b), a factor of 37% was applied to calculate the effective far-field stress. For example, with a pressure transducer reading of 6.14 MPa, the effective far-field stress  $p'_o$  was 2.27 MPa. Loading stopped when a significant failure occurred, or the apparatus reached its maximum capacity. The stress state at the onset of visible spalling was then compared with analytical stress state predictions.



Acoustic emission (AE) data was acquired using a six-channel board and data acquisition system from the MISTRAS group, operated through AEWin software. Six WSA-30 AE sensors, with an operating frequency range of 100–1000 kHz and a resonance frequency of 125 kHz, were mounted on three faces of the rock specimen to capture event occurrences (Figure 4.2d). The seismic waveforms were amplified by 60 dB, and a threshold of 30 dB was applied to filter out environmental and machine noise, ensuring the selection of relevant signals. This setup facilitated the detection of elastic waves associated with microcracking and failure processes, offering detailed insights into the evolution of damage in the specimens (Gautam et al., 2023; Lockner, 1993). In this investigation, parametric AE data used are count and cumulative count to indicate cracking intensity in each loading stage.

Before unloading the specimen, a red-dyed flowable resin was filled to the excavated area to preserve the final deformation profile and infiltrate the damaged zone around the tunnel. Once the resin had completely solidified, the specimen was unloaded and removed from the true-triaxial cell. The cubical specimen was then sliced for post-mortem analysis, consisting of one longitudinal section and six half-axial cross-sections (Wibisono et al., 2024). From the post-mortem analysis, the maximum distance from the tunnel centerline to the outermost extent of resin infiltration into the damaged rock mass was inferred as the experimental plastic radius  $R_p$  or excavation damage zone  $EDZ$ . Additionally, the thickness of the spalled materials observed in the macro-photographs of the sections was measured to quantify the experimental depth of spalling  $D_f$ .

#### 4.3.2 Analog Brittle Rock

The analog brittle rock used in this study was prepared through a mortar-mixing process to mimic the properties of sandstone. The mixture comprised Type I/II Portland Cement, F-75 Ottawa sand, and water. Table 4.1 summarizes the mechanical properties of this analog brittle rock. The specimen was designed to be "very weak" in uniaxial compressive strength  $\sigma_c$  yet exhibit brittle characteristics. This analog rock is categorized as "very weak", according to a system acknowledged by the International Society of Rock Mechanics (1978). This weak and brittle characteristic of the material offers critical advantages: reducing the need for a high-capacity loading apparatus and accommodating a large specimen to facilitate induced failure observation inside the excavated tunnel (Wibisono et al., 2024). During an unconfined compression test (UCT), brittle behavior was identified through distinct peak shear strength, followed by a sudden and well-defined strain softening response. In addition to the stress-strain behavior under UCT, several rockburst tendency criteria—such as the strength brittleness index, brittleness index modified and burst energy coefficient—were used to validate the brittle response of the specimen (Wibisono et al., 2022). This reproducible analog brittle rock design (mix O) served as the test material for all experiments performed in this study.

Table 4.1 Summary of analog sandstone mechanical properties from previous laboratory characterization. The mix design is denoted with Mix O.

Properties	Mix O
Uniaxial compressive strength, $\sigma_c$ (MPa)	3.07
Brazilian splitting strength, $\sigma_t$ (MPa)	0.45
Tangent Young's Modulus, $E_{50}$ (GPa)	0.94
Poisson's ratio, $\nu$	0.21

### 4.3.3 Tunnel Model Test Results

Following excavation, the borehole caliper measured the tunnel diameter at three locations: the tunnel portal, mid-point, and near the tunnel face. The average tunnel radius  $R_T$  was determined to be 25.52 mm, closely matching the radius of the miniature TBM excavation head. Figure 4.3a. presents the initial tunnel profile post-excavation, revealing slight, consistent irregularities rather than a perfectly smooth surface. Table 4.2 summarizes the experimental measurements, which are later compared with empirical correlations and analyzed further using element test data.

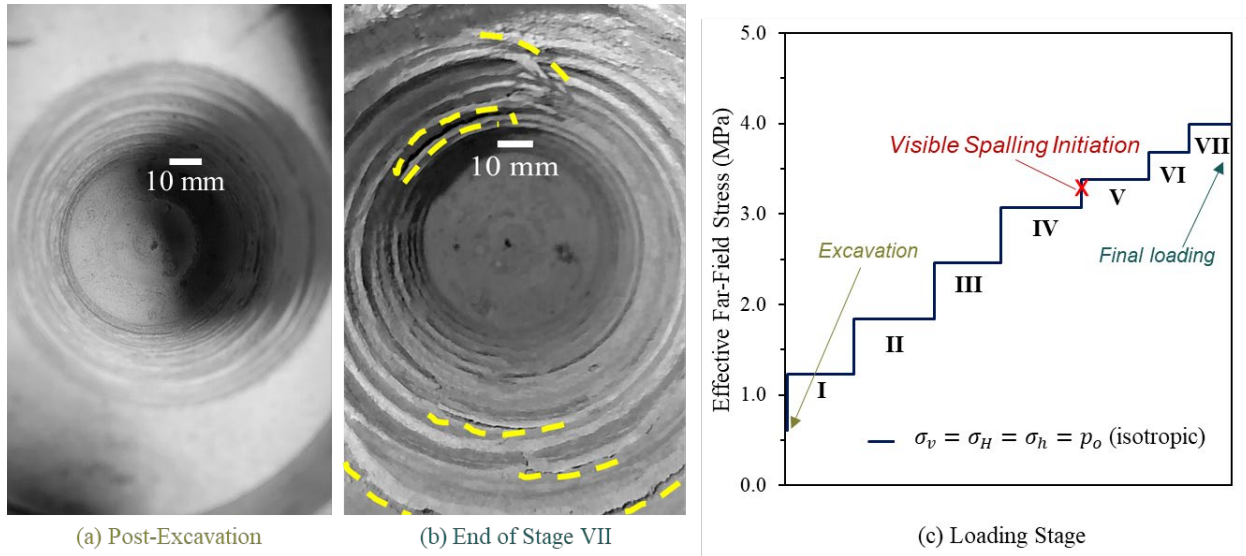


Figure 4.3 a) Initial tunnel profile after excavation with miniature TBM, (b) final tunnel profile after the loading stage VII, and (c) Effective far-field stress  $p'_o$  applied during the loading stage to the specimen in miniature TBM and true-triaxial cell experimental schematics. Yellow dashed lines in (b) highlight the final spalling failure. In (c), the visible spalling failure was first observed during the transition from loading stage IV to stage V at  $p'_o = 3.2$  MPa, indicated with a red cross mark. (For interpretation of the references to color in this figure legend, the reader is referred to the Web version of this article.)

Table 4.2 Summary of the initial tunnel model boundary condition and experiment results, including tangential stress  $\sigma_\theta$ , final spalling depth  $D_f$ , and depth of plastic radius  $R_p$  or excavation damage zone  $EDZ$  based on resin infiltration..

Experimental data	Note	Value
Average tunnel radius, $R_T$ (mm)	Initial stage	25.52
Tangential stress at tunnel wall, $\sigma_\theta$ (MPa)	Visible spalling initiation stage, $\sigma_{\theta-initiation}$	6.4
	Final loading stage, $\sigma_{\theta-final}$	7.94
Depth of spalling, $D_f$ (mm)	-	26.03 – 27.56
Depth of plastic radius $R_p$ or excavation damage zone $EDZ$ (mm)	-	26.01 – 37.00

The loading phase consisted of seven incremental stages (Figure 4.3c), each lasting approximately 120 hours to ensure a steady-state condition around the tunnel boundary. Spalling failure was first visually observed between loading stages IV and V (Wibisono et al., 2023b), occurring at an effective far-field stress  $p'_0$  of 3.2 MPa. Based on Kirsch's solution for a circular tunnel, the tangential stress at the tunnel boundary is defined as  $\sigma_\theta = 3\sigma_v - \sigma_h$ . Under isotropic loading conditions, where  $\sigma_v = \sigma_h = p'_0$ , the solution reduces to  $p'_0 = \sigma_\theta/2$ . Thus, at the initiation of spalling, the maximum tangential stress  $\sigma_{\theta.initiation}$  at the tunnel boundary was 6.4 MPa.

By the final loading stage VII, the maximum tangential stress  $\sigma_{\theta.final}$  reached 7.94 MPa. Figure 4.3b shows the spalling around the tunnel at the end of this stage, with failure characterized by spread and diffused spalling. Most spalling appeared as very thin cracks, with close to sub-parallel wall detachment attempts at a minimal entry angle  $\alpha$ . At the tunnel crown (Figure 4.3b), conjugated shear was observed at a slightly greater angle, showing more pronounced detachment attempts. However, only a few actual wall detachments occurred in the tunnel.

Figures 4.4a and 4.4b present the longitudinal view of the recovered specimen and the half-axial (HA) section taken 100 mm from the tunnel portal, respectively. The dashed green lines marking the darkened regions of the specimen indicate the extent of resin infiltration ( $R_p$  or  $EDZ$ ). The white dotted lines delineate the thickness of the spalled rock, corresponding to the depth of spalling failure  $D_f$ . Figures 4.4c and 4.4d provide a closer view of the tunnel damage in Figure 4.4b, captured using macrophotography.

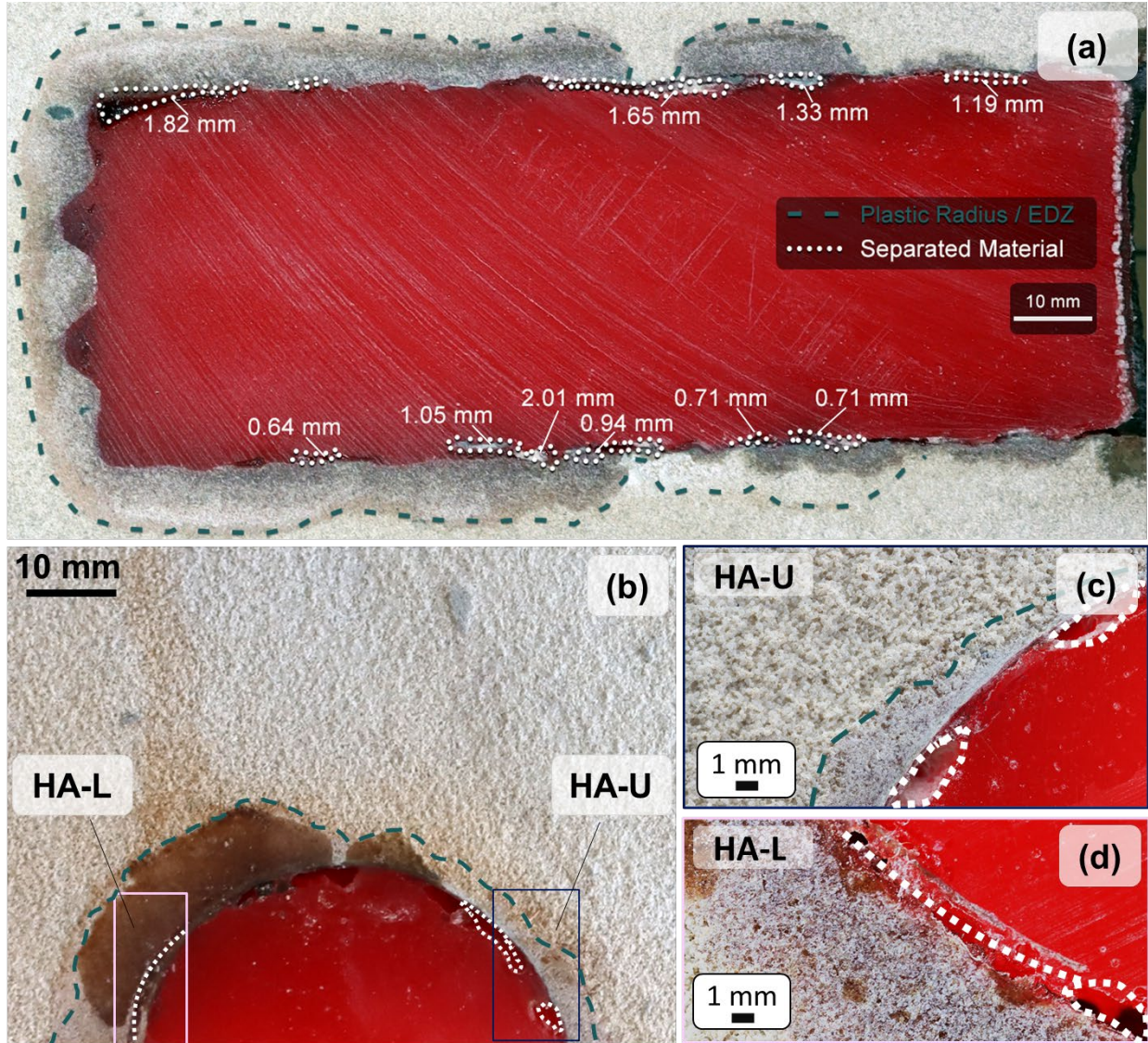


Figure 4.4 (a) Longitudinal section of the recovered specimen with cured epoxy resin (red color), (b) half-axial section located 100 mm from the tunnel portal. Epoxy resin was injected into the opening after the final loading stage to preserve final deformation. Annotations show the infiltrated resin (plastic radius  $R_p$  or EDZ) and the thickness of spalled rock observed in the section. (c) and (d) provide a closer view of the tunnel damage observed in (b). (For interpretation of the references to color in this figure legend, the reader is referred to the Web version of this article.)

In both the longitudinal and HA sections, resin infiltration around the tunnel wall—marked as  $R_p$  or EDZ—ranges from 0.51 to 11.15 mm (1.99-43.69% of the tunnel radius  $R_T$ ), giving an experimental plastic radius  $R_p$  between 26.1 to 37 mm. Additionally, the depth of spalling failure  $D_f$  ranges from 26.03 to 27.56 mm, as noted in Figure 4.4a. The measured values for damage observed in Figures 4.4c and 4.4d align with those from the longitudinal section measurements. Figure 4.4d further confirmed the occurrence of thin spalling failure with a minimal entry angle  $\alpha$ , where the angle was measured to be less than  $5^\circ$ .



## 4.4 New Experimental Procedure to Determine Tunnel Spalling Potential

### 4.4.1 Three-Dimensional State-of-Stress at Tunnel Wall

Figure 4.5 illustrates the tunnel boundary's stress state through two- and three-dimensional visualizations. The two-dimensional is limited to the zone near the portal, whereas realistically, the perturbed lateral stress parallel to the tunnel axis appears to affect the confinement state. After excavation (unloading), the radial stress at the immediate tunnel wall is negligible, but radial stress increases radially outward from the tunnel wall, influencing brittle failure mechanisms.

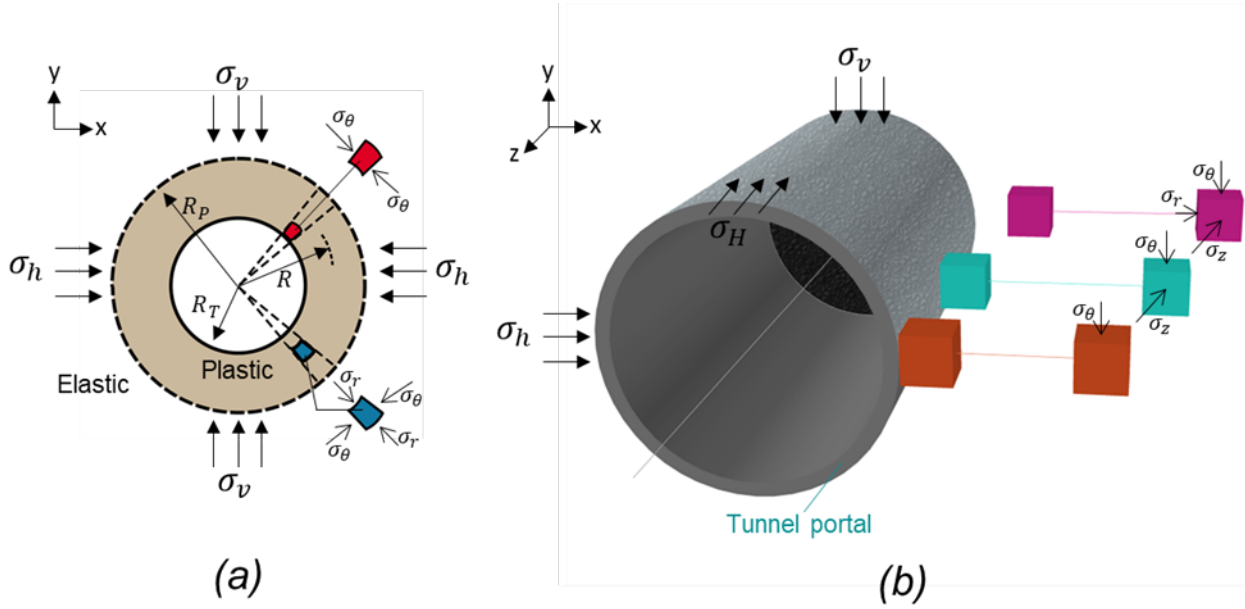


Figure 4.5 Visualizations of the stress state at the tunnel boundary: (a) two-dimensional cross-sectional view showing tangential and radial stress distribution and (b) three-dimensional view illustrating tangential, radial, and longitudinal stress distribution throughout the tunnel length.

For a two-dimensional tunnel (i.e., a plane stress condition), an unconfined compression test (UCT) condition can represent the stress state at the tunnel boundary. Here, the minimum principal stress at the tunnel boundary is the radial stress  $\sigma_r = \sigma_3 = 0$ , while the tangential stress  $\sigma_\theta$  serves as the maximum principal stress  $\sigma_1 \neq 0$ . Assuming that the tunnel is under compression around a highly stress excavation, the tangential stress  $\sigma_\theta$  yields the tunnel wall and causes failure if it exceeds the UCS of the rock  $\sigma_c$ , as shown in Figure 4.5a. This consideration appears to oversimplify the stress state and underestimate rock strength, as tunnels are subjected to complex three-dimensional loading.

Under isotropic loading conditions in a three-dimensional tunnel, the stress state at the boundary is modified due to the presence of intermediate confinement (Figure 4.5b). This intermediate confinement near the tunnel boundary manifests as longitudinal stress  $\sigma_z$ , contributing to fracturing (Rahjoo, 2019; Su et al., 2023). This results in a biaxial stress state at the tunnel boundary, involving axial unloading during

excavation, where  $\sigma_r = 0$  and  $\sigma_\theta, \sigma_z \neq 0$  (Cai 2008). Intermediate confinement stress has been reported to provide a strengthening effect to rock based on its magnitude (Feng et al., 2020; Garg et al., 2021; Wang et al., 2020; Yun et al., 2010). Hence, consideration of intermediate confinement in three-dimensional loading is crucial for accurately predicting and mitigating brittle failure. To estimate the tangential stress at failure  $\sigma_{\theta f}$  under two- and three-dimensional state-of-stress, triaxial compression (TC) and triaxial extension (TE) tests are adopted. The required stress to induce failure is adopted as  $\sigma_{\theta f}$  and will be referred to for each test as  $\sigma_{f-test}$  (i.e.,  $\sigma_{f-UCT} = \sigma_c$ ,  $\sigma_{f-TC}$ ).

#### 4.4.2 Triaxial Compression and Triaxial Extension States-of-Stress

A conventional triaxial chamber—Hoek cells—was employed for a set of TC and TE tests to predict tangential failure stress or spalling strength  $\sigma_f$ . Of note, the TC with 0 MPa did not use Hoek cells but followed the UCT standard (ASTM, 2017). All the TC tests follow the International Society of Rock Mechanics (ISRM) suggested method with testing procedure type I—an individual test, loaded at a constant strain rate such that failure occurs within 5-15 minutes of loading (Kovari et al., 1983). The peak axial load and confinement at the point of specimen failure are plotted to obtain the best-fit failure envelope in the  $\sigma_1$  vs.  $\sigma_3$  plane. Additionally, the Brazilian splitting strength  $\sigma_t$  from analog rock mechanical properties (Table 4.1) is included when developing the failure envelopes to account for tensile behavior ( $\sigma_3 < 0$ ).

TE test is adopted to simulate the encountered biaxial stress state at the tunnel boundary (Figure 4.5b). Additionally, the unloading process enables more accurate stress path replication that reflects the path experienced at the wall during the tunnel model experiment (Section 4.3.3). Figure 4.6 provides a detailed comparison between the testing conditions of TE and TC tests. The positioning of the specimen in the loading apparatus is similar to that in a TC test. However, the loading arrangement is conceptually rotated perpendicularly to simulate the confinement stress as the major and intermediate principal stresses  $\sigma_1$  and  $\sigma_2$  acting on the specimen (Figure 4.6b). In the unconfined extension test (UET), the minor principal stress  $\sigma_3$  is controlled by the axial loading apparatus and is completely unloaded to simulate the excavation or sudden release due to spalling rock detachment. On the other hand, TE allows partial unloading to simulate the stress state further away from the tunnel wall.

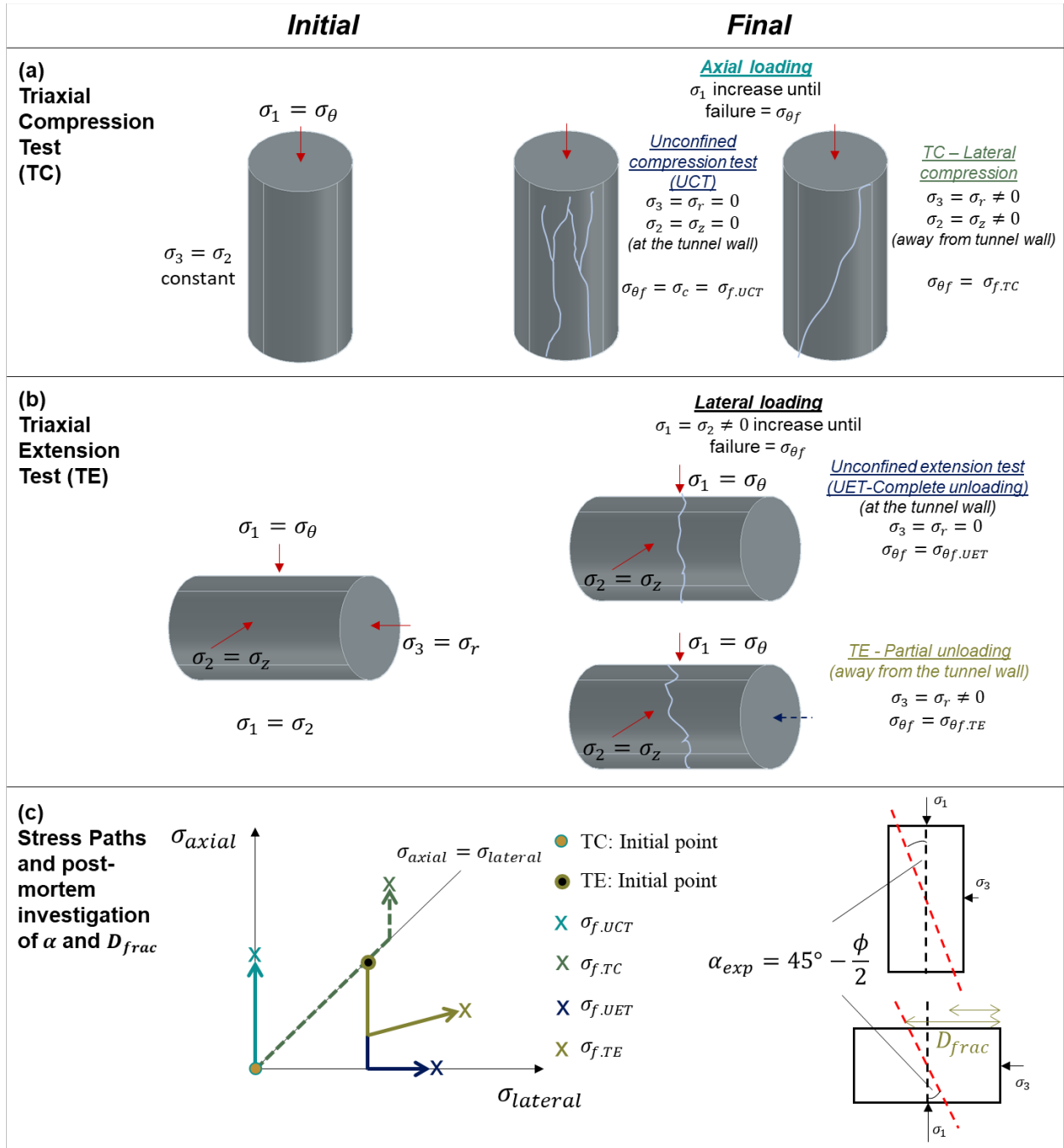


Figure 4.6 Initial and final configurations of the laboratory cylindrical tests (element tests) for (a) the TC test, (b) the TE test performed in this study, and (c) the illustration of the stress paths in these tests and post-mortem investigation to obtain failure plane angle  $\alpha_{exp}$  and fracture depth  $D_{frac}$ . The required stress to induce failure is adopted as  $\sigma_{\theta f}$  and will be referred to for each test as  $\sigma_{f-test}$ .

TE tests follow a stress path involving unloading and lateral compression (Figure 4.6c): (1) The specimen is isotropically loaded in the triaxial chamber until the designated stress condition is achieved (e.g.,  $p_0 = 0.5 \cdot \sigma_c$ ); (2) the axial load  $\sigma_3$  is then reduced to simulate  $\sigma_r = 0$  (complete unloading-UET) or a specific initial loading (partial unloading-triaxial extension test), representing the initial in-situ radial stress state of the rock mass before spalling occurs (e.g.,  $\sigma_3 = 0.2 \cdot \sigma_c$ ); (3) lateral confinement pressures  $\sigma_1$  and  $\sigma_2$  are increased to simulate the tangential and longitudinal stresses,  $\sigma_\theta$  and  $\sigma_z$ , at the tunnel wall until failure is observed; (4) the peak lateral confinement is recorded as the required stress to induce failure  $\sigma_{\theta f-UET}$  and  $\sigma_{\theta f-TE}$ ; (5) post-mortem investigation for the failed specimen to obtain the failure plane angle  $\alpha_{exp}$  and depth of fracture  $D_{frac}$ . The theoretical failure plane is calculated using this equation  $\alpha = (45^\circ - \phi/2)$  relative to the major principal axis (Figure 4.6c).

Though the TE methodology represents an advanced testing approach, they have some limitations. One limitation is the assumption of equal confinement pressures ( $\sigma_1 = \sigma_2$ ), which may not accurately reflect the anisotropic stress conditions present at the in-situ tunnel wall. Another limitation is that the axial loading used a displacement-controlled apparatus. Mainly, for the TE test with partial unloading, the axial platen is initially held at a specific  $\sigma_{3-initial}$  loading. As lateral confinement increases, the platen cannot maintain a constant loading. Instead, it leads to the recompression of the specimen  $\sigma_3 \geq \sigma_{3-initial}$ . Therefore, synchronization and complete recording of axial and lateral data are required to accurately simulate the rock mass's stress state accurately. The final axial stress state is reported to obtain the failure envelope accurately. This synchronization ensures an accurate capture of the complete stress path and enables the development of a reliable failure envelope.

In a typical TE test, a dog bone-shaped specimen is often used with justification to reduce the potential for axial splitting, especially under low confinement (Brace, 1964; Hoek and Brown, 2019). Nevertheless, the purpose of replicating the stress path at the tunnel model wall in this study is perceived to be sufficient with a cylindrical specimen. Using a cylindrical specimen is also justified because the axial splitting potential was not observed and is typically found where the axial tensile force is applied to the specimen.

#### 4.4.3 Comparisons of Results of TC and TE Element Tests

Three confinement levels were tested for both TC and TE to obtain the best-fitting failure envelopes from each, along with the Brazilian splitting strength  $\sigma_t$ . For the TC test, the three confinement levels were 0, 1.5, and 3 MPa, while for TE, the confinement levels were 0, 0.1, and 0.4 MPa. Although the confinement levels for TE were considered small, they were designed as the initial load, which increased as lateral compression progressed (as explained in Section 4.4.2). Table 4.3 presents the stress states recorded to induce failure in these tests and the failed specimen characterization results. The stress states for both TC and TE tests were plotted with Mohr circles in shear stress  $\tau$  vs. normal stress  $\sigma_n$  plane



to derive the failure envelopes using best-fit curves (Figures 4.7a and 4.7b). The failure envelopes were fitted using a hyperbolic curve for the TC test (TC-fitting) and TE test (TE-fitting). The equations for each fitting are as follow:

$$\text{For TC with } R^2 = 0.99, \tau_{TC} = -\frac{23.96}{(\sigma_n + 4.91)} + 5.46 \quad (4.1a)$$

$$\text{For TE with } R^2 = 0.99, \tau_{TE} = -\frac{6.49}{(\sigma_n + 2.15)} + 3.86 \quad (4.1b)$$

Table 4.3 Summary of TE and TC test results, including minor confining pressure at failure  $\sigma_3$ , differential stress  $\sigma_1 - \sigma_3$ , measured failure plane angle  $\alpha_{exp}$ , and depth of fracture  $D_{frac}$ . The last two parameters were measured from the failed cylindrical specimens (see Figures 4.6 and 4.7).

Test type	Minor confining pressure at failure $\sigma_3$ (MPa)	Differential stress $\sigma_1 - \sigma_3$ (MPa)	Measured failure plane angle $\alpha_{exp}$ (°)	Depth of fracture $D_{frac}$ (mm)
TC	0	3.07	5-13°	-
TC	1.5	4.86	35-38°	-
TC	3.0	6.69	-	-
TE	0	3.96	0-5°	10-36
TE	0.77	4.63	10-20°	21-47
TE	1.98	5.89	25-30°	25-55

The key feature of the TE-fitting is the steeper angle approaching  $\sigma_n = 0$ , which is attributed to the higher failure stress  $\sigma_{f-UT}$  in comparison to  $\sigma_{f-UCT}$ . This is due to the intermediate confinement, which led to a biaxial stress state. The following Eqs. (4.2) were used to estimate the tangential friction angle  $\phi_t$  at each point on the failure envelope:

$$\tan \phi_t = \frac{d\sigma_n}{d\tau} \quad (4.2a)$$

$$\text{For TC, } \frac{d\sigma_n}{d\tau_{TC}} = \frac{23.96}{(\sigma_n + 4.91)^2} \quad (4.2b)$$

$$\text{For TE, } \frac{d\sigma_n}{d\tau_{TE}} = \frac{6.49}{(\sigma_n + 2.15)^2} \quad (4.2c)$$

where at  $\sigma_n = 0$ , estimated  $\phi_t$  for TC and TE are  $44.8^\circ$  and  $54.5^\circ$ , respectively. Using Kirsch's solution, the radial stress  $\sigma'_r$  was calculated for final loading boundary conditions. As  $\sigma_n$  progresses with radially distance from the tunnel, corresponding mobilized  $\phi_{t(m)}$  are plotted in Figure 4.7c.

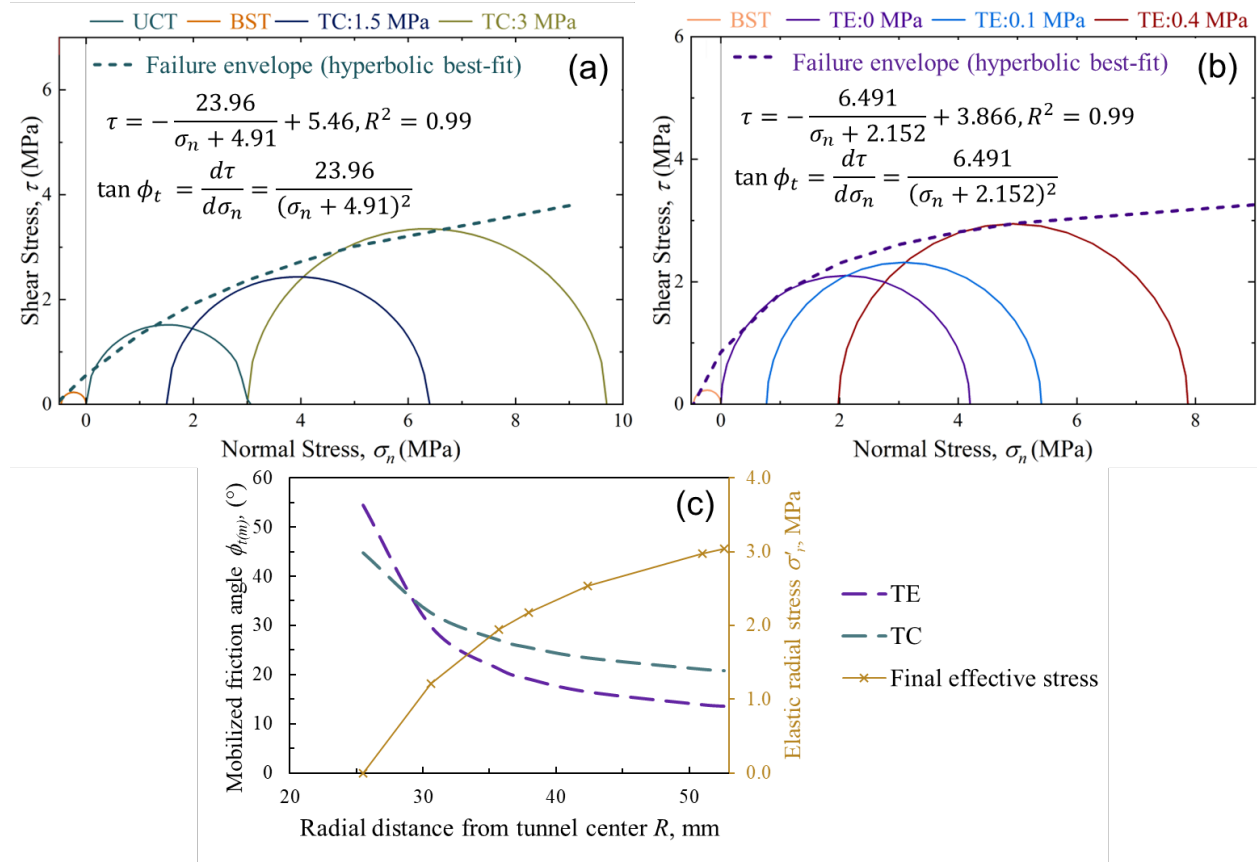


Figure 4.7 Derived failure envelopes from the best-fit hyperbolic curves, generated using data from: (a) BST and TC tests (TC-fitting) and (b) BST and TE tests (TE-fitting). (c) provides the mobilized friction angle  $\phi_{t(m)}$  resulting from varying normal stress further from the tunnel, which estimated using Kirsch's elastic solution.

Figure 4.8 shows the failed specimens from the TC tests under varying confining pressure. In Figure 4.8a, the specimen tested at 0 MPa confinement (UCT) shows sub-vertical failure planes with an angle  $\alpha_{exp}$  between  $5-13^\circ$ . The sub-vertical planes suggest an immediate and rapid stress release along axial dominant orientations, highlighted by dashed black lines indicating the approximated fracture planes. In contrast, Figure 4.8b displays a specimen tested at 1.5 MPa confinement, which exhibited a single, distinct shear plane. The transition from multiple conjugated shear fractures to a singular shear plane at higher confinement reflects the increase in ductility as confinement increases, indicating that TC tests with more confinement promote relatively more localized and controlled failure modes.

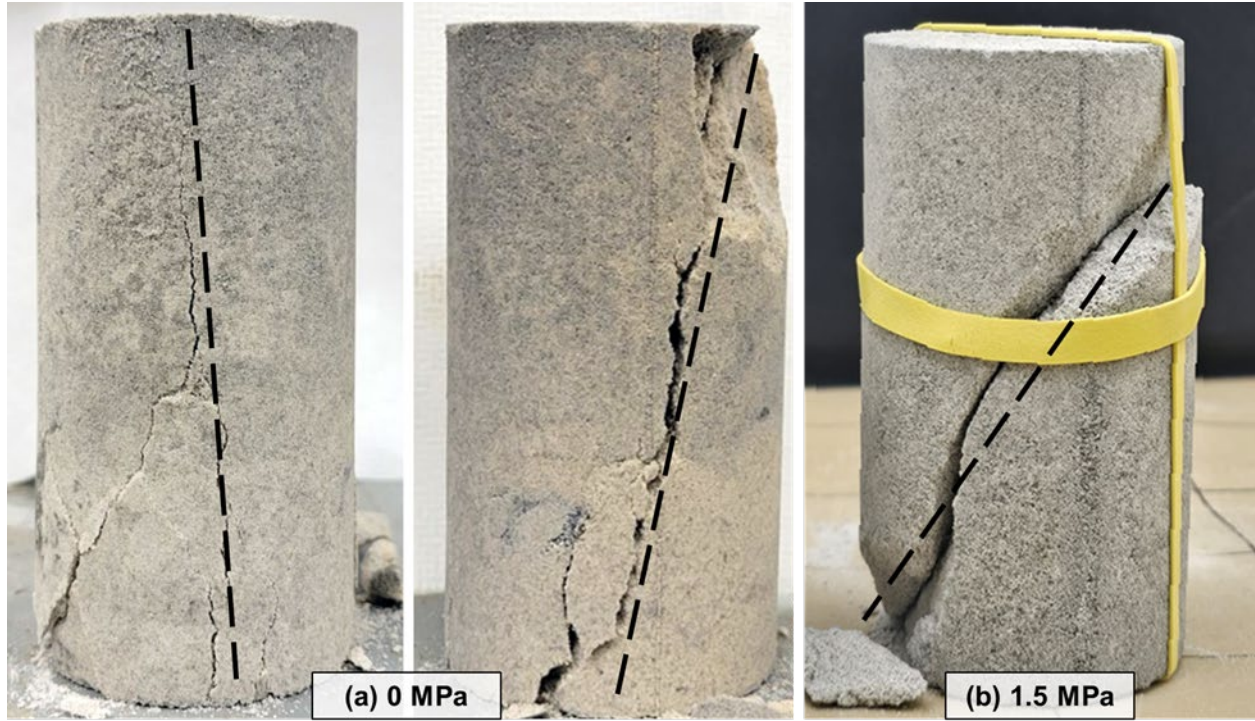


Figure 4.8 Failed specimens from (a) TC at 0 MPa confinement showing sub-parallel failure planes and (b) TC at 1.5 MPa confinement showing a distinct shear plane. Black dashed lines indicate an approximated fracture plane in the specimens.

Figure 4.9 presents the failed specimens from the TE tests with distinct fracture planes formed under different unloading conditions. The failure angle  $\alpha_{exp}$  for each specimen is highlighted with dashed black lines. This failure angle  $\alpha_{exp}$  corresponds to the theoretical failure plane angle or the spalling entry angle  $\alpha$  (as shown in Figure 4.6c). Dashed red arrows indicate the distance between the fracture plane and the unloaded side, denoted as  $D_{frac}$ . In Figure 4.9a, complete axial unloading to 0 MPa (UET) resulted in a smaller, angled fracture plane  $\alpha_{exp}$  ranging between  $3^\circ$  and  $5^\circ$ . TE tests with partial axial unloading, shown in Figures 4.9b and 4.9c, produced progressively larger  $\alpha_{exp}$  as summarized in Table 4.3. The observed failure modes were primarily shear—based on smooth failure surfaces along with observed fine debris. At  $\sigma_3 = 0$  which is typically assumed to demonstrate extensional failure mode, the specimens in Figure 4.9a show more of a mixed mode/hybrid based on conjugated shear displacement and sub-perpendicular to minor principal stress. Regarding the depth of fracture  $D_{frac}$ , increased confinement seems to pull the failure plane closer to the center point of the specimen. Compared to TC tests, the  $D_{frac}$  from TE tests demonstrate potential for spalling depth predictive capability in tunnels.

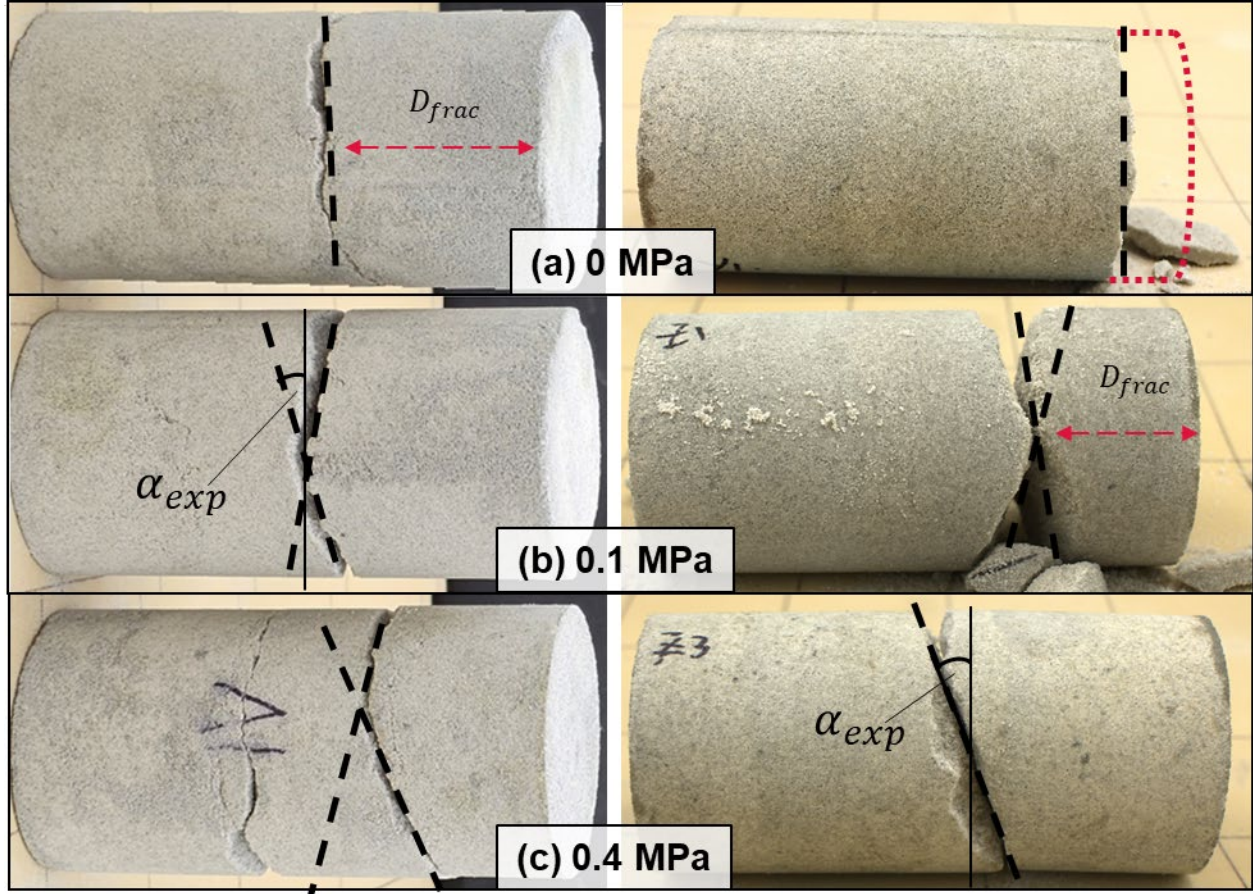


Figure 4.9 Failed specimens from TE tests indicating distinct fracture planes. The failure angle  $\alpha_{exp}$  measurements are highlighted by dashed black lines, while dashed red arrows represent the distance between the fracture plane and the unloaded side  $D_{frac}$ : (a) complete axial unloading to 0 MPa, (b) partial axial unloading to 0.1 MPa, and (c) partial axial unloading to 0.4 MPa.

#### 4.4.4 Spalling Strength Predictions

The element test results were applied to the tunnel model experiment, where four failure stresses  $\sigma_f$  were evaluated: (1) peak failure stress from UCT  $\sigma_{f-UCT}$ , (2) failure stress prediction at  $\sigma_3 = 0$  from TC fitting  $\sigma_{f-TC}$ , (3) peak failure stress from UET  $\sigma_{f-UET}$ , and (4) failure stress prediction at  $\sigma_3 = 0$  from TE fitting  $\sigma_{f-TE}$ . These failure stresses were compared with the tangential stress state at the tunnel wall during two key periods in the tunnel model test: spalling initiation and the final loading stage. Figure 4.10 presents a bar chart comparing the spalling strength  $\sigma_f$  with the tangential stresses observed during these critical periods  $\sigma_{\theta-initial}$  and  $\sigma_{\theta-final}$ . The tangential stresses at the visible spalling initiation and the final loading stages are 6.4 and 7.94 MPa, respectively (as shown in Table 4.2).

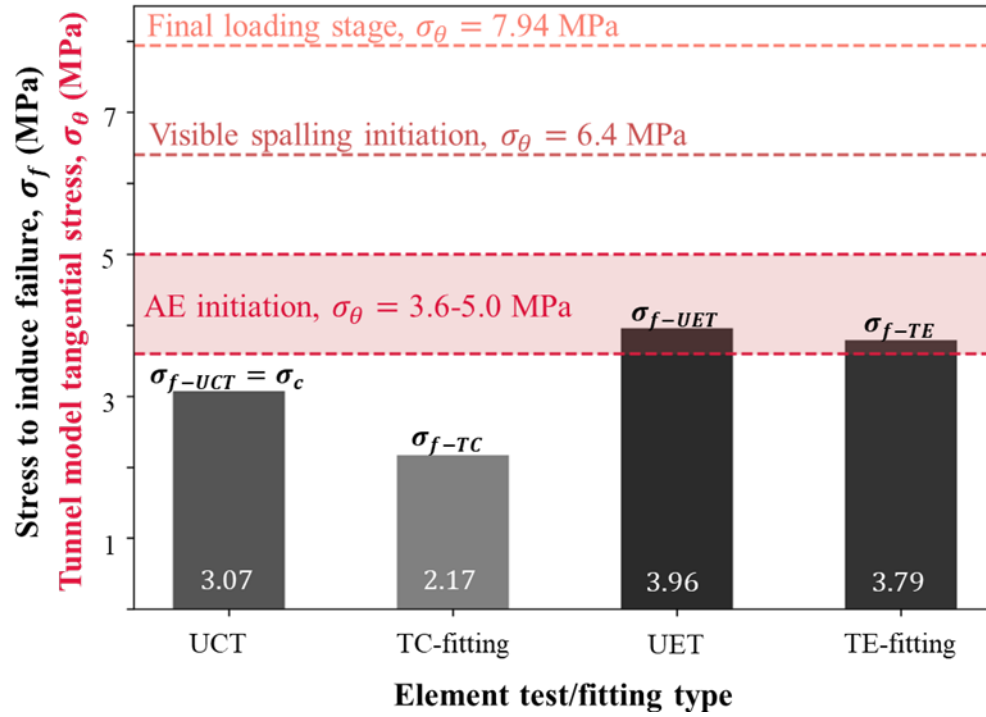


Figure 4.10 Comparison of experimental data and fitted points from cylindrical element tests (TC, TE, BST), along with tangential stress  $\sigma_\theta$  values from the tunnel model experiment at the visible spalling initiation and the final loading stage.

The visible spalling initiation was the primary reference point for comparison with the failure stresses. Notably, all predicted failure stresses are lower than the tangential stress state observed at visible spalling initiation. This lower prediction suggests the failure mechanisms could be triggered well intrinsically before spalling/failure becomes observable at the tunnel wall. An important observation is that the TE tests provide a higher strength bound, most likely due to the biaxial stress state and intermediate confinement. In contrast, the TC tests tend to underestimate the strength of the rock under three-dimensional conditions. Figure 4.11 presents AE data recorded during the loading stages, showing increased cracking intensity based on AE counts at both prediction points. The higher intensity near the TE prediction points suggests that TE results offer a more reliable basis for spalling initiation prediction.



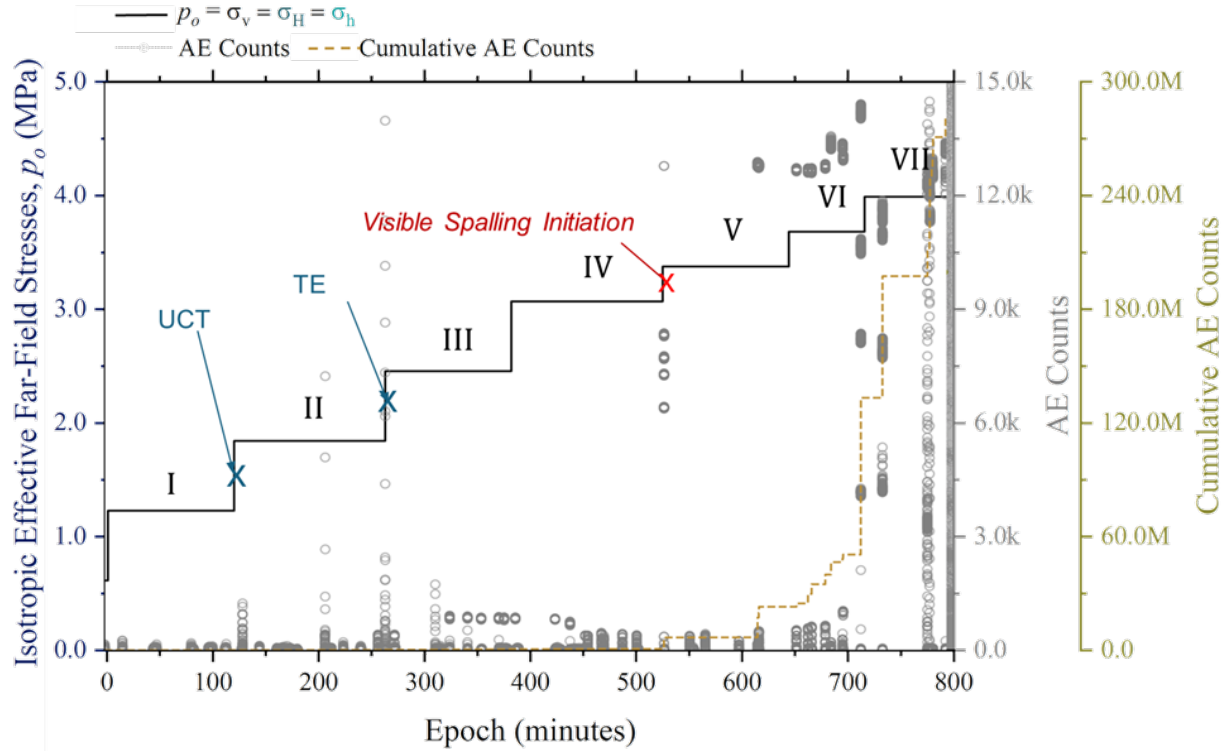


Figure 4.11 Applied stress conditions on the  $300 \times 300 \times 300 \text{ mm}^3$  specimen with a 51 mm circular opening and acoustic emission (AE) monitoring counts during the loading stage. The plot shows the isotropic effective far-field stresses ( $p_o, \sigma_v, \sigma_H, \sigma_h$ ), AE counts, and the cumulative AE counts from six channels. Using a two-dimensional elastic solution, UCT and TE prediction (blue cross marks) are close to loading stage I and II, respectively.

Regarding the final loading stage tangential stress, it was not intended to be directly compared with the failure stresses. Instead, this final state serves as a second reference point to assess the progress of stress change from spalling initiation. This difference is later used to compare with empirical spalling depth predictions (Section 4.4.5). The gap between visible spalling and the final loading stage is 1.54 MPa, approximately a 24% increase. Since spalling or fracturing is known to propagate under increasing stress until the rock is fully damaged and loses its load-bearing capacity, this increase is perceived to reflect the progression of damage in the rock mass near the tunnel wall.

#### 4.4.5 Depth of Spalling Predictions

To explore the predictive capability of the depth of fracture from cylindrical element tests  $D_{frac}$  in estimating the tunnel depth of spalling  $D_f$ , scaling factor analysis was first conducted. This analysis is based on the TE tests, where distinct and measurable  $D_{frac}$  values were observed during post-mortem investigation. An illustrative specimen at the tunnel boundary, with a cylinder diameter of 5 mm and height of 10 mm, was used to predict tunnel depth of spalling  $D_f$ . Scaling was applied using the empirical strength-scale relationship by Hoek and Brown (1980), as follows:

$$\frac{\sigma_{f-d}}{\sigma_{f-50}} = \left(\frac{50}{d}\right)^{0.18} \quad (4.3)$$

where  $d$  is the specimen diameter and  $\sigma_{f-d}$  is the failure stress for a cylindrical specimen of diameter  $d$ . Based on the results from TE test  $\sigma_{f-UET}$  where  $\sigma_3 = 0$ , the spalling strength  $\sigma_f$  for the 5 mm diameter specimen was found to be 1.52 times higher than that for the 50 mm diameter specimen. Assuming the extent of damage follows this scaling law, the  $D_{frac}$  from TE tests when  $\sigma_3 = 0$  MPa were adjusted. Initially reported as 10-36 mm (approximately 10-36% of the specimen length), the scaled values were reduced to 6.6-23.8% of the specimen length. When one multiplies these percentages by the illustrative specimen length (10 mm), the predicted fracture depth ranges between 0.66 to 2.38 mm from the tunnel wall. This calculation yields prediction values of  $D_{f-TE}$  that range from 26.16 to 27.88 mm. This result aligns with the observed tunnel model spalling depth  $D_f$  of 26.03 to 27.56 mm, suggesting that the scaling adjustment appropriately reflects the tunnel model spalling conditions.

The exclusion of  $D_{frac}$  data from TE test with higher axial confinement  $\sigma_3$  was made due to concerns about the fracture plane positioning with a higher axial load. The axial load in these cases was high enough to recompress the cylinder, causing the fracture plane to centralize at the center point of the specimen. Additionally, the absence of a sizeable spalling entry angle  $\alpha$  in the tunnel model indicates that the applied stress level may not have been sufficient to induce more extensive damage.

The TE test-based, scaled  $D_{frac}$  prediction and the tunnel model depth of spalling  $D_f$  (Table 4.2) were compared with the strength ratio empirical correlation (Diederichs, 2007; Martin et al., 1999). The correlation predicts the normalized depth of spalling to the tunnel radius  $D_f/R_T$ , based on the ratio of maximum tangential to compressive strength  $\sigma_\theta/\sigma_c$ . As noted in Section 4.4.1, the required stress to induce failure is denoted as  $\sigma_f$  for each test, which is then applied to the shear strength ratio of the  $x$ -axis. The original empirical criteria were developed for full-scale tunnels, indicating a damage progression line intersecting with the  $y$ -axis at 0.4. This value is referred to as the typical crack initiation level relative to the UCS  $\sigma_c$  (Diederichs, 2007). The 0.4 value may also correspond to a simple arithmetic relation involving Poisson's ratio and the compressive-to-tensile strength ratio (Barton and Shen, 2017).

By calculating the tangential stresses at both the spalling initiation and final loading stages, it was found that ratio  $\sigma_\theta/\sigma_f$  increased by 23.8%, as discussed in Section 4.4.4. Applying this same increase to the initial value of  $\sigma_\theta/\sigma_f = 0.4$  during the spalling initiation, the expected  $\sigma_\theta/\sigma_f$  at final loading stage is 0.49. Figure 4.12 presents the plotted results for the measured spalling depth from post-mortem investigation, primarily for the final loading stage. In contrast to the original empirical equation, the  $y$ -axis here represents the absolute depth of spalling failure  $D_f$  rather than the normalized depth relative to the tunnel radius  $D_f/R_T$ . The plotted range of  $D_{f-TE}$  data (26.16 - 27.88 mm) and  $D_f$  value (26.03 – 27.57

mm) align well with Martin's empirical prediction within the confidence interval limit. The failure state in the tunnel model is classified as minor spalling according to Diederichs et al. (2009).

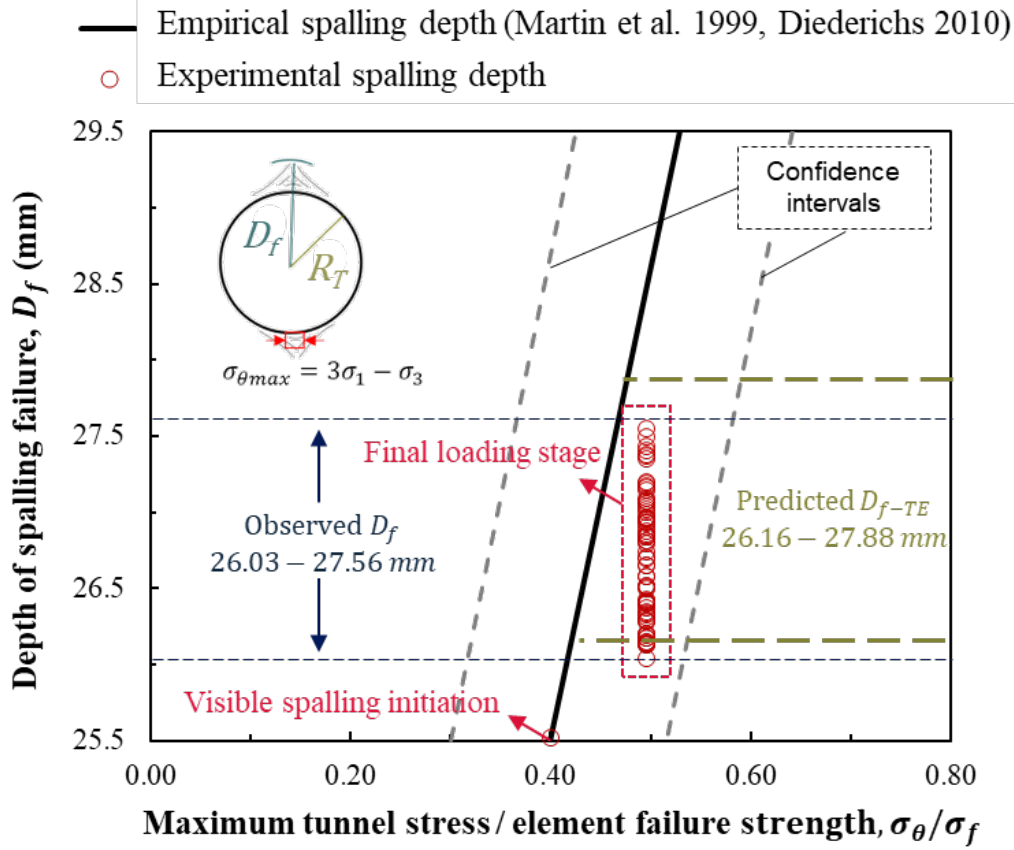


Figure 4.12 Depth of spalling  $D_f$  comparison from the laboratory-scale model with the predicted spalling depth from the TE test  $D_{f-TE}$  and empirical spalling depth correlations (after Martin et al. 1999 and Diederichs 2010). The y-axis shows the absolute spalling depth with  $R_T=25.52$  mm. In the original equation, the UCS  $\sigma_c$  is used in the x-axis, while in this study, it is represented with the element failure strength  $\sigma_f$ .

#### 4.4.6 Spalling Geometry Predictions

Test results suggest that the TE tests with  $\sigma_3 = 0$  produced fracture planes at significantly lower angles compared to UCTs, likely because of lateral compression. The estimated tangential friction angle  $\phi_t$  when  $\sigma_n = 0$ , derived from the best-fit TE failure envelope in Eqs. (4.1) and Figure 4.7, was higher than that derived from the best-fit TC failure envelope (Eqs. 4.2). Consequently, the theoretical fracture plane from the TE tests corresponds to a lower angle  $\alpha$ , approaching the high spalling initiation angle observed in the tunnel model experiment (Figure 4.3b). The radial stress  $\sigma_r$  at the tunnel wall, which is unloaded to zero due to tunneling, was more accurately simulated by the TE tests. In contrast,



conventional TC tests with their higher entry angles  $\alpha$  and lower friction angles  $\phi_t$  may overestimate both the spalling initiation and the extent of tunnel damage.

Theoretical logarithmic spiral (log-spiral) plastic slip lines prediction was performed on both TC and TE models using the tangential friction angle  $\phi_t$  from the best-fit failure envelopes in  $\tau$  vs.  $\sigma_n$  regime. The log-spiral slip lines, modeled as equiangular spirals, follow the equation (Heuer and Hendron, 1971):

$$\frac{r}{R_t} = e^{\pm \cot(45^\circ + \frac{\phi_t}{2})} \quad (4.4)$$

where the slip lines intersect the tunnel wall at an angle of  $\alpha = 45^\circ - \phi_t/2$ , like the theoretical failure angle in cylindrical element testing  $\alpha_{exp}$ . Figure 4.13a illustrates the log-spiral slip lines around the tunnel boundary, while Figures 4.13b and 4.13c depict the slip lines using tangential friction angle  $\phi_t$  from the best-fit TE and TC tests at  $\sigma_3 = 0$  (Figure 4.7). The slip lines are spaced at  $40^\circ$  intervals and mirrored symmetrically, forming a radially symmetric, nine-point geometry with  $D_1$  and  $D_2$  marking the first and second intersections. This configuration represents the spread and diffusion of damage under isotropic loading, consistent with tunnel model test results. Due to localized stress concentrations, fewer slip lines are expected for boundary conditions under anisotropic loading. The Python code to generate the log-spiral slip lines is available in the supplementary material.

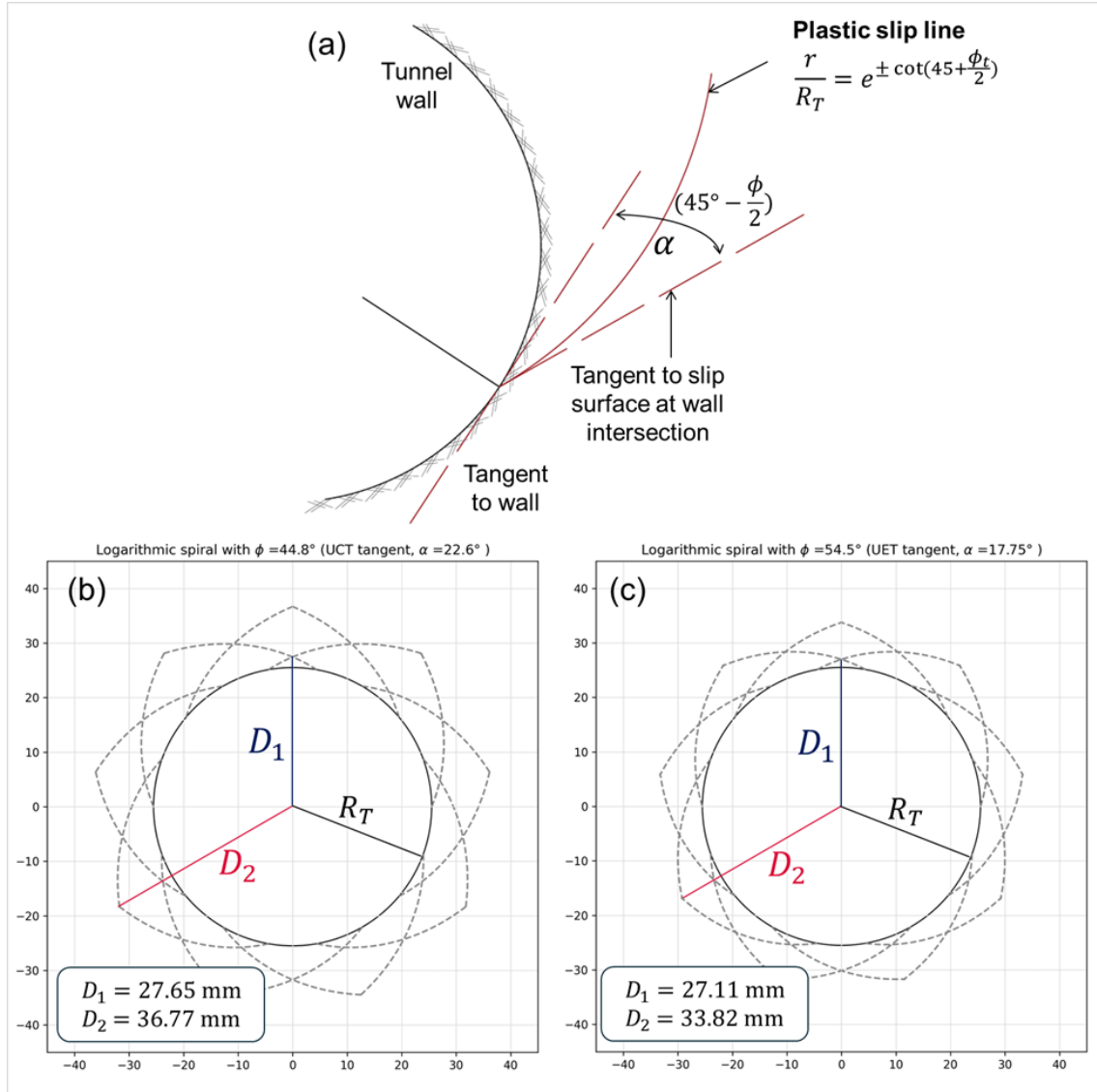


Figure 4.13 (a) Illustration of theoretical plastic slip lines (after Heuer and Hendron 1971) and developed equiangular log-spiral slip lines around the tunnel boundary with (a)  $\phi_{t-UCT} = 44.8^\circ$  from TC-fitting and (b)  $\phi_{t-UET} = 54.5^\circ$  from TE-fitting.

Figures 4.13b and 13c demonstrate that the damage extent is 8.7% greater with the lower friction angle (TC) compared to the higher friction angle (TE). The inverse relationship between the entry angle  $\alpha$  and friction angle  $\phi_t$  affects the progression of the symmetrical slip lines until they intersect. Figure 4.14 presents overlays of the developed theoretical log-spiral slip lines using  $\phi_t$ , applied to the tunnel model's 50 mm and 100 m advance half-axial cross-sections. Due to the nature of isotropic loading, predicting the exact location of tunnel damage is challenging. Once initiated, strain softening reduces load-bearing capacity, allowing damage to progress and become more pronounced than in other areas. This explains why the crown region in the half-axial sections exhibited more damage and resin infiltration than the invert.

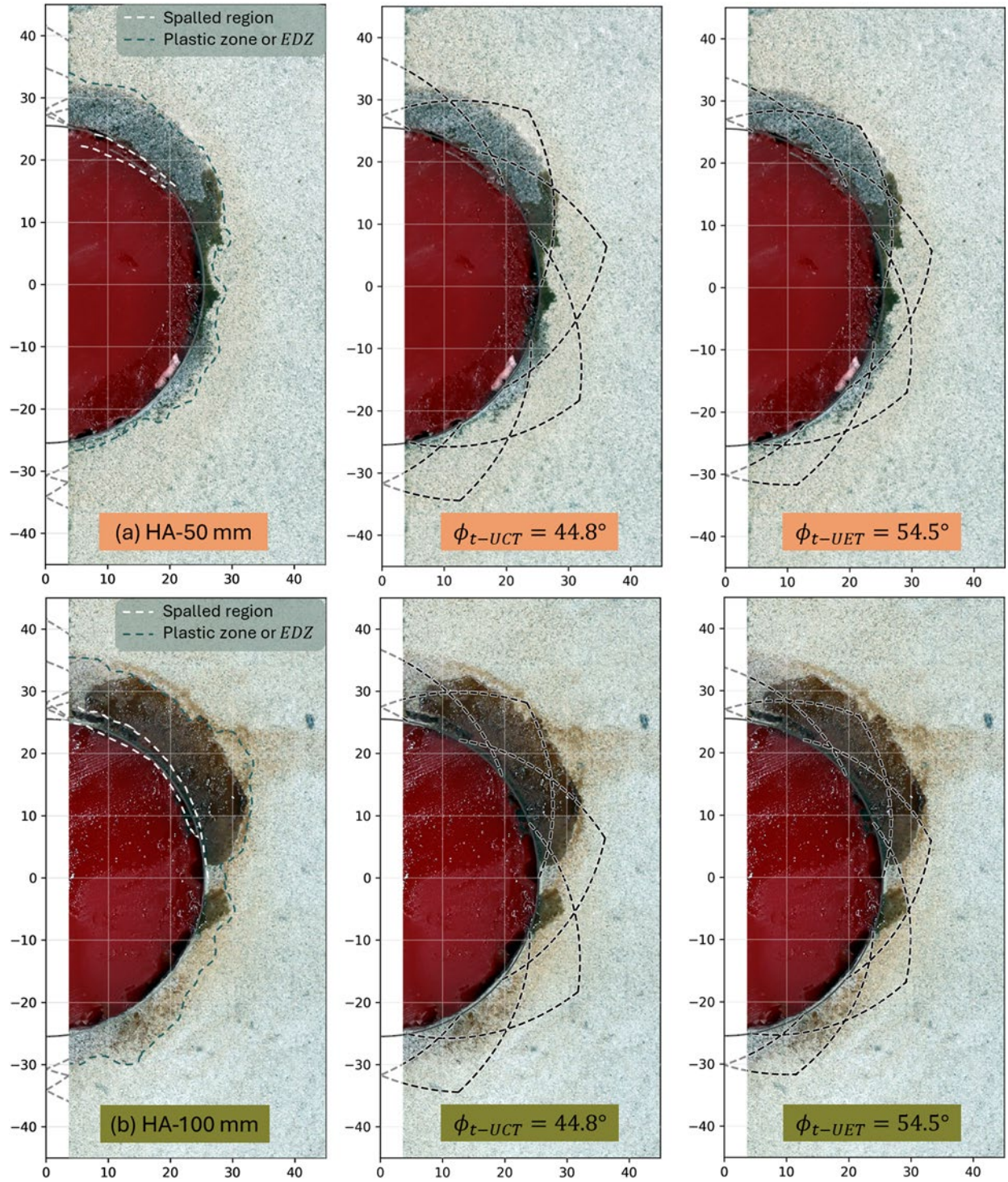


Figure 4.14 Equiangular log-spiral slip lines prediction (black dashed lines) with  $\phi_{t-UCT} = 44.8^\circ$  and  $\phi_{t-UET} = 54.5^\circ$ , overlaid on half-axial tunnel model cross-sections (after Wibisono et al. 2024). The distances from the portal to the section (tunnel advance) are (a) 50 mm and (b) 100 mm. The white and green dashed lines indicate the spalled region and plastic radius  $R_p$  in the original half-axial section. Axes units are in mm. (For interpretation of the references to color in this figure legend, the reader is referred to the Web version of this article.)

The log-spiral slip lines, based on tangential friction angle  $\phi_t$  at  $\sigma_n = 0$ , accurately captured the resin-infiltrated zone  $R_p$  or  $EDZ$  at a 100 mm and 50 mm tunnel depth for TC and TE, respectively. The increase in the tangential friction angle  $\phi_t$  is particularly important, as it provides a more realistic justification of the low entry angle  $\alpha$  at  $\sigma_3 = 0$ . These results suggest that the theoretical log-spiral slip lines with the input of tangential friction angle  $\sigma_t$  has the potential to predict the extent of  $R_p$  or  $EDZ$ . However, there are two caveats: (1) the method is restricted to isotropic loading conditions and (2) it assumes idealized, radially symmetric plastic slip lines (nine-point geometry), as the termination points of the log-spiral lines remain uncertain. While this approach shows the potential in predicting  $R_p$  or  $EDZ$ , it does not yield a sub-parallel fracture with  $\alpha$  less than  $10^\circ$ .

An alternative approach was then explored by developing log-spiral slip lines directly from TC and TE experimental results. Using the experimental entry angle  $\alpha_{exp}$  to estimate a higher friction angle for Eq. (4.4) provided predictions better aligned with the spalling geometry. Figure 4.15 presents overlays of the developed theoretical log-spiral slip lines using  $\alpha_{exp}$  on the half-axial cross-sections of the tunnel model. The TE experimental entry angle  $\alpha_{exp} = 5^\circ$  closely matched the spalling geometry in both the HA-50 mm and HA-100 mm sections. Nevertheless, the conventional TC test model overestimated the spalled region, predicting its extent nearly twofold.



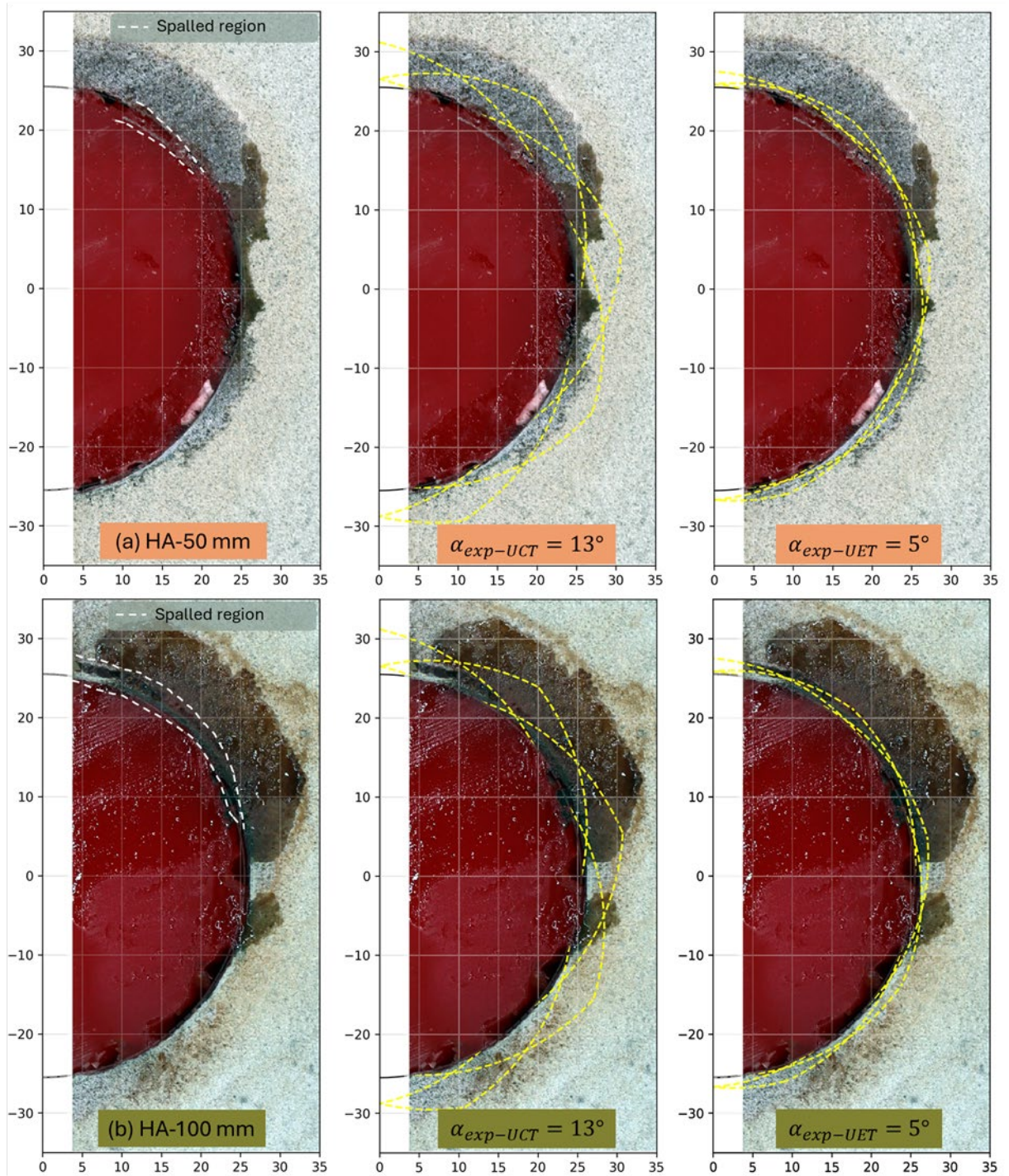


Figure 4.15 Equiangular log-spiral slip lines prediction (yellow dashed lines) with  $\alpha_{exp-UCT} = 13^\circ$  and  $\alpha_{exp-UET} = 5^\circ$ , overlaid on half-axial tunnel model cross-sections (after Wibisono et al. 2024). The distances from the portal to the section (tunnel advance) are as follows: (a) 50 mm and (b) 100 mm. The white dashed lines indicate the spalled region in the original half-axial section. Axes units are in mm. (For interpretation of the references to color in this figure legend, the reader is referred to the Web version of this article.)

#### 4.5 Implication to Tunnel Spalling Predictions

In the TE test at  $\sigma_1 = \sigma_2$ , failure stresses  $\sigma_f$  or spalling strengths were observed to be higher compared to the TC test (Table 4.3). In the test with  $\sigma_3 = 0$ , the failure stress  $\sigma_{f-UT}$  exceeded  $\sigma_{f-UCT}$  of mix O (3.07 MPa) by 29%. This finding is consistent with previous studies on other rock types. For instance, Ramsey and Chester (2004) found that the biaxial compressive strength of Carrara marble was 41.3% higher than its  $\sigma_c$  of 92 MPa. Bobich (2005) reported that Berea sandstone exhibited a 22.2% increase in biaxial compressive strength compared to its UCS of 79 MPa. The results suggest that the intermediate confinement enhances rock strength under confined conditions, as supported by Patel (2018) and further confirmed through confined Brazilian tests by Li and Ghassemi (2021). In the tunnel model test (Figure 4.10), the narrowing gap between the TE element strength  $\sigma_{f-TE}$  and the tangential stress  $\sigma_{\theta-initial}$  narrowed implies that intrinsic failure mechanisms may have been initiated earlier than visually detectable, supporting the need for further investigation. Future studies should assess spalling strength from element tests using with deeper analysis of AE data monitoring, particularly in tunnel models or borehole breakout tests. Comprehensive AE data analysis, as demonstrated by Ishida et al. (2017), Du et al. (2020), and Moradian et al. (2024), offers valuable insights into the intrinsic mechanisms by identifying cracking and damage progression stages in the rock under boundary stress changes.

The alignment between the depth of spalling from the tunnel model  $D_f$  and prediction values from TE test  $D_{f-TE}$  to the empirical spalling depth correlations demonstrate the potential to refine spalling extent predictions. This correspondence is robust at the immediate tunnel boundary, where  $\sigma_r = 0$ . The observed spalling in the experiment was sparse and shallow with a very small entry angle  $\alpha$ , indicating that the final load applied in the true-triaxial cell was insufficient to induce more pronounced fracturing and damage. Future studies should consider increasing the applied loads to further explore the limits of spalling prediction accuracy similar loading capacity to a weaker material yet exhibiting brittle response (Wibisono et al., 2023b).

The findings in Section 4.4.5-4.4.6 demonstrate that intermediate confinement stresses, particularly those parallel to the tunnel axis, influence brittle behavior and the angle of faulting. The minimal failure plane angle observed at the tunnel wall, where confinement is lowest, is consistent with findings from Zeng et al. (2019) on cylindrical sandstone specimens under TE conditions. Beyond the variation in failure plane angle  $\alpha_{exp}$ , the angle progression towards more radial confinement from the TE test in the model indicated the development of more pronounced shear fractures. With more confinement, the fracture plane angle  $\alpha_{exp}$  became more pronounced, indicating a transition toward more ductile behavior. This observation is consistent with the literature, which showed a transition from extensional to

conjugated shear fractures, further coupled with bulging under higher confinement (Nygård et al., 2006; Wong and Baud, 2012).

The mobilized friction angle  $\phi_{t(m)}$  in the tunnel model test (Figure 4.7c) further enhances the understanding of the failure surface extent. The V-shaped notch, typically observed under high anisotropic stress can be attributed to this transitional rock response, where multiple shear fractures intersect. This failure mode illustrates the differential response of the rock mass to tensile and shear mechanisms (Schoenball et al., 2014). While factors such as rock heterogeneity and fracture propagation may also contribute to spalling and damage prediction, this study with homogeneous brittle rock provides experimental evidence that brittle shear behavior can be triggered at shallow entry angles  $\alpha$ , leading to spalling and damage progression.

While Martin et al. (1994) found no evidence of tensile cracks during physical inspections of spalling development at the mine-by-experiment, Barton and Shen (2017) addressed through observation and numerical modeling that, whether in shallow or deep spalling, pure tensile spalling is unlikely. They found that shear fracturing is the dominant mechanism for deep spalling. In this study, very thin spalling with a steep angle measured from the minor principal stress direction in the tunnel model became physical evidence of shear-driven fractures and not extensional fractures. The steep angle may resemble extensional fractures, appearing perpendicular to  $\sigma_3$ , but it can also result from shear-induced dilation along the shear fracture surface, triggering the mobilization of friction angle (Gutierrez et al., 2023). Additionally, fracture morphology from the final tunnel profile (Figure 4.3b) and element tests at minimum confinement (Figures 4.8 and 4.9) showed fine debris, suggesting traces of shear failure dominance due to violent rupture (C. cheng Liu et al., 2020; Pratomo et al., 2024). This observation indicates that the classical brittle shear mechanism primarily drives spalling within homogeneous, massive rock under isotropic stress conditions.

#### 4.6 Summary and Conclusions

This investigation analyzed spalling failure in a brittle, isotropically loaded tunnel. The triaxial extension (TE) test with cylindrical specimens was introduced as a novel approach to better understand spalling mechanisms and damage extent. The new methodology to assess tunnel spalling introduced a new perspective in brittle failure prediction, incorporating three-dimensional stress considerations. Using conventional Hoek Cells, the TE test setup offered practical advantages while effectively capturing key parameters that conventional tests did not assess. These include (1) biaxial stress strength, (2) the depth of fracture  $D_{frac}$ , and (3) the failure plane angle  $\alpha_{exp}$ . These factors are fundamental to understanding brittle failure mechanisms in tunnels excavated through high-stress, massive rock masses with sparse jointing.

The simulated biaxial stress state required higher failure stresses than the more traditional two-dimensional representation from unconfined compression tests. The spalling initiation predicted by the TE

test approached the higher tangential stress state observed in the tunnel model, where spalling began visually. The closer alignment of TE test results, particularly with the support of AE data, offered stronger validation for spalling onset predictions. Moreover, the TE test results, combined with a scaling factor, offered predictive capability for spalling depth  $D_{f-TE}$  that matched the observed tunnel spalling depth  $D_f$ , with empirical correlations supporting these findings.

The TE test consistently yielded higher failure stresses than those from the triaxial compression (TC) test, particularly as it approached  $\sigma_n = 0$  that simulated tunnel boundary stress conditions. This resulted in steeper failure envelope gradient that explained the sparse, thin spalling observed in the tunnel model. The high tangential friction angle  $\phi_t$  theoretically demonstrated a lower theoretical shearing failure plane  $\alpha$ . The log-spiral theoretical slip line models were developed using TE and TC test parameters. The model with the TE test parameters allowed the predictions to align closely with the post-mortem investigation of the tunnel model, significantly enhancing the model's reliability. The TE test also showed a transition to more ductile behavior under partial unloading, reinforcing the role of confinement in fracture mode transitions and explaining the observed spalling pattern.

The use of log-spiral slip lines effectively modeled the plastic radius  $R_p$  or excavation damage zone *EDZ* with the derived tangential friction angles  $\phi_t$  from both TC and TE tests. However, the spalling profile at the tunnel model with minimum entry angles was best represented through log-spiral slip lines with the input of the experimental entry angle  $\alpha_{exp}$  from the TE test. These results demonstrated that spalling was predominantly driven by brittle shear behavior, challenging the assumption that tensile or extensional fracturing is the dominant mechanism. Instead, pronounced brittleness at low confinement  $\sigma_3$ , supported by the curved failure angles, reinforced this shear-driven nature of spalling.

These conclusions demonstrate that integrating empirical data from experimental modeling, such as the TE test, with large-scale tunnel models significantly improves spalling prediction. Incorporating TE test parameters into log-spiral analysis marks a substantial advancement in understanding spalling mechanisms. These findings offer valuable insights into tunnel design and mitigation strategies in brittle rock masses, providing a more comprehensive tool for addressing spalling challenges in high-stress conditions.

#### **4.7 Supporting Information**

Python codes for generating the log-spiral slip lines around the tunnel boundary are accessible at <https://github.com/mcdmans/brittle-slip-lines>



## CHAPTER 5 ROCKBURST ANALYSIS IN TUNNEL UNDER ANISOTROPIC LOADING BASED ON LARGE-SCALE TUNNEL MODEL EXPERIMENT AND TRIAXIAL EXTENSION TEST<sup>1</sup>

### 5.1 Abstract

Brittle failure in tunnel excavation progressively reduces the load-bearing capacity of the rock mass, often leading to violent rockburst failure. Detached rocks from the tunnel boundary can injure personnel and disrupt operations. However, the factors contributing to the extent of brittle failure damage and its progression, such as face support and confinement dependency, are not fully understood. This study investigates the rockburst progression of an unsupported tunnel excavated through a  $300 \times 300 \times 300 \text{ mm}^3$  cubical analog rock specimen. The tested material was an analog sedimentary rock designed to exhibit brittle behavior while maintaining low uniaxial compressive strength. This tunnel model experiment employed a true-triaxial cell and a mock miniature tunnel boring machine (TBM) apparatus to simulate realistic excavations. After the excavation, the 51 mm diameter tunnel was gradually loaded in anisotropic conditions to induce failure. The final failed tunnel profile was injected with resin before unloading and removing, allowing for digitized 3D reconstructions of the cross-section cuts to analyze damage evolution along the tunnel. Two key questions were addressed: (1) What mechanisms lead to brittle failure progression in the excavated tunnel model? (2) What are other contributing factors that affect the extent of damage? Our observations revealed distinct V-shaped notch failure patterns, initiated with localized spalling that led to rockburst. These patterns were characterized primarily by shear failure with mobilized fracturing angles further away from the tunnel wall, significantly triggered by the anisotropic stress state. A detailed examination of the localized failure zone identified face support and confinement as factors that influence the extent of damage. A series of triaxial compression (TC) and triaxial extension (TE) tests were performed to further explore the effects of confinement and unloading on brittle behavior near the tunnel wall. These loading paths are associated with the role of brittle-to-ductile response of the host rock in damage prediction and fracture angle mobilization, providing valuable insights to improve the understanding of brittle shear failure and fracturing and rockbursts in tunnels. A novel aspect of this study is the development of progressive Bézier curves to predict the successive progression of fracturing into the tunnel wall, leading to the creation of V-shaped dog-earing and rockbursts in tunnels. This study enhances understanding of brittle instabilities, contributing to safer design and improved risk management practices in rock engineering.

---

<sup>1</sup> This chapter will be submitted as a full journal paper for publication in an international peer-reviewed rock mechanics journal.

## 5.2 Introduction

Brittle spalling and rockbursts frequently occur as failure mechanisms in hard, massive rock, especially in deep underground excavations. When stress exceeds peak shear strength, brittle rock materials experience damage due to micro-cracking accumulation and faulting, leading to a strain-softening response (Alonso et al., 2003; Egger, 2000a). This response degrades the rock load-bearing capacity and reduces the effectiveness of the installed ground support (Primadiansyah et al., 2024). The spalling mechanism near the tunnel wall is generally recognized to initiate through extensional fracturing. This fracturing is oriented sub-parallel to the localized tangential stress. Also, spalling can progress either violently or nonviolently (Diederichs, 2007a; Martin and Christiansson, 2009). These fractures vary from surficial cracks to severe spalling, potentially leading to rock bursting (Alcaino-Olivares et al., 2024; Duan et al., 2019; Keneti and Sainsbury, 2020; Orllepp and Stacey, 1994; Su et al., 2023). The extent of brittle failure damage is associated with the highly damaged zone *HDZ*, within the excavation damage zones *EDZ* (Perras and Diederichs, 2016; Siren et al., 2015). These phenomena not only compromise the structural integrity of tunnels but also pose significant safety risks for personnel and construction equipment. Therefore, a deeper understanding is crucial for mitigating brittle instabilities.

Extensive laboratory and in-situ experimental investigations have been conducted on brittle failure (Feng et al., 2018; Gong et al., 2018; Haimson, 2007; Lee and Haimson, 1993; Qiu et al., 2018; Read and Martin, 1991; T. Siren et al., 2015a). While in-situ tests on large-scale structures are vital, laboratory-scale experiments are essential for efficiently understanding brittle failure mechanisms (Jacobsson et al., 2015; Lin et al., 2015). Figure 5.1 illustrates the rock mechanics testing methodology for modeling stress states adjacent to the underground excavation. The methodology includes various stress simulation attempts such as unconfined, biaxial, triaxial, and true-triaxial compression, highlighting the major, intermediate, and minor principal stresses applied to the specimen. Near the tunnel portal, radial and longitudinal stress at the tunnel wall is zero, leaving a state of unconfined compression. As the tunnel advances, radial stress remains zero while longitudinal stress is nonzero, resulting in a biaxial compression stress state (Cai, 2008). Notably, this biaxial compression state can be simulated using a triaxial extension test with a minor principal stress of zero. Behind the tunnel face, the stress state can be replicated with conventional triaxial compression (TC) tests or true-triaxial/polyaxial compression tests (Fairhurst and Hudson, 1999; Singh et al., 1998). The most advanced research introduces a circular tunnel into the true-triaxial cell to better simulate the rock stress state (Luo et al., 2020; Pan et al., 2020; Wibisono et al., 2024). In a tunnel model experiment, applied far-field stresses are denoted by  $\sigma_v$ ,  $\sigma_H$ , and  $\sigma_h$ . The direction of lateral stresses on a cubical specimen in a true-triaxial setup is interchangeable based on the stress magnitude arrangement ( $\sigma_H \geq \sigma_h$ ).

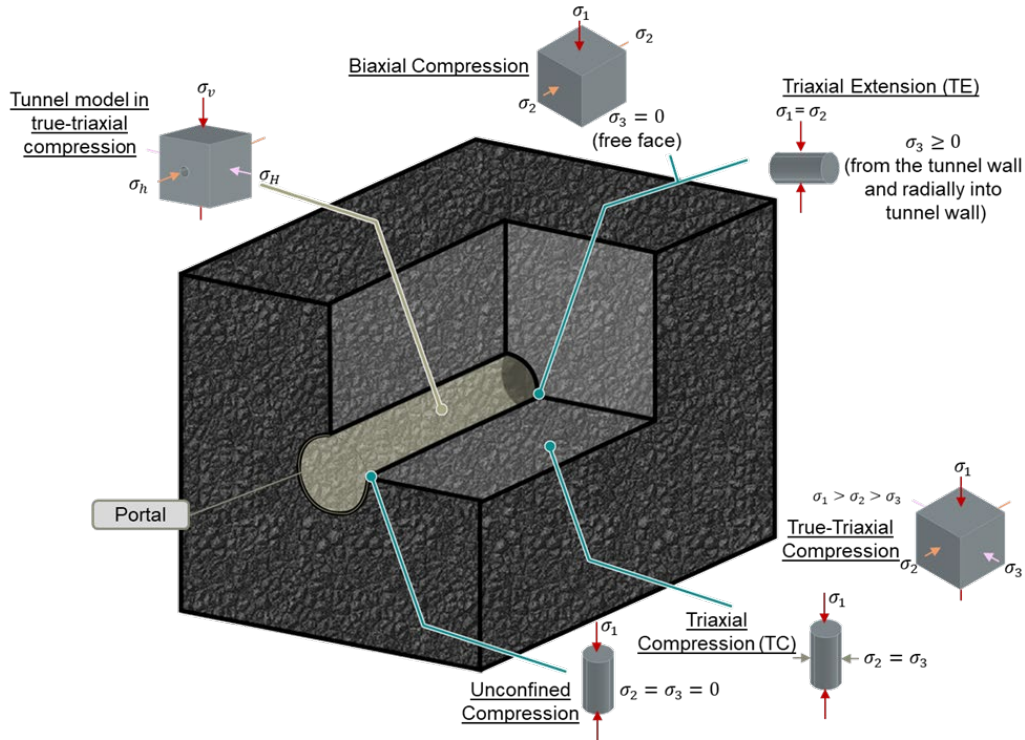


Figure 5.1 Rock mechanics testing methodology for modeling stress states adjacent to the underground excavation.  $\sigma_1$ ,  $\sigma_2$ , and  $\sigma_3$  represent the major, intermediate, and minor principal stresses applied to the specimen, respectively. In tunnel model experiments, applied far-field stresses are denoted by  $\sigma_v$ ,  $\sigma_H$ , and  $\sigma_h$ .

Table 5.1 summarizes laboratory studies of brittle failure around circular openings (also referred to as borehole breakout). These studies employed a true-triaxial cell and anisotropic loading conditions, with two opening categories: (1) those with prefabricated openings (Addis et al., 1990; Cheon et al., 2011; Gong et al., 2019, 2018; Lin et al., 2020; Rawlings et al., 1993) and (2) those with the capability to excavate while the rock is loaded (Gong et al., 2023b; Haimson, 2003; Haimson and Herrick, 1989; Herrick and Haimson, 1994; Lee and Haimson, 1993). Studies using the latter type typically feature opening diameters of  $\leq 25$  mm, requiring more load to induce failure (Martin et al., 1994). Cheon et al. (2011) and Gong et al. (2019) used diameters of 60 and 50 mm of prefabricated opening, respectively, but did not showcase abrupt brittle failure that poses high risks in excavation. Despite these extensive laboratory investigations (Table 5.1), predicting brittle failure remains challenging due to the complex anisotropic stress states encountered during tunneling with the evolving nature of brittle failure progression (Shen and Barton, 2018). Rock mass response to tensile and shear mechanisms also affects fracturing behavior (Sahara et al., 2017). These studies often overlook factors such as face support, detailed failure progression, and confinement dependency.

Table 5.1 Laboratory studies of spalling around circular openings with true-triaxial cells under anisotropic loading. The presentation order in the table is organized by the experiment type and chronological order.

Experiment type	Test principle	Specimen geometry and opening diameter $\phi$	Rock/analog rock properties	Observed failure mode	Reference
	<p><math>k_1 = 0.6 - 1</math> <math>k_2 = 0.4 - 1</math></p>	<p><math>400 \times 400 \times 400 \text{ mm}^3</math> and <math>500 \times 500 \times 500 \text{ mm}^3</math></p> <p><math>\phi = 50.8 \text{ mm}</math></p>	<p>Weak Sandstone (mortar); UCS = 0.5 MPa, E = 0.19 GPa.</p> <p>Gres des Vosges Sandstone; UCS = 24.4 MPa, E = 0.99 GPa.</p>	<p><math>k_1 = k_2 = 0.6</math></p> <p>Extensional and shear failure mechanism, identified with log-spiral formation around the opening.</p>	<p>Addis et al. (1990); Rawling et al. (1993)</p>
True-triaxial with prefabricated hole	<p><math>k_1 = 0.12 - 0.3</math> <math>k_2 = 0 - 0.09</math></p>	<p><math>290 \times 290 \times 290 \text{ mm}^3</math></p> <p><math>\phi = 60 \text{ mm}</math></p>	<p>Mortar; UCS = 38 MPa, E = 11.5 GPa, <math>\nu = 0.21</math></p>	<p>Visible macro cracks to heavy spalling, V-shaped notch.</p>	<p>Cheon et al. (2011)</p>
	<p>Case I: <math>\sigma_z &gt; \sigma_x &gt; \sigma_y</math> <math>\sigma_x = 0.28 - 0.5 \sigma_z</math> <math>\sigma_y = 0.28 - 0.43 \sigma_z</math></p> <p>Case II: <math>\sigma_z &gt; \sigma_y &gt; \sigma_x</math> <math>\sigma_y = 0.42 \sigma_z</math> <math>\sigma_x = 0.36 \sigma_z</math></p>	<p><math>100 \times 100 \times 100 \text{ mm}^3</math></p> <p><math>\phi = 50 \text{ mm}</math></p>	<p>Red Sandstone; UCS = 97.6 MPa, E = 18.6 GPa. Changtai Granite; UCS = 261 MPa</p>	<p>Case I <math>\sigma_z &gt; \sigma_x &gt; \sigma_y</math></p> <p>Spalling and burst/ejection of material, V-shaped notch</p>	<p>Gong et al (2018, 2019)</p>

Table 5.1 Continued.

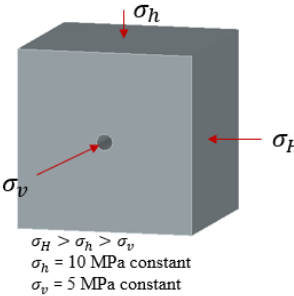
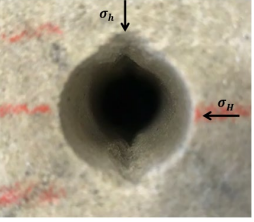
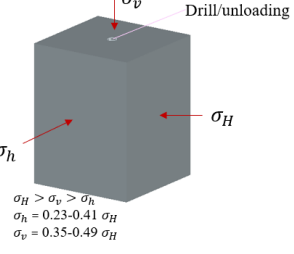
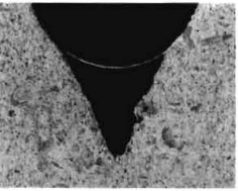
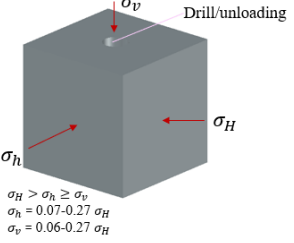
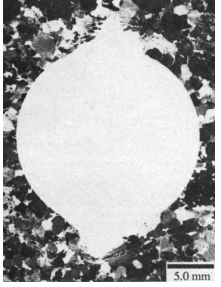
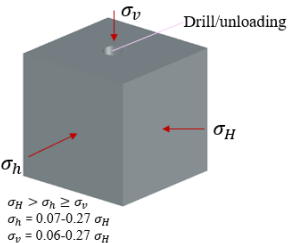
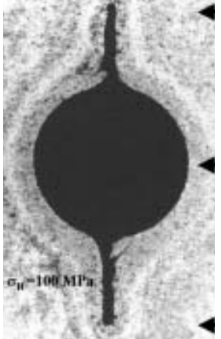
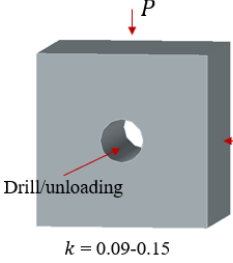
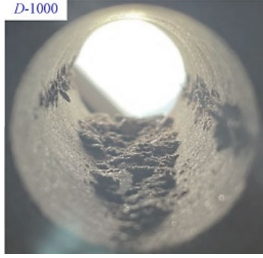
Experiment type	Test principle	Specimen geometry and opening diameter $\phi$	Rock/analog rock properties	Observed failure mode	Reference
True-triaxial with prefabricated hole	 <p> <math>\sigma_H &gt; \sigma_h &gt; \sigma_v</math>  <math>\sigma_h = 10 \text{ MPa constant}</math>  <math>\sigma_v = 5 \text{ MPa constant}</math> </p>	$120 \times 120 \times 120 \text{ mm}^3$ $\phi = 11 \text{ mm}$	Sandstone; UCS = 42.3 MPa, $E = 7.5 \text{ GPa}$	 <p>V-shaped notch breakout formation</p>	Lin et al. (2020)
	 <p> <math>\sigma_H &gt; \sigma_v &gt; \sigma_h</math>  <math>\sigma_h = 0.23-0.41 \sigma_H</math>  <math>\sigma_v = 0.35-0.49 \sigma_H</math> </p>	$130 \times 130 \times 170 \text{ mm}^3$ $130 \times 130 \times 180 \text{ mm}^3$ $\phi = 11 \text{ and } 20 \text{ mm}$	Alabama Limestone; UCS = 43 MPa $E = 28 \text{ GPa}$ $\nu = 0.27$	 <p>V-shaped notch breakout formation, episodic spalling</p>	Haimson and Herrick (1989); Herrick and Haimson (1994)
True-triaxial with capability to excavate	 <p> <math>\sigma_H &gt; \sigma_h &gt; \sigma_v</math>  <math>\sigma_h = 0.07-0.27 \sigma_H</math>  <math>\sigma_v = 0.06-0.27 \sigma_H</math> </p>	$100 \times 100 \times 100 \text{ mm}^3$ $\phi = 21 \text{ mm}$	Lac du Bonnet Granite; UCS = 167 MPa, $E = 55 \text{ GPa}$ , $\nu = 0.3$	 <p>Extensile cracks forming V-shaped notch breakout formation</p>	Lee and Haimson (1993)
	 <p> <math>\sigma_H &gt; \sigma_h &gt; \sigma_v</math>  <math>\sigma_h = 0.07-0.27 \sigma_H</math>  <math>\sigma_v = 0.06-0.27 \sigma_H</math> </p>	$150 \times 150 \times 230 \text{ mm}^3$ $\phi = 23 \text{ mm}$	Berea Sandstone; UCS = 22 – 53 MPa	 <p>Think and long tabular borehole breakouts, orthogonally to <math>\sigma_H</math></p>	Haimson (2003)

Table 5.1 Continued.

Experiment type	Test principle	Specimen geometry and opening diameter $\phi$	Rock/analog rock properties	Observed failure mode	Reference
True-triaxial with <b>capability to excavate</b>	 <p><math>P</math></p> <p><math>kl</math></p> <p>Drill/unloading</p> <p><math>k = 0.09-0.15</math></p>	$100 \times 100 \times 100 \text{ mm}^3$ $\phi = 25 \text{ mm}$	Red Sandstone; UCS = 97.6 MPa, E = 18.6 GPa	 <p>Spalling and burst/ejection of material, V-shaped notch</p>	Gong et al. (2023)

This study investigates these factors by developing reproducible analog material and a controlled tunnel model experiment to simulate brittle failure. The tunnel model experiment features a true-triaxial cell as the loading unit (Frash et al., 2014b) and a mock miniature tunnel boring machine (TBM) as the excavation unit (Arora et al., 2021). Acoustic emission (AE) monitoring tracks acoustic wave patterns during excavation and loading, detecting microfracture initiation and propagation to provide insight into damage progression within the specimen. This setup enables detailed analysis under well-controlled and instrumented conditions, which are difficult to achieve in field settings. Section 5.3 details the experimental framework in this study, including analog material characterization, tunnel model setup, and triaxial extension (TE) test. The TE test considers the biaxial stress state and unloading conditions to provide an additional biaxial peak shear strength. This TE peak shear strength and uniaxial compressive strength (UCS) results are evaluated using AE monitoring data and visible failure stress initiation from the tunnel model experiment. Tunnel damage and rockburst progression at the loading stage under anisotropic stress conditions ( $\sigma_v > \sigma_H > \sigma_h$ ) are documented. The study explores two critical discussions: (1) comparisons with well-established empirical correlations and analytical approaches and (2) the influence of face support, detailed failure progression, and confinement dependency. Ultimately, this investigation showcases enhanced insight into understanding rockburst progression mechanisms. Also, this study explores other factors that contribute to tunnel brittle failure through experimental evidence.



## 5.3 Experimental Frameworks

### 5.3.1 Material Characterization, Tunnel Model Experiment, and Loading Path

The tunnel model experiment consists of a circular excavation through a cubical analog material placed in a true-triaxial cell. These components are illustrated in Figure 5.2. as tunnel model experimental schematics. Additionally, acoustic emission (AE) transducers monitor seismic signals during excavation and loading stages. However, detailed AE analysis is beyond the scope of this study.

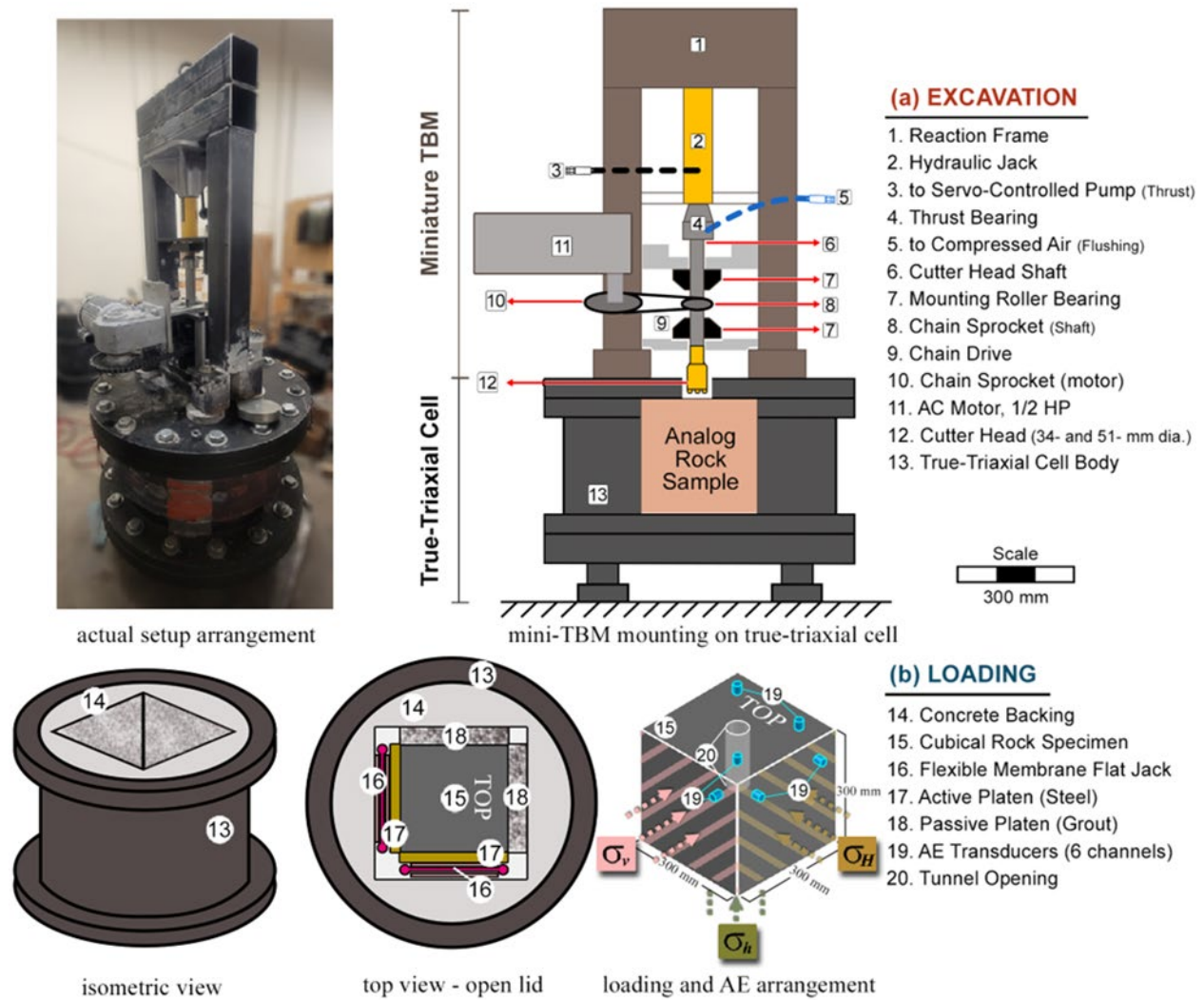


Figure 5.2 Tunnel model experimental schematics: (a) Photo and details of the excavation unit arrangement (after Arora et al. 2021); (b) Loading unit arrangement, including details of the AE transducer locations and applied loading illustration on the cubical specimen (Wibisono et al., 2023a).

The material was a developed analog sedimentary rock. All specimens were fabricated following the mortar mixing process, mimicking sedimentary rock with accurate control of the components. This effort ensures the reproducibility of the physical and mechanical properties across various specimen

geometries. The specimens primarily consist of Type I/II Portland cement, F-75 Ottawa sand, and water. Aside from the  $300 \times 300 \times 300 \text{ mm}^3$  cubical specimen for this tunnel model experiment, additional cylindrical specimens were prepared for material characterization. The characterization involved a series of physical properties, unconfined compression tests (UCT), Brazilian tension tests, and TC tests. Additionally, more cylindrical specimens were made for TE tests, which will be discussed further in Section 5.3.2.

Table 5.2 summarizes the mix design and properties of this weak analog rock. The analog rock mix design features a 4% cement content  $C$  (cement mass relative to total solid mass) and a 1.2 water-to-cement ratio  $w/cm$ . Several engineering treatments were applied to the standard analog sedimentary rock (Wibisono et al., 2022) to improve brittleness response while reducing the UCS. These weak and brittle characteristics minimize the need for a high-capacity loading apparatus, allowing geometry that facilitates direct tunnel observation. The engineering treatments include the following: (1) fine-uniformly graded aggregate usage, (2) cement content reduction, (3) curing time reduction, (4) air-entraining admixture usage, (5) saturation and freeze exposure, and (6) thermal exposure (Wibisono, 2024). This analog rock is categorized as "very weak," according to the International Society of Rock Mechanics (1978), with a UCS of 1.68 MPa. The improved analog rock has been evaluated to have more brittle responses with reduced UCS. Further details regarding the analog sedimentary rock development are documented in Wibisono and Gutierrez (forthcoming).

Table 5.2 Summary of mechanical properties of analog sedimentary rock mix and Mohr-Coulomb fitting parameters based on previous laboratory characterization results. The mix design, called Mix B, exhibits improved brittle response with reduced UCS (Wibisono, 2024).

Properties	Mix B
Uniaxial compressive strength, $\sigma_c$ (MPa)	1.68
Tangent Young's modulus, $E_{50}$ (GPa)	0.76
Brazilian splitting strength, $\sigma_t$ (MPa)	0.19
Poisson's ratio, $\nu$	0.22
Cohesion, $c$ (MPa)	0.28
Friction angle, $\phi$ ( $^\circ$ )	43.24

As shown in the loading schematics (Figure 5.2b), the true-triaxial cell uses flexible membrane flat jacks positioned behind stiff steel platen, enabling controlled loading on three active sides. This configuration allows the application of normal stresses up to 13 MPa on each active side, simulating the three far-field stresses,  $\sigma_v$ ,  $\sigma_H$ , and  $\sigma_h$  (Figure 5.2b). The opposing vertical sides functioned as passive boundaries, filled with rigid, high-strength, cast-in-place, non-shrink precision grout to ensure a tight fit between the specimen and the true-triaxial cell. A rigid steel platen with a central opening was placed on



the horizontal passive side, allowing excavation and tunnel observation. This setup required applying a 37% adjustment factor to the effective far-field stress calculation based on the reported stress distribution near the specimen's center (Frash et al., 2014). For example, the reading at the pressure transducer of 8.0 MPa gives the effective far-field stress of 2.96 MPa. Removing the true-triaxial cell steel top lid facilitates specimen placement to the true-triaxial cell. With the steel top lid in place, hydraulic lines for loading schematics and acoustic emission cables are routed through a 63 mm circular opening. The steel top lid also features a 75 mm diameter central opening for excavation and tunnel observation access.

Integrating the true-triaxial cell with a miniature TBM enables scale-model experiments to assess responses during tunnel excavation. This excavation process replicates actual excavation under true-triaxial stress conditions in a cubical rock specimen (Figure 5.2a). The tunnel in this study is excavated vertically to reach the geometric center of the specimen. Two diameters of the excavation unit are available with the 34- and 51-mm diameter tungsten-carbide-button-bit cutter head that is mounted on a hollow drilling rod (Figure 5.3a). The excavation unit is driven by thrust and torque units. All units are assembled into a reaction frame that holds the entire system to form the excavation schematics (Figure 5.2a). The thrust unit includes a hydraulic jack, syringe pump setup, and a thrust bearing. A control program, DIscO (Dynamic Teledyne Isco D-series Syringe Pump Control), developed in LabVIEW, logs the volume and flow rate of hydraulic fluid from and to the pump (Frash, 2016). The excavation face pressure is set in a continuous constant pressure (CCP) mode. The torque unit is powered by a constant-speed AC motor equipped with two chain sprocket gears and a chain. The hollow drilling rod attached to the excavation unit is designed to facilitate debris removal from the tunnel face with a compressed air connection (Figure 5.2a). The excavation with the 51 mm diameter cutter head leaves a clearance gap of approximately 124 mm—about five times the tunnel radius—between the tunnel wall and the specimen boundary. This clearance is optimized through several trials to minimize the impact of boundary confinement on the tunnel excavation face. Further details regarding the miniature TBM configuration are documented in Arora et al. (2021).

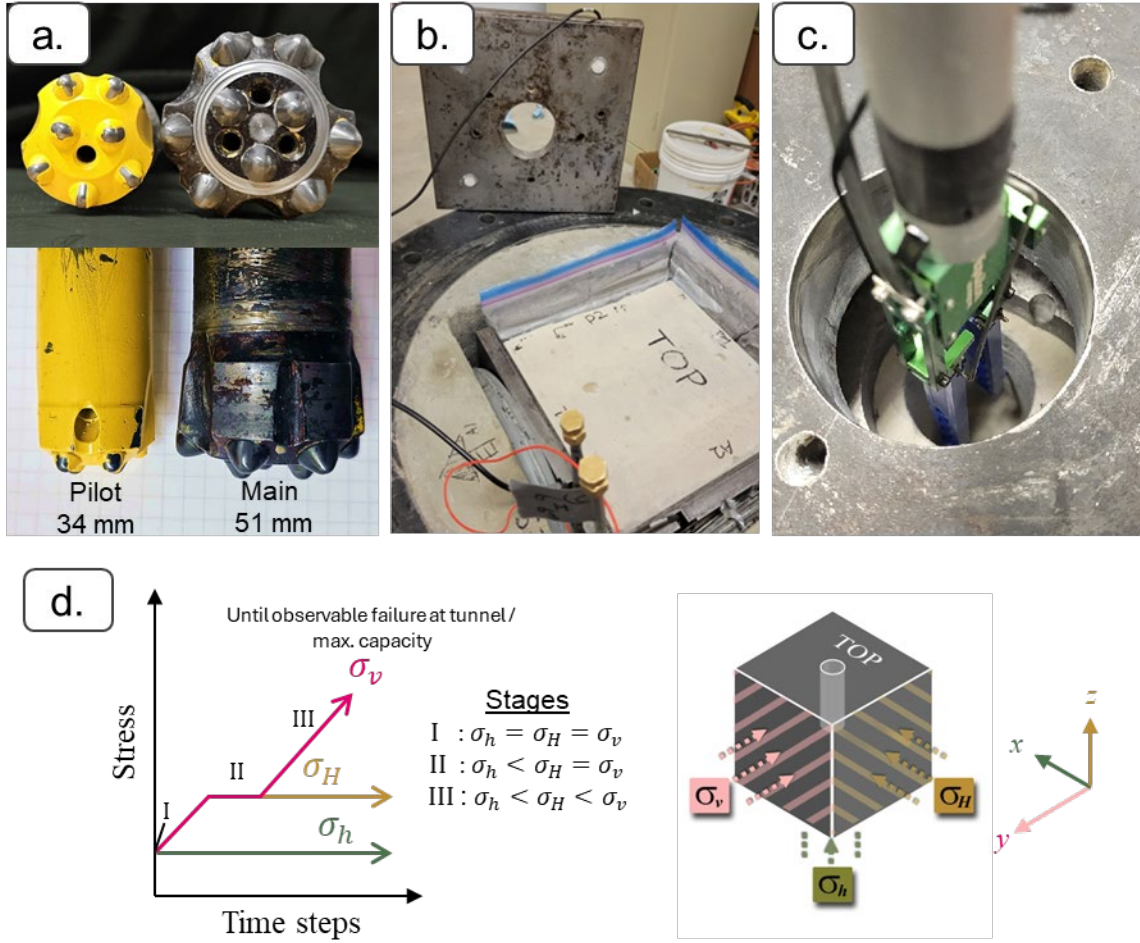


Figure 5.3 Tunnel model experiment with true-triaxial cell and miniature-TBM: (a) two excavation heads for pilot and main tunnel excavation, (b) specimen, loading unit, and AE transducers assembly, (c) tunnel profile measurement using digital borehole caliper, and (d) loading path plan. Of note, the least far-field stress  $\sigma_h$  is applied parallel to the tunnel axis.

The tunnel model experiment involves four primary stages: (1) assembling, (2) excavating, (3) loading, and (4) preserving deformation. First, the cubical analog specimen was placed inside the true-triaxial cell with active and passive loading units, steel platens, and AE transducers (Figure 5.3b). The steel top lid of the true-triaxial cell was then placed before connecting all the jacks to the hydraulic pumps and mounting the miniature TBM. The specimen is initially loaded (isotropic, 0.6 MPa) to ensure it remains in position. The excavation stage commenced as the excavation head contacted and rotated to the rock specimen. The thrust pressure of 0.6 MPa was maintained for the miniature TBM to match with isotropic loading. Once approximately half of the specimen length (150 mm) was excavated, the miniature TBM was dismantled. This dismantling process allowed enough time for the rock specimen to stabilize regarding AE signals before transitioning to the loading stage (Wibisono et al., 2023a). A digital borehole caliper (Figure 5.3c) was used to measure the diameter of the excavated tunnel profile at three different

advances: near the portal, halfway, and near the face. Measurements were taken from springlines and crown to tunnel invert. These six values were then averaged to obtain the general diameter of the tunnel. Due to the configuration of the setup, the measurements for this diameter can only be performed after the excavation and loading stages.

As depicted in Figure 5.3d, the loading stage involved several steps. The specimen was monotonically loaded in compression under isotropic conditions ( $\sigma_v = \sigma_H = \sigma_h$ ), until the preset  $\sigma_h$  level was reached. Subsequently,  $\sigma_h$  was held constant while  $\sigma_v$  and  $\sigma_H$  were monotonically increased until the predetermined  $\sigma_H$  was achieved. Finally, lateral stresses  $\sigma_h$  and  $\sigma_H$  were maintained at constant levels, and vertical stress  $\sigma_v$  was monotonically increased. This monotonic loading was stopped until a significant failure was observed, or the maximum capacity of the loading was reached. In this study, the  $\sigma_h$  was applied parallel to the tunnel axis, where both  $\sigma_v$  and  $\sigma_H$  were applied in a plane normal to the tunnel axis. Before unloading, the tunnel was cleaned from the ejected debris, photographed for failed tunnel documentation, and injected with epoxy resin to preserve its structure. After the resin had solidified, the specimen was unloaded by releasing pressure from the three hydraulic jacks. The specimen was then recovered by removing the steel top lid for further investigation.

Acoustic emission (AE) signals were recorded using a six-channel acquisition system provided by MISTRAS, operated via AEwin software to monitor the damage. The experiment employed six WSA-30 AE transducers with an operating frequency range of 100–1000 kHz and a resonance frequency of 125 kHz (MISTRAS Group, 2013). The transducers were positioned on three sides of the rock specimen to capture AE events (Figure 5.2b). The setup enabled the detection of elastic waves from microcracking, which provided crucial insights into the progression of internal damage (Hampton et al., 2018; Lockner, 1993). As in the UCT, the damage initially occurred internally, beginning with crack closure, followed by crack initiation, the onset of strain localization, crack damage, and post-peak responses (Hoek and Martin, 2014). The recorded seismic waveforms were amplified by 40 dB, and a 35 dB threshold was applied to filter out environmental and mechanical noise, ensuring signal clarity. Although AE was also monitored during the excavation, allowing further analysis as in Gautam et al. (2023) and Moradian et al. (2024), AE analysis in this study focuses solely on the loading stage. In this investigation, AE parameters such as event count and cumulative count were used to quantify cracking activity during each loading stage. Wibisono and Gutierrez (forthcoming) present a detailed analysis of AE parametric data from the loading stage, exploring potential precursors to the onset of spalling.

### 5.3.2 Laboratory Tests for Prediction Points of Spalling Initiation

In the context of a two-dimensional tunnel under plane stress conditions, the failure stress state at the tunnel boundary is represented by the UCT scenario. Radial stress signifies the minor principal stress ( $\sigma_r = \sigma_3 = 0$ ), while tangential stress serves as the maximum principal stress ( $\sigma_\theta = \sigma_1 > 0$ ). These stresses induce

tunnel wall yielding and lead to failure if the stress state exceeds the Mohr-Coulomb failure envelope of the rock that defined as:

$$\sigma_{1f} = K_p \cdot \sigma_{3f} + 2c \cdot \sqrt{K_p} \quad (5.1a)$$

$$K_p = \frac{1 + \sin \phi}{1 - \sin \phi} \quad (5.1b)$$

With internal support pressure  $p_i = 0$ , observation at the tunnel wall ( $R_T = R$ ) where  $\sigma_r = \sigma_3 = 0$  and  $\sigma_{1f} = \sigma_{\theta f-UCT}$ , Eq. (5.1a) simplifies to:

$$\sigma_{\theta f-UCT} = 2c\sqrt{K_p} \quad (5.2)$$

This expression yields the theoretical UCS according to the Mohr-Coulomb failure criterion.

Unlike two-dimensional analysis, in-situ tunnel boundaries have a more complex stress state (Figures 5.1 and 5.4b). The three-dimensional effect and stress rotation near the tunnel boundary affect fracturing conditions, as exemplified by the cases of tunnel instability (e.g., the mine-by-experiment V-notch spalling, slabbing failure) (Martin and Chandler, 1994). A growing trend in academic research is the consideration of three-dimensional confinement, which affects fracturing (Al-Ajmi and Zimmerman, 2005; Rahjoo, 2019; Saceanu et al., 2022). For instance, lateral stress transformation into longitudinal stress  $\sigma_z$  (intermediate confinement) in polar coordinates contributes to the biaxial stress state at the tunnel boundary. This stress state is characterized by  $\sigma_r = 0$  and  $\sigma_\theta, \sigma_z \neq 0$  (Cai, 2008).

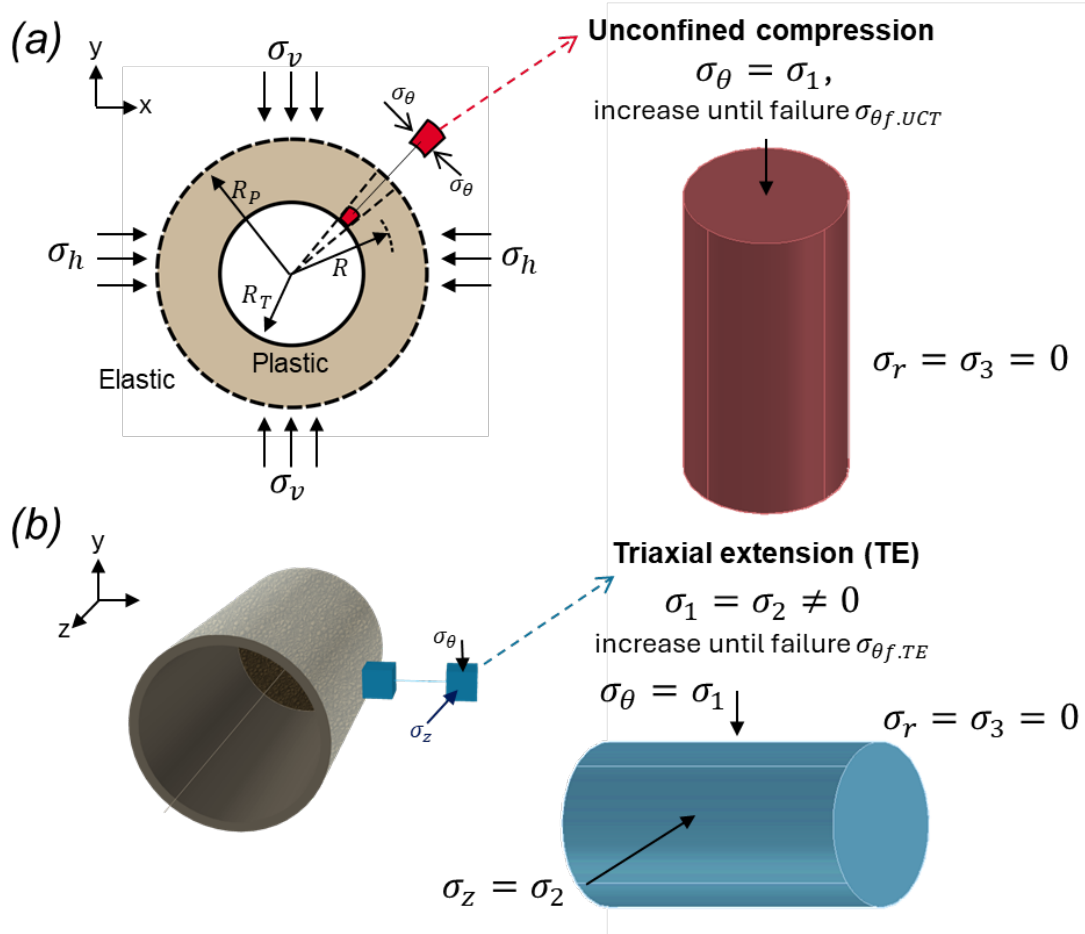


Figure 5.4 Simulation of stress states at the tunnel boundary during excavation-induced unloading using cylindrical laboratory tests: (a) two-dimensional consideration using UCT and (b) three-dimensional consideration using triaxial extension (TE) test.

The TE test is proposed to investigate the biaxial stress state at the tunnel boundary. This test uses a conventional triaxial chamber (Hoek cell) with an axial unloading scheme. This approach allows the simulation of the encountered stress path around the wall of the tunnel model experiment (Section 5.3.1). A small wall segment is modeled as a horizontally placed cylindrical specimen. Figure 5.4b illustrates this concept, applying the major and intermediate principal stresses,  $\sigma_1$  and  $\sigma_2$  through lateral confinement on the specimen. The stress configuration in TC ( $\sigma_1 > \sigma_2 = \sigma_3$ ) is conceptually modified into TE ( $\sigma_1 = \sigma_2 > \sigma_3$ ). The axial loading and unloading to the specimen are displacement-controlled compression platen, applying minor principal stress  $\sigma_3$ . The same dual Teledyne Isco 65DM syringe pump setup in the tunnel model experiment is used to apply confinement to the Hoek cell, programmed using the DIsc software (Frash, 2016). This software allows data logging and controlling the connected syringe pumps. The software has two different modes for fluid injection—constant pressure and constant flow—which will be discussed in the test procedure.

The TE test involves the following steps:

- 1) Isotropic loading of the specimen within the triaxial chamber until the designated stress condition is achieved (e.g.,  $p_0 = 0.5 \cdot \sigma_c$ ). For this, the control of the Isco pump uses the constant pressure mode to reach the designated stress state, along with the pressure transducer reading from the axial compression platen.
- 2) Unloading the axial plate to simulate  $\sigma_r = 0$  for biaxial stress state condition or a certain loading level to simulate the stress state away into the tunnel wall (e.g.,  $\sigma_3 = 0.2 \cdot \sigma_c$ ).
- 3) Increasing lateral confinement pressure ( $\sigma_1$  and  $\sigma_2$ ) to simulate the tangential and longitudinal stresses ( $\sigma_\theta$  and  $\sigma_z$ ) at the tunnel wall until failure is observed. The control of the Isco pump uses the constant flow rate mode. This mode allows hydraulic oil injections into the confinement chamber at a decided flow rate until a significant pressure drop indicates specimen failure.
- 4) Noting the peak confinement as the required stress to induce failure or the TE peak shear strength  $\sigma_{\theta f-UNET}$  for unconfined extension test (UNET) for  $\sigma_3 = \sigma_r = 0$  or  $\sigma_{\theta f-TE}$  for  $\sigma_3 = \sigma_r \neq 0$ .

However, this state-of-the-art approach has limitations; for instance, the identical confinement state of  $\sigma_1 = \sigma_2$  does not accurately reflect the stress conditions at the tunnel wall. Additionally, the unloading rate is fixed and needs to be manually adjusted to match varying stress states. The axial loading apparatus, being a displacement-controlled compression machine, cannot be programmed to maintain constant loading. Consequently, during step (3), where axial unloading does not proceed to full release, the pressure transducer at the top loading platen records an increase in load as the specimen dilates due to increased confinement ( $\sigma_1 = \sigma_2$ ). This reactive force, as a generated tensile force  $-\sigma_3$ , is then reapplied to the specimen and acts again as the minor principal stress. Documentation of this reactive force is essential in observing the stress path and developing a reliable failure envelope.

## **5.4 Results**

### **5.4.1 Excavation Process, Tunnel Geometry, Loading Path, and Acoustic Emission Counts**

Two excavations were performed using 34- and 51-mm excavation heads, corresponding to the pilot and main tunnels. Consequently, both mounting and dismounting of the miniature TBM were performed twice. This approach aimed to investigate a potential size effect within this experiment and to determine if pilot excavation could reduce the likelihood of brittle failure instabilities. Pilot tunnel excavation achieved a 75 mm advance over approximately 33 minutes.

The loading for the excavated pilot tunnel was partial, primarily intended to record acoustic emission (AE) data. This decision not to load the pilot tunnel until failure was budgetary. The maximum

effective far-field stresses applied to the pilot tunnel were 1.2, 0.9, 0.6 MPa ( $\sigma_v$ ,  $\sigma_H$ , and  $\sigma_h$ ). According to the two-dimensional closed-form elastic solution for a circular tunnel,  $\sigma_\theta = 3\sigma_v - \sigma_H$ , this stress state of failure initiation gives a maximum  $\sigma_\theta$  at the tunnel boundary of 2.7 MPa. The tunnel did not exhibit any observable failure but showed yielding, which was measured using the digital borehole caliper. The average diameter before the loading was 34.85 mm, which converged to 34.22 mm (1.81% deformation) after loading. The tunnel was then unloaded to initial isotropic loading (0.6 MPa) before excavating the main tunnel.

Main tunnel excavation took 43 minutes at a designated TBM thrust pressure of 0.6 MPa to achieve a 142 mm advance. The excavation time was faster for the first 75 mm since part of the excavation had been accomplished with the pilot tunnel excavation. Unlike the partial loading for tunnel pilot, the excavated main tunnel was loaded until significant failure was observed (Figure 5.3d). Figure 5.5 presents the effective far-field stress to time, superimposed by the AE counts and cumulative AE counts throughout the loading stage. The data presented extends up to 12 minutes, during which the maximum effective far-field stresses were applied ( $\sigma_v = 3.9$  MPa). At the failure initiation (mm:ss = 4:35), the effective far-field stresses were 1.6, 1.2, and 0.6 MPa ( $\sigma_v$ ,  $\sigma_H$ , and  $\sigma_h$ ). Using the same elastic solution, this stress state at the onset of visual spalling gives the maximum  $\sigma_\theta$  of 3.6 MPa at the tunnel boundary.

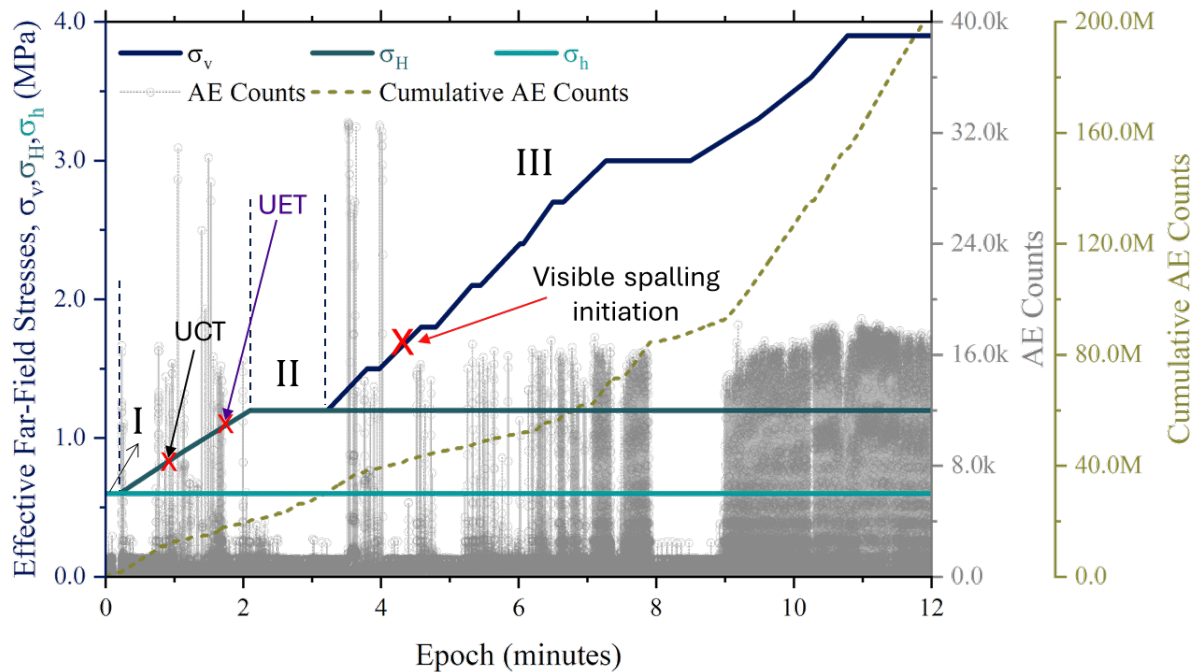


Figure 5.5 Applied stress conditions on the  $300 \times 300 \times 300$  mm<sup>3</sup> specimen with a 51 mm circular opening and acoustic emission (AE) monitoring counts during the loading stage. The plot shows the effective far-field stresses ( $\sigma_v$ ,  $\sigma_H$ ,  $\sigma_h$ ) and the cumulative AE counts from all channels, with the red cross marking the point of visible spalling initiation. The loading stages are marked with Roman numerals, as shown in the plot. (For interpretation of the references to color in this figure legend, the reader is referred to the Web version of this article.)

The average main tunnel diameter before the loading stage was 51.47 mm. However, the post-loading measurement with a digital borehole caliper was not performed due to the V-notch shaped generation and catastrophic failure at the final loading stage.

#### **5.4.2 V-Notch Spalling Generation throughout Time during Loading, Final Deducted Damage Zones**

Spalling generation documentation was taken outside of the tunnel portal using a UHD 60FPS video recorder. Time stamps were synchronized with AE recording and effective far-field stress, establishing a global time reference for the loading stage (denoted by mm:ss). At certain intervals, video frames were extracted to capture the progression of brittle failure in areas with concentrated tangential stress—particularly at the tunnel springlines. Figure 5.6a presents the video frames, denoted with anisotropic loading stress level  $k$  where  $k = \sigma_v / \sigma_H$ . The initial grain ejection occurred at  $k=1.45$  with timestamp 04:35, followed by relatively larger ejected grains from the springline near the marked "x1". Further brittle failure progression at "x1" was initially obscured due to the integrity of the portal until  $k=2.75$  with time stamp 06:35. This collapsing portal is shown at the lower end of the figure as fracturing dislocated the "x1" mark towards the opening. However, between the  $k=1.45$  and  $k=2.75$ , slabs and shear debris (fine grains) were observed flowing into the tunnel more aggressively and violently.

Figure 5.6b shows the final failure of tunnel with "x1" mark still visible before the tunnel was cleaned up of ejected debris (Figure 5.6c). The cleaned tunnel shows that the major damage occurred at the springline with extended damage in the crown section near the portal (left handside). The final tunnel failure profile that had been injected with resin becomes the only recoverable specimen, as shown in Figure 5.6d.



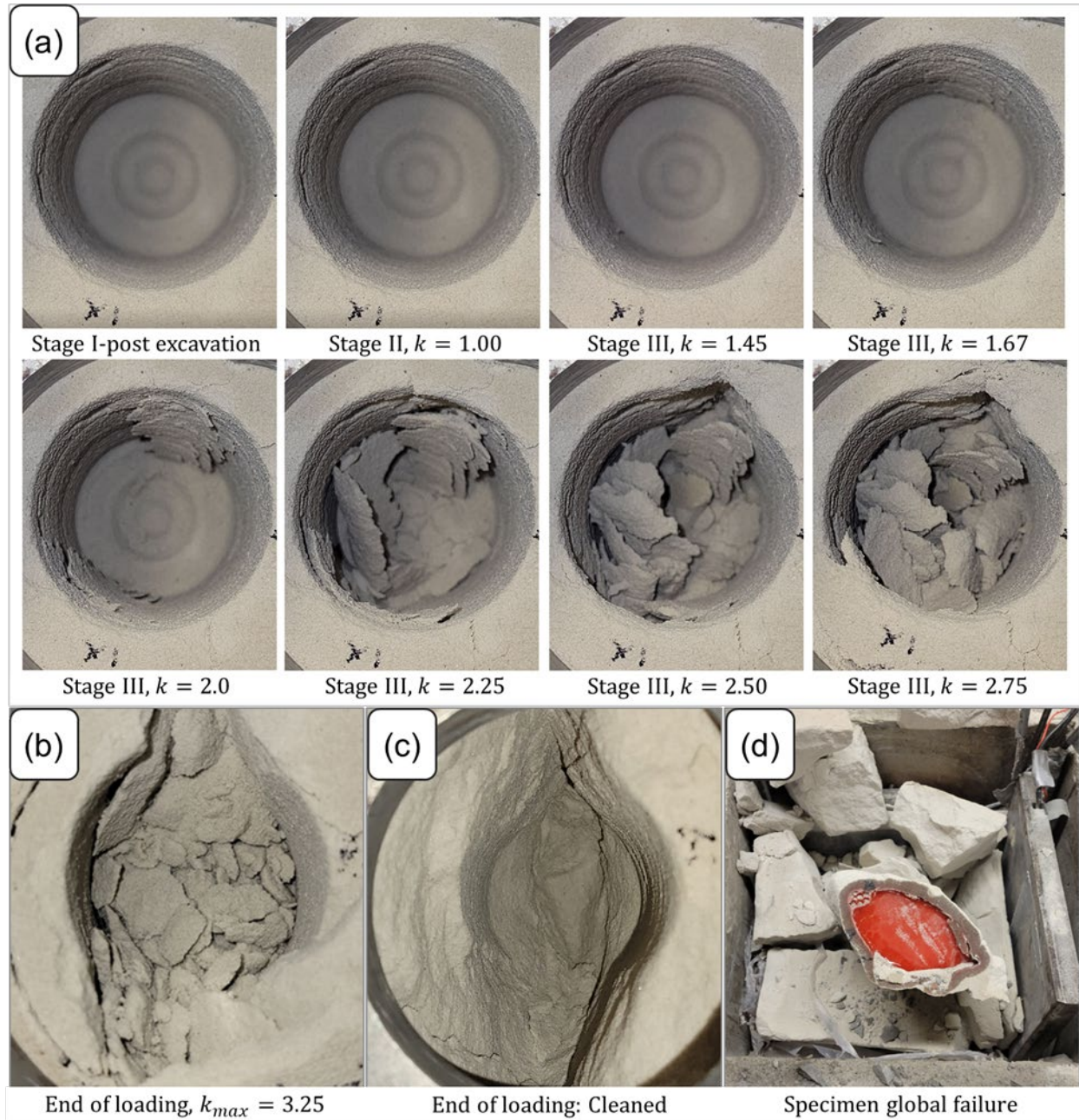


Figure 5.6 (a) Progression of spalling failure throughout the loading stage with increasing anisotropy  $k = \sigma_v/\sigma_H$ , (b) final failure of the tunnel before cleanup, (c) final failure of the tunnel after cleanup, and (d) specimen recovery process showing the complete failure of the cubical specimen.

The recovered specimen was cut to approximately 30 mm wide to observe the final tunnel failure profile. Seven cross-section cuts, marked with Roman numerals (I-VII), were photographed as shown in Figure 5.7. Four cut parts were macro-photographed to detail the damage, denoted with A, B, C, and D, respectively. Resin infiltration in the rock indicated both a highly damaged zone *HDZ* and an excavation damage zone *EDZ*. The *HDZ* appeared as a dark-colored zone due to resin bonding, indicating high macro-fracture intensity. Most of the *HDZ* had spalled and were manually removed.

On the other hand, the *EDZ* showed less discoloration with observed cracks, likely due to localized plastic damage. Some *EDZ* were separated from the recovered specimen, and some were lost during cutting. The damage zone shown in A demonstrated a partially fractured wall where two distinct angles (later referred to as the exit angle  $\omega_n$  in Section 5.5—Brittle failure geometry) formed and increased with distance from the tunnel. Macro-photograph B showed three distinct layers: resin, *HDZ*, and *EDZ*. Lastly, log-spiral fractures were observed in C and D, highlighting the complex failure mechanism in brittle failure progression.

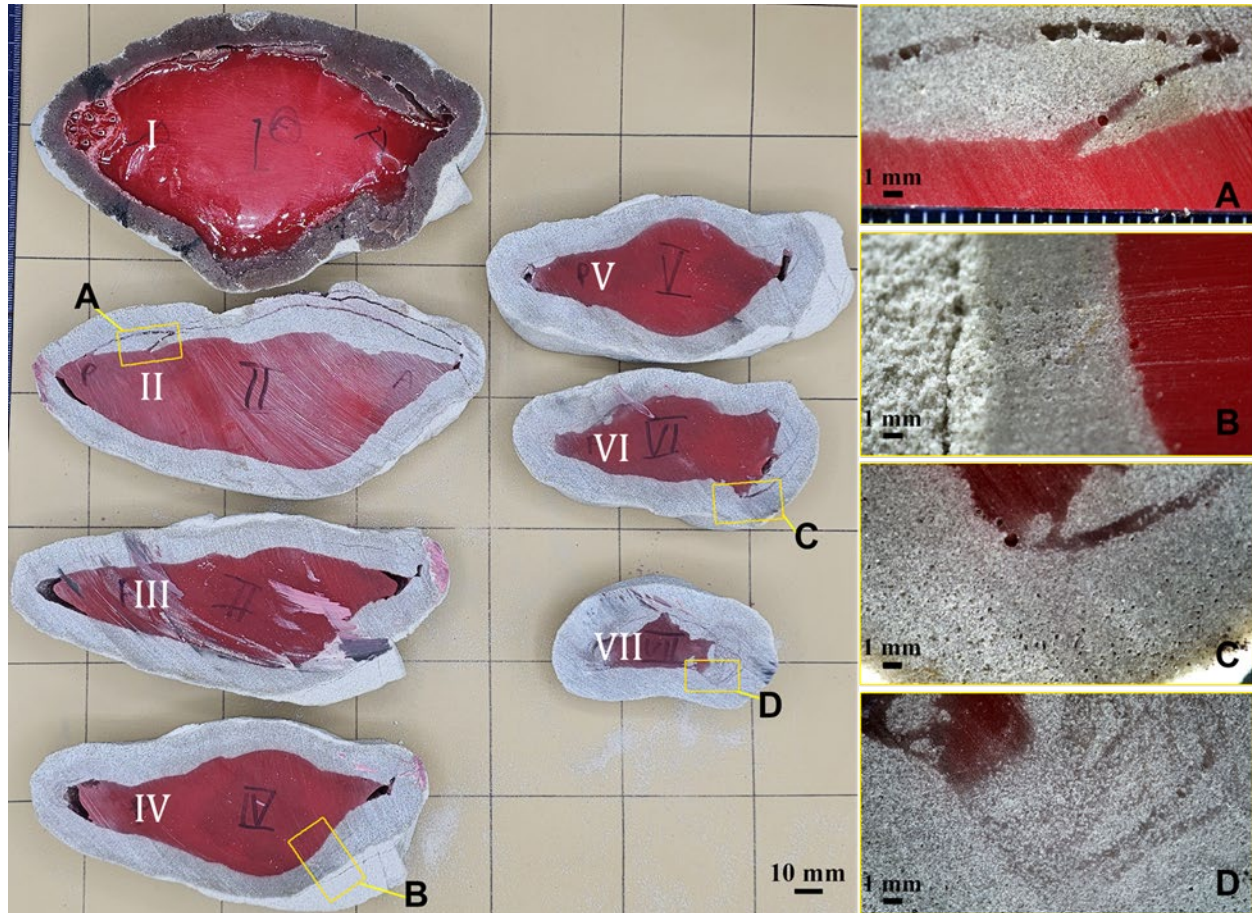


Figure 5.7 Cross-section cuts from recovered specimen with roman numeral markings, with four macro-photographed denoted with A, B, C, and D. Red color indicates the solidified resin that was injected into the failed tunnel profile before unloading.

Figure 5.8 shows the digitized cross-section cuts into 3D space, illustrating the extent of damage throughout the tunnel. In this figure, the yellow points represent the digitized tunnel profile from the photographs, while the light red mesh represents the interpolated surface between the measured points. The excavated main tunnel is displayed in Figures 5.8b and 5.8c, with light grey shade for pre- and post-loading comparison. The solidified resin helped to capture the failed tunnel profile on each cross-section



cut. The longitudinal distances of cuts I-V from the initial tunnel face were 142, 106.8, 82.9, 54.6, and 25.6 mm, respectively, with cuts VI and VII extending beyond the initial tunnel face.

This diverging, tabular V-shaped failed profile indicates that the extent of damage decreases towards the tunnel face. For cross-section cuts V-VII, the damage appears significantly smaller than the excavated main tunnel, particularly for cuts VI and VII, which likely occurred due to the tunnel face profile not being fully flat. The tapered end from the main excavation head (Figure 5.3a) left the face with an undulating inner section, which also failed during the loading stage. Additionally, these cuts confirmed that the failed geometry of both springlines was different in size.

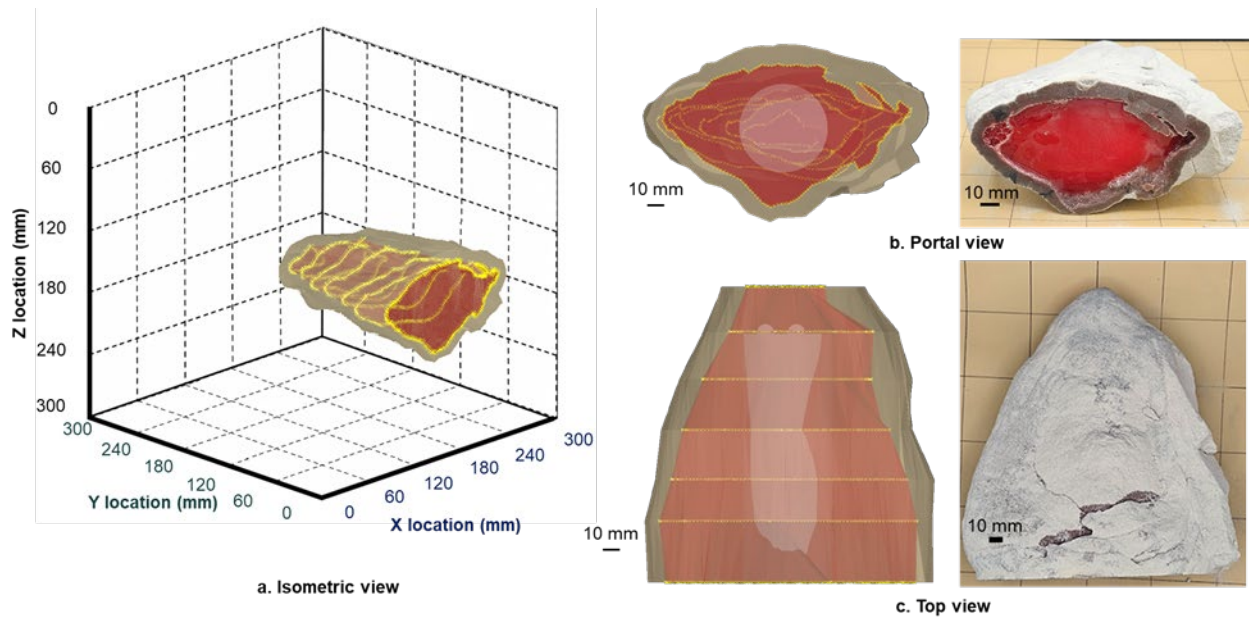


Figure 5.8 Failed tunnel specimen from cross-section cuts digitization: (a) isometric view, (b) portal view, and (c) top view. Yellow cross marks represent the digitization of actual fracture locations from the images in Figure 5.7. The light red surface represents the interpolated spline between these points to illustrate the final tunnel profile. The brown surface is digitized from the recovered failed specimen. In (b) and (c), the white highlights indicate the initial main tunnel profile, with the actual recovered specimen shown adjacent to the digitized representation.

#### 5.4.3 Analog Rock Failure Envelopes

Failure envelopes were best fitted from two sets of laboratory tests (TC and TE), along with the Brazilian splitting strength  $\sigma_t$ . For the TC test, the four confinement levels were 0 (UCT), 0.6, 0.75, and 1 MPa, while for TE, the confinement levels were 0 (UET), 0.1, and 0.3 MPa. Although the confinement levels for TE were considered small, they were designed as the initial load, which increased as lateral compression progressed (as explained in Section 5.3.2.). Table 5.3 outlines the differential stresses that

induce failure during these tests and the corresponding characterization of the failed specimen. Figure 5.9 provides the failed specimens and their measurement parameters  $\alpha_{exp}$  and  $D_{frac}$ .

Table 5.3 Summary of TE and TC test results, including minor confining pressure at failure  $\sigma_3$ , differential stress  $\sigma_1 - \sigma_3$ , measured failure plane angle  $\alpha_{exp}$ , and depth of fracture  $D_{frac}$ . The last two parameters were measured from the failed cylindrical specimens (see Figures 5.6 and 5.7).

Test type	Minor confining pressure at failure $\sigma_3$ (MPa)	Differential stress $\sigma_1 - \sigma_3$ (MPa)	Measured failure plane angle $\alpha_{exp}$ (°)	Depth of fracture $D_{frac}$ (mm)
TC	0	1.68	0-5°	-
TC	0.6	3.88	10-15°	-
TC	0.75	5.72	15-22°	-
TC	1.0	7.1	20-25°	-
TE	0	2.09	3-5°	6-18
TE	0.68	5.03	5-7°	35-40
TE	0.83	6.15	5-10°	40-45
TE	1.0	7.23	8-10°	46-50

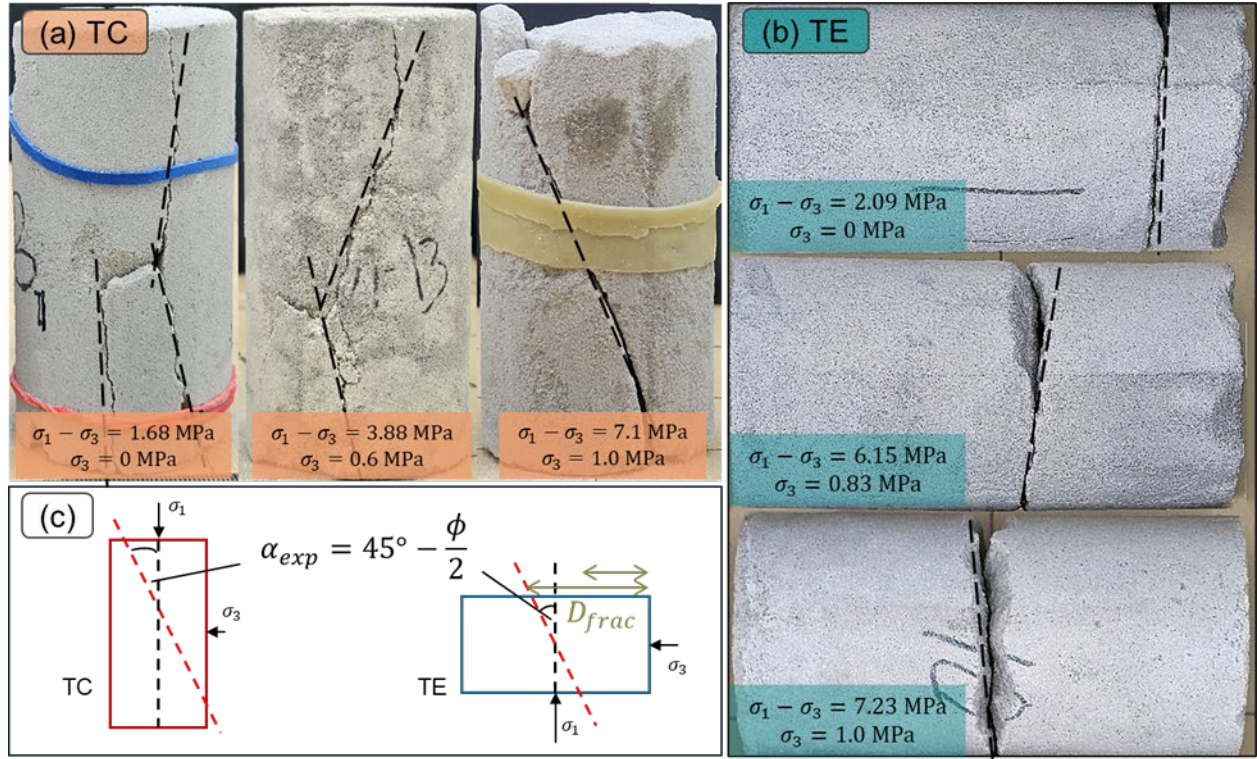


Figure 5.9 Failed specimens from (a) TC and (b) TE tests showing fracture planes. (c) illustrates the measurement of fracture depth  $D_{frac}$  in TE tests and the failure plane angle  $\alpha_{exp}$  measurements from both tests.

Differential stress states from both TC and TE tests were represented using Mohr circles in shear stress  $\tau$  vs. normal stress  $\sigma_n$  plane, and the failure envelopes were derived by applying best-fit curves (Figures 5.10a and 5.10b). A hyperbolic curve was used to model the failure envelopes for the TC (TC-fitting) and TE (TE-fitting) tests. The equations for these fitting curves are as follows:

$$\text{For TC with } R^2 = 0.99, \tau_{TC} = -\frac{62.3}{(\sigma_n + 7.08)} + 9.1 \quad (5.3a)$$

$$\text{For TE with } R^2 = 0.99, \tau_{TE} = -\frac{71.6}{(\sigma_n + 7.19)} + 10.24 \quad (5.3b)$$

As  $\sigma_n$  approaches zero, the estimated tangential friction angle  $\phi_t$  for TC and TE are  $51.18^\circ$  and  $54.13^\circ$ , respectively, based on the failure envelope derived using  $\tan \phi_t = d\sigma_n/d\tau$ .



initiation at  $k = 1.45$  (4:35). As noted in Figure 5.5, the predicted time points for UCT and UET are 0:56 and 1:45, respectively.

The observed gap between the spalling initiation predictions and the actual visible onset could also be attributed to two factors: 1) The stress gradient within the cubical rock specimen is more complex than anticipated, or 2) significantly, while failure initiation was documented visually at  $k = 1.45$ , the inherent structure of the tunnel wall may have already been compromised internally, which was not visible. However, the acoustic emission count data significantly rose closely to both spalling initiation prediction points, supporting the latter factor (Figure 5.5).

## 5.5 Brittle Failure Geometry

The cross-sectional cuts (Figures 5.7 and 5.8) were analyzed using two methods: the depth of failure  $D_f$  and an improved analytical plastic slip lines model. Both analyses addressed the brittle-to-ductile (BTD) transition, with the latter emphasizing the evolving stress anisotropy around the tunnel boundary. In developing the improved plastic slip lines, the approach considers the mobilized fracturing angles, which consist of the entry angle  $\alpha_n$  and the exit angle  $\omega_n$ . This confinement dependency aligns with the BTD transition concept described by Nygård et al. (2006) in cylindrical tests, where the rock mass response shifts from extensional fracturing to shear banding (Figure 5.11a).

In this study, TC results showed a consistent pattern, with the measured fracture plane angle  $\alpha_{exp}$  increasing with higher confining pressure (Figure 5.9a). In contrast, TE results under similar levels of confinements showed less significant changes in the measured fracture plane angle  $\alpha_{exp}$  (Table 5.3), supporting the fact that the transition pressure is higher in extension than compression (Byerlee, 1968). Additionally, with the loading path for confined TE in Section 5.3.2., the stress conditions further from the tunnel face appeared to be better represented by TC rather than TE. Therefore, further analysis used TC results to address the BTD transition. When applied to the tunnel boundary, both  $\alpha$  and  $\omega$  were observed to change with increasing confinement and radial distance (Figure 5.11b). The formation of the final V-shaped notches was attributed to brittle rock responses under high anisotropic stress, involving both extensional and shear fractures, as noted by Vardoulakis (1988).



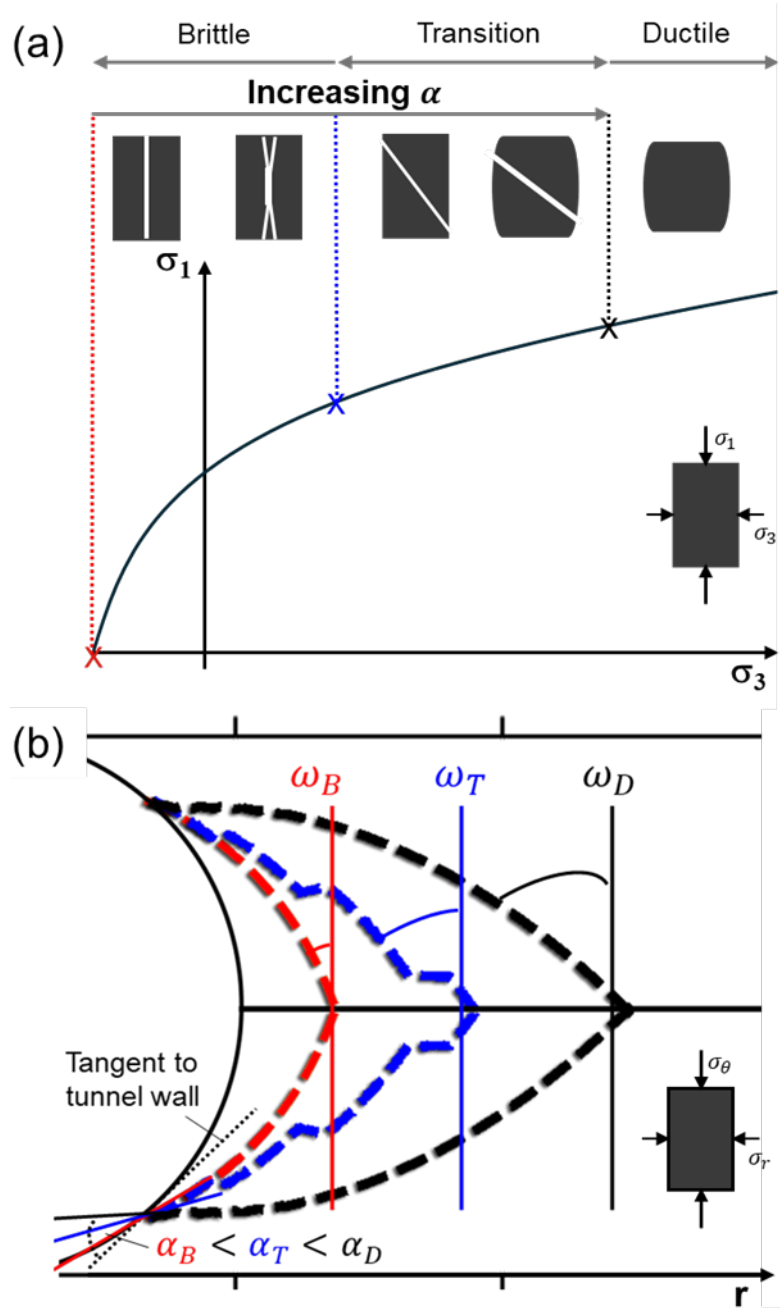


Figure 5.11 (a) Failure envelope in  $\sigma_1 - \sigma_3$  plane, illustrating potential failure modes and fracturing from cylindrical tests across the brittle-to-ductile transition as confinement increases, and (b) the corresponding changes for the fracturing angles, with the entry angle  $\alpha_n$  and exit angle  $\omega_n$ , as the damage progresses radially outward from the tunnel wall under increasing confinement.

Based on this understanding, Figure 5.12a illustrates the damage progression observed in the tunnel model test. Axial stress-axial strain (Figure 5.12b) and volumetric strain-axial strain (Figure 5.12c) curves from TC tests further validate the BT-D transition. The stress-strain curves exhibit post-peak variations transitioning from strain-softening to hardening. The volumetric strain curves indicate

increased ductility and reduced dilation under higher confining pressure, which align with the localized damage progression observed in Figure 5.12a. Annotations (1), (2), and (3) in the stress-strain plots correspond to stages of brittle failure (B), transitional failure (T), and ductile failure (D), respectively. These annotations are estimated based on radial distances from the tunnel wall ( $x/R_T$ ), highlighting the variations in failure response as confinement increases.

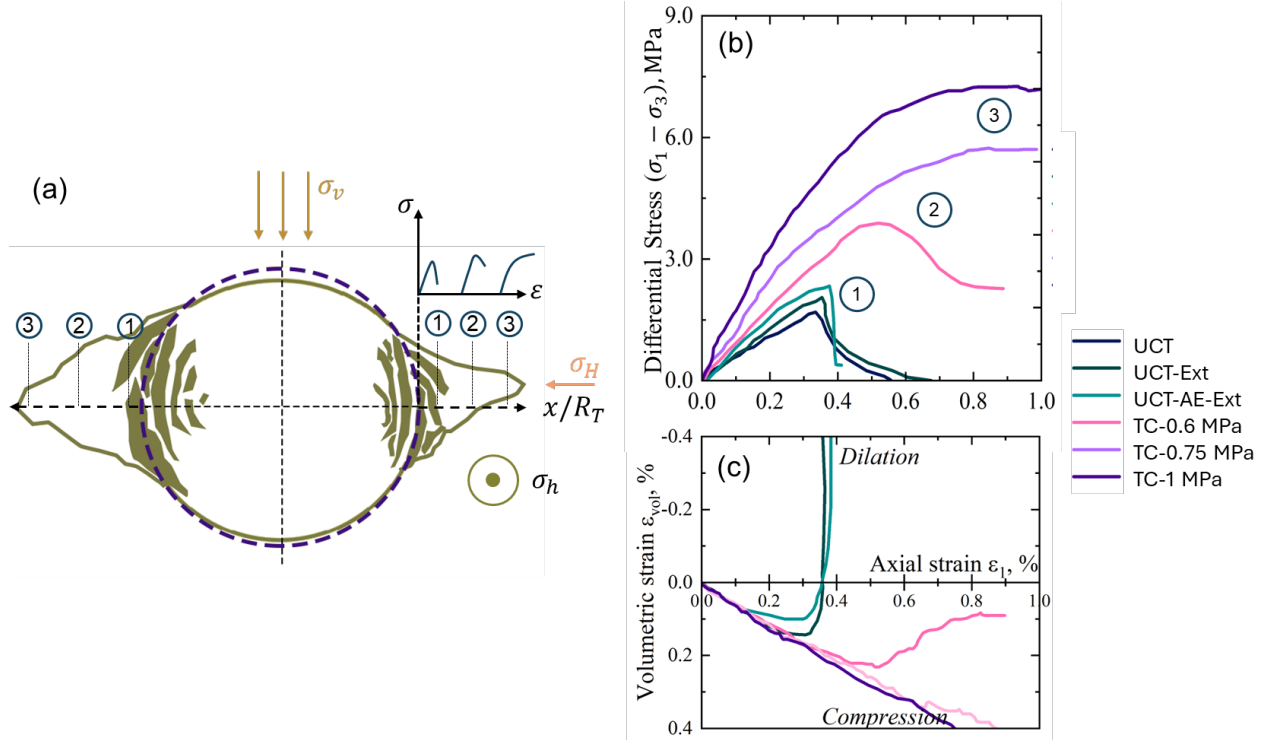


Figure 5.12 (a) Illustration of observed spalling progression in the model tunnel cross-section with hypothesized stress-strain curves of the tunnel wall extending into the rock mass, (b) stress-strain curves, and (c) volumetric strain curves of mix B from both UCT and TC tests. Annotations (1), (2), and (3) in the stress-strain plots indicate increasing ductility with radial distance from the tunnel wall represented as  $> x/R_T$ .

In the subsequent sections, the depth of failure  $D_f$  refer to the final geometry, while the improved theoretical plastic slip lines are used to model the progression of brittle damage.

### 5.5.1 Depth of Failure $D_f$

#### 5.5.1.1 Empirical Correlation

This study compares the measured cut sections with the well-known empirical correlation for predicting the depth of failure  $D_f$  based on the stress ratio  $SR$  (Martin et al., 1999). The empirical equation is:

$$\frac{D_f}{R_T} = 0.49(\pm 0.1) + 1.25(SR) \quad (5.4)$$

where  $SR$  is defined as the ratio of maximum tangential stress  $\sigma_\theta$  to the UCS  $\sigma_c$ . The original criteria, developed for full-scale tunnels, predicts the empirical line intersecting the  $y$ -axis at 0.4, representing the typical crack initiation level relative to UCS (Diederichs, 2007a).

This intersection at 0.4 was interpreted as the stress state where visible spalling failure was observed in tunnel model test, with  $k = 1.45$ . The vertical and horizontal stresses  $\sigma_v$  and  $\sigma_H$  were 1.74 and 1.2 MPa, respectively. Using Kirsch's solution for a circular tunnel, the initial tangential stress at the tunnel boundary  $\sigma_{\theta-initial}$  was 4.2 MPa. At the final loading stage, with applied  $\sigma_v$  and  $\sigma_H$  of 3.9 and 1.2 MPa, the tangential stress  $\sigma_{\theta-final}$  increased to 10.5 MPa. This demonstrates a 261% increase from the initial stress state. Using 0.4 as the initial reference point and assuming constant  $\sigma_c$ , the final stress ratio becomes 1.04, aligning with the scaling in the empirical equation.

Unlike the previous study, which estimated  $D_f$  based on  $D_{frac}$  from TE test at  $\sigma_3 = 0$  (Wibisono and Gutierrez, forthcoming), the current study seems unsuitable for direct comparison. The observed brittle failure here involved higher stress anisotropy and the formation of multiple slabs, which collectively formed the final V-notch depth. This complexity makes it challenging to derive a single fracture parameter from the element test to predict the extensive damage in the tunnel model. A potential direction for future research could involve evaluating the thickness of the formed slabs to explore possible correlations with  $D_{frac}$ . This slab thickness evaluation may provide insights into how individual slabs evolve under different stress configurations and contribute to the final  $D_f$ .

### 5.5.1.2 Analytical Radial Confinement on Brittle-to-Ductile Transition

Another approach to estimating the failure depth was to evaluate the predetermined BTD transition  $D_{f-BTD}$ . Using Kirsch's equation, radial stress  $\sigma_r$  away from the tunnel wall is estimated. The TC stress-strain curves (Figure 5.12b) identified a confining pressure of 1 MPa as the transition point. This transition point corresponds to a target radial stress  $\sigma'_r$  of 1 MPa, to be evaluated at a specific distance  $r$  away from the tunnel wall. Kirsch's equation to calculate the radial stress  $\sigma_r$  at a given distance  $r$  is given as follows:

$$\sigma'_r = \frac{\sigma'_v + \sigma'_H}{2} \left( 1 - \frac{R_T^2}{r^2} \right) + \frac{p'_i R_T^2}{r^2} + \frac{(\sigma'_v - \sigma'_H)}{2} \left( 1 + \frac{3R_T^4}{r^4} - \frac{4R_T^2}{r^2} \right) \cos 2\theta \quad (5.5)$$

where  $p'_i$  is internal pressure, which is zero in this study, and  $\theta$  is the angle measured from the v-H plane. The proposed predetermination point of the BTD transition during the loading stage was based on the significant rise in AE at  $k = 1.25$ , with  $\sigma_v$  and  $\sigma_h$  of 1.44 and 1.2 MPa, respectively. Given these parameters, the distance  $r$  that translates to  $D_{f-BTD}$  was calculated to be 49.4 mm.

### 5.5.1.3 Results from cross-section cuts

The depth of brittle damage  $D_f$  from the cross-section cuts I-V (Figures 5.7 and 5.8) was measured digitally (Figure 5.13a) to obtain two values: right and left springlines, which were then averaged for a third value. The values were plotted, along with empirical and analytical predictions (Figure 5.13b). Unlike the original empirical plotting, this study adopts the absolute brittle damage depth  $D_f$  on the y-axis, rather than the normalized depth  $D_f/R_T$ . The data points from each section, which share the same  $x$ -values corresponding to the calculated final loading stage, were slightly offset to prevent overlapping. Cuts VI and VII were omitted from this measurement since they represent extended damage further into the tunnel face.

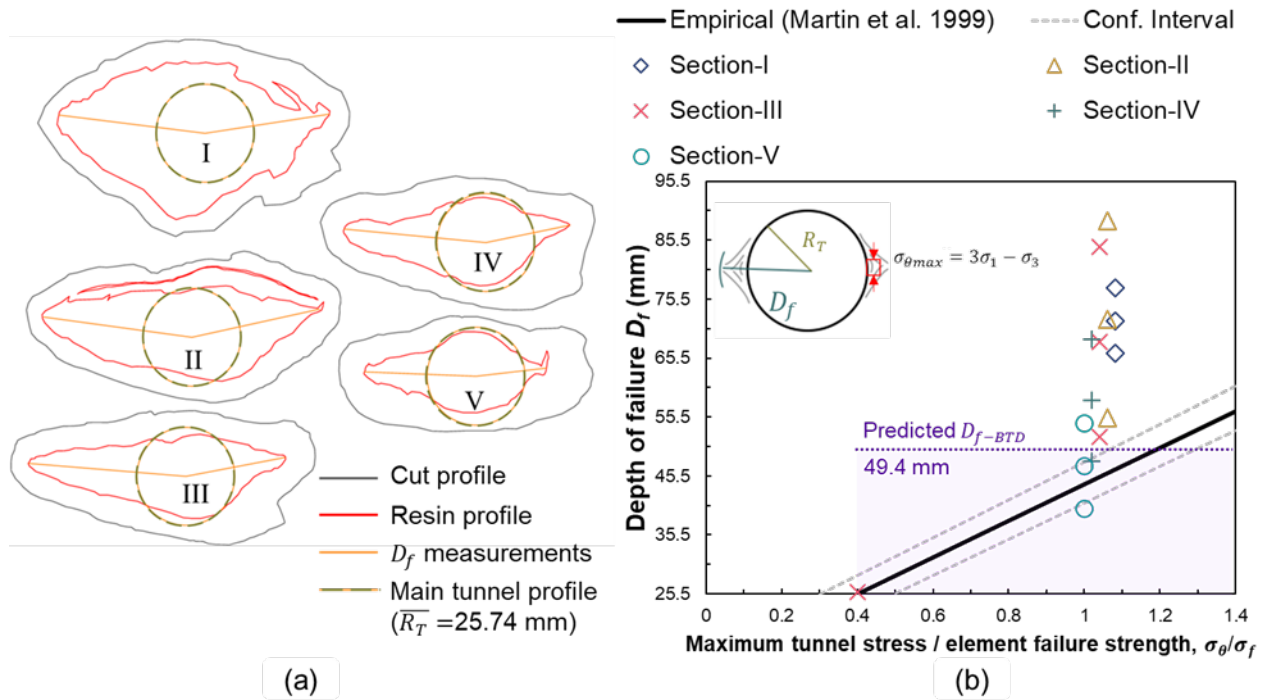


Figure 5.13 (a) Depth of spalling measurement  $D_f$  from digitized cross-section Section I-V and (b) comparison of the measured spalling depth  $D_f$  with the predicted spalling depth  $D_{f-BTD}$  and empirical damage predictions (after Martin et al. 1999). Measured data points from each section were slightly offset to prevent overlapping, as they share the same  $x$ -values corresponding to the final loading stage.

These plots demonstrate that the empirical and  $D_{f-BTD}$  prediction lines remained valid up to 54.6 mm distance (about two times  $R_T$ ) from the tunnel face (Cuts IV-V), based on the right springline values. The remaining data points fall beyond the prediction line, indicating more damage than predicted. This underprediction showcases the limitation of the model, which did not consider the unsupported longitudinal distance away from the tunnel face. However, this insight emphasizes emerging degradation mechanisms, particularly in long-span unsupported tunnels in brittle rock.

Additionally, when using the empirical relationship, it is crucial to acknowledge the differences in boundary conditions and site-specific stress conditions which manifested failure at the excavation boundary (e.g., the smoothness of the excavation boundary and particular transition into other failure modes) (Cai and Kaiser, 2014; Shen and Barton, 2018).

### 5.5.2 Analytical Plastic Slip Line Prediction using Progressive Bézier Curving

As stress localizes, the circular tunnel geometry gradually elongates into more stable elliptical shapes, adapting to the evolving anisotropic loading conditions. The observed brittle failure progression in the tunnel model corresponds to slabbing/buckling-shear rupture bursting as one of the strainburst modes (Zhai et al., 2020). This bursting mode depends on rock lithology and radial stress gradient. The fracturing behavior identified in this study reveals clear precursors, such as grain ejection, slab splitting or buckling, and the development of intersecting shear bands, which characterize the brittle failure progression. The theoretical elastic-plastic solution predicts that plastic slip lines follow equiangular logarithmic spirals in representing shear banding geometry. These spirals are a function of the internal friction angle  $\phi$ , as described by the following equation (Heuer and Hendron, 1971):

$$\frac{r}{R_T} = e^{\pm \cot\left(45^\circ + \frac{\phi}{2}\right)} \quad (5.6)$$

where  $r$  is the radial distance and  $R_T$  is tunnel radius. While this logarithmic spiral relies solely on the friction angle  $\phi$ , it does not provide information on where the slip line begins and ends. Therefore, a novel approach using a quadratic Bézier curve offers an alternative method for modeling the failure zone, accounting for extended tunnel damage and additional parameters beyond the friction angle alone. In Figures 5.11a and 5.14b, the red dashed lines represent two intersected log-spiral curves with  $\phi_t$  from TE at  $\sigma_n = 0$ , which could not extend further and model the observed damage in cut IV.

A quadratic Bézier curve is defined as (Sapidis and Frey, 1992):

$$q(t) = (1-t)^2 b_0 + 2t(1-t)b_1 + t^2 b_2, \quad 0 \leq t \leq 1 \quad (7)$$

where  $b_0 = (x_0, y_0)$ ,  $b_1 = (x_1, y_1)$ , and  $b_2 = (x_2, y_2)$  are three control points of the curve (Fig. 5.14a). In the context of brittle failure, these control points are fitted to the failed tunnel profile based on the breakout width angle  $\beta$  and damage parameter  $\zeta$ . The control points  $b_0$ ,  $b_1$ , and  $b_2$  in polar coordinates are calculated as follows:



These Bézier curves were then fitted and rotated to align with the observed damage from the failed tunnel cross-sections. The fitting parameters  $\beta$ ,  $\zeta$ , and the rotation factor (Figure 5.15) enabled the curves to represent the realistic progression of brittle instabilities accurately. Given the variation in damage extent at the springlines and across different cuts, the ranges for these fitting parameters were provided near the model. The ranges were initialized with low values of  $20^\circ$  for  $\beta$  and 1.04 for  $\zeta$ , corresponding to the minimum entry angle observed at the tunnel spalling initiation (Figure 5.6 – Stage III,  $k=1.67$ ). Another basis for these low values was the steep angle of shear fracturing mechanisms relative to the minor principal stress in tunnel projects with spalling (Wibisono and Gutierrez, forthcoming). The onset of spalling can appear like extensional fractures, likely due to the dilation of fracture planes during shearing (Gutierrez et al., 2023).

Furthermore, the brittle damage progressed differently, appearing to be influenced by: (1) distance from the tunnel face, (2) progressive load-bearing degradation due to strain softening, where the damaged zone became more vulnerable to further degradation, (3) a slight tunnel offset within the cubical specimen, potentially leading to an uneven load distribution resulting in longer, narrower damage on the left springline, and (4) frictional boundary conditions that may have influenced the traversing load distribution (Frash et al., 2014), though further data would be needed to quantify this effect to current analog rock.

The converging damage pattern from the tunnel face to the portal (Figures 5.7, 5.8, and 5.13) highlights the effect of face support. The tunnel face, resembling the unexcavated tunnel core, provides gradually diminishing radial resistance as one moves farther from the face toward the exposed boundary (Vlachopoulos and Diederichs, 2009). This results in more significant damage farther from the face as resistance decreases. Moreover, as the strain-softening response progresses, the initially damaged sections exhibit more damage than the later ones.

In addition, the right springline appears to have experienced a suppressed brittle-to-ductile transition relative to the opposing side, potentially due to higher confinement levels. This earlier transition limited fracture coalescence and shear band intersection, producing a shallower failure depth than on the opposing side. These findings align with observations made by Ortlepp (1997) in the mine-by-experiment tunnel, where the invert section exhibited a smaller notch due to additional confining stress from trapped micro-slabs.



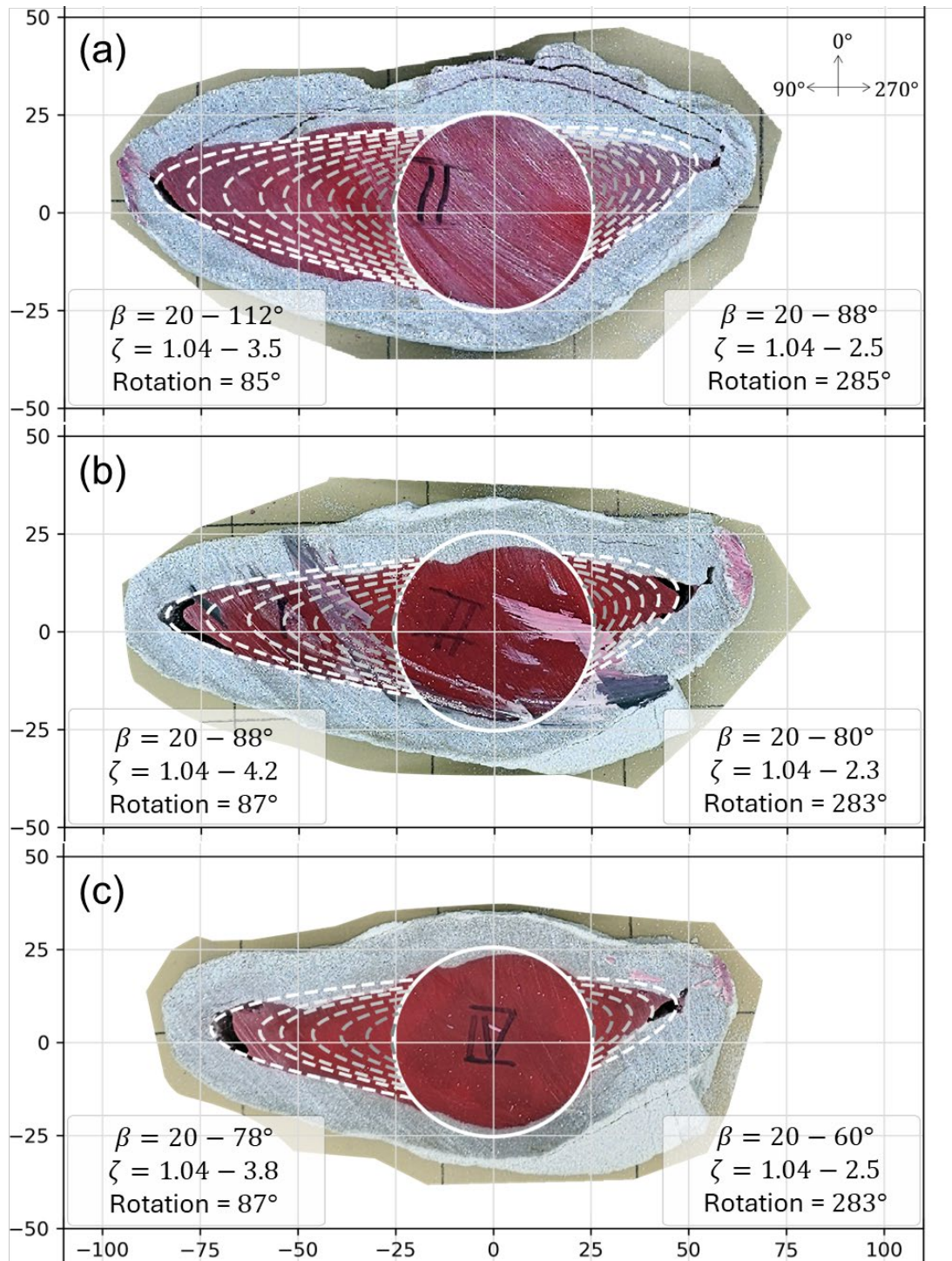
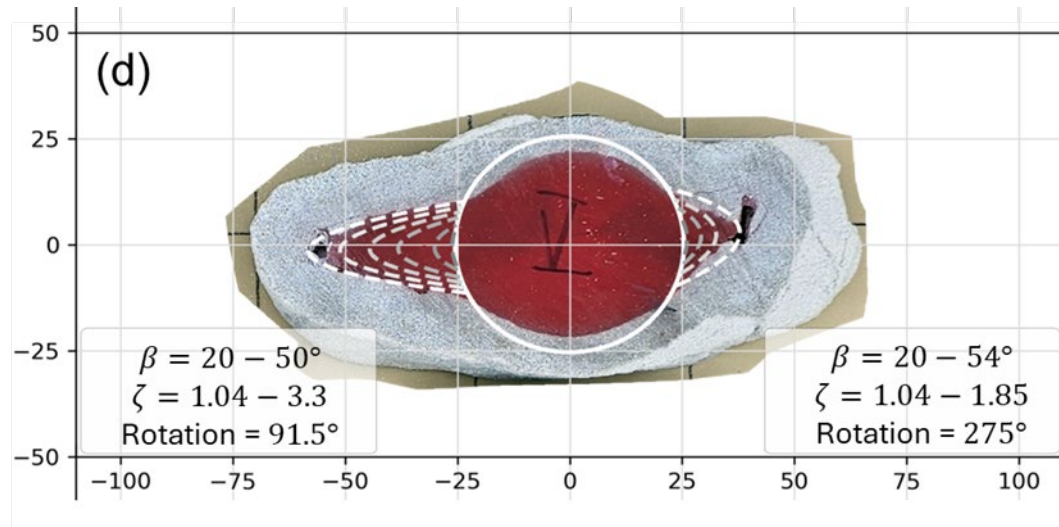


Figure 5.15 Bézier slip line modeling of the final failure profiles from (a) Section-II, (b) Section-III, (c) Section-IV, and (d) Section-V. The darker to brighter gradient dashed lines represent the progression of the fracturing angles following the brittle-to-ductile transition. The bottom left and right legends show the parameters used to fit the actual failure profiles (breakout width  $\beta$ , damage factor  $\zeta$ , and notch tip counter-clockwise rotation) at the left and right springline, respectively. (For interpretation of the references to color in this figure legend, the reader is referred to the Web version of this article).

Figure 5.165 Continued.



## 5.6 Conclusions

This study extensively analyzed brittle damage and failure progression in tunnel excavation under anisotropic stresses through laboratory experiments, addressing the mechanisms and contributing factors of brittle failure. The experimental framework underscored the critical influence of stress anisotropy gradients, longitudinal confinement stress, face support, and rock mass response on spalling progression. The following conclusions are drawn:

- (1) This large-scale tunnel model experiment with analog brittle rock material, true-triaxial cell, miniature TBM, and AE monitoring simulated the progression of brittle failure at a circular tunnel wall under increasing stress anisotropy. The integration of element tests (TC and TE) enabled the characterization of material response under confinement and unloading conditions. The developed methodology was adaptable, allowing further investigation into spalling and rockburst due to ease of repeatability, material preparation, and simple loading arrangements.
- (2) Brittle instabilities were concentrated in regions with the highest tangential stress near the tunnel boundary. The initial failure mechanisms involved conjugate shear spalling at low entry angles relative to the direction of tangential stress, yielding thin, detached slabs at the wall. As the deviatoric load increased, the newly created geometry led to more violent rock ejection.
- (3) Confinement, inhibiting longitudinal and radial stresses deeper into the tunnel wall, influenced the transition of rock mass response. Shear slip lines intersected at potentially brittle-to-ductile transition due to confinement, forming the final V-shaped notch. This phenomenon was supported by physical evidence from the recovered failed tunnel specimen and cylindrical specimens under confinement.
- (4) The assessment of the observed depth of failure  $D_f$  from different sections showed that empirical prediction and brittle-to-ductile transition analysis were accurate only within one tunnel diameter

from the face. Beyond this point, damage increased as virtual face support degraded, allowing for more damage and further progression due to strain softening.

- (5) Using progressive Bézier curves for the plastic slip lines effectively modeled the observed damage zones from Sections II-V. The slip lines development considered the gradual progression of both breakout width  $\beta$  and damage factor  $\zeta$ , which were anisotropy dependent. The model closely resembled the increasing fracturing angles (entry angle  $\alpha_n$  and exit angle  $\omega_n$ ) further away from the tunnel wall.

## **5.7 Supporting Information**

Python codes for generating the progressive Bézier curves for the plastic slip lines around the tunnel boundary are accessible at <https://github.com/mcdoans/brittle-slip-lines>

## CHAPTER 6 SUMMARY AND CONCLUSIONS

The primary focus of this dissertation was to enhance the understanding of tunnel brittle instabilities through a series of laboratory experimental investigations. These investigations focused on (1) developing analog brittle rock model; (2) performing a series of tunnel model tests using a true-triaxial cell, a miniature TBM, and AE monitoring; and (3) propose more robust brittle failure analytical and prediction methods. While detailed conclusions are presented in each chapter, the major contributions and conclusions of this dissertation are summarized below.

### 6.1. Summary of Work Done

This dissertation makes several key contributions to the current understanding of brittle instabilities in tunneling and underground excavation:

- Established an analog brittle rock with a notably low UCS, which facilitates the replication of experimental conditions, reduces the need for high-capacity loading, and enhances the observation of brittle failure mechanisms.
- Demonstrated the applicability of large-scale true-triaxial cell and miniature TBM for simulating brittle instabilities such as spalling and rockbursting in tunnel excavation. The experiments provided valuable insights failure mechanisms and stress-dependent behaviors under field conditions, among other findings.
- Proposed the triaxial extension (TE) test method to assess the effects of intermediate confinement and unloading at the tunnel wall. This method used a conventional Hoek cell with a different loading path and stress configuration to conceptually simulate the biaxial stress-state at the tunnel wall.
- Identified a shear-driven mechanism that initiates spalling at a very small entry angle through tunnel model spallings and TE test results. The steep angle measured from the minor principal stress may resemble extensional fractures, forming perpendicular failure plane to  $\sigma_3$ . However, it could also form through shear-induced dilation along the shear fracture surface, causing the friction angle to mobilize.
- Improved the analytical log-spiral plastic slip line to the quadratic Bézier curve as an alternative method for modeling the brittle failure zone. The curving accounts for extended tunnel damage and additional parameters beyond the friction angle alone, such as breakout width  $\beta$  and damage factor  $\zeta$ .
- Proposed a methodology in identifying precursors to damage and spalling onset based on parametric AE analysis. This included a temporal deconstruction procedure using time-frequency domain signatures and  $b$ -value analysis.

## 6.2. Major Conclusions

The major conclusions of this research are as follows:

- The developed analog material was classified as sedimentary rock-like based on its Poisson's ratio, density, elastic modulus ratio, and strength ratio. Mix B closely mimicked the behavior of intact sedimentary rocks, making it well-suited for experiments requiring weak yet brittle characteristics. The rock-like development with reliable repeatability enabled large-sample testing, reduced high-capacity loading, and facilitated tunnel wall observations.
- The failure mode observed in the large-scale unsupported tunnel model test was primarily influenced by the loading conditions, whether isotropic or anisotropic. In the isotropic test, post-mortem investigation in the longitudinal cross-section revealed shear localization and micro-fracturing, identifying damage zones—Construction Damage Zone *CDZ*, Highly Damage Zone *HDZ*, and Excavation Damage Zone *EDZ*, and spalled material—each corresponding to distinct stages on the stress-strain curve observed in cylindrical triaxial compression (TC) tests.
- Spalling was characterized as a form of shear failure with steep angles relative to minor principal stress, challenging the notion of purely extensional failure. The theoretical log-spiral slip lines, derived from rock friction angle and inversely related to spalling entry angles, highlighted the brittle shear mechanisms underlying spalling. Lower confinement conditions promoted brittle responses, with steeper rock failure envelopes yielding higher theoretical friction angles and reinforcing the shear-driven nature of spalling.
- Triaxial extension (TE) tests provided a more accurate method for predicting spalling initiation and progression near the tunnel wall, identifying parameters such as biaxial shear strength, failure plane angle, and spalling zone thickness that conventional tests did not capture. The biaxial shear strength better represented the tunnel wall behavior with a consideration of both tangential and longitudinal stresses. The TE test results showed that the entry angle of failure was smaller with higher theoretical friction angles, suggesting a strong relationship between entry angle and material properties, further refining the understanding of spalling initiation.
- The experiments validated the instantaneous degradation characteristic of brittle materials, with damage extending progressively from the initial failure zone. Under anisotropic stress, a more significant extent of damage appeared near the portal, approximately six tunnel radii from the tunnel face. Initial failure involved conjugate shear spalling at low entry angles relative to the direction of tangential stress, yielding thin, detached slabs. As the deviatoric load increased, the newly created geometry led to more intense rock ejection and shear debris flow.
- Confinement notably influenced the transition of rock mass response around the tunnel boundary. High tangential stress concentrations initiated pronounced spalling and rapid degradation, with an

entry angle  $\alpha_n$  nearly parallel to the tangential stress direction. Further into the rock mass, the transition from brittle-to-ductile response, as observed in the cylindrical TC tests, allowed the gradual progression of fracturing angles. This formed characteristic V-notch or dog-earing patterns as both the entry angle  $\alpha_n$  and exit angle  $\omega_n$  widened.

- The development of plastic slip lines can be explained using quadratic Bézier curves. The Bézier slip lines required three control points and incorporated two parameters—breakout width  $\beta$  and damage factor  $\zeta$ —dependent on stress anisotropy. These Bézier curves improved the accuracy of modeling extended tunnel damage beyond the limitations of log-spiral models with consideration of the gradual progression of control points. The model closely resembled the widening fracturing angles further from the tunnel wall.

### 6.3. Recommendations for Future Work

This dissertation has developed experimental frameworks and provided evidence addressing fundamental issues of brittle instabilities in tunneling. While this work represents significant progress, it also leaves certain questions unanswered or newly-raised, suggesting directions for further research. These include:

1. Introducing variations into the analog rock model to investigate the effects of rock mass discontinuity, inhomogeneity, and anisotropy. The proposed TE testing methodology could serve as an initial approach, offering a broad overview, particularly advantageous given the considerable effort required for large-scale tunnel model testing.
2. Implementing mitigation strategies for brittle tunnel failure, coupled with additional monitoring methods such as fiber optics. This would provide comprehensive damage and deformation data, improving the understanding of ground-support interactions and enabling more accurate detection of precursors to brittle damage and spalling onset.
3. Combining numerical modeling with experimental data to further validate constitutive models and account for three-dimensional confinement. This approach would be valuable for investigating brittle failure effects on tunnel intersections, multiple adjacent tunnel headings, and curved tunnel alignments, where complex stress rotations occur around the boundaries.

## REFERENCES

- Abramowicz M, Kowalski R. The influence of short time water cooling on the mechanical properties of concrete heated up to high temperature. *Journal of Civil Engineering and Management* 2005;11:85–90. <https://doi.org/10.1080/13923730.2005.9636336>.
- Addis MA, Barton NR, Bandis SC, Henry JP. Laboratory Studies on the Stability of Vertical and Deviated Boreholes 1990. <https://doi.org/10.2118/20406-MS>.
- Aki K. Maximum likelihood estimate of  $b$  in the formula  $\log N=a-bM$  and its confidence limits. *Bull Earthquake Res Inst, Tokyo Univ* 1965;43:237–9.
- Al-Ajmi AM, Zimmerman RW. Relation between the Mogi and the Coulomb failure criteria. *International Journal of Rock Mechanics and Mining Sciences* 2005;42:431–9. <https://doi.org/10.1016/J.IJRMMS.2004.11.004>.
- Alcaino-Olivares R, Paraskevopoulou C, Perras MA. Assessing Long-Term Excavation Damage in Switzerland’s Bedretto Adit: A Field Investigation in the Northern Section. *Geotechnical and Geological Engineering* 2024;1–19. <https://doi.org/10.1007/S10706-023-02735-8/FIGURES/8>.
- Alonso E, Alejano LR, Varas F, Fdez-Mañín G, Carranza-Torres C. Ground response curves for rock masses exhibiting strain-softening behaviour. *Int J Numer Anal Methods Geomech* 2003;27:1153–85. <https://doi.org/10.1002/NAG.315>.
- Amitrano D. Brittle-ductile transition and associated seismicity: Experimental and numerical studies and relationship with the  $b$  value. *J Geophys Res Solid Earth* 2003;108:2044. <https://doi.org/10.1029/2001JB000680>.
- Andersson C, Rinne M, Staub I, Wanne T. The On-Going Pillar Stability Experiment at the Äspö Hard Rock Laboratory, Sweden. *Elsevier Geo-Engineering Book Series* 2004;2:389–94. [https://doi.org/10.1016/S1571-9960\(04\)80072-7](https://doi.org/10.1016/S1571-9960(04)80072-7).
- Arizzi A, Cultrone G. Mortars and plasters—how to characterise hydraulic mortars. *Archaeological and Anthropological Sciences* 2021 13:9 2021;13:1–22. <https://doi.org/10.1007/S12520-021-01404-2>.
- Arora K, Gutierrez M, Hedayat A. Physical model simulation of rock-support interaction for the tunnel in squeezing ground. *Journal of Rock Mechanics and Geotechnical Engineering* 2022;14:82–92. <https://doi.org/10.1016/J.JRMGE.2021.08.016>.
- Arora K, Gutierrez M, Hedayat A. New physical model to study tunnels in squeezing clay-rich rocks. *Geotechnical Testing Journal* 2021;44. <https://doi.org/10.1520/GTJ20200081>.
- Arora K, Gutierrez M, Hedayat A. Experimental setup for studying tunnels in squeezing ground conditions. *Tunnels and Underground Cities: Engineering and Innovation meet Archaeology, Architecture and Art*, CRC Press; 2019, p. 3515–24.
- Arzúa J, Alejano LR. Dilation in granite during servo-controlled triaxial strength tests. *International Journal of Rock Mechanics and Mining Sciences* 2013;61:43–56. <https://doi.org/https://doi.org/10.1016/j.ijrmms.2013.02.007>.
- Ashby MF, Sammis CG. The damage mechanics of brittle solids in compression. *Pure Appl Geophys* 1990;133:489–521. <https://doi.org/10.1007/BF00878002>.
- ASTM. ASTM Standard C150/C150M - 21 - Standard Specification for Portland Cement. *Book of Standards*. 04.01, 2021a.



- ASTM. ASTM Standard C192/C192M – 19 Standard Practice for Making and Curing Concrete Test Specimens in the Laboratory. Book of Standards, vol. 04.01, 2021b. <https://doi.org/10.1520/C0511-21>.
- ASTM. ASTM Standard C511 - 21 - Standard Specification for Mixing Rooms, Moist Cabinets, Moist Rooms, and Water Storage Tanks Used in the Testing of Hydraulic Cements and Concretes. Book of Standards, vol. 04.02, 2021c. [https://doi.org/10.1520/C0192\\_C0192M-19](https://doi.org/10.1520/C0192_C0192M-19).
- ASTM. ASTM Standard D7012-14e1 - Standard Test Methods for Compressive Strength and Elastic Moduli of Intact Rock Core Specimens under Varying States of Stress and Temperatures. Book of Standards, vol. 04.09, 2017.
- ASTM. ASTM Standard C260-10 Standard Specification for Air-Entraining Admixtures for Concrete. Book of Standards, vol. 04.02, 2010. <https://doi.org/10.1520/C0260-10>.
- Aubertin M, Gill DE, Simon R. On the Use of the Brittleness Index Modified (BIM) to Estimate the Post-Peak Behavior of Rocks. 1st North American Rock Mechanics Symposium 1994.
- Barton N, Lien R, Lunde J. Engineering classification of rock masses for the design of tunnel support. *Rock Mechanics Felsmechanik Mécanique Des Roches* 1974;6:189–236. <https://doi.org/10.1007/BF01239496>.
- Barton N, Shen B. Risk of shear failure and extensional failure around over-stressed excavations in brittle rock. *Journal of Rock Mechanics and Geotechnical Engineering* 2017;9:210–25. <https://doi.org/10.1016/J.JRMGE.2016.11.004>.
- Barton N. A Low Strength Material For Simulation Of The Mechanical Properties Of Intact Rock Mechanics Models. *International Society of Rock Mechanics, Proceedings* 1970;1.
- Bender B. Maximum likelihood estimation of b values for magnitude grouped data. *Bulletin of the Seismological Society of America* 1983.
- Bieniawski ZT, Grandori R. Predicting TBM excavability-part II. *Tunnels & Tunnelling International* 2007.
- Bieniawski ZT, Hawkes I. Suggested methods for determining tensile strength of rock materials. *International Journal of Rock Mechanics and Mining Sciences* 1978;15:99–103.
- Bobich JK. Experimental analysis of the extension to shear fracture transition in Berea Sandstone 2005.
- Boggs S. Principles of stratigraphy and sedimentology. *Principles of Stratigraphy and Sedimentology* 2006:676.
- Brace WF. Brittle fracture of rocks. *State of Stress in the Earth's Crust* 1964:111–74.
- Bradley WB. Failure of Inclined Boreholes. *J Energy Resour Technol* 1979;101:232–9. <https://doi.org/10.1115/1.3446925>.
- Brady BHG, Brown ET. Rock strength and deformability. *Rock Mechanics for Underground Mining* 2007:85–141. [https://doi.org/10.1007/978-1-4020-2116-9\\_4](https://doi.org/10.1007/978-1-4020-2116-9_4).
- Brown ET, Hoek E. *Underground excavations in rock*. CRC Press; 1980.
- Byerlee JD. Brittle-ductile transition in rocks. *J Geophys Res* 1968;73:4741–50. <https://doi.org/10.1029/JB073I014P04741>.

- Cai M. Prediction and prevention of rockburst in metal mines – A case study of Sanshandao gold mine. *Journal of Rock Mechanics and Geotechnical Engineering* 2016;8:204–11. <https://doi.org/10.1016/J.JRMGE.2015.11.002>.
- Cai M. Influence of intermediate principal stress on rock fracturing and strength near excavation boundaries—Insight from numerical modeling. *International Journal of Rock Mechanics and Mining Sciences* 2008;45:763–72. <https://doi.org/10.1016/J.IJRMMS.2007.07.026>.
- Cai M, Kaiser PK. In-situ rock spalling strength near excavation boundaries. *Rock Mech Rock Eng* 2014;47:659–75. <https://doi.org/10.1007/S00603-013-0437-0/FIGURES/14>.
- Cai M, Kaiser PK, Morioka H, Minami M, Maejima T, Tasaka Y, Kurose H. FLAC/PFC coupled numerical simulation of AE in large-scale underground excavations. *International Journal of Rock Mechanics and Mining Sciences* 2007;44:550–64. <https://doi.org/10.1016/J.IJRMMS.2006.09.013>.
- Carter BJ. Size and stress gradient effects on fracture around cavities. *Rock Mech Rock Eng* 1992;25:167–86. <https://doi.org/10.1007/BF01019710/METRICS>.
- Castro L, Bewick R, Carter T. An overview of numerical modelling applied to deep mining. *Innovative Numerical Modeling in Geomechanics* 2012:393–414. <https://doi.org/10.1201/b12130-22>.
- Chen SK, Chen PY, Wu YM, Chen CC, Chan CH. Temporal Variations of Earthquake Magnitude-Frequency Relation in the Source Area of  $M \geq 6.0$  Earthquakes: A Systematic Survey in Taiwan. *Earth and Space Science* 2023;10:e2023EA002927. <https://doi.org/10.1029/2023EA002927>.
- Cheon DS, Jeon S, Park C, Song WK, Park ES. Characterization of brittle failure using physical model experiments under polyaxial stress conditions. *International Journal of Rock Mechanics and Mining Sciences* 2011;48:152–60. <https://doi.org/10.1016/J.IJRMMS.2010.10.001>.
- Chipping DH. Sedimentary structure and environment of some thick sandstone beds of turbidite type. *Journal of Sedimentary Research* 1972;42:587–95. <https://doi.org/10.1306/74D725CC-2B21-11D7-8648000102C1865D>.
- Cho N, Martin CD, Sego DC, Jeon J. Dilation and spalling in axially compressed beams subjected to bending. *Rock Mech Rock Eng* 2010;43:123–33. <https://doi.org/10.1007/S00603-009-0049-X/FIGURES/17>.
- Colombo IngS, Main IG, Forde MC. Assessing Damage of Reinforced Concrete Beam Using “b-value” Analysis of Acoustic Emission Signals. *Journal of Materials in Civil Engineering* 2003;15:280–6. [https://doi.org/10.1061/\(ASCE\)0899-1561\(2003\)15:3\(280\)](https://doi.org/10.1061/(ASCE)0899-1561(2003)15:3(280)).
- Cox SJD, Meredith PG. Microcrack formation and material softening in rock measured by monitoring acoustic emissions. *International Journal of Rock Mechanics and Mining Sciences & Geomechanics Abstracts* 1993;30:11–24. [https://doi.org/10.1016/0148-9062\(93\)90172-A](https://doi.org/10.1016/0148-9062(93)90172-A).
- Cruz CR, Gillen M. Thermal expansion of Portland cement paste, mortar and concrete at high temperatures. *Fire Mater* 1980;4:66–70. <https://doi.org/10.1002/FAM.810040203>.
- Dakoulas P, Sun Y. Fine Ottawa Sand: Experimental Behavior and Theoretical Predictions. *Journal of Geotechnical Engineering* 1992;118:1906–23. [https://doi.org/10.1061/\(ASCE\)0733-9410\(1992\)118:12\(1906\)](https://doi.org/10.1061/(ASCE)0733-9410(1992)118:12(1906)).
- David C, Menéndez B, Bernabe Y. The mechanical behaviour of synthetic sandstone with varying brittle cement content. *International Journal of Rock Mechanics and Mining Sciences* 1998;35:759–70.

- Deere DU, Miller RP. Engineering Classification and Index Properties for Intact Rocks. 1966.
- des Rivières J-L, Goodman R. Acclimatization: Adapting Conventional Tunnel Lining Techniques to Overstress Rock Conditions. Rapid Excavation and Tunneling Conference 2023, 2023, p. 422–34.
- Detournay E, Cheng AH-D. 5 - Fundamentals of Poroelasticity. In: FAIRHURST C, editor. Analysis and Design Methods, Oxford: Pergamon; 1993, p. 113–71.  
<https://doi.org/https://doi.org/10.1016/B978-0-08-040615-2.50011-3>.
- Diederichs MS. The 2003 Canadian geotechnical colloquium: Mechanistic interpretation and practical application of damage and spalling prediction criteria for deep tunnelling. Canadian Geotechnical Journal 2007a;44:1082–116. <https://doi.org/10.1139/T07-033/ASSET/IMAGES/LARGE/T07-033F32.JPEG>.
- Diederichs MS. The 2003 Canadian geotechnical colloquium: Mechanistic interpretation and practical application of damage and spalling prediction criteria for deep tunnelling. Canadian Geotechnical Journal 2007b;44:1082–116. <https://doi.org/10.1139/T07-033/ASSET/IMAGES/LARGE/T07-033F32.JPEG>.
- Diederichs MS. Manuel Rocha Medal Recipient Rock Fracture and Collapse Under Low Confinement Conditions. Rock Mech Rock Eng 2003;36:339–81. <https://doi.org/10.1007/S00603-003-0015-Y/METRICS>.
- Diederichs MS, Carter T, Martin D. Practical Rock Spall Prediction in Tunnels, 2009.
- Diederichs MS, Kaiser PK, Eberhardt E. Damage initiation and propagation in hard rock during tunnelling and the influence of near-face stress rotation. International Journal of Rock Mechanics and Mining Sciences 2004;41:785–812. <https://doi.org/10.1016/J.IJRMMS.2004.02.003>.
- Dineva S, Dahner C, Beck D, Agostinetti NP, Mihaylov D, Guclu IE. Changes in seismicity, stress, and stress proxies before and after the large seismic event with Mw 4.2 on May 18, 2020 in Kiirunavaara Mine (Sweden). 58th US Rock Mechanics/Geomechanics Symposium, Golden: ARMA; 2024.
- Dong L, Zhang Y, Bi S, Ma J, Yan Y, Cao H. Uncertainty investigation for the classification of rock micro-fracture types using acoustic emission parameters. International Journal of Rock Mechanics and Mining Sciences 2023;162:105292. <https://doi.org/10.1016/J.IJRMMS.2022.105292>.
- Dresen G, Stanchits S, Rybacki E. Borehole breakout evolution through acoustic emission location analysis. International Journal of Rock Mechanics and Mining Sciences 2010;47:426–35. <https://doi.org/10.1016/J.IJRMMS.2009.12.010>.
- Du K, Li X, Tao M, Wang S. Experimental study on acoustic emission (AE) characteristics and crack classification during rock fracture in several basic lab tests. International Journal of Rock Mechanics and Mining Sciences 2020;133:104411. <https://doi.org/10.1016/J.IJRMMS.2020.104411>.
- Du K, Luo X, Liu M, Liu X, Zhou J. Understanding the evolution mechanism and classification criteria of tensile -shear cracks in rock failure process from acoustic emission (AE) characteristics. Eng Fract Mech 2024;296:109864. <https://doi.org/10.1016/J.ENGFRACMECH.2024.109864>.
- Du K, Tao M, Li X bing, Zhou J. Experimental Study of Slabbing and Rockburst Induced by True-Triaxial Unloading and Local Dynamic Disturbance. Rock Mech Rock Eng 2016;49:3437–53. <https://doi.org/10.1007/s00603-016-0990-4>.

- Duan K, Ji Y, Wu W, Kwok CY. Unloading-induced failure of brittle rock and implications for excavation-induced strain burst. *Tunnelling and Underground Space Technology* 2019;84:495–506. <https://doi.org/10.1016/J.TUST.2018.11.012>.
- Eberhardt E, Diederichs M, Rahjoo M. Pre-peak Brittle Fracture Damage, 2016, p. 623–57.
- Edelbro C. Numerical modelling of observed fallouts in hard rock masses using an instantaneous cohesion-softening friction-hardening model. *Tunnelling and Underground Space Technology* 2009;24:398–409. <https://doi.org/10.1016/J.TUST.2008.11.004>.
- Egger P. Design and construction aspects of deep tunnels (with particular emphasis on strain softening rocks). *Tunnelling and Underground Space Technology* 2000a;15:403–8. [https://doi.org/10.1016/S0886-7798\(01\)00008-6](https://doi.org/10.1016/S0886-7798(01)00008-6).
- Egger P. Design and construction aspects of deep tunnels (with particular emphasis on strain softening rocks). *Tunnelling and Underground Space Technology* 2000b;15:403–8. [https://doi.org/10.1016/S0886-7798\(01\)00008-6](https://doi.org/10.1016/S0886-7798(01)00008-6).
- Einstein H. Physical Modelling in Rock Mechanics and Rock Engineering. *Rock Mech Rock Eng* 2024;1–18. <https://doi.org/10.1007/S00603-024-04106-Y/FIGURES/33>.
- Fairhurst CE, Hudson JA. Draft ISRM suggested method for the complete stress-strain curve for intact rock in uniaxial compression. *International Journal of Rock Mechanics and Mining Sciences* (1997) 1999;36:279–89.
- Farhadian H. A new empirical chart for rockburst analysis in tunnelling: Tunnel rockburst classification (TRC). *Int J Min Sci Technol* 2021;31:603–10. <https://doi.org/10.1016/J.IJMST.2021.03.010>.
- Feng XT, Kong R, Yang C, Zhang X, Wang Z, Han Q, Wang GA A Three-Dimensional Failure Criterion for Hard Rocks Under True Triaxial Compression. *Rock Mech Rock Eng* 2020;53:103–11. <https://doi.org/10.1007/S00603-019-01903-8/METRICS>.
- Feng XT, Liu J, Chen B, Xiao Y, Feng G, Zhang F. Monitoring, Warning, and Control of Rockburst in Deep Metal Mines. *Engineering* 2017;3:538–45. <https://doi.org/10.1016/J.ENG.2017.04.013>.
- Feng XT, Xu H, Qiu SL, Li SJ, Yang CX, Guo HS, Cheng Y, Gao YH. In Situ Observation of Rock Spalling in the Deep Tunnels of the China Jinping Underground Laboratory (2400 m Depth). *Rock Mech Rock Eng* 2018;51:1193–213. <https://doi.org/10.1007/s00603-017-1387-8>.
- Feng XT, Young RP, Reyes-Montes JM, Aydan Ö, Ishida T, Liu JP, Liu H. ISRM Suggested Method for In Situ Acoustic Emission Monitoring of the Fracturing Process in Rock Masses. *Rock Mech Rock Eng* 2019;52:1395–414. <https://doi.org/10.1007/S00603-019-01774-Z/METRICS>.
- Frash LP. DIscO 1.16 User Manual 2016.
- Frash LP, Gutierrez M, Hampton J. True-triaxial apparatus for simulation of hydraulically fractured multi-borehole hot dry rock reservoirs. *Int J Rock Mech Min Sci* 2014a;70:496–506. <https://doi.org/10.1016/J.IJRMMS.2014.05.017>.
- Frash LP, Gutierrez M, Hampton J. True-triaxial apparatus for simulation of hydraulically fractured multi-borehole hot dry rock reservoirs. *International Journal of Rock Mechanics and Mining Sciences* 2014b;70:496–506. <https://doi.org/10.1016/J.IJRMMS.2014.05.017>.
- Garg P, Pandit B, Mishra B, Babu GLS. Development of a poly-axial platen for testing true-triaxial behavior of rocks. <https://doi.org/10.1139/CGJ-2020-0247> 2021;58:1839–54. <https://doi.org/10.1139/CGJ-2020-0247>.

- Gautam PK, Gutierrez M. Acoustic Emission Characteristics on the UCS of a Synthetic Rock. 58th US Rock Mechanics/Geomechanics Symposium, Golden: 2024.
- Gautam PK, Gutierrez M, Wibisono DY, Majumder D. Crack Classification During Tunneling in Scale Model Testing Using Acoustic Emission. 57th US Rock Mechanics/Geomechanics Symposium 2023. <https://doi.org/10.56952/ARMA-2023-0147>.
- Gercek H. Poisson's ratio values for rocks. *International Journal of Rock Mechanics and Mining Sciences* 2007;44:1–13. <https://doi.org/10.1016/J.IJRMMS.2006.04.011>.
- Gong F, Luo Y, Li XB, Si XF, Tao M. Experimental simulation investigation on rockburst induced by spalling failure in deep circular tunnels. *Tunnelling and Underground Space Technology* 2018;81:413–27. <https://doi.org/10.1016/J.TUST.2018.07.035>.
- Gong F, Si XF, Li XB, Wang SY. Experimental Investigation of Strain Rockburst in Circular Caverns Under Deep Three-Dimensional High-Stress Conditions. *Rock Mech Rock Eng* 2019;52:1459–74. <https://doi.org/10.1007/S00603-018-1660-5/FIGURES/20>.
- Gong F, Wang Y, Luo S. Rockburst proneness criteria for rock materials: Review and new insights. *J Cent South Univ* 2020;27:2793–821. <https://doi.org/10.1007/s11771-020-4511-y>.
- Gong F, Wu W, Ren L. Rockburst process and strength-weakening effect of the high-stress circular tunnel under internal unloading. *Journal of Rock Mechanics and Geotechnical Engineering* 2023a;15:864–85. <https://doi.org/10.1016/J.JRMGE.2022.10.016>.
- Gong QM, Yin LJ, Wu SY, Zhao J, Ting Y. Rock burst and slabbing failure and its influence on TBM excavation at headrace tunnels in Jinping II hydropower station. *Eng Geol* 2012a;124:98–108. <https://doi.org/10.1016/J.ENGGE.2011.10.007>.
- Gong QM, Zhao J. Influence of rock brittleness on TBM penetration rate in Singapore granite. *Tunnelling and Underground Space Technology* 2007;22:317–24. <https://doi.org/10.1016/J.TUST.2006.07.004>.
- Goodman RE. *Introduction to rock mechanics*. vol. 2. Wiley New York; 1989.
- Gottsbacher L, Klammer A, Schubert W, Marschallinger R, Hofmann P, Zobl F, Hofmann P, Ketcham R, Edey D. Combination of various laboratory tests to investigate rock burst. *Rock Mechanics for Natural Resources and Infrastructure Development- Proceedings of the 14th International Congress on Rock Mechanics and Rock Engineering, ISRM 2019, Foz Do Iguassu, Brazil: CRC Press; 2020*, p. 1700–6.
- Gulia L, Wiemer S. Real-time discrimination of earthquake foreshocks and aftershocks. *Nature* 2019 574:7777 2019;574:193–9. <https://doi.org/10.1038/s41586-019-1606-4>.
- Gutierrez M, Katsuki D, Nygaard R. Shear Failure and Fracturing of Horizontally Layered Shale. 15th ISRM Congress & 72nd Geomechanics Colloquium, Salzburg, Austria: OnePetro; 2023.
- Haach VG, Vasconcelos G, Loureno PB. Influence of aggregates grading and water/cement ratio in workability and hardened properties of mortars. *Constr Build Mater* 2011;25:2980–7. <https://doi.org/10.1016/J.CONBUILDMAT.2010.11.011>.
- Haimson B. Micromechanisms of borehole instability leading to breakouts in rocks. *International Journal of Rock Mechanics and Mining Sciences* 2007;44:157–73. <https://doi.org/10.1016/J.IJRMMS.2006.06.002>.

- Haimson B, Rudnicki JW. The effect of the intermediate principal stress on fault formation and fault angle in siltstone. *J Struct Geol* 2010;32:1701–11. <https://doi.org/10.1016/J.JSG.2009.08.017>.
- Haimson BC. Borehole breakouts in Berea sandstone reveal a new fracture mechanism. *Pure Appl Geophys* 2003;160:813–31. <https://doi.org/10.1007/PL00012567/METRICS>.
- Haimson BC, Herrick CG. Borehole breakouts and in situ stress. 12th annual energy-sources technology conference and exhibition, Houston, New York, 1989, vol. 22, 1989, p. 17–22.
- Hajiabdolmajid V. Modeling brittle failure of rock. *Rock Mechanics and Engineering Volume 1*, CRC Press; 2017, p. 593–621.
- Hajiabdolmajid V, Kaiser P. Brittleness of rock and stability assessment in hard rock tunneling. *Tunnelling and Underground Space Technology* 2003;18:35–48. [https://doi.org/10.1016/S0886-7798\(02\)00100-1](https://doi.org/10.1016/S0886-7798(02)00100-1).
- Halder SK, Tišljär J. Chapter 1 - Rocks and Minerals. In: Halder SK, Tišljär J, editors. *Introduction to Mineralogy and Petrology*, Oxford: Elsevier; 2014, p. 1–37. <https://doi.org/10.1016/B978-0-12-408133-8.00001-8>.
- Hampton J, Gutierrez M, Matzar L, Hu D, Frash L. Acoustic emission characterization of microcracking in laboratory-scale hydraulic fracturing tests. *Journal of Rock Mechanics and Geotechnical Engineering* 2018;10:805–17. <https://doi.org/10.1016/J.JRMGE.2018.03.007>.
- Hardy HR. Applications Of Acoustic Emission Techniques To Rock And Rock Structures: A State-Of-The-Art Review. *ASTM Special Technical Publication* 1981:4–92. <https://doi.org/10.1520/STP28342S>.
- He M, Cheng T, Qiao Y, Li H. A review of rockburst: Experiments, theories, and simulations. *Journal of Rock Mechanics and Geotechnical Engineering* 2023;15:1312–53. <https://doi.org/10.1016/J.JRMGE.2022.07.014>.
- He M, Miao JL, Feng JL. Rock burst process of limestone and its acoustic emission characteristics under true-triaxial unloading conditions. *Int J Rock Mech Min Sci* 2010;47:286–98. <https://doi.org/10.1016/J.IJRMMS.2009.09.003>.
- Herrick CG, Haimson BC. Modeling of Episodic Failure Leading to Borehole Breakouts in Alabama Limestone 1994.
- Heuer RE, Hendron AJ. Geomechanical model study of the behavior of underground openings in rock subjected to static loads: Report 2: Tests on unlined openings intact rock. 1971.
- Hoek E, Brown ET. The Hoek–Brown failure criterion and GSI – 2018 edition. *Journal of Rock Mechanics and Geotechnical Engineering* 2019;11:445–63. <https://doi.org/10.1016/J.JRMGE.2018.08.001>.
- Hoek E, Kaiser P. *Support of Underground Excavation in Hard Rock* 1995.
- Hoek E, Marinos PG. *Tunnelling in Overstressed Rock* 2009.
- Hoek E, Martin CD. Fracture initiation and propagation in intact rock – A review. *Journal of Rock Mechanics and Geotechnical Engineering* 2014;6:287–300. <https://doi.org/10.1016/J.JRMGE.2014.06.001>.
- Hu X, Su G, Chen G, Mei S, Feng X, Mei G, Huang X. Experiment on Rockburst Process of Borehole and Its Acoustic Emission Characteristics. *Rock Mech Rock Eng* 2019;52:783–802. <https://doi.org/10.1007/S00603-018-1613-Z/FIGURES/24>.

- Hu X, Su G, Li Z, Xu C, Yan X, Liu Y, Yan L. Suppressing rockburst by increasing the tensile strength of rock surface: An experimental study. *Tunnelling and Underground Space Technology* 2021;107. <https://doi.org/10.1016/j.tust.2020.103645>.
- Huang JT, Airey DW. Properties of artificially cemented carbonate sand. *Journal of Geotechnical and Geoenvironmental Engineering* 1998;124:492–9.
- Hucka V, Das B. Brittleness determination of rocks by different methods. *International Journal of Rock Mechanics and Mining Sciences & Geomechanics Abstracts* 1974;11:389–92. [https://doi.org/10.1016/0148-9062\(74\)91109-7](https://doi.org/10.1016/0148-9062(74)91109-7).
- Hudson JA, Crouch SL, Fairhurst C. Soft, stiff and servo-controlled testing machines: a review with reference to rock failure. *Eng Geol* 1972;6:155–89. [https://doi.org/10.1016/0013-7952\(72\)90001-4](https://doi.org/10.1016/0013-7952(72)90001-4).
- Indraratna B. Development and applications of a synthetic material to simulate soft sedimentary rocks. *Geotechnique* 1990;40:189–200. <https://doi.org/10.1680/GEOT.1990.40.2.189>.
- Ishida T, Labuz JF, Manthei G, Meredith PG, Nasser MHB, Shin K, Yokoyama T, Zang A. ISRM Suggested Method for Laboratory Acoustic Emission Monitoring. *Rock Mech Rock Eng* 2017;50:665–74. <https://doi.org/10.1007/S00603-016-1165-Z/FIGURES/8>.
- ISRM. Suggested methods for determining tensile strength of rock materials. *International Journal of Rock Mechanics and Mining Sciences & Geomechanics Abstracts* 1978;15:99–103. [https://doi.org/10.1016/0148-9062\(78\)90003-7](https://doi.org/10.1016/0148-9062(78)90003-7).
- Jacobsson L, Appelquist K, Lindkvist JE. Spalling Experiments on Large Hard Rock Specimens. *Rock Mech Rock Eng* 2015;48:1485–503. <https://doi.org/10.1007/s00603-014-0655-0>.
- Jiao Y, Zhang Y, Zhang M, Fu L, Zhang L. Investigation of fracture modes in pervious asphalt under splitting and compression based on acoustic emission monitoring. *Eng Fract Mech* 2019;211:209–20. <https://doi.org/10.1016/J.ENGFRACMECH.2019.02.025>.
- Johnson GR, Olhoeft GR. Section II: Densities of rocks and minerals. *Practical Handbook of Physical Properties of Rocks and Minerals*, CRC Press; 1989, p. 173.
- Johnston IW, Choi SK. A synthetic soft rock for laboratory model studies. <https://doi.org/10.1680/Geot1986362251> 1986;36:251–63. <https://doi.org/10.1680/GEOT.1986.36.2.251>.
- Kaiser PK. *From Common to Best Practices in Underground Rock Engineering* 2019.
- Kaiser PK. Challenge of managing highly stressed ground in civil and mining projects *Ground Support for Constructability of deep underground excavation* 2016.
- Kaiser PK, Kim BH. Characterization of Strength of Intact Brittle Rock Considering Confinement-Dependent Failure Processes. *Rock Mech Rock Eng* 2015;48:107–19. <https://doi.org/10.1007/S00603-014-0545-5/FIGURES/11>.
- Kaiser PK, McCreath DR, Tannant DD. *Canadian Rockburst Support Handbook* 1996:1.4.
- Kamada T, Iwanami M, Nagataki S. Acoustic emission discrimination of crack types in reinforced concrete beams. *FRAMCOS-3*, 1998, p. 57–66.
- Kassir MK, Bandyopadhyay KK, Reich M. *Thermal Degradation Of Concrete In The Temperature Range From Ambient To 315°C (600°F)* 1996.



- Kawata T, Nakano Y, Matsumoto T, Mito A, Pittard F, Noda H. Challenge in high-speed TBM excavation of long-distance water transfer tunnel, pahang-selangor raw water transfer tunnel, Malaysia. ISRM International Symposium - 8th Asian Rock Mechanics Symposium, ARMS 2014 2014;2112–21.
- Keneti A, Sainsbury BA. Development of a comparative index for the assessment of the severity of violent brittle failures around underground excavations. *Eng Geol* 2020;270:105596. <https://doi.org/10.1016/J.ENGGEOL.2020.105596>.
- Khadivi B, Heidarpour A, Zhang Q, Masoumi H. Characterizing the cracking process of various rock types under Brazilian loading based on coupled Acoustic Emission and high-speed imaging techniques. *International Journal of Rock Mechanics and Mining Sciences* 2023;168:105417. <https://doi.org/10.1016/J.IJRMMS.2023.105417>.
- Kim BH, Walton G, Larson MK, Berry S. Investigation of the anisotropic confinement-dependent brittleness of a Utah coal. *Int J Coal Sci Technol* 2021;8:274–90. <https://doi.org/10.1007/s40789-020-00364-7>.
- Kirsch EG. Die Theorie der Elastizität und die Bedingungen der Festigkeitslehre. *Zeitschrift Des Vereines Deutscher Ingenieure* 1898;42:797–807.
- Klammer A, Peintner C, Gottsbacher L, Biermann J, Bluemel M, Schubert W, Marcher T. Investigation of the Influence of Grain-Scale Heterogeneity on Strainburst Proneness Using Rock-Like Material. *Rock Mech Rock Eng* 2023;56:407–25. <https://doi.org/10.1007/S00603-022-03078-1>.
- Klammer A, Peintner C, Lagger M, Blümel M, Schubert W. Investigations of rockburst propensity of artificial samples containing different aggregates. *ISRM AfriRock - Rock Mechanics for Africa* 2017;2017-Octob:189–200.
- Kovari K, Tisa A, Einstein HH, Franklin JA. Suggested methods for determining the strength of rock materials in triaxial compression: Revised version. *Intl J of Rock Mech & Mining Sci & Geomechanic Abs* 1983;20.
- Kusui A, Villaescusa E, Funatsu T. Mechanical behaviour of scaled-down unsupported tunnel walls in hard rock under high stress. *Tunn Undergr Space Technol* 2016;60:30–40. <https://doi.org/10.1016/J.TUST.2016.07.012>.
- Kwaśniewski M, Szutkowski I, Wang JA. Study of ability of coal from seam 510 for storing elastic energy in the aspect of assessment of hazard in Porabka-Klimontow Colliery. *Sci Rept Silesian Technical University* 1994.
- Labuz JF, Dai ST, Papamichos E. Plane-strain compression of rock-like materials. *International Journal of Rock Mechanics and Mining Sciences & Geomechanics Abstracts* 1996;33:573–84. [https://doi.org/10.1016/0148-9062\(96\)00012-5](https://doi.org/10.1016/0148-9062(96)00012-5).
- Lama RD, Vutukuri VS. Handbook on mechanical properties of rocks. Vol. II. Clausthal. Trans Tech Publications 1978.
- Lapins S, Goitom B, Kendall JM, Werner MJ, Cashman KV., Hammond JOS. A Little Data Goes a Long Way: Automating Seismic Phase Arrival Picking at Nabro Volcano With Transfer Learning. *J Geophys Res Solid Earth* 2021;126:e2021JB021910. <https://doi.org/10.1029/2021JB021910>.
- Lee M, Haimson B. Laboratory study of borehole breakouts in Lac du Bonnet granite: a case of extensile failure mechanism. *International Journal of Rock Mechanics and Mining Sciences & Geomechanics Abstracts* 1993;30:1039–45. [https://doi.org/10.1016/0148-9062\(93\)90069-P](https://doi.org/10.1016/0148-9062(93)90069-P).

- Lei X, Masuda K, Nishizawa O, Jouniaux L, Liu L, Ma W, Satoh T, Kusunose K. Detailed analysis of acoustic emission activity during catastrophic fracture of faults in rock. *J Struct Geol* 2004;26:247–58. [https://doi.org/10.1016/S0191-8141\(03\)00095-6](https://doi.org/10.1016/S0191-8141(03)00095-6).
- Li CC. Rockbolting Design. *Rockbolting* 2017;125–76. <https://doi.org/10.1016/B978-0-12-804401-8.00005-3>.
- Li J, Gong SY, He J, Cai W, Zhu GA, Wang CB, Chen T. Spatio-temporal assessments of rockburst hazard combining b values and seismic tomography. *Acta Geophysica* 2017;65:77–88. <https://doi.org/10.1007/S11600-017-0008-Y/METRICS>.
- Li LR, Deng JH, Zheng L, Liu JF. Dominant Frequency Characteristics of Acoustic Emissions in White Marble During Direct Tensile Tests. *Rock Mech Rock Eng* 2017;50:1337–46. <https://doi.org/10.1007/S00603-016-1162-2/FIGURES/7>.
- Li Y, Ghassemi A. Rock Failure Envelope and Behavior Using the Confined Brazilian Test. *J Geophys Res Solid Earth* 2021;126. <https://doi.org/10.1029/2021JB022471>.
- Lin H, Oh J, Canbulat I, Stacey TR. Experimental and Analytical Investigations of the Effect of Hole Size on Borehole Breakout Geometries for Estimation of In Situ Stresses. *Rock Mech Rock Eng* 2020;53:781–98. <https://doi.org/10.1007/S00603-019-01944-Z/FIGURES/19>.
- Lin P, Liu H, Zhou W. Experimental study on failure behaviour of deep tunnels under high in-situ stresses. *Tunnelling and Underground Space Technology* 2015;46:28–45. <https://doi.org/10.1016/J.TUST.2014.10.009>.
- Liu CC, Zhang QY, Xiang W, Zhou XY. Experimental Study on Characteristics and Mechanism of Macrography and Mesoscopic Failure of Deep Granite from Beishan. *Geotechnical and Geological Engineering* 2020;38:3815–30. <https://doi.org/10.1007/S10706-020-01260-2/FIGURES/19>.
- Liu X, Han M, He W, Li X, Chen D. A New b Value Estimation Method in Rock Acoustic Emission Testing. *J Geophys Res Solid Earth* 2020a;125:e2020JB019658. <https://doi.org/10.1029/2020JB019658>.
- Liu X, Liang Z, Zhang Y, Liang P, Tian B. Experimental study on the monitoring of rockburst in tunnels under dry and saturated conditions using AE and infrared monitoring. *Tunnelling and Underground Space Technology* 2018;82:517–28. <https://doi.org/10.1016/j.tust.2018.08.011>.
- Liu X, Liu Z, Li X, Gong F, Du K. Experimental study on the effect of strain rate on rock acoustic emission characteristics. *International Journal of Rock Mechanics and Mining Sciences* 2020b;133:104420. <https://doi.org/10.1016/J.IJRMMS.2020.104420>.
- Lockner D. The role of acoustic emission in the study of rock fracture. *International Journal of Rock Mechanics and Mining Sciences & Geomechanics Abstracts* 1993;30:883–99. [https://doi.org/10.1016/0148-9062\(93\)90041-B](https://doi.org/10.1016/0148-9062(93)90041-B).
- Lockner DA, Byerlee JD, Kuksenko V, Ponomarev A, Sidorin A. Quasi-static fault growth and shear fracture energy in granite. *Nature* 1991 350:6313 1991;350:39–42. <https://doi.org/10.1038/350039a0>.
- Luo Y, Gong FQ, Li XB, Wang SY. Experimental simulation investigation of influence of depth on spalling characteristics in circular hard rock tunnel. *Journal of Central South University* 2020 27:3 2020;27:891–910. <https://doi.org/10.1007/S11771-020-4339-5>.

- Martin CD, Chandler NA. The progressive fracture of Lac du Bonnet granite. *International Journal of Rock Mechanics and Mining Sciences & Geomechanics Abstracts* 1994;31:643–59. [https://doi.org/10.1016/0148-9062\(94\)90005-1](https://doi.org/10.1016/0148-9062(94)90005-1).
- Martin CD, Christiansson R. Estimating the potential for spalling around a deep nuclear waste repository in crystalline rock. *International Journal of Rock Mechanics and Mining Sciences* 2009;46:219–28. <https://doi.org/10.1016/J.IJRMMS.2008.03.001>.
- Martin CD, Kaiser PK, McCreath DR. Hoek-Brown parameters for predicting the depth of brittle failure around tunnels 1999.
- Martin CD, Martino JB, Dzik EJ. Comparison of borehole breakouts from laboratory and field tests 1994. <https://doi.org/10.2118/28050-MS>.
- Martin CD, Read RS, Martino JB. Observations of brittle failure around a circular test tunnel. *International Journal of Rock Mechanics and Mining Sciences* 1997;34:1065–73. [https://doi.org/10.1016/S1365-1609\(97\)90200-8](https://doi.org/10.1016/S1365-1609(97)90200-8).
- Martino JB, Chandler NA. Excavation-induced damage studies at the Underground Research Laboratory. *International Journal of Rock Mechanics and Mining Sciences* 2004;41:1413–26. <https://doi.org/10.1016/J.IJRMMS.2004.09.010>.
- Mazaira A, Konicek P. Intense rockburst impacts in deep underground construction and their prevention. *Canadian Geotechnical Journal* 2015;52:1426–39. <https://doi.org/10.1139/CGJ-2014-0359/ASSET/IMAGES/LARGE/CGJ-2014-0359F10.JPEG>.
- Mehta P, Monteiro P. Concrete: microstructure, properties, and materials. McGraw-Hill Education; 2014.
- Meng F, Wong LNY, Zhou H. Rock brittleness indices and their applications to different fields of rock engineering: A review. *Journal of Rock Mechanics and Geotechnical Engineering* 2021;13:221–47. <https://doi.org/10.1016/J.JRMGE.2020.06.008>.
- Meng Q, Zhang M, Han L, Pu H, Chen Y. Acoustic Emission Characteristics of Red Sandstone Specimens Under Uniaxial Cyclic Loading and Unloading Compression. *Rock Mech Rock Eng* 2018;51:969–88. <https://doi.org/10.1007/S00603-017-1389-6/FIGURES/12>.
- Mirshekari M, Ghayoomi M, Borghei A. A Review on Soil-Water Retention Scaling in Centrifuge Modeling of Unsaturated Sands. *Geotechnical Testing Journal* 2018;41:979–97. <https://doi.org/10.1520/GTJ20170120>.
- MISTRAS Group. WSA Sensor Product Data Sheet. Princeton Junction, NJ, USA: 2013.
- Mogi K. Pressure Dependence of Rock Strength and Transition from Brittle Fracture to Ductile Flow. 1966.
- Moradian O, Gutierrez M, Wibisono DY, Gautam PK. TBM Performance Evaluation Using Seismic Data During Excavation: A Comparative Examination of Clustering Algorithms. 5th International Conference on Information Technology in Geo-engineering, Golden: 2024.
- Moradian Z, Einstein HH, Ballivy G. Detection of Cracking Levels in Brittle Rocks by Parametric Analysis of the Acoustic Emission Signals. *Rock Mech Rock Eng* 2016;49:785–800. <https://doi.org/10.1007/S00603-015-0775-1/FIGURES/17>.
- Moss A, Kaiser PK. An operational approach to ground control in deep mines. *Journal of Rock Mechanics and Geotechnical Engineering* 2022;14:67–81. <https://doi.org/10.1016/J.JRMGE.2021.05.008>.

- Mutke G, Pierzyna A, Barański A. b-value as a criterion for the evaluation of rockburst hazard in coal mines 2016.
- Naji AM, Emad MZ, Rehman H, Yoo H. Geological and geomechanical heterogeneity in deep hydropower tunnels: A rock burst failure case study. *Tunnelling and Underground Space Technology* 2019;84:507–21. <https://doi.org/10.1016/J.TUST.2018.11.009>.
- Nanjo KZ, Yukutake Y, Kumazawa T. Activated volcanism of Mount Fuji by the 2011 Japanese large earthquakes. *Scientific Reports* 2023 13:1 2023;13:1–15. <https://doi.org/10.1038/s41598-023-37735-4>.
- Naylor M, Orfanogiannaki K, Harte D. Exploratory data analysis: magnitude, space, and time. Community Online Resource for Statistical Seismicity Analysis 2010. <https://doi.org/10.5078/corssa-92330203>.
- Neville AM, Brooks JJ. *Concrete technology* 2010:442.
- Nygård R, Gutierrez M, Bratli RK, Høeg K. Brittle–ductile transition, shear failure and leakage in shales and mudrocks. *Mar Pet Geol* 2006;23:201–12. <https://doi.org/10.1016/J.MARPETGEO.2005.10.001>.
- Obert L, Duvall WI. Use of subaudible noises for the prediction of rock bursts: part II. US Department of the Interior, Bureau of Mines; 1942.
- Ohno K, Ohtsu M. Crack classification in concrete based on acoustic emission. *Constr Build Mater* 2010;24:2339–46. <https://doi.org/10.1016/J.CONBUILDMAT.2010.05.004>.
- Ohtsu M, Shiotani T, Shigeishi M, Kamada T, Yuyama S, Watanabe T, Suzuki T, van Mier J, Vogel T, Grosse C, Helmerich R, Forde M, Moczko A, Breyse D, Ivanovich S, Sajna A, Aggelis D, Lacidogna G. Recommendation of RILEM TC 212-ACD: Acoustic emission and related NDE techniques for crack detection and damage evaluation in concrete: Test method for classification of active cracks in concrete structures by acoustic emission. *Materials and Structures/Materiaux et Constructions* 2010;43:1187–9. <https://doi.org/10.1617/S11527-010-9640-6/FIGURES/2>.
- Ortlepp WD. *Rock Fracture and Rockbursts : an illustrative study*. Johannesburg: The South African Institute of Mining and Metallurgy; 1997.
- Ortlepp WD, Stacey TR. Rockburst mechanisms in tunnels and shafts. *Tunnelling and Underground Space Technology* 1994;9:59–65. [https://doi.org/10.1016/0886-7798\(94\)90010-8](https://doi.org/10.1016/0886-7798(94)90010-8).
- Palchik V. Influence of porosity and elastic modulus on uniaxial compressive strength in soft brittle porous sandstones. *Rock Mech Rock Eng* 1999;32:303–9. <https://doi.org/10.1007/S006030050050/METRICS>.
- Palmström A. Characterizing Rock Burst and Squeezing by the Rock Mass Index. *Design and Construction of Underground Structures* 1995;c:23–5.
- Pan PZ, Miao S, Wu Z, Feng XT, Shao C. Laboratory Observation of Spalling Process Induced by Tangential Stress Concentration in Hard Rock Tunnel 2020. [https://doi.org/10.1061/\(ASCE\)GM.1943-5622.0001620](https://doi.org/10.1061/(ASCE)GM.1943-5622.0001620).
- Patel S. Impact of Confined Extension on the Failure Envelope of Intact Low-Porosity Rock 2018. <https://doi.org/10.7939/R3W95143K>.
- Paterson MS, Wong TF. Experimental rock deformation - The brittle field. *Experimental Rock Deformation - The Brittle Field* 2005:1–347. <https://doi.org/10.1007/B137431/COVER>.

- Perras MA, Diederichs MS. Predicting excavation damage zone depths in brittle rocks. *Journal of Rock Mechanics and Geotechnical Engineering* 2016;8:60–74.  
<https://doi.org/10.1016/J.JRMGE.2015.11.004>.
- Pinto C, Fonseca J. Mechanical behavior of high strength granite for new prestressed stone structures. *International Journal of Rock Mechanics and Mining Sciences* 2013;60:452–60.  
<https://doi.org/10.1016/J.IJRMMS.2012.12.010>.
- Powell-Palm MJ, Rubinsky B, Sun W. Freezing water at constant volume and under confinement. *Communications Physics* 2020 3:1 2020;3:1–8. <https://doi.org/10.1038/s42005-020-0303-9>.
- Pratomo FY, Karakus M, Nguyen GD, Bui HH. Micro- and macro-scale fracture behaviour of brittle rocks: Comparison between the conventional Brazilian test and the advanced universal snap-back indirect tensile test (AUSBIT). *International Journal of Rock Mechanics and Mining Sciences* 2024;183:105897. <https://doi.org/10.1016/J.IJRMMS.2024.105897>.
- Primadiansyah AA. Measurement of stress fracturing and bulking for deformation-based ground support design calibration in a deep caving operation 2024. <https://doi.org/10.14288/1.0440616>.
- Primadiansyah AA, Eberhardt E, Campbell R, Firmanulhaq S, Silaen H, Perdana A. Integrating Stress Fracturing and Bulking Monitoring for Deformation-Based Ground Support Design Calibration in a Deep Caving Operation 2024. <https://doi.org/10.56952/ARMA-2024-0481>.
- Qaidahiyani N, Widodo NP. Study of Displacement Distribution Around Circular Opening Affected by Presence of Discontinuities Using Laboratory Biaxial Test. *Proc. Asian Rock Mechanics Symposium, Bali, Indonesia, 2016, 2016*.
- Qiu S, Feng XT, Zhang X, Kong R. Brittleness and Ductility of Rocks. *Rockburst: Mechanisms, Monitoring, Warning, and Mitigation*, 2018, p. 117–50. <https://doi.org/10.1016/B978-0-12-805054-5.00005-6>.
- Rahjoo M. Directional and 3-D confinement-dependent fracturing, strength and dilation mobilization in brittle rocks 2019. <https://doi.org/10.14288/1.0384518>.
- Ramsey JM, Chester FM. Hybrid fracture and the transition from extension fracture to shear fracture. *Nature* 2004 428:6978 2004;428:63–6. <https://doi.org/10.1038/nature02333>.
- Rao GMN, Murthy CR, Raju NMS. Characterization of Micro and Macro Cracks in Rocks by Acoustic Emission. *Acoustic emission: standards and technology update*, ASTM International; 1999.
- Rao MVMS, Lakshmi KJP. Analysis of b-value and improved b-value of acoustic emissions accompanying rock fracture. *Curr Sci* 2005;89:1577–82.
- Rath S, Ouchi M, Puthipad N, Attachaiyawuth A. Improving the stability of entrained air in self-compacting concrete by optimizing the mix viscosity and air entraining agent dosage. *Constr Build Mater* 2017;148:531–7. <https://doi.org/10.1016/J.CONBUILDMAT.2017.05.105>.
- Rawlings CG, Barton NR, Bandis SC, Addis MA, Gutierrez M. Laboratory and Numerical Discontinuum Modeling of Wellbore Stability. *Journal of Petroleum Technology* 1993;45:1086–92.  
<https://doi.org/10.2118/25869-PA>.
- Read RS. 20 years of excavation response studies at AECL's Underground Research Laboratory. *International Journal of Rock Mechanics and Mining Sciences* 2004;41:1251–75.  
<https://doi.org/10.1016/J.IJRMMS.2004.09.012>.
- Read RS, Martin CD. Mine-By Experiment Final Design Report. AECL Research 1991.

- Rice-Birchall E, Faulkner DR, Bedford JD. The manufacture, mechanical properties, and microstructural analysis of synthetic quartz-cemented sandstones. *International Journal of Rock Mechanics and Mining Sciences* 2021;146:104869. <https://doi.org/https://doi.org/10.1016/j.ijrmms.2021.104869>.
- Richter CF. *Elementary Seismology* 1958.
- Rocscience Inc. *RSDData User Guide* 2022.
- Rojat F, Labiouse V, Kaiser PK, Descoeudres F. Brittle rock failure in the steg lateral adit of the lötschberg base tunnel. *Rock Mech Rock Eng* 2009;42:341–59. <https://doi.org/10.1007/S00603-008-0015-Z/METRICS>.
- Russenes BF. *Analysis of rock spalling for tunnels in steep valley sides*. Norwegian Institute of Technology 1974.
- Saceanu MC, Paluszny A, Zimmerman RW, Mas Ivars D. Fracture growth leading to mechanical spalling around deposition boreholes of an underground nuclear waste repository. *International Journal of Rock Mechanics and Mining Sciences* 2022;152:105038. <https://doi.org/10.1016/J.IJRMMS.2022.105038>.
- Safiuddin M, Hearn N. Comparison of ASTM saturation techniques for measuring the permeable porosity of concrete. *Cem Concr Res* 2005;35:1008–13. <https://doi.org/10.1016/J.CEMCONRES.2004.09.017>.
- Sagar RV, Prasad BKR, Kumar SS. An experimental study on cracking evolution in concrete and cement mortar by the b-value analysis of acoustic emission technique. *Cem Concr Res* 2012;42:1094–104. <https://doi.org/10.1016/J.CEMCONRES.2012.05.003>.
- Sahara DP, Schoenball M, Gerolymatou E, Kohl T. Analysis of borehole breakout development using continuum damage mechanics. *International Journal of Rock Mechanics and Mining Sciences* 2017;97:134–43. <https://doi.org/10.1016/J.IJRMMS.2017.04.005>.
- Sapidis NS, Frey WH. Controlling the curvature of a quadratic Bézier curve. *Comput Aided Geom Des* 1992;9:85–91. [https://doi.org/10.1016/0167-8396\(92\)90008-D](https://doi.org/10.1016/0167-8396(92)90008-D).
- Schneider CA, Rasband WS, Eliceiri KW. NIH Image to ImageJ: 25 years of image analysis. *Nat Methods* 2012;9:671–5. <https://doi.org/10.1038/nmeth.2089>.
- Schoenball M, Sahara DP, Kohl T. Time-dependent brittle creep as a mechanism for time-delayed wellbore failure. *International Journal of Rock Mechanics and Mining Sciences* 2014;70:400–6. <https://doi.org/10.1016/J.IJRMMS.2014.05.012>.
- Scholz CH. The frequency-magnitude relation of microfracturing in rock and its relation to earthquakes. *Bulletin of the Seismological Society of America* 1968;58:399–415. <https://doi.org/10.1785/BSSA0580010399>.
- Shen B, Barton N. *Rock fracturing mechanisms around underground openings*. Geomechanics and Engineering 2018.
- Shen B, Siren T, Rinne M. Modelling Fracture Propagation in Anisotropic Rock Mass. *Rock Mech Rock Eng* 2015;48:1067–81. <https://doi.org/10.1007/S00603-014-0621-X>.
- Shull PJ. *Nondestructive evaluation : theory, techniques, and applications* 2002.
- Singh B, Goel RK, Mehrotra VK, Garg SK, Allu MR. Effect of intermediate principal stress on strength of anisotropic rock mass. *Tunnelling and Underground Space Technology* 1998;13:71–9. [https://doi.org/10.1016/S0886-7798\(98\)00023-6](https://doi.org/10.1016/S0886-7798(98)00023-6).

- Siren T. Excavation damage zones, fracture mechanics simulation and in situ strength of migmatitic gneiss and pegmatitic granite at the nuclear waste disposal site in Olkiluoto, Western Finland. School of Engineering, 2015.
- Siren T, Hakala M, Valli J, Kantia P, Hudson JA, Johansson E. In situ strength and failure mechanisms of migmatitic gneiss and pegmatitic granite at the nuclear waste disposal site in Olkiluoto, Western Finland. *International Journal of Rock Mechanics and Mining Sciences* 2015a;79:135–48. <https://doi.org/10.1016/J.IJRMMS.2015.08.012>.
- Siren T, Kantia P, Rinne M. Considerations and observations of stress-induced and construction-induced excavation damage zone in crystalline rock. *International Journal of Rock Mechanics and Mining Sciences* 2015b;73:165–74. <https://doi.org/10.1016/J.IJRMMS.2014.11.001>.
- Siren T, Uotinen L, Rinne M, Shen B. Fracture Mechanics Modelling of an In Situ Concrete Spalling Experiment. *Rock Mech Rock Eng* 2015;48:1423–38. <https://doi.org/10.1007/S00603-014-0646-1>.
- Stimpson B. Modelling materials for engineering rock mechanics. *International Journal of Rock Mechanics and Mining Sciences* And 1970;7:77–121. [https://doi.org/10.1016/0148-9062\(70\)90029-X](https://doi.org/10.1016/0148-9062(70)90029-X).
- Su G, Chen Y, Jiang Q, Li C, Cai W. Spalling failure of deep hard rock caverns. *Journal of Rock Mechanics and Geotechnical Engineering* 2023;15:2083–104. <https://doi.org/10.1016/J.JRMGE.2022.11.021>.
- Su G, Feng X, Wang J, Jiang J, Hu L. Experimental Study of Remotely Triggered Rockburst Induced by a Tunnel Axial Dynamic Disturbance Under True-Triaxial Conditions. *Rock Mech Rock Eng* 2017;50:2207–26. <https://doi.org/10.1007/s00603-017-1218-y>.
- Sun XM, Xu HC, Zheng LG, He MC, Gong WL. An experimental investigation on acoustic emission characteristics of sandstone rockburst with different moisture contents. *Science China Technological Sciences* 2016 59:10 2016;59:1549–58. <https://doi.org/10.1007/S11431-016-0181-8>.
- Tatone BSA, Abdelaziz A, Grasselli G. Example framework for evaluation of synthetic rock-like materials as applied to a commercial gypsum cement. *International Journal of Rock Mechanics and Mining Sciences* 2023;169:105445. <https://doi.org/10.1016/J.IJRMMS.2023.105445>.
- Trzeciak M, Sone H. Polyaxial failure criteria for in situ stress analysis using borehole breakouts: Review of existing methods and development of an empirical alternative. *International Journal of Rock Mechanics and Mining Sciences* 2024;182:105864. <https://doi.org/10.1016/J.IJRMMS.2024.105864>.
- Tsang CF, Bernier F, Davies C. Geohydromechanical processes in the Excavation Damaged Zone in crystalline rock, rock salt, and indurated and plastic clays—in the context of radioactive waste disposal. *International Journal of Rock Mechanics and Mining Sciences* 2005;42:109–25. <https://doi.org/10.1016/J.IJRMMS.2004.08.003>.
- Tunstall LE. A study of surfactant interaction in cement-based systems and the role of the surfactant in frost protection. Princeton University, 2016.
- Tunstall LE, Ley MT, Scherer GW. Air entraining admixtures: Mechanisms, evaluations, and interactions. *Cem Concr Res* 2021;150:106557. <https://doi.org/10.1016/J.CEMCONRES.2021.106557>.



- Ulusay R. The ISRM suggested methods for rock characterization, testing and monitoring: 2007–2014. Springer; 2015.
- Ulusay R, Hudson J. The Blue Book--The Complete ISRM Suggested Methods for Rock Characterization, Testing and Monitoring: 1974--2006. Ankara: ISRM Turkish National Group and the ISRM; 2007.
- Vardoulakis I, Sulem J, Guenot A. Borehole instabilities as bifurcation phenomena. *International Journal of Rock Mechanics and Mining Sciences & Geomechanics Abstracts* 1988;25:159–70. [https://doi.org/10.1016/0148-9062\(88\)92298-X](https://doi.org/10.1016/0148-9062(88)92298-X).
- Vazaios I, Vlachopoulos N, Diederichs MS. Assessing fracturing mechanisms and evolution of excavation damaged zone of tunnels in interlocked rock masses at high stresses using a finite-discrete element approach. *Journal of Rock Mechanics and Geotechnical Engineering* 2019;11:701–22. <https://doi.org/10.1016/J.JRMGE.2019.02.004>.
- Vlachopoulos N, Diederichs MS. Improved longitudinal displacement profiles for convergence confinement analysis of deep tunnels. *Rock Mech Rock Eng* 2009;42:131–46. <https://doi.org/10.1007/S00603-009-0176-4/METRICS>.
- Wang C. Evolution, monitoring and predicting models of rockburst: Precursor information for rock failure. *Evolution, Monitoring and Predicting Models of Rockburst: Precursor Information for Rock Failure* 2017:1–188. <https://doi.org/10.1007/978-981-10-7548-3/COVER>.
- Wang JA, Park HD. Comprehensive prediction of rockburst based on analysis of strain energy in rocks. *Tunnelling and Underground Space Technology* 2001;16:49–57. [https://doi.org/10.1016/S0886-7798\(01\)00030-X](https://doi.org/10.1016/S0886-7798(01)00030-X).
- Wang Y, Meng H, Long D. Experimental investigation of fatigue crack propagation in interbedded marble under multilevel cyclic uniaxial compressive loads. *Fatigue Fract Eng Mater Struct* 2021;44:933–51. <https://doi.org/10.1111/FFE.13404>.
- Wang Z, Feng XT, Yang C, Zhou Y, Xu H, Han Q, Gao YH Experimental investigation on fracturing process of marble under biaxial compression. *Journal of Rock Mechanics and Geotechnical Engineering* 2020;12:943–59. <https://doi.org/10.1016/J.JRMGE.2020.05.002>.
- Wesseloo J. Addressing misconceptions regarding seismic hazard assessment in mines: b-value,  $M_{max}$ , and space-time normalization. *The Journal of the Southern African Institute of Mining and Metallurgy* 2020;120. <https://doi.org/10.17159/2411>.
- Westerholm M, Lagerblad B, Silfwerbrand J, Forssberg E. Influence of fine aggregate characteristics on the rheological properties of mortars. *Cem Concr Compos* 2008;30:274–82. <https://doi.org/10.1016/J.CEMCONCOMP.2007.08.008>.
- Wibisono DY. Development of a very weak analog sandstone for brittle instability modelling in underground excavation 2024. <https://doi.org/10.25676/11124/179037>.
- Wibisono DY, Gutierrez M. Development of a very weak analogue sedimentary rock for experimental study to model brittle instability in tunneling. *Geotechnical Testing Journal*. Forthcoming.
- Wibisono DY, Gutierrez M. Investigation of Tunnel Spalling Using a Large-Scale Tunnel Model and Triaxial Extension Experiments. Forthcoming.
- Wibisono DY, Gutierrez M. Rockburst Analysis in Tunnel Under Anisotropic Loading Based on Large-Scale Tunnel Model Experiment and Triaxial Extension Test. Forthcoming.

- Wibisono DY, Gutierrez M. Identifying Acoustic Emission Precursors For Rock Spalling Onset Using Tunnel Model Schematics In A True-Triaxial Apparatus. Forthcoming.
- Wibisono DY, Arora K, Gutierrez M. Laboratory Characterization of a Synthetic Sandstone for Tunnel Rockburst Study. Paper presented at the 56th U.S. Rock Mechanics/Geomechanics Symposium, Santa Fe, NM: ARMA; 2022.
- Wibisono DY, Gutierrez M, Majumder D, Gautam PK. Development of a Weak But Brittle Analog Sediment Rock for Experimental Study. 57th US Rock Mechanics/Geomechanics Symposium 2023a. <https://doi.org/10.56952/ARMA-2023-080>.
- Wibisono DY, Arora K, Majumder D, Gutierrez M. Laboratory-Scale Rockburst Physical Model Testing Using a True-Triaxial Cell. IOP Conf Ser Earth Environ Sci 2023b;1124:12039. <https://doi.org/10.1088/1755-1315/1124/1/012039>.
- Wibisono DY, Gutierrez M, Majumder D. Experimental investigation of tunnel damage and spalling in brittle rock using a true-triaxial cell. International Journal of Rock Mechanics and Mining Sciences 2024;182:105884. <https://doi.org/https://doi.org/10.1016/j.ijrmms.2024.105884>.
- Woessner J, Wiemer S. Assessing the Quality of Earthquake Catalogues: Estimating the Magnitude of Completeness and Its Uncertainty. Bulletin of the Seismological Society of America 2005;95:684–98. <https://doi.org/10.1785/0120040007>.
- Wong TF, Baud P. The brittle-ductile transition in porous rock: A review. J Struct Geol 2012;44:25–53. <https://doi.org/10.1016/J.JSG.2012.07.010>.
- Wu Z, Zhang B, Weng L, Liu Q, Wong LNY. A New Way to Replicate the Highly Stressed Soft Rock: 3D Printing Exploration. Rock Mech Rock Eng 2020;53:467–76. <https://doi.org/10.1007/S00603-019-01926-1/FIGURES/7>.
- Xiao YX, Feng XT, Chen BR, Feng G. Latest Developments on Analysis of Data Monitored. Rockburst: Mechanisms, Monitoring, Warning, and Mitigation 2018:317–38. <https://doi.org/10.1016/B978-0-12-805054-5.00052-4>.
- Yu W, Wang W, Chen X, Du S. Field investigations of high stress soft surrounding rocks and deformation control. Journal of Rock Mechanics and Geotechnical Engineering 2015;7:421–33. <https://doi.org/10.1016/J.JRMGE.2015.03.014>.
- Yun X, Mitri HS, Yang X, Wang Y. Experimental investigation into biaxial compressive strength of granite. International Journal of Rock Mechanics and Mining Sciences 2010;47:334–41. <https://doi.org/10.1016/J.IJRMMS.2009.11.004>.
- Zeng B, Huang D, Ye S, Chen F, Zhu T, Tu Y. Triaxial extension tests on sandstone using a simple auxiliary apparatus. International Journal of Rock Mechanics and Mining Sciences 2019;120:29–40. <https://doi.org/10.1016/J.IJRMMS.2019.06.006>.
- Zhai S, Su G, Yin S, Zhao B, Yan L. Rockburst characteristics of several hard brittle rocks: A true triaxial experimental study. Journal of Rock Mechanics and Geotechnical Engineering 2020;12:279–96. <https://doi.org/10.1016/J.JRMGE.2019.07.013>.
- Zhang J, Peng W, Liu F, Zhang H, Li Z. Monitoring Rock Failure Processes Using the Hilbert–Huang Transform of Acoustic Emission Signals. Rock Mech Rock Eng 2016;49:427–42. <https://doi.org/10.1007/S00603-015-0755-5/FIGURES/10>.

- Zhang ZH, Deng JH. A new method for determining the crack classification criterion in acoustic emission parameter analysis. *International Journal of Rock Mechanics and Mining Sciences* 2020;130:104323. <https://doi.org/10.1016/J.IJRMMS.2020.104323>.
- Zhao XG, Wang J, Cai M, Cheng C, Ma LK, Su R, Zhao F, Li DJ. Influence of unloading rate on the strainburst characteristics of beishan granite under true-triaxial unloading conditions. *Rock Mech Rock Eng* 2014;47:467–83. <https://doi.org/10.1007/S00603-013-0443-2>.
- Zhao Y, Li X, Huang L, Zhang Z, Xu Z. Characteristic stress variation and microcrack evolution of granite subjected to uniaxial compression using acoustic emission methods. *Journal of Rock Mechanics and Geotechnical Engineering* 2024. <https://doi.org/10.1016/J.JRMGE.2023.11.023>.
- Zhu H, Yan J, Liang W. Challenges and Development Prospects of Ultra-Long and Ultra-Deep Mountain Tunnels. *Engineering* 2019;5:384–92. <https://doi.org/10.1016/J.ENG.2019.04.009>.
- Zhu W, Baud P, Wong T. Micromechanics of cataclastic pore collapse in limestone. *J Geophys Res Solid Earth* 2010;115. <https://doi.org/https://doi.org/10.1029/2009JB006610>.
- Zoback MD, Moos D, Mastin L, Anderson RN. Well Bore Breakouts And In Situ Stress. *J Geophys Res* 1985;90:5523–30. <https://doi.org/10.1029/JB090IB07P05523>.

## APPENDIX A IDENTIFYING ACOUSTIC EMISSION PRECURSORS FOR ROCK SPALLING ONSET USING TUNNEL MODEL IN A TRUE-TRIAxIAL APPARATUS<sup>1</sup>

### A.1 Abstract

Rock spalling is a type of brittle instability that occurs during tunnel excavation. Spalling degrades the rock mass, reducing its load-bearing capacity and compromising tunnel safety. Identifying precursors allows for timely mitigation measures and helps manage emerging changes during excavation and long-term tunnel stability. This study identifies acoustic emission (AE) signals that precede brittle spalling onset in a 51 mm diameter circular tunnel model. The tunnel was excavated in a  $300 \times 300 \times 300 \text{ mm}^3$  cubical analog rock specimen placed in the true-triaxial apparatus. The specimen was then incrementally loaded under three independent anisotropic compressive loadings until spalling failure was observed. Six wideband AE transducers were attached to the specimen to monitor seismic activity throughout the loading stage. This research aims to address two key questions: (1) What are possible precursors for spalling onset that can be identified from AE data? (2) Is there any strategy to improve the reliability and resolution of the precursors? The anisotropy and stress changes within the specimen promoted V-shaped notch failure progression at the tunnel wall characterized by extensional and shear fracturing. AE monitoring provided insights into the spalling onset, with specific signal patterns identified as precursors through frequency domain analysis (peak amplitude, average frequency, and rise angle) and *b*-value analysis. Temporal deconstruction emerged as the key strategy for AE parametric analysis, enhancing resolution into visible spalling onset and damage progression compared to physical observation. Both time interval analysis and moving number of hits were showcased to demonstrate the potential of each method. Identifying AE precursors enables the development of reliable early warning systems for brittle instabilities. This advancement enhances safety in tunneling and other underground excavation projects.

### A.2 Introduction

Brittle instability affects rock mass integrity, posing substantial risks during tunnel excavations and long-term stability. Unlike the squeezing response caused by the plastic flow of ductile rock, brittle rock exhibits fracturing from excessively induced stress, which eventually enlarges the opening (Bradley, 1979; Egger, 2000b). These fractures can range from superficial cracks to severe spalling. Fractures can even lead to strain bursting (Alcaino-Olivares et al., 2024; Diederichs, 2007b; Duan et al., 2019; Edelbro, 2009; Ortlepp and Stacey, 1994; Su et al., 2023). Such fractures reduce the load-bearing capacity of the

---

<sup>1</sup> This chapter will be submitted as a full journal paper for publication in an international peer-reviewed rock mechanics journal.

rock mass and render support systems ineffective (Kaiser et al., 1996; Primadiansyah, 2024). Over time, changes in stress conditions around supported tunnels, such as those induced by nearby additional excavations, can further compromise stability (Shen et al., 2015). This degradation poses safety hazards to personnel involved in tunneling and underground operations and increases maintenance costs (Moss and Kaiser, 2022).

Understanding and mitigating spalling becomes critical as tunneling projects advance into challenging geological conditions (Zhu et al., 2019). Identifying precursors to brittle spalling enables timely mitigation measures, helping manage changes during excavation and ensuring long-term tunnel stability. Acoustic emission (AE) and microseismic (MS) monitoring have long been recognized as a method for detecting precursors of rock failure (Hampton et al., 2018; Hardy, 1981; Lockner, 1993; Obert and Duvall, 1942; Shull, 2002). Historically, underground miners intuitively understood the importance of audible acoustic waves, evacuating mines when they heard cracking sounds from timber supports or crackling pops from the rock. Modern monitoring techniques build on this principle, using instruments to capture and analyze AE (high-frequency events) or MS (low-frequency events) associated with rock fracturing (Dresen et al., 2010; L. R. Li et al., 2017; Meng et al., 2018; Moradian et al., 2016). These efforts in capturing and analyzing acoustic events have led to predictive approaches as the basis for the prevention and control of brittle failure hazards (Wang, 2017). The similarities between AE and MS facilitate cross-collaborative efforts between field and laboratory, enhancing the understanding and mitigating the rock failure process.

This research addresses these critical issues by showcasing parametric AE data analysis methods. The explored methods will help understand brittle failure progression and visible onset in tunnel model schematics. Data was recorded from six AE transducers mounted on a cubical analog rock specimen with an excavated circular opening. This specimen was excavated and loaded in a true-triaxial apparatus developed at the Colorado School of Mines (Frash et al., 2014b). The analog rock was designed to exhibit a brittle response while having low uniaxial compressive strength (UCS) (Wibisono et al., 2023a). This tunnel model experiment allows for detailed analysis under well-controlled and instrumented conditions, which are difficult to replicate in the field.

The study focuses on documenting tunnel damage and spalling progression during the incremental loading stage under anisotropic stress conditions ( $\sigma_v > \sigma_H > \sigma_h$ ). Key aspects explored include the following: (1) parametric AE analysis for frequency domain analysis and  $b$ -value, (2) evaluation of temporal deconstruction features extraction towards visible spalling onset, and (3) improvements in the reliability and resolution of precursors. Ultimately, this investigation showcases alternative pathways for developing a more robust predictive monitoring strategy for brittle failure instabilities.

### A.3 Methodology

#### A.3.1 Tunnel Model Experiment Loading Path

The tunnel model experiment systematically loads a cubical analog rock specimen with an excavated opening within a true-triaxial apparatus. AE transducers monitor seismic activities during both the excavation and loading stages. The loading schematics (Figure A.1a) show that the true-triaxial apparatus uses circular flat jacks behind square stiff steel platens. This arrangement allows the application of independent compressive stresses up to 13 MPa on each active side. The three far-field stresses provided by the loading schematics are identified as the vertical stress  $\sigma_v$ , intermediate horizontal stress  $\sigma_H$ , and minor horizontal stress  $\sigma_h$ . The magnitude and direction of these stresses determine their specific denotation. This configuration enables the vertical tunnel to experience stress conditions similar to those of a horizontal tunnel in the field.

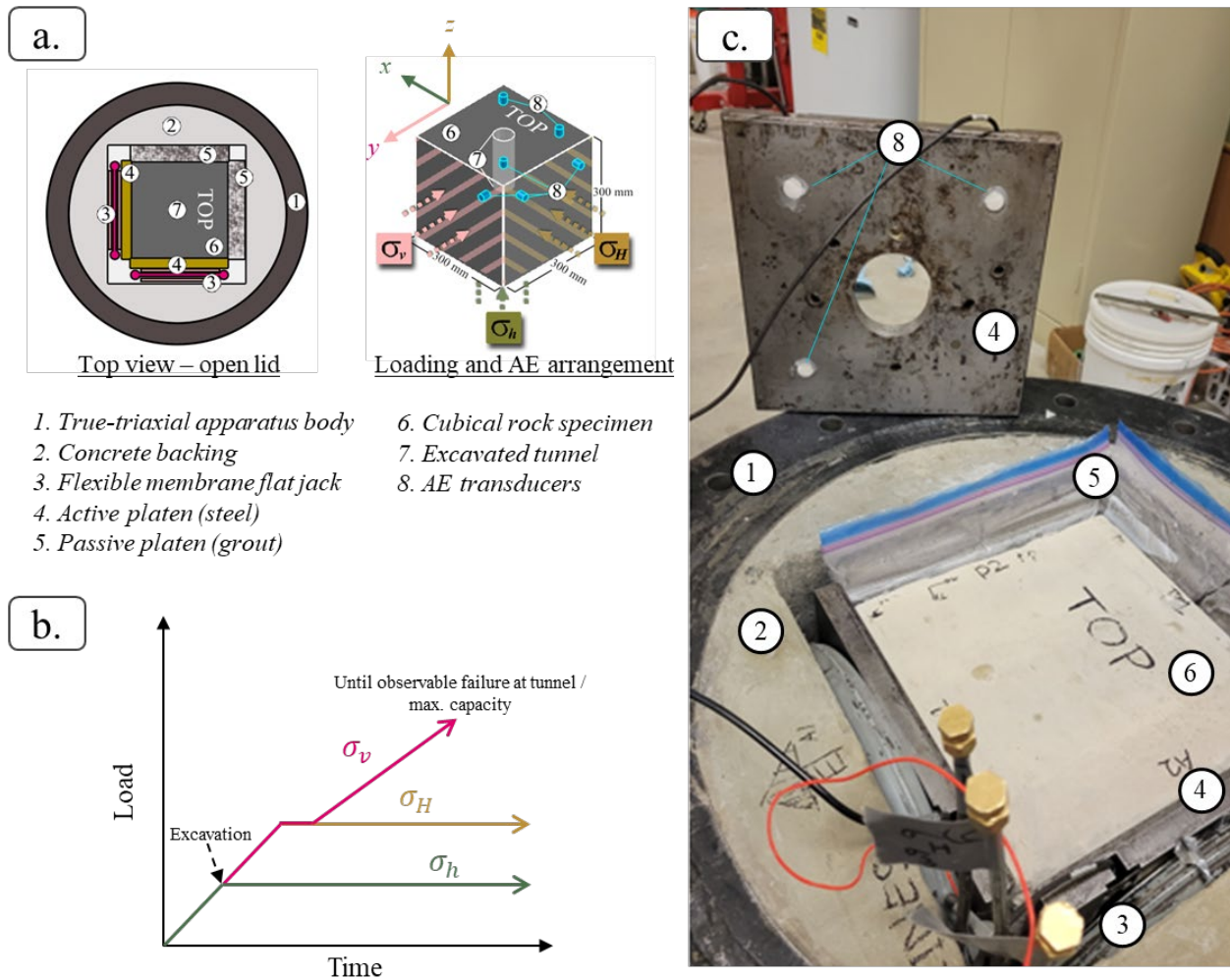


Figure A.1 Experimental setup: (a) loading schematics illustration, (b) loading path, (c) actual test assembly with opened steel top lid, showing specimen placement, loading schematics, hydraulic lines, and AE routing.

The setup and specimen placement are facilitated by removing the true-triaxial apparatus steel top lid (Figure A.1c). The steel top lid allows routing of hydraulic lines and AE cables through a 63 mm diameter circular opening for loading schematics. It also features a 75 mm diameter central opening for excavation and tunnel observation access. The opening orientation is vertical, excavated by the mock miniature tunnel boring machine (TBM) before the loading stage.

The specimen was then excavated until the advance reached its geometric center. The excavation with a 51 mm diameter cutter head leaves a clearance gap between the tunnel wall and the specimen boundary of approximately 124 mm—about five times the tunnel radius  $R_T$ . This clearance was optimized through several trials to minimize boundary effects on the excavated tunnel. Further details regarding the miniature TBM setup are documented in Arora et al. (2019). During the excavation, the specimen was initially loaded (isotropic, 0.6 MPa) to ensure it remained in position. Once the designated tunnel length was excavated, the miniature TBM was dismounted. This dismounting process allows the rock specimen to stabilize regarding AE signals before transitioning to the loading stage (Wibisono et al., 2023b). Previous studies on similar analog rocks, such as Gautam et al. (2023) and Moradian et al. (2024), provided extensive AE data analysis during TBM excavation. However, AE data during excavation is beyond the scope of this study.

The loading stage, depicted in Figure A.1b, involved several steps. The specimen was kept under initial isotropic conditions ( $\sigma_v = \sigma_H = \sigma_h$ ). Subsequently,  $\sigma_h$  was held constant while  $\sigma_v$  and  $\sigma_H$  were monotonically increased until the predetermined  $\sigma_H$  was achieved. Finally, lateral stresses  $\sigma_h$  and  $\sigma_H$  were maintained at constant levels, and vertical stress  $\sigma_v$  was monotonically increased. This monotonic loading continued until significant failure was observed or the maximum capacity of the loading was reached. In this study, the  $\sigma_h$  was oriented parallel to the tunnel axis, whereas  $\sigma_v$  and  $\sigma_H$  were applied perpendicular to the tunnel axis.

### A.3.2 Analog Rock Characterization

The material used was a specially developed analog sedimentary rock. All specimens were molded using a mortar mixing procedure to replicate sedimentary rock with accurate constituent control. This method ensures consistent physical and mechanical properties across various geometries. The specimens were primarily made of Type I/II Portland cement, F-75 Ottawa sand, and distilled water. In addition to the  $300 \times 300 \times 300$  mm<sup>3</sup> cubical specimen for the tunnel model experiment, additional cylindrical specimens were prepared for material characterization. This characterization included a series of physical properties, unconfined compression tests (UCT), Brazilian splitting tests (BST), and triaxial compression tests.

Table A.1 summarizes the mechanical properties of this analog sedimentary rock. The analog rock mix design features a 4% cement content  $C$  (relative to the total solid mass) and a 1.2 water-to-



cement ratio  $w/cm$ . Several engineering treatments were applied to the standard analog sedimentary rock to enhance brittle behavior while reducing its UCS. These weak and brittle characteristics minimize the need for a high-capacity loading apparatus, allowing for larger specimen geometry. The engineering treatments included (1) using fine-uniformly graded aggregate usage, (2) reducing cement content, (3) shortening curing time, (4) adding air-entraining admixtures, (5) subjecting the specimen to saturation and freeze exposure, and (6) applying thermal exposure (Wibisono, 2024). According to the International Society of Rock Mechanics (1978), this analog rock is categorized as “very weak” with a UCS of 1.68 MPa. The improved analog sedimentary rock was evaluated to have more brittle responses while lower in UCS. Further details regarding the development of the analog sedimentary rock are documented in Wibisono and Gutierrez (forthcoming).

Table A.1 Summary of laboratory characterization results of the analog sedimentary rock mix.

Properties	Value
Average UCS $\sigma_{\theta f,UCT}$ (MPa)	1.68
Average Elastic Modulus $E_{50}$ (GPa)	0.76
Average Brazilian splitting strength $\sigma_t$ (MPa)	0.19
Poisson’s ratio, $\nu$	0.22

### A.3.3 AE Monitoring and Processing Framework

The AE system monitors the acoustic events associated with rock damage within the loaded specimen (Ishida et al., 2017; Zhang et al., 2016). The monitoring in this experiment included a six-channel board and a control system, both supplied by the MISTRAS Group and programmed using the AEwin software. This configuration allowed six  $wS\alpha$  AE transducers usage with a frequency response ranging from 100 to 1000 kHz and a resonant frequency of 125 kHz. These transducers were mounted within prefabricated housings integrated into the loading steel plates attached to the cubical specimen (Figure A.1c). To improve AE data quality, a cover plate and a buffer of open cell packing foam were used to maintain tight contact between the rock and transducers. Additionally, a thin layer of vacuum gel served as the coupling agent. The quality of AE transducer installation was tested prior to complete assembly using auto-sensor tests (AST), a functionality of the AEwin software. A hit is recorded when a signal surpasses the threshold, and an event is recorded when four or more transducers detect a hit. For this experiment, a threshold of 35 dB and a pre-amplification gain setting of 40 dB were set.

During the loading stage, the parametric AE data were processed to obtain AE frequency domain signatures and  $b$ -values. These outputs were temporally deconstructed throughout the loading stage based on time intervals. This deconstruction aimed to identify potential AE precursors in the damage

progression and the visible onset of spalling. An emerging strategy was attempted to enhance the reliability of the precursors by proposing advanced deconstruction with the moving number of hits. Figure A.2 illustrates the different approaches of temporal deconstruction used in this study. Based on time intervals, the first approach considered any number of hits within designated time sampling windows, resulting in varying numbers of sample hits. Initially, a discrete sampling approach was used (Figure A.2a), but it provided rough deconstruction trends. A smooth overlap of 25% backward and forward (Figure A.2b) was then applied to improve resolution and continuity. Based on the moving number of hits, the second approach defined specific time sampling windows based on the running number of hits (Lei et al., 2004). The counting also adopted smooth steps to enhance resolution and continuity.

In contrast to the first approach, this method, with a designated number of hits and steps, made the precursor identification more stable overall. Notably, all AE data processing in this study included filtering to exclude records with durations of 0  $\mu$ s and energy of 0, which could disrupt average frequency calculations. The Python codes to perform these analyses are available in the Supporting Information.

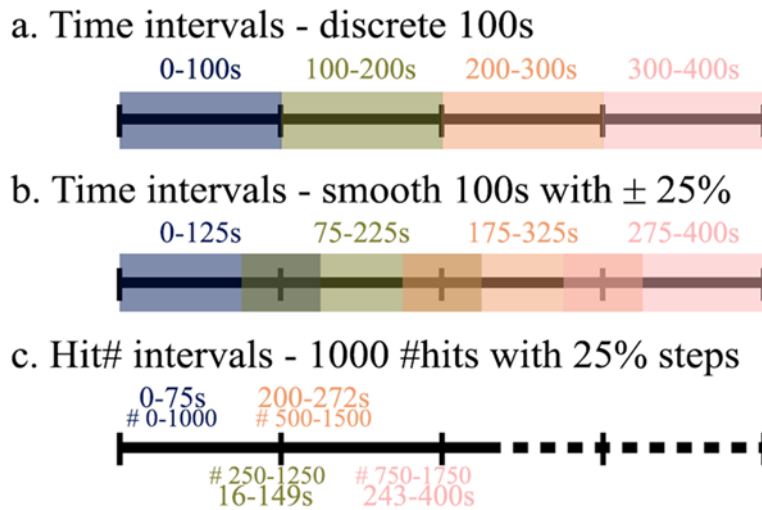


Figure A.2 Temporal deconstruction methods examples for AE analysis during the loading stage: (a) time intervals using discrete 100-second windows, (b) time intervals with smooth overlapping windows ( $\pm 25\%$ ), and (c) moving number of hits, using windows with 1,000 hits and 25% steps.

### *AE frequency domain signatures*

There were two evaluated AE frequency signatures: (1) average frequency  $AF$  with peak amplitude  $AMP$  and (2) average frequency and rise angle ( $AF/RA$ ). The  $AF$  refers to the ratio of the AE ring count and duration (Ohno and Ohtsu, 2010).  $AMP$  is the maximum AE signal excursion during an AE hit.  $RA$  is the ratio of rise time to peak amplitude, where rise time is defined as the duration between AE hit arrival and peak amplitude.

For the first signature,  $AF - AMP$  relationship was clustered. The  $AMP$  is clustered into low and high-amplitude domains. Low-amplitude (LA) signals typically 60 dB or less and indicate pre-existing cracks closure and microcracks initiation. High-amplitude (HA) signals correspond to the propagation of cracks with an amplitude exceeding 60 dB, indicating a medium-to-larger scale cracking mechanism (Rao et al., 1999). Cluster zones in the frequency domain are based on prior characterization work on identical analog rock using cylindrical tests (Gautam and Gutierrez, 2024). These clusters are determined according to the predominant frequencies observed at various stages of stress-strain within a series of UCTs. Four distinct cluster zones were identified to differentiate among different frequency ranges: frequencies below 143 kHz were categorized as very low frequency (VLF), those falling between 143 and 226 kHz were labeled as low frequency (LF), frequencies ranging from 226 to 308 kHz were designated as intermediate frequency (IF), and frequencies between 308 and 360 kHz were classified as high frequency (HF). Any frequency data falling outside of these defined zones were considered outliers.

Next,  $AF/RA$  signatures were also clustered to identify cracking mode. This method is widely applied in studies of rock (Du et al., 2024; Khadivi et al., 2023; Pratomo et al., 2024; Zhao et al., 2024). This technique uses a reference gradient line to cluster between tensile and shear cracks. Besides the direct plotting, the moving average method of  $AF/RA$  was performed for comparison as suggested by (Ohtsu et al., 2010). For this one,  $AF$  and  $RA$  values were plotted using a moving average of a minimum 50 AE hits. In tunnel spalling characterization, pure tensile is arguable as dilational shear cracking makes the fractures look like extensional fractures (Gutierrez et al. 2023; Wibisono and Gutierrez forthcoming). In this study, tensile cracking is further referred to as dilational shear cracking.

The AE parametric amplitude, measured in dB, needs to be converted back to voltage units to calculate the  $RA$  value in ms/V. This conversion was done using the following equation:

$$V_{max} = 10^{\frac{dB_{AE} + dB_{PA}}{20}} * 0.001 \text{ mV} \quad (\text{A.1})$$

where  $dB_{AE}$  is the parametric AE amplitude in dB,  $dB_{PA}$  is the pre-amplifier gain setting in dB, and  $V_{max}$  is the output voltage in mV. The parametric data shows rise time in  $\mu\text{s}$  where, if divided into mV, become identical with millisecond per volt ms/V. AE hits with low  $AF$  and high  $RA$  generally represent the development of shear-type cracks. In contrast, AE hits with high  $AF$  and low  $RA$  represent dilational dominant cracking mode. The reference line to distinguish dilational and shear crack is adopted from Du et al. (2024) based on UCTs and Brazilian tension tests on white sandstone, with  $AF - 110 \text{ kHz} = RA \times 5.57 \times 10^{-2} \text{ ms/V}$ . This selection was based on similarities of testing and data acquisition parameters (e.g., pre-amplifier setting of 40 dB, signal acquisition rate of 1.0 MHz).

### *AE energy b-value*

AE record of amplitude and hits arrival time was processed to obtain  $b$ -value. The AE energy  $b$ -value calculation adopted the Gutenberg-Richter (GR) law, commonly employed by seismologists to signify the correlation between earthquake magnitude and its frequency spectrum. Seismologists frequently use this  $b$ -value for an input to improve earthquake and local seismic risk mitigation (Gulia and Wiemer, 2019; Wesseloo, 2020). The  $b$ -value represents the log-linear slope of the power-law distribution that indicates the correlation of the number of larger magnitudes to that of smaller magnitudes. As described by Eq. (A.2), the GR law links the cumulative frequency of earthquake events exceeding given magnitude  $N(M \geq m)$ , with real, positive constants  $a$  (earthquake productivity) and  $b$  (average earthquake size distribution) (Richter, 1958).

$$\log_{10}[N(M \geq m)] = a - bm \quad (\text{A.2})$$

On a laboratory scale, this  $b$ -value is often related to the fracture development process of rock (Amitrano, 2003). The fracture development corresponds to the damage progression throughout the specimen under loading conditions, which may leave the temporal footprint of  $b$ -value. The formation of microcracks is linked to a high number of low-amplitude events that are represented by a larger  $b$ -value. On the contrary, macrocracks generation produces fewer low-amplitude events that proportionately decrease the  $b$ -value (Lockner et al., 1991; Scholz, 1968). Additionally, researchers associate the amplitude events scale with the cracking mechanism, identifying smaller amplitude signals to shear-dominant and more significant amplitude events to tensile-dominant (Kamada et al., 1998; Rao et al., 1999). As  $AMP$  output from AEwin is measured in decibels, the  $AMP$  is divided by 20 to produce a comparable  $b$ -value to that reported in the seismic literature (Cox and Meredith, 1993; Sagar et al., 2012). Eq. (A.2) is then modified as follows to comply with power law distribution of acoustic events on a laboratory scale (Colombo et al., 2003; Rao and Lakshmi, 2005),

$$\log_{10} N(\geq A_{dB}) = a - b \frac{A_{dB}}{20} \quad (\text{A.3})$$

where  $A_{dB}$  is the peak amplitude of the AE signals in decibels (dB),  $b$  is the calculated slope of the linear trend of the  $\log_{10} N(\geq A_{dB})$  known as  $b$ -value, and  $a$  is a constant that exceeds the scope of this analysis. Since the  $AMP$  is recorded in 1 dB incremental, the divided value of  $A_{dB}$  is then rounded to two decimal places with an interval of 0.05 (X. Liu et al., 2020a). A minimum of 50 events per bin of magnitude is adopted in acceptance criteria for stable  $b$ -value estimation to minimize error.

This study calculated the  $b$ -value throughout the test to monitor the temporal evolution of cracking processes during the loading stage. The trend was then evaluated as a potential precursor to be compared to the observed spalling onset in the loaded tunnel model. Adopting Eq. (A.3), the evolution of  $b$ -value was attempted using a developed Python code to allow temporal deconstruction in AE monitoring

from base  $b$ -values calculation code provided by Lapins (2021). The relevant input parameters for this modified code were time (minute) and amplitude (dB), recorded from each AE channel. Appendix A provides the code and sample file to automatically obtain the  $b$ -value temporal footprint that can be customized for a different time or moving number of hits sampling methods.

The maximum likelihood method is the well-known approach for calculating the  $b$ -value of a catalog (Aki, 1965; Bender, 1983). This method assumes that the data is exponentially distributed and that the maximum magnitude is infinite. The latter is obviously not physically plausible, but it is generally assumed that the sample at hand is not large enough to sample the maximum possible magnitude for a region (Naylor et al., 2010). The mean and the uncertainty of  $b$ -value  $\hat{b}$  can be estimated by (Aki, 1965):

$$\hat{b} = \frac{\log_{10}(e)}{\bar{M} - \left(M_c - \frac{\Delta M_{bin}}{2}\right)} \quad (\text{A.4a})$$

$$\sigma(\hat{b}) = \frac{\hat{b}}{\sqrt{n}} \quad (\text{A.4b})$$

where  $\bar{M}$  is the mean magnitude,  $M_c$  is the magnitude of the completeness,  $\Delta M_{bin}$  is the bin width of the magnitude catalog,  $\sigma(\hat{b})$  is the standard error at a 68% confidence interval, and  $n$  is the number of the data within the magnitude catalog. The magnitude of completeness  $M_c$  defined as the point where the frequency-magnitude distribution (FMD) deviates from the Gutenberg-Richter law (straight-line regression).

Two methods of obtaining  $M_c$  were evaluated: the maximum curvature method (MAXC) and goodness-of-fit tests (GFT). The MAXC method determines  $M_c$  at the peak of the first derivative of the FMD curve, as described by Woessner and Wiemer (2005). The GFT method estimates  $M_c$  by comparing the observed FMD with synthetic GR distributions formulated according to Eq. (A.3). The smallest cut-off magnitude  $M_c$  is determined where the residual between the observed and synthetic FMD is below a designated threshold. The threshold was 5% of the sum of the observed cumulative number of events from each magnitude bin, ensuring the synthetic distribution closely matches the observed data. This 5% threshold was indirectly used to determine whether the R-values were within the 90% and 95% confidence levels for a good fit.

## A.4 Results

### A.4.1 Tunnel Geometry, Actual Loading Path, and Acoustic Emission Counts

Spalling generation was documented outside the tunnel portal using an ultra-high-definition (UHD) video recorder. The high rate of 60 frames per second (FPS) ensures precise visualization of the spalling progression. Time stamps were synchronized with AE recording and effective far-field stress, establishing a global time reference for the loading stage (denoted by mm:ss). At intervals, video frames

were captured to remark on the progression of spalling in areas with concentrated tangential stress, particularly at the tunnel springlines (Figure A.3). Initial grain ejection occurred at 4:35, followed by relatively larger ejected grains, marked with a red dashed circle, at 4:38.

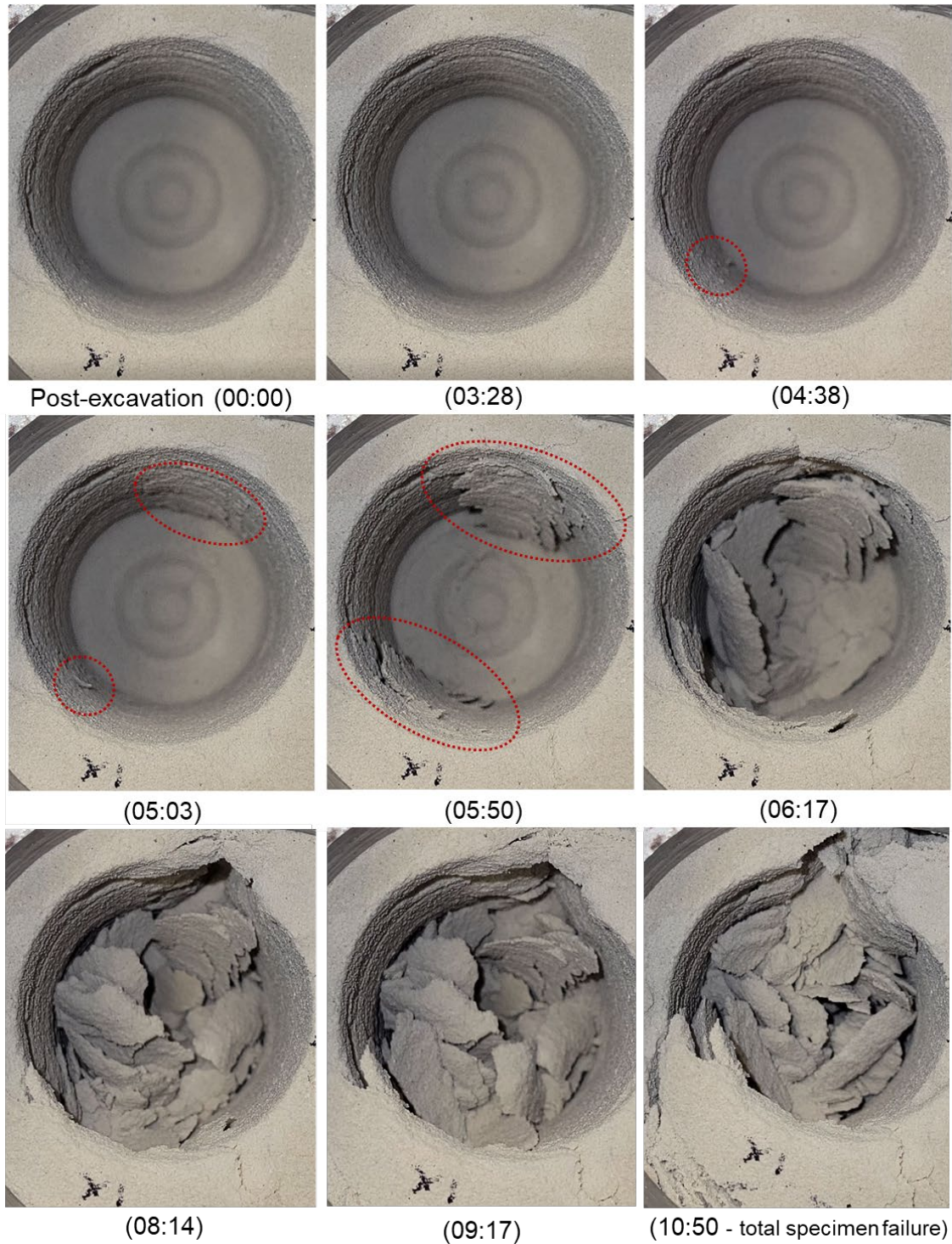


Figure A.3 Progression of spalling failure documentation throughout the loading stage from the portal. Time is shown in minutes and seconds (mm:ss) and has been synchronized with the AE data.



Figure A.4 presents the effective far-field stress over time, superimposed with the AE counts and cumulative AE counts throughout the loading stage. The data presented is shown for up to 12 minutes, corresponding to the duration until the maximum applied far-field stresses were reached. At the visible onset of spalling (mm:ss = 4:35), the effective far-field stresses were 1.6, 1.2, and 0.6 MPa for  $\sigma_v$ ,  $\sigma_H$ , and  $\sigma_h$ , respectively. Using the two-dimensional closed-form elastic solution (Kirsch 1898), this stress state at spalling onset results in a maximum  $\sigma_\theta = 3 \cdot \sigma_v - \sigma_H$  at the tunnel boundary of 3.6 MPa, yielding a  $\sigma_\theta/\sigma_c$  ratio of 2.14. Further, AE analysis from each respective channel focused on the critical period from 3 to 6 minutes, where damage progression leading to the visible spalling onset was observed. The analysis spanned up to 10 minutes for all channel data to observe the general trend throughout the loading stage.

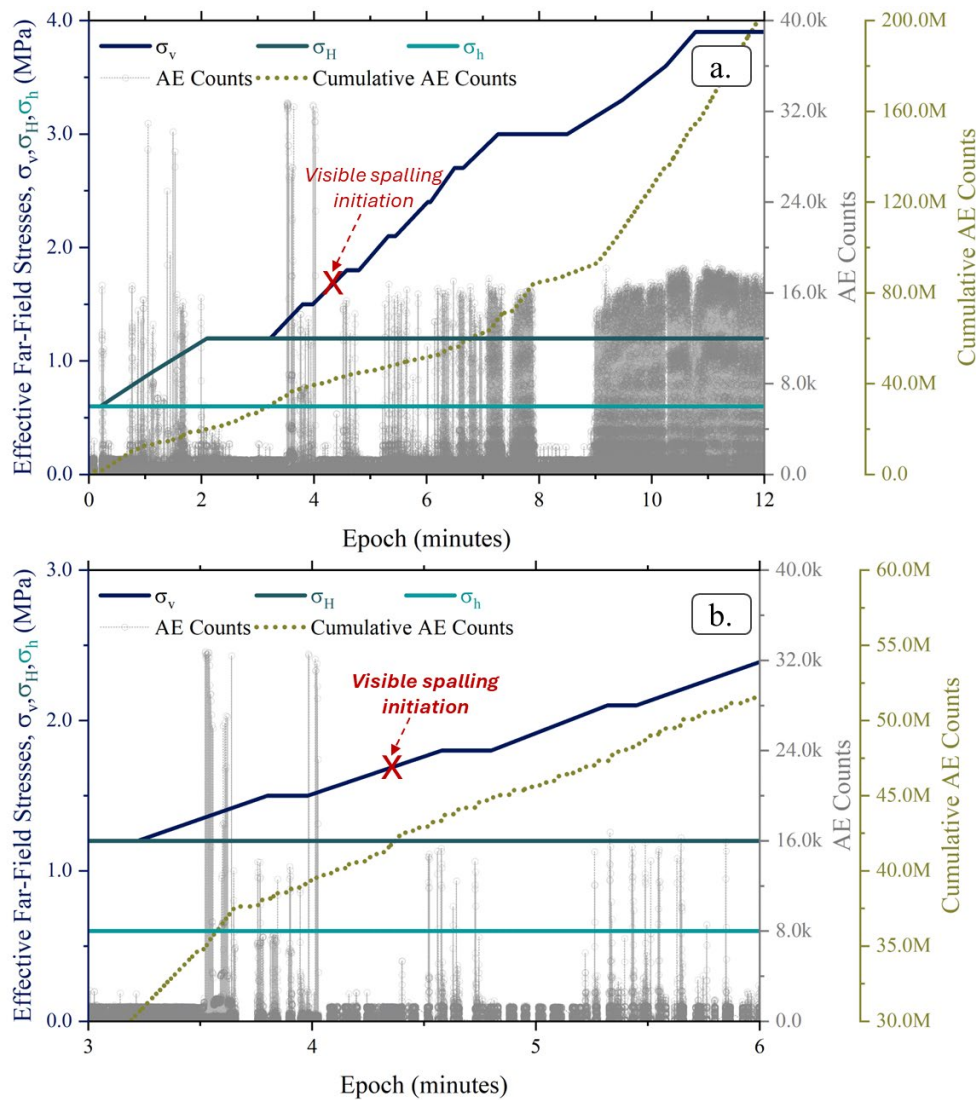


Figure A.4 Applied stress conditions on the  $300 \times 300 \times 300 \text{ mm}^3$  specimen with a 51 mm circular opening, along with acoustic emission (AE) monitoring data during (a) the first 12 minutes and (b) the 3-6 minute interval of the loading stage. The plot displays the effective far-field stresses ( $\sigma_v, \sigma_H, \sigma_h$ ), AE counts, and the cumulative AE counts from all channels. Additionally, the red cross mark highlights the point of visible spalling onset.



#### A.4.2 Temporal AE Frequency Domain Signatures and Crack Classification

Figures A.5 and A.6 present the  $AF - AMP$  clustering and  $AF - RA$  plot for every hit from all channels during the loading stage. Both plots were somewhat challenging to interpret, so temporal quantifications were performed. Due to similar observed trends, the approach using a moving number of hits to define the time interval was not presented in these frequency domain signatures.

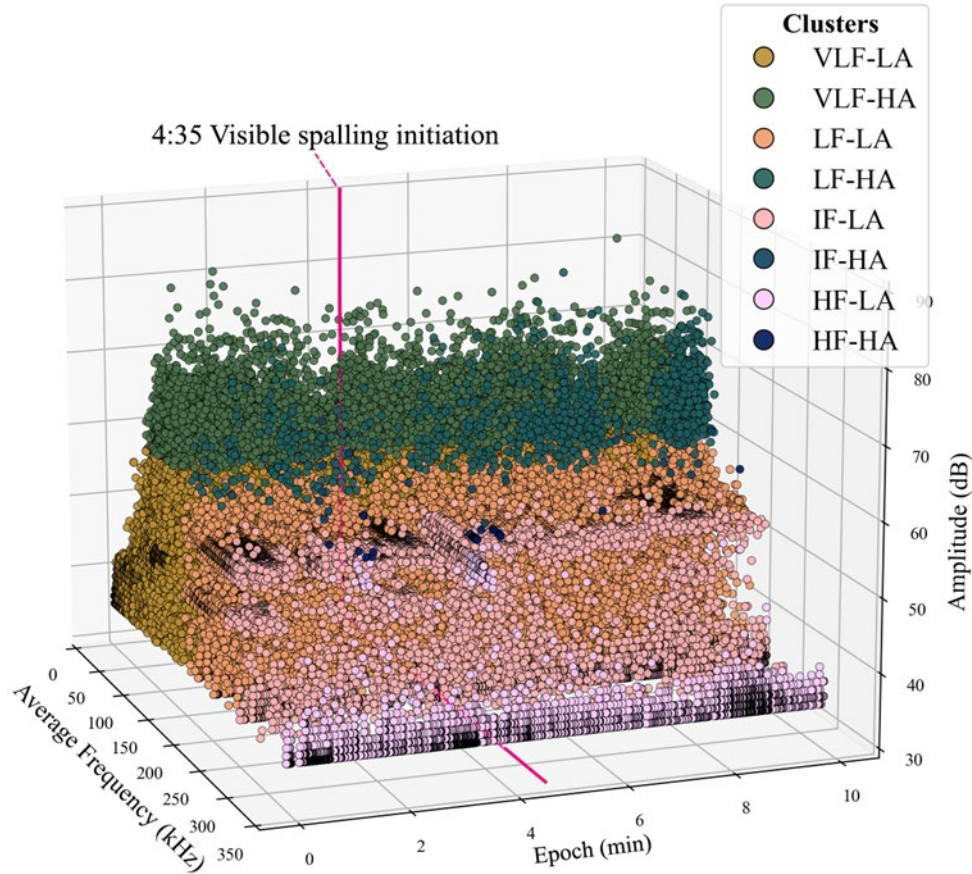


Figure A.5 Average frequency and peak amplitude clustering during loading stage with time remark on visible spalling initiation (4:35). The clustering limit for each category is based on a previous study of AE characterization on an identical mix design (Gautam and Gutierrez, 2024).

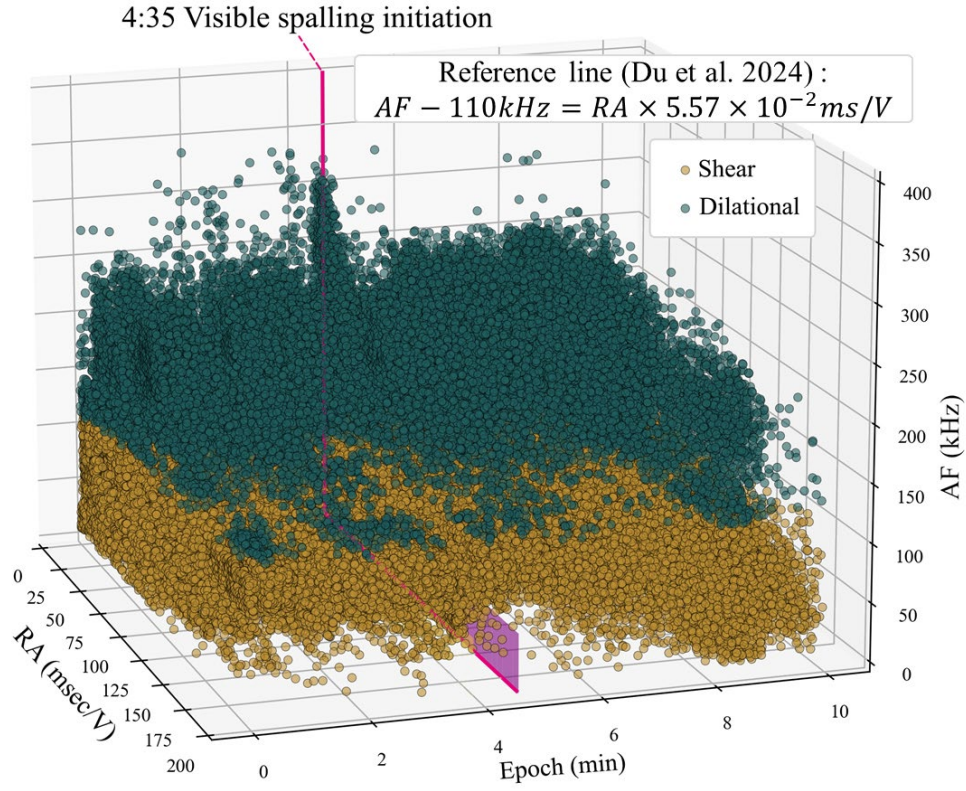


Figure A.6 AF-RA plot over 10 minutes of loading stage with time remark on visible spalling initiation (4:35).

The first quantification for  $AF - AMP$  clusters focused on minutes 3 to 6 (Figure A.7). Percentages of  $AF - AMP$  clusters (e.g., VLF-LA, HF-HA, etc.) were temporally deconstructed using two-bin time samplings, with 3-second and 0.6-second spans for low and high resolutions, respectively. Superimposing visible spalling onset to the clustering quantification suggested that the dynamics of AE event-type percentages could reveal potential precursors.

From Figure A.7, the clustering of AE event types throughout the loading stage was dominated by VLF-LA signals, comprising over 70% of observations. In the 3-second sampling span of deconstruction (Figure A.7a), the prevalence of VLF-LA signals overshadowed other signal types. With lower computational demands due to fewer sampling bins, the 3-second span revealed fluctuational peaks in LA signals that approached the visible spalling onset. This trend was consistent across all LA signals.

Conversely, for LF-HA and VLF-HA signals, distinct peaks were detected before the visible spalling onset, indicating that large-scale cracking occurred less frequently, consistent with visual observation. Notably, peaks in the remaining HA signals became prominent as they approached the visible spalling onset, potentially indicating a progressive accumulation of large-scale cracking leading up to LF-HA and VLF-HA signals at spalling initiation.

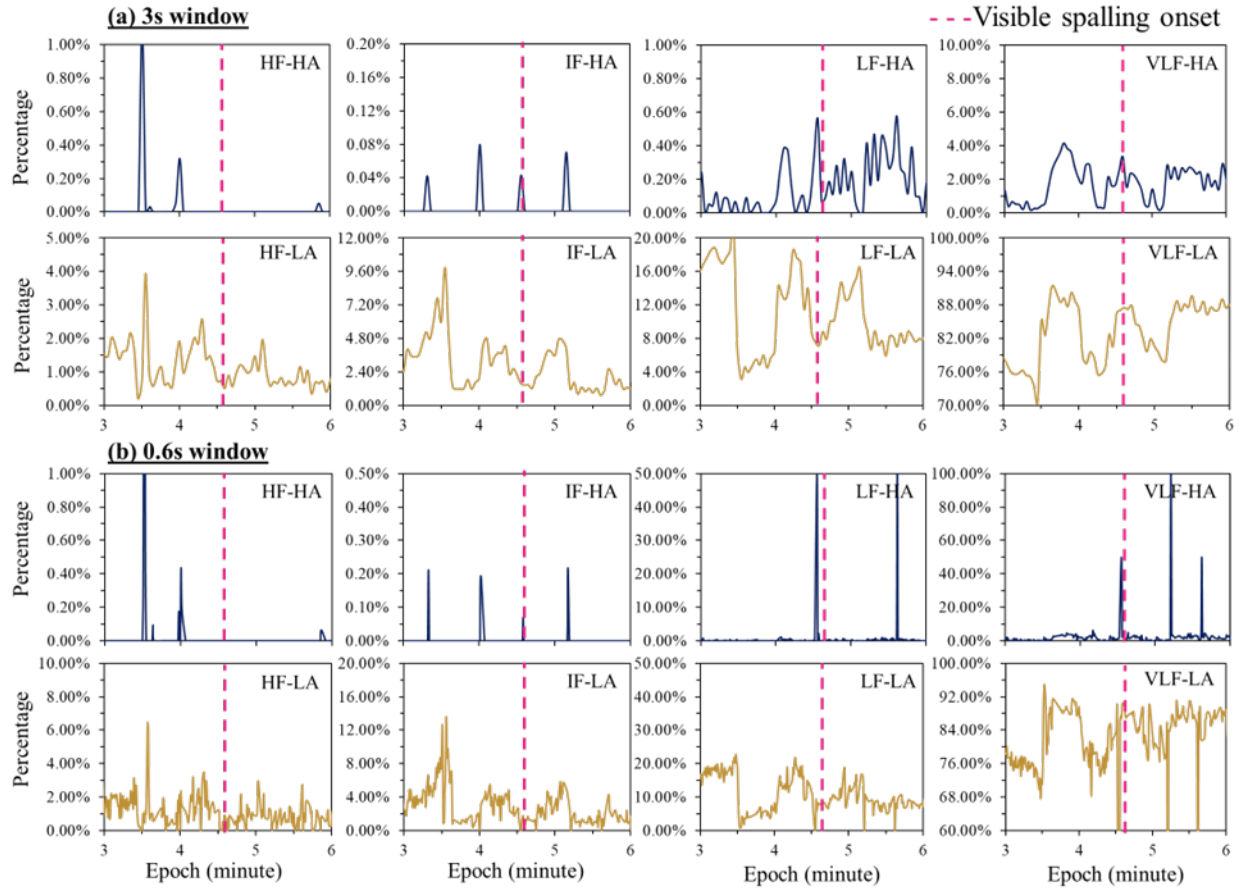


Figure A.7 Average frequency and peak amplitude clustering during loading stage with time remark on visible spalling initiation (4:35). The clustering limit for each category is based on a previous study of AE characterization on an identical mix design (Gautam and Gutierrez, 2024).

The higher-resolution sampling (0.6 seconds) provided more pronounced trends than 3-second span. Most LA signals exhibited peaks adjacent to 03:30. LF-LA and VLF-LA were already dominating before 04:10, supporting the hypothesis of microcrack initiation and closure of cracks around the tunnel boundary. For HA signals, the trend resembled physical observation (Figure A.7b). For instance, LF-HA and VLF-HA signals distinctly increased at the time of visible spalling onset in the experiment. Notably, these HA signals comprised less than 10% of observations for most loading stage but rose to 100% at the onset of visible spalling. These LF-HA and VLF-HA signals also exhibited additional peaks after visible spalling, suggesting macrocrack generation and spalling progression. The general observation is that an accumulation of peaks from HA during fluctuations of LA signals may serve as a potential precursor to spalling initiation and further violent damage.

For the second quantification, the process involved quantifying the percentages of dilational and shear cracks from  $AF - RA$  reference line within specific time windows. Notably, the crack percentages within each time window summed to 100%. Figure A.8 displays these percentages as diverging bar charts,

enhanced with overlays visible spalling onset time remark. The temporal resolution was set discretely at 0.2 seconds to achieve high-resolution analysis while maintaining a minimum of 50 hits per time window.

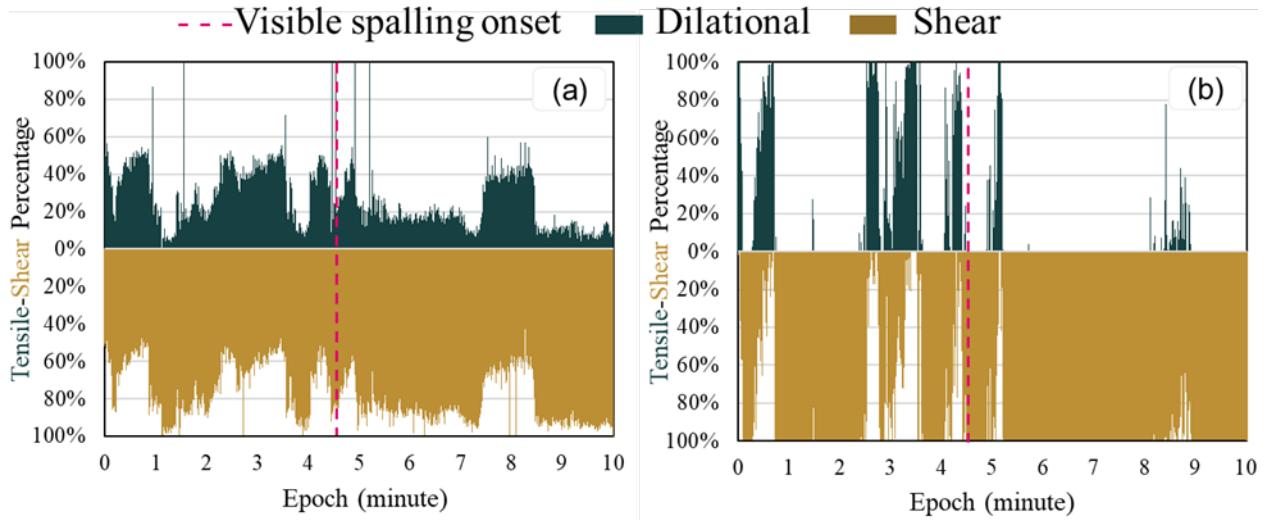


Figure A.8 Diverging bar charts showing the temporal evolution of tensile-shear percentage based on the selected *AF – RA* reference line with 0.2 second time sampling. Two approaches were used, which are (a) direct and (b) moving average.

The temporal deconstruction showed the percentages of each mode of cracks within a designated sampling window. The direct plotting (Figure A.8a) demonstrated interesting shifts between dilational and shear dominant cracking throughout the 10 minutes of the loading stage. Notably, the shear mode of cracking spiked to 100% before the visible spalling onset. However, the moving average plotting (Figure A.8b) showed more explicit shifts between dilational and shear for better potential precursors. This moving average method effectively identified trends and distinguished cracking mechanisms, thereby improving the precursor for spalling onset.

Shear was the predominant failure mechanism, consistent with the loading path under true-triaxial confinement and increasing deviatoric stress. The dilational mode cracking exhibited intermittent spikes of 100% prior to the visible spalling onset, followed by a temporary suppression of this cracking mode. Subsequently, dilational cracking surged again, reaching 100% intermittently for 15 seconds as it approached the visible spalling onset. This sudden shift suggested an additional precursor to spalling onset. After the onset of spalling, the dominant failure mode shifted back to shear, with dilational cracking activity observed for the first 40 seconds, and an intermittent period occurred beginning around 8:30. Further increases in  $\sigma_v$  led to predominant shear cracking with subsequent dilational cracking, marking the onset of total specimen failure (Figure A.3). The collected data after that point of the loading stage can be disregarded due to compromised specimen integrity, which could affect the intercommunication between AE transducers.

### A.4.3 Temporal AE Energy $b$ -Value

$M_c$  was determined individually for each AE channel (CH1-CH6) based on its specific FMD at every sampling interval. Figure A.9a presents an example of FMD as the semi-linear relationship between  $(A_{dB}/20)$  and  $\log_{10} N(A_{dB})$  from the test. This relationship represents the  $b$ -value's geometry as the slope of the regression line with GFT's  $M_c$ . Figure A.9b presents the GFT plot of the corresponding example to define the GFT's  $M_c$ .

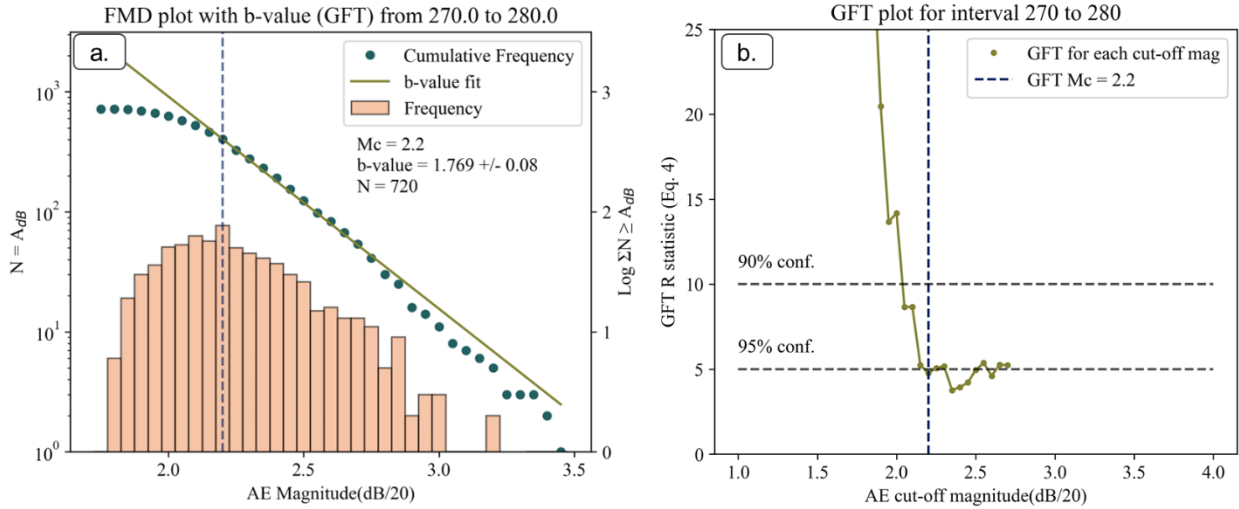


Figure A.9 (a) FMD plot from time interval 270s-280s with  $b$ -value calculation with goodness-of-fit (GFT) tests method and (b) GFT plot for determining AE magnitude of completeness  $M_c$  (blue vertical dashed lines).  $N$  denoted the number of hits considered in each  $b$ -value estimation.

Figure A.10 presents the cumulative and discrete frequency distribution of events with a given amplitude, classified per each AE transducer/channel (CH). The overall trend was found to be similar as the cumulative frequency decreased with higher amplitude, and most AE hits observed had amplitudes between 40 and 55 dB. However, AE CH 1 and CH 4 exhibit a 10 dB difference in peak dominant amplitudes, with CH 1 recording 40-44 dB and CH 4 recording 50-54 dB. This disparity was attributed to the positioning of the AE transducers, which affects the distance to the source location. Most cracking mechanisms were expected at the springlines in this anisotropic loading condition due to the high tangential stress concentration. Additionally, the distance and material properties allow elastic wave attenuation that is beyond the scope of this study.



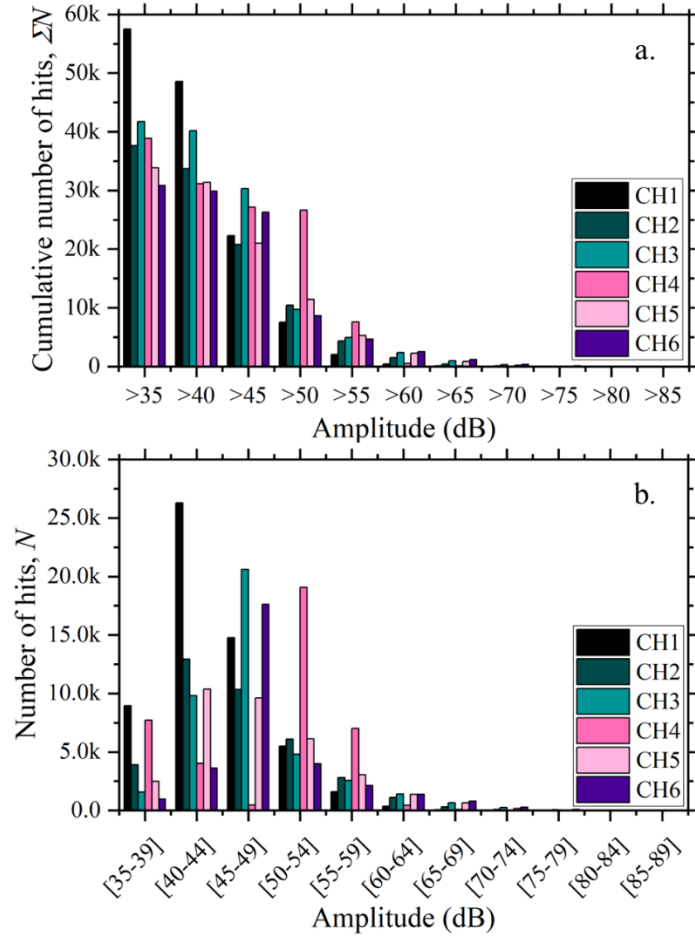


Figure A.10 Statistical relationship between AE amplitude and frequency during loading stage: (a) the cumulative amplitude distribution and (b) the amplitude distribution.

For the first deconstruction approach, the selected time window for comparison is 10 and 20 seconds. Attempts with a 10-second time window using the discrete sampling method were omitted due to insufficient events per bin for stable  $b$ -value estimation. For moving hits deconstruction, the selected number of hits was 1500, with 375 steps. Figure A.11 summarizes the temporal evolution of calculated AE  $b$ -values with selected deconstruction and sampling methods. To better represent the temporal footprint,  $b$ -values were normalized to the maximum  $b$ -value obtained in each specific channel. Of note, two  $M_c$  methods were evaluated to identify better precursors. Figures A.11a, A.11b, A.11d, and A.11f use the MAXC method, while Figures A.11c, A.11e, and A.11g use the GFT method. These  $b$ -value trends are superimposed with the critical time point of observed spalling onset from the experiment (4:35). Some channel results were not displayed to improve trend visibility. Additionally, the 10-second smooth time interval with GFT was not included since the pattern fluctuated too much. Most of the GFT's  $M_c$  with 10-second time intervals were out of 90-95% confidence interval.

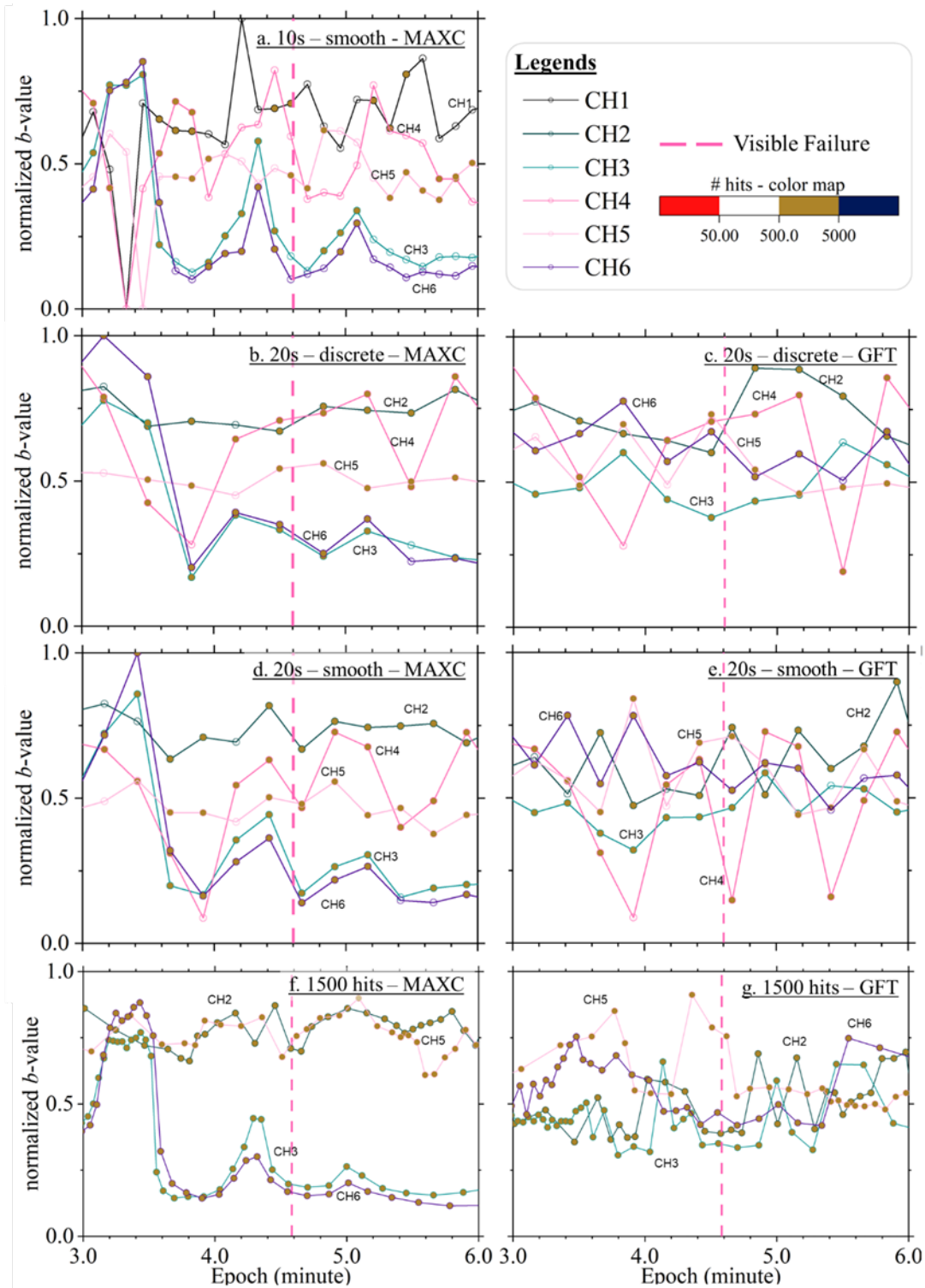


Figure A.11  $b$ -values assessments using multiple approaches focusing on minutes 3-6, highlighting the onset of visible spalling. Plots (a), (b), (d), and (f) show the MAXC method for 10-second smooth interval, 20-second discrete interval, 20-second smooth interval, and 1500 hits moving window, respectively. Plots (c), (e), and (g) illustrate the GFT method for a 20-second discrete interval, 20-second smooth interval, and 1500 hits moving window, respectively. The trends indicate varying precursor visibility through  $b$ -value fluctuations concerning spalling onset.



The variations from 3:00 towards the visible initiation of spalling demonstrated interesting trends. The 10-second interval (Figure A.11a) appeared to give the sharpest variation compared to other intervals, attributed to varying hits. Even with the smooth sampling method, most data points showed the number of hits between 50-500 since the time window was only 10 seconds. As expected with 20-second intervals, the discrete method (Figure A.11b) showed more data points with fewer hits compared to the smoother method (Figure A.11c). The trends were particularly interesting for CH3, CH4, and CH6 as the  $b$ -value sharply decreased approaching 4:00. There was a slight increase before decreasing again towards the onset of spalling. However, with a more stable estimation of the number of hits (Figure A.11f), the precursors appeared more distinct on CH3 and CH6 and similarly on CH2 and CH5, with less variation but showing the same trend.

For the GFT method, the  $b$ -value evolution over time intervals showed a decreasing trend towards the onset of spalling. Generally, the trend from GFT appeared to fluctuate more than the MAXC method, making precursor identification difficult. Although an overall decreasing trend was observed with GFT, the fluctuations after the onset of spalling made the results inconclusive. However, the deconstruction approach using a moving number of hits (Figure A.11g) demonstrated a converging decrease toward the onset of spalling. This differed from the time interval estimations, where precursors were identified more clearly. Ultimately, the deconstruction with a moving number of hits provided more distinct precursors, particularly towards the onset of spalling (Figures A.11f and A.11g).

Since the provided code enabled direct plotting on time intervals of interest, Figures A.12 and A.13 present  $b$ -value estimations before and after 4:35 (275 seconds) for a 20-second smooth interval (GFT) and moving number of hits (MAXC), respectively. This feature facilitates a more reliable cross-check closer to the time interval of interests, which is essential for back-analysis. With more data, researchers can improve the early warning alerts before abrupt brittle failure.

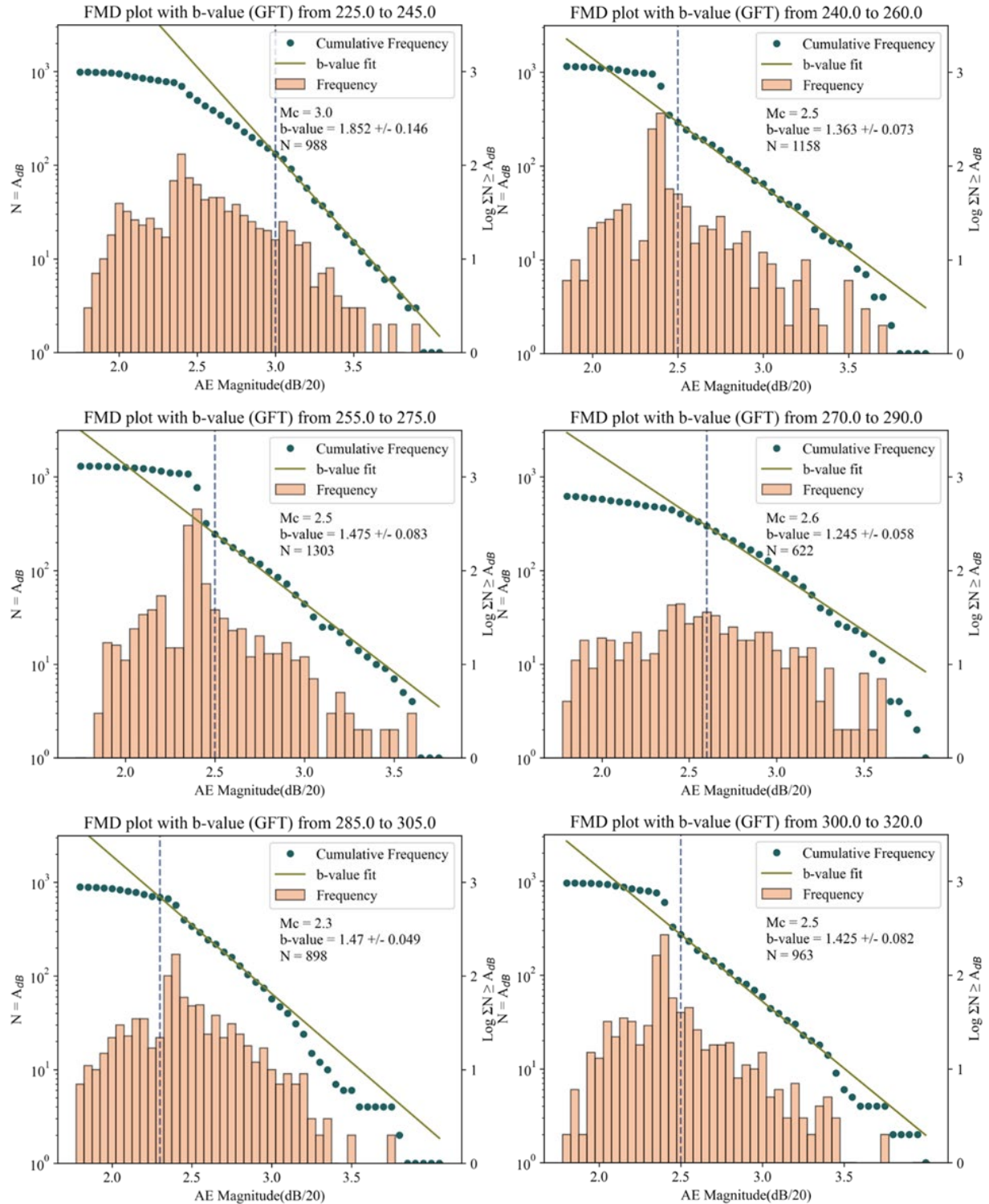


Figure A.12  $b$ -values assessments using multiple approaches focusing on minutes 3-6, highlighting the onset of visible spalling. Plots (a), (b), (d), and (f) show the MAXC method for 10-second smooth interval, 20-second discrete interval, 20-second smooth interval, and 1500 hits moving window, respectively. Plots (c), (e), and (g) illustrate the GFT method for a 20-second discrete interval, 20-second smooth interval, and 1500 hits moving window, respectively. The trends indicate varying precursor visibility through  $b$ -value fluctuations concerning spalling onset.

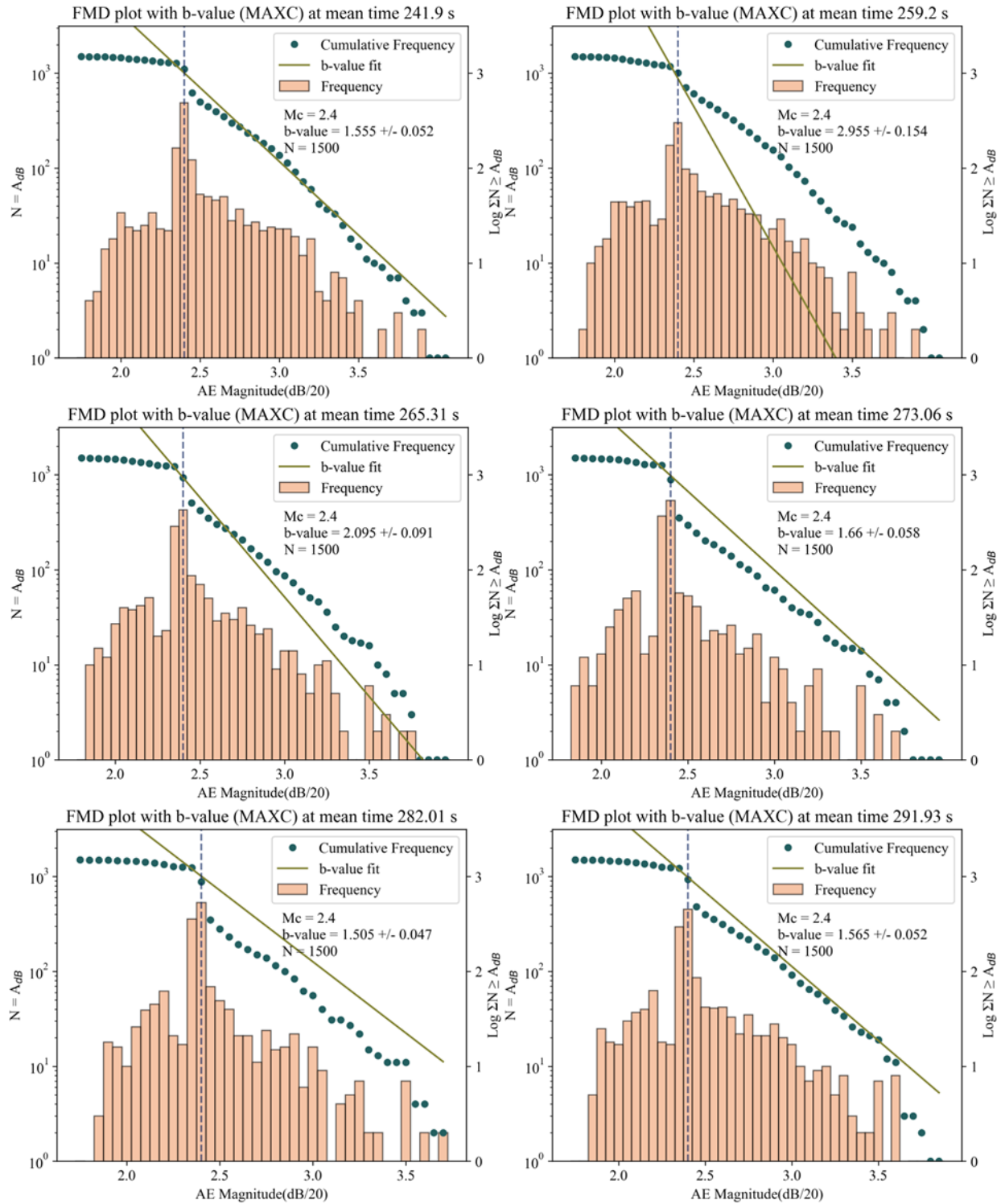


Figure A.13 **b**-values assessment closer to the time of visible spalling onset (4:35—275 seconds) using 1500 hits moving window and MAXC. The plots displayed are from CH 6 with an observation period of 240 to 300 seconds.

The analysis further spanned up to 10 minutes for combined AE channels to observe the general trend throughout the loading stage (Figure A.14). Similarly to per channel basis, different deconstruction approaches and  $M_c$  determinations were applied for comparison. Three resolutions were attempted for the moving number of hits, which generally showed a similar pattern. On the other hand, the time interval methods were attempted to its finest resolution based on the minimum capacity to get a stable estimation of  $b$ -values (Figs 14a and b). Among all those methods, the patterns fairly aligned to each other, showing similar rise and fall throughout the loading stage. However, Figures A.14c and A.14d demonstrate that the moving number of hits deconstruction provided better precursors than using the time interval. The difference in data point density allowed better classification of which cracks led to macro failure (highlighted in pink shade before the visible spalling onset).

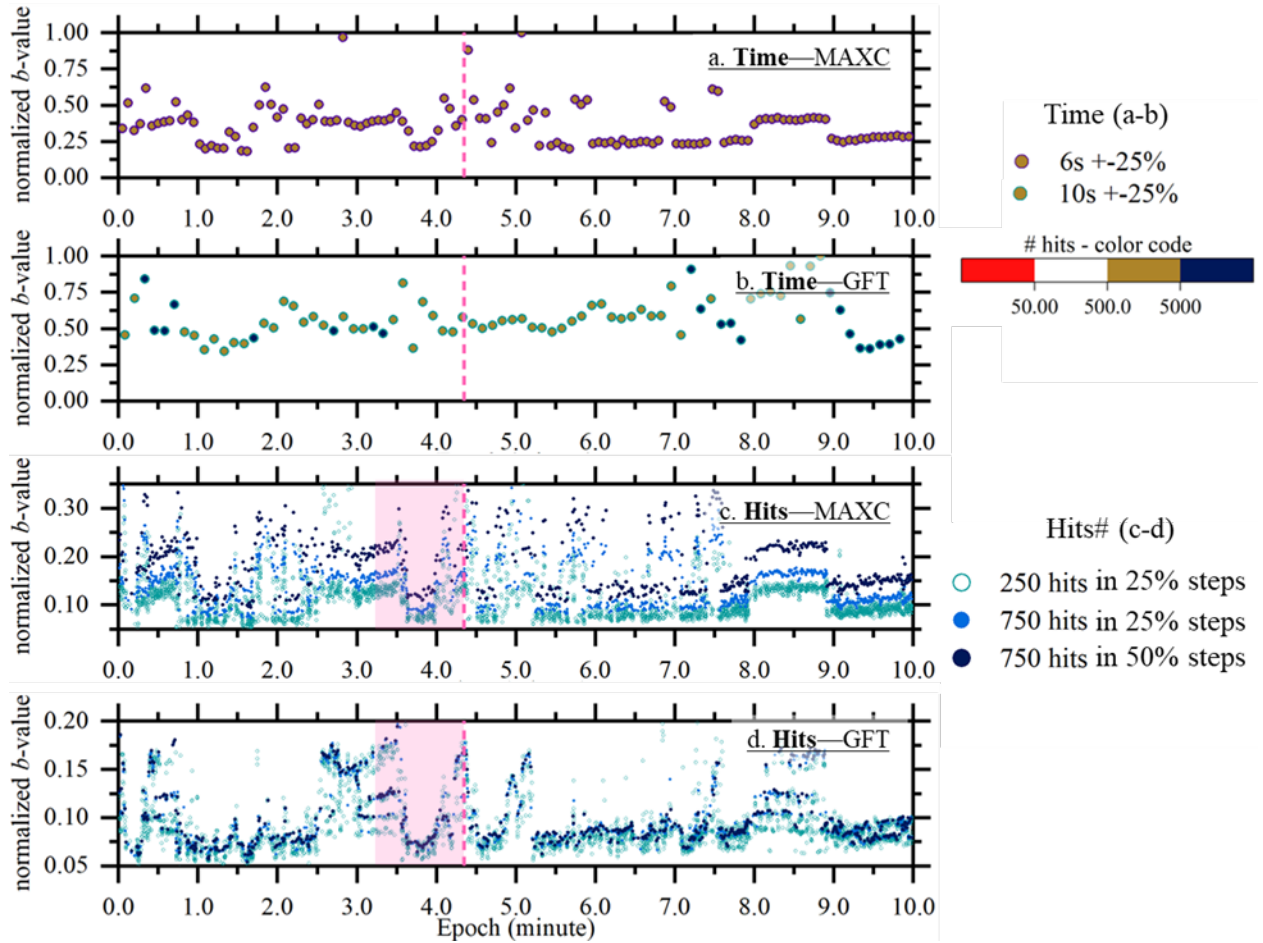


Figure A.14  $b$ -values assessment closer to the time of visible spalling onset (4:35—275 seconds) using 1500 hits moving window and MAXC. The plots displayed are from CH 6 with an observation period of 240 to 300 seconds.

Several vital observations emerged into three zones: (1) initial loading, (2) towards visible spalling alignment, and (3) towards greater damage extent after visible spalling onset. During the initial loading zone, the AE  $b$ -value fluctuated consistently. The fluctuations were along with narrow-range AE

energy  $b$ -values, suggesting smaller-scale cracking within the specimen. Notably, a significant drop in AE  $b$ -value occurred about a minute before the visible spalling onset. A pronounced decrease in AE  $b$ -value signaled a shift toward dilational-dominant cracking and the potential for macrocrack propagation—the shift indicating internal failure mechanisms without observable spalling onset at the tunnel boundary.

Closer to the visible spalling onset time remarks, the  $b$ -value increased and then dropped at 4:35, coinciding with the physical observation. The delayed visible spalling onset suggested that microcrack generation and propagation preceded microfractures' material ejection and coalescence. These occurred within the rock mass prior to the progression of the dilational-shear fractures and eventual V-shaped notch. The data after the spalling onset remains stable until significant fluctuation approaching 9:00. The rise observed in minutes 8-9 was due to an intermittent delay in loading increment (Figure A.4a). Immediately after the load change, the data point density increased with a sudden drop that indicated macrocrack propagation. This macrocracking led to total specimen failure at the end of the loading stage (Figure A.3). Importantly, the  $b$ -value trend showcased the potential precursors to the observed spalling onset and abrupt failure due to changes in boundary stress condition.

## **A.5 Discussions**

### **A.5.1 Uncertainties of AF/RA**

Currently, the primary methods for establishing the reference line are from experimental analysis, with additional cluster and frequency dominant analysis. Experimental analysis involves direct observation and measurement of acoustic emission (AE) signals during controlled laboratory experiments (Du et al., 2020; Hu et al., 2019). Cluster analysis categorizes AE signals from the experiment into groups based on their characteristics, facilitating the identification of patterns related to different failure mechanisms (Jiao et al., 2019; Wang et al., 2021). Frequency characteristics analysis examines the frequency content of recorded AE signals to distinguish between various types of fractures (Zhang and Deng, 2020).

This study adopted the reference line used to differentiate between dilational and shear cracks from Du et al. (2024), based on UCTs and Brazilian tension tests on white sandstone. Similarities, such as a pre-amplifier gain of 40 dB and signal acquisition rate of 1.0 MHz, were considered appropriate. However, this approach was not ideal. The AF/RA deconstruction may not be the optimal technique for defining failure mechanisms due to more uncertainties in determining the tensile-shear reference line, as highlighted by Dong et al. (2023). These complexities arise from various factors, including the source scale, trigger time, and rock sample characteristics, which can significantly influence the AF/RA method for identifying rock micro-fracture types.

Despite the challenges, the AF/RA deconstruction was applied in this study to explore alternative approaches for identifying precursor signals. The results demonstrated good agreement with the visible onset of spalling. The weak analog rock specimen in this study likely promoted both intergranular and

transgranular cracking, as noted by Du et al. (2020). For instance, the specimen's low cohesion, with only 4% cementitious material (Table A.1), facilitates shear dominant failure towards compression. This characteristic makes it a suitable setting for observing the transition between dilational and shear dominant failures. Notably, AF/RA moving average plotting (Figure A.8b) provided valuable insights into the visible spalling initiation on the tunnel model profile.

### **A.5.2 Implications for Real-Time Monitoring**

Real-time monitoring of underground excavations has significant implications for improving safety and mitigation measures, particularly at greater depths or in seismically active areas. Unlike laboratory AE monitoring, which is controlled and well-characterized, in situ AE monitors the initiation and extension of microcracks in rock masses within their natural environment. AE is effective for analyzing local failures within small rock volumes. It also helps investigate the progression of large-scale fractures from the initiation and coalescence of small-scale cracks (Cai et al., 2007; Hardy, 1981). MS monitoring, on the other hand, uses lower frequency signals and can detect large-scale cracks over longer propagation distances, making it more suitable for wide-range monitoring. Despite the differences in frequency range, the complementary nature of AE and MS monitoring techniques allows for a comprehensive understanding of the fracturing processes in rock masses (Feng et al., 2019).

Several underground excavations have adopted  $b$ -value temporal deconstruction techniques in back-analyzing seismic histories. For instance, coal mines in Poland (Mutke et al., 2016), the Sanhejian coal mine in China (J. Li et al., 2017), and the Kiirunavaara Mine in Sweden (Dineva et al., 2024) have reported the temporal assessment of  $b$ -values, showing a decreasing trend toward significant seismic/rockburst events. Although  $b$ -values are typically used in crustal-scale earthquake studies (Chen et al., 2023; Nanjo et al., 2023), their application to smaller AE/MS monitoring in underground excavations provides valuable insights on predicting brittle failure instabilities.

However, it is crucial to acknowledge site-specific limitations when implementing predictive monitoring techniques. Factors such as geological variability, sensor placement, completeness of data, and data acquisition parameters can significantly influence the effectiveness and accuracy of real-time monitoring systems (Feng et al., 2017; Liu et al., 2018; X. Liu et al., 2020b; Wang, 2017; Xiao et al., 2018). Comprehensive data collection and thorough documentation are essential for back-analysis processes, which can further refine and improve the resolution of monitoring efforts. Focusing on the quantity and quality of data collected during excavations will enable more precise analyses and better-informed decision-making. This approach can help identify precursor signals and understand the complex interactions leading to rock failures, ultimately enhancing the safety and efficiency of underground excavation operations and long-term stability.

## A.6 Conclusions

An extensive AE analysis of damage progression and spalling onset from the tunnel model experiment was presented. This study provided alternative exploratory methods emphasizing temporal deconstruction to identify spalling onset precursors. The following conclusions are drawn from this work:

- (1) The incremental anisotropy loading applied in the tunnel model experiment reflected boundary stress changes like those induced in an in-situ tunnel. This experimental approach helped comprehend tunnel excavation and long-term stability, emphasizing the importance of predictive monitoring strategies.
- (2) The onset identified in the experiment corresponded well with AE analysis. This alignment confirmed the efficacy of AE monitoring in detecting early signs of brittle failure instabilities through high-frequency events. The analysis of AE data in both the Time-frequency domain and  $b$ -value, from individual or combined channels enhanced the understanding of damage progression and spalling onset.
- (3) Different deconstruction methods, such as discrete, smooth sampling, and moving average approaches, were explored to improve precursor identification. Achieving higher resolution with narrow time intervals and minimal hits proved crucial for robust estimation despite requiring more computational efforts.
- (4) LF-LA and VLF-LA dominated the AE data for LA signals, comprising up to 90% of the percentage. These signals corresponded to the crack closure and damage of microcracks. The trend resembled physical observation for HA signals, with LF-HA and VLF-HA indicating macrocrack generation and spalling progression.
- (5) Analysis of  $AF - RA$  analysis showed a transition from dominant shear to dilation as spalling became visible. Resolution improvements were noted with moving-average plotting.
- (6) A moving number of hits in temporal  $b$ -value analysis provided more stable estimations than time-interval-based methods. These combined efforts offer a pathway for developing timely and effective monitoring strategies for brittle failure instabilities in tunnel excavation.

Further research is necessary to investigate long-term monitoring strategies, the effect of heterogeneity discontinuities, and brittle behavior characterization. Implementing machine-learning algorithms can further refine AE data processing techniques, improving the accuracy and reliability of precursor detection in brittle failure scenarios. Albeit with limitations, more historical data in site-specific situations could enable the development of predictive algorithms with significant potential.



## APPENDIX A - DATA FROM THE PROJECT

Table A.1 - Summary of TE and TC test results, including minor confining pressure at failure  $\sigma_3$ , differential stress  $\sigma_1 - \sigma_3$ , measured failure plane angle  $\alpha_{exp}$ , and depth of fracture  $D_{frac}$ . The last two parameters were measured from the failed cylindrical specimens.

Test type	Minor confining pressure at failure $\sigma_3$ (MPa)	Differential stress $\sigma_1 - \sigma_3$ (MPa)	Measured failure plane angle $\alpha_{exp}$ (°)	Depth of fracture $D_{frac}$ (mm)
TC	0	3.07	5-13°	-
TC	1.5	4.86	35-38°	-
TC	3.0	6.69	-	-
TE	0	3.96	0-5°	10-36
TE	0.77	4.63	10-20°	21-47
TE	1.98	5.89	25-30°	25-55

Table A.2 - Summary of TE and TC test results, including minor confining pressure at failure  $\sigma_3$ , differential stress  $\sigma_1 - \sigma_3$ , measured failure plane angle  $\alpha_{exp}$ , and depth of fracture  $D_{frac}$ . The last two parameters were measured from the failed cylindrical specimens.

Test type	Minor confining pressure at failure $\sigma_3$ (MPa)	Differential stress $\sigma_1 - \sigma_3$ (MPa)	Measured failure plane angle $\alpha_{exp}$ (°)	Depth of fracture $D_{frac}$ (mm)
TC	0	1.68	0-5°	-
TC	0.6	3.88	10-15°	-
TC	0.75	5.72	15-22°	-
TC	1.0	7.1	20-25°	-
TE	0	2.09	3-5°	6-18
TE	0.68	5.03	5-7°	35-40
TE	0.83	6.15	5-10°	40-45
TE	1.0	7.23	8-10°	46-50

## APPENDIX B – TECHNOLOGY TRANSFER ACTIVITIES

### 1 Accomplishments

#### 1.1 What was done? What was learned?

This project aimed to enhance the understanding of brittle instabilities in tunnels through laboratory experiments. The study involves (1) developing an analog brittle rock model, (2) conducting tunnel model tests using a true-triaxial loading cell, a miniature tunnel boring machine (TBM), and acoustic emission (AE) monitoring, and (3) proposing improved analytical and predictive methods for brittle failure. The analog rock was designed to replicate brittle sedimentary rock behavior while maintaining low uniaxial compressive strength (UCS). This allowed for larger specimen sizes and compatibility with low-capacity loading equipment, making it easier to observe progressive tunnel failure. Using the true-triaxial setup and mock TBM enabled realistic simulations of tunneling, capturing the effects of stress unloading and face support. Detailed post-mortem analysis revealed damage mechanisms such as surficial spalling and V-shaped notches caused by progressive shear fracturing, reflecting a brittle-to-ductile transition. AE sensors monitored microcracking in real-time, identifying early indicators of brittle failure. The study also introduced triaxial extension (TE) tests to improve predictions of spalling under more representative stress conditions compared to traditional triaxial compression (TC) tests. TE tests better captured damage characteristics such as entry angles and fracture depth. In tunnel models, steeply angled thin spalling suggested shear-driven fractures rather than purely extensional ones, with fracture surfaces likely forming from shear-induced dilation and friction mobilization. A novel aspect of the research is the use of quadratic Bézier curves to track fracturing progression based on damage and breakout width. This method offers a more accurate depiction of tunnel damage under anisotropic stress than traditional models relying solely on friction angle and logarithmic spirals. The project advanced the understanding of brittle failure in tunnel excavation. The experimental methods and models developed provide practical tools for mitigating spalling and rockburst risks, contributing to safer and more reliable designs in brittle rock environments.

#### 1.2 How have the results been disseminated?

Dissemination through 1 journal paper and 6 international conference presentations. Additionally, 2 journal papers have been submitted and are under review and 2 journal papers are being finalized for submission. Furthermore, Doandy Wibisono dissertation was funded by UTC-UTI and is archived at Colorado School of Mines Library.

### 2 Participants and Collaborating Organizations

Name: Colorado School of Mines

Location: Golden, CO, USA

Contribution: All research performed on campus

### 3 Outputs

*Journal publications*

Wibisono, D.\*, Gutierrez, M. and Majumder, D. (2024),” Experimental Investigation of Tunnel Damage and Spalling in Brittle Rock Using a True-Triaxial Cell,” *International Journal of Rock Mechanics and Mining Sciences*, accepted for publication.

Moradian, O., Gutierrez, M., Wibisono, D.Y. and Gautam, P.K. (2024), “TBM Performance Evaluation Using Seismic Data During Excavation: A Comparative Examination of Clustering Algorithms,” *Proc. 5th Intl. Conf. Information Tech. Geo-Engineering (5th ICITG)*, Colorado School of Mines, Golden, CO, USA August 5-8, 2024, pp. 352-361.

Wibisono, D.Y.\*, Gutierrez, M., Majumder, D. and Gautam, P.K. (2023), “Development of a Weak but Brittle Analog Sediment Rock for Experimental Study,” *Proc. 57th US Rock Mechanics / Geomechanics Symposium*, Atlanta, GA, June 2023.

Gautam, P.K., Gutierrez, M., Wibisono, D.Y. and Majumder, D. (2023), “Crack classification during tunneling in scale model testing using acoustic emission,” *Proc. 57th US Rock Mechanics / Geomechanics Symposium*, Atlanta, GA, June 2023.

Wibisono, D.Y.\*, Arora, K., Majumder, D., Gutierrez, M. (2022), “Laboratory-Scale Rockburst Physical Model Testing Using a True-Triaxial Cell,” *2022 European Rock Mechanics Conference (Eurock 2022)*, Espoo, Finland, September 12-15, 2022.

Wibisono, D.Y.\*, Arora, K. and Gutierrez, M. (2022), “Laboratory Characterization of a Synthetic Sandstone,” *Proc. 56th US Rock Mechanics/Geomechanics Symposium*, Santa Fe, New Mexico, USA, 26-29 June 2022, paper no. ARMA 22–60.

Gutierrez, M., Wibisono, D.Y.\* and Majumder, D. (2023), “Investigation of Tunnel Spalling Using Scale Model True-Triaxial Experiment,” *Proc. 15th International Conference on Underground Construction* (Prague 2023), Prague, Czech Republics, May 29-31, 2023.

#### **4 Outcomes**

The designed experimental setup has been successful in studying the failure behavior of tunnels constructed in brittle ground conditions. Further, the proposed experimental procedure can be helpful in determining and mitigating potential catastrophic failures of tunnels in brittle and valuable for the appropriate design of appropriate tunnel supports.

#### **5 Impacts**

The research contained in this report, submitted journal publications, conference presentations and Ph.D. thesis provides the basis for the time-dependent behavior of tunnels in squeezing ground. The new approach will allow for a more scientific, data driven, and logical evaluation of the interaction between the tunnel support system and the squeezing ground.